UNIVERSITÄT BREMEN

GEOCHEMICAL MODELS OF SB(-AS,AU,AG) MINERALIZATION IN ARCHAEAN AND MODERN HYDROTHERMAL SETTINGS

-

Examples from the Murchison Greenstone Belt and the Manus back-arc basin

DISSERTATION

zur Erlangung des
Doktorgrades der Naturwissenschaften
(Dr. rer. nat.)
am Fachbereich Geowissenschaften
der Universität Bremen

vorgelegt von

Nikki Blaauwbroek

Bremen, Okt 2016

Referent:

Prof. Dr. Wolfgang Bach

Koreferent:

PD Dr. Frank Lisker

Contents

Contents

List of Figures **V**

List of Tables **IX**

List of Minerals **XI**

Abbreviations **XIII**

Abstract **XV**

Kurzfassung **XIX**

Acknowledgements **XXIII**

1 Introduction **1**
- 1.1 Historical uses of antimony (Sb) 1
- 1.2 Physicochemical properties and geochemical behavior of Sb 3
- 1.3 Types of antimony deposits 4
- 1.4 Types of antimony deposits 8
- 1.5 Archaean VMS-mineralization 12
- 1.6 Modern arc and back arc basins 13
- 1.7 Hydrothermal activity at back-arc basins 15

2 Motivation and outline **21**
- 2.1 Motivation 21
- 2.2 Outline 23
- 2.3 Scientific contributions 26

3 A geochemical model of the Sb-As mineralization in the Murchison Greenstone belt **29**

3.1 Introduction 32
3.1.1 Regional geology 36
3.2 Methods 38
3.3 Results 41
3.3.1 Fieldwork 41
3.3.2 Petrography and mineral chemistry 48
3.3.3 Trace element compositions of carbonates 52
3.3.4 Stable isotope compositions and geothermometry 55
3.3.5 Geochemical calculations and reaction path model results 58
3.4 Discussion 69
3.4.1 Fluid source and temperatures of mineralization 69
3.4.2 Paragenetic constraints on metasomatic mass transfers in the different lithological units 73
3.4.3 Trapping mechanisms of Sb enrichment in the AL – the role of metasomatic reactions 76
3.5 Summary and conclusions 83
3.6 Acknowledgements 83

4 Sb-As-Au mineralization at the Murchison Greenstone Belt, South Africa 93

4.1 Introduction 95
4.1.1 The Murchison Greenstone Belt 96
4.2 Methods 98
4.3 Results 103
4.3.1 Fieldwork 103
4.3.2 Petrography and bulk mineralogy 105
4.3.3 Major and minor metal concentrations 118
4.3.4 Geochemical modelling 126
4.4 Discussion 134
4.4.1 Orogenic gold deposit style 134
4.4.2 Sb-As-Au mineralization 136
4.4.3 Model results 137
4.5 Conclusions 138
4.6 Acknowledgments 139

5 Geochemical modeling insight into Sb-As-Au-Ag mineralization at the PacManus basin, Papua New Guinea 147
5.1 Introduction . . . 149
5.1.1 Sb, As, Au and Ag enrichment in arc and back-arc settings . . . 150
5.2 Regional background hydrothermal system PACManus . . . 153
5.2.1 Prominent vent sites located at PACManus site . . . 155
5.3 Materials and Methods . . . 158
5.4 Results . . . 162
5.4.1 Fluids samples . . . 162
5.5 Whole rock dataset . . . 167
5.6 Geochemical models . . . 179
5.7 Discussion and conclusion . . . 189
5.7.1 Role of magma degassing . . . 190
5.7.2 Transport and deposition . . . 192
5.7.3 Zone refining and supergenous enrichment as trapping mechanisms . . . 194
5.8 Acknowledgements . . . 197

6 Summary and Outlook 207

List of Figures

1.1 Industrial use of antimony 2
1.2 Antimony world production and reserve 3
1.3 Orogenic gold deposits 5
1.4 Distribution of Archaean cratons and greenstone belts 9
1.5 Sketch of a typical Archaean greenstone belt 11
1.6 Localities of Au deposits 13
1.7 Localities of hydrothermal systems 15

3.1 Geological map of the Murchison Greenstone Belt 33
3.2 Linear relationship between temperature and ΔMgs-Dol 40
3.3 Photos of sample locations I 44
3.4 Photos of sample locations II 45
3.5 BSE images 50
3.6 Paragenetic sequence I 51
3.7 Paragenetic sequence II 52
3.8 Composition plot of carbonates 56
3.9 Cr_2O_3 vs Mg# of fuchsite, chlorite and dravite 57
3.10 Histogram Sb content 61
3.11 REE+Y of carbonates 62
3.12 Stable isotope of dolomite and magnesite 63
3.13 Activity diagram for Fe-Sb-Cu-S-O-H at 250 and 350 C 66
3.14 Reaction path modeling up to 600 °C 67
3.15 Reaction path modeling from 500 to 300 °C 68

4.1 Geological map of Murchison Greenstone Belt 99
4.2 XRD plot of A080 107
4.3 XRD plot of M121 107
4.4 Plate A080 108
4.5 Plate A082 109
4.6 Plate B028 110

4.7 Plate B033 111
4.8 Plate Bm048 112
4.9 Plate M122B 113
4.10 [Plate M123 114
4.11 Plate M124 115
4.12 Plate M126 116
4.13 Plate Mm107 117
4.14 Metal trace content 121
4.15 Elemental map of arsenopyrite 125
4.16 Elemental map of stibnite 126
4.17 Activity diagrams of Fe-Sb-S-O; 150-500 °C 127
4.18 Activity diagrams of Fe-As-S-O; 150-400 °C 129
4.19 Activity diagram of Sb and Sb at 400 °C with varying concentrations . . . 129
4.20 Activity diagram of Sb-minerals at 250 °C 130
4.21 Activity diagram of Sb at 250 °C 131
4.22 Activity diagram of Sb at 350 °C 131
4.23 Activity diagram of Sb-Cu at 350 °C 132
4.24 Activity diagram of As-Cu at 350 °C 133
4.25 Activity diagram of Au at 250 and 350 °C 133

5.1 Geological map of the Manus Basin 153
5.2 Detailed bathymetry map of Fenway, Satanic Mills and Roman Ruins . . 155
5.3 Photographs at the Bambus cruise (2011) (Bach et al., 2011). 156
5.4 Fluid samples I 163
5.5 Fluid samples II 165
5.6 Fluid samples III 166
5.7 Fluid samples IV 167
5.8 Plate of thin sections 168
5.9 Whole rock dataset sorted by locality 174
5.10 Whole rock dataset sorted by vent type 175
5.11 Mineral mode open conduit system 176
5.12 Mineral mode massive sulfide system 176
5.13 Mineral mode diffuser system 177

5.14 Mineral mode inactive system 177
5.15 Solubility of Sb, As, Au and Ag 180
5.16 T-X sections of Fenway 183
5.17 T-X sections of Roman Ruins 184
5.18 T-X sections of Satanic Mills 185
5.19 Step by step reaction path modeling, simulating zone refining 186
5.20 pH dependence 187
5.21 Zone refining plot of Satanic Mills 188
5.22 Zone refining plot of Fenway 189

List of Tables

3.1 Sb-hosted Precambrian and younger suture zones 34
3.2 ΔDol-H_2O values at 293-673 K 40
3.3 Sample description 42
3.4 Mineral formula's of chlorite, fuchsite and dravite 49
3.5 Stibnite 53
3.6 Arsenopyrite 55
3.7 Average REE+Y values of carbonates 58
3.8 Stable isotope of dolomite and magnesite 59
3.9 Temperature calculations 60
3.10 Temperature and ΔDol-H_2O calculation 60

4.1 Sample summary and methods employed. 98
4.2 Log K values Sb-species 100
4.3 Log K values As-species 101
4.4 Log K values Au-species 101
4.5 Log K values Sb-As minerals 102
4.6 Petrological overview of most prominent sulfide minerals at MGB 106
4.7 EMPA results of pyrite 119
4.8 EMPA results of pyrrhotite 120
4.9 EMPA results of chalcopyrite 122
4.10 Metal trace content 123

5.1 Fluid samples dataset 164
5.2 Overview vent sites and vent types 169
5.3 Whole rock dataset 170
5.4 Mineral mode calculations 172

List of Minerals

STIBNITE	Sb_2S_3
TRIOXIDE	Sb_2O_3
PENTOXIDE	Sb_2O_5
SODIUM ANTIMONATE	$NaSbO_3$
TRISFULFIDE	Sb_2S_3
PENTASULFIDE	Sb_2S_5
TRIACETATE	$Sb(CH_3COO))_3$
SENARMONTITE	Sb_2O_3
JAMESONITE	$Pb_4FeSb_6S_{14}$
BERTHIERITE	$FeSb_2S_4$
GUDMUNDITE	$FeSbS$
ULLMANNITE	$NiSbS$
VALENTINITE	Sb_2O_3
GERSDORFFITE	$NiAsS$
WESTERVELDITE	$(Fe, Ni)As$

Abbreviations

AL	Antimony Line
AVF	Arc volcanic front
BABB	Back arc basin basalt
DT	Djual Transform
EMB	East Manus Basin
ETZ	Extensional Transform Zone
MSC	Manus Spreading Center
MGB	Murchison Greenstone belt
MOR	Mid Oceanic Ridge
SEDEX	Sedimentary exhalative deposits
SER	South Eastern Ridges
VMS	Volcanogenic massive sulfide
WT	Weiting Transform

Abstract

The topic of this PhD project was to deduce new geochemical models of Sb(-As,Au,Ag) mineralization in Archaean and modern hydrothermal settings by studying extended datasets from the Murchison Greenstone Belt (MGB) and the Manus back-arc basin. To emphasize the parallels of the Antimony deposit (AL) deposit with modern back-arc massive sulfide mineralization systems, an in depth qualitative and quantitative research of the Sb(-As, Au, Au) behavior in magmatic-hydrothermal hypogene and supergene deposits has been performed. The MGB has been interpreted as an Archaean orogenic gold deposit, which has been formed under greenschist facies conditions with hydrothermal alteration assemblages developed whilst undergoing ductile to brittle deformation, with temperatures around 200-420 °C and CO_2-rich fluids. The primary mineralization is connected to an ore fluid originating from a granitoid magmatic or a metamorphic devolatization model, where the phase relations clearly indicate a shift from low $f\ S_2$ and low $f\ O_2$ to high $f\ S_2$ and low $f\ O_2$, caused by carbonation and silification. These alteration processes have been identified in this study were induced by serpentinization and listvenitization, caused by alteration and metasomatic reactions involving meta-ultramafic rocks and felsic protoliths. From these results I propose that metasomatic reactions involving ultramafic rocks may make for efficient traps of Sb and likely other elements, like As, Ag, and Au.

The Sb, As, Ag and Au enrichments at the VMS deposit at PACManus are more pronounced by a complex reaction path of magmatic degassing influenced by deep-seated seawater-rock interaction of zone refining as well as near-seafloor sulfide deposition of supergeneous enrichments, consequently re-working the primary sulfide mounds at a sweet spot around 270 °C and pH between 2-3.

The dominant Sb species responsible for the Sb enrichments at these hydrothermal systems at temperatures between 250-400 °C has been deduced to be the oxidized $Sb(OH)_3$, whereas main epithermal Sb-mineralization at $T < 150$ °C is related to reduced bisulfide Sb-complexes. A further striking and important observation is the unmistakable strong correlation between the geochemical behavior between As-Ag and Sb-Au. These results imply that Sb is still present within hydrothermal systems at higher temperature and therefore could play an essential role within Au-rich hydrothermal ore deposits. The complexity of the geochemical behavior of Sb-Au is explained by the contradicting behavior of reduced and oxidized complexes of Sb and Au (as well as As and Ag). This study has shown that slight variations in temperature, oxygen fugacity and pH of the percolating carrier fluid in combination with variations in buffering capacities of host rock material can cause great diversities in metal and metalloids speciation within ore deposits. Furthermore, the importance of geochemical analyses of non-prominent metal concentrations within the field of ore petrology should be acknowledged.

Kurzfassung

Im Rahmen dieser Doktorarbeit wurden auf Grundlage von umfangreichen Datensätzen aus dem Murchison Greenstone Belt (MGB) und dem Manus Backarc-Becken neue geochemische Modelle zur Sb (± As ± Au ± Ag) Mineralisation in archaischen sowie rezenten Hydrothermalsystemen entwickelt. Um die Parallelen zwischen den archaischen Vererzungen der Antimonlinie und rezenten Backarc Massivsulfidmineralisationen herauszuarbeiten wurden umfassende qualitative und quantitative Untersuchungen des geochemischen Verhaltens von Sb (± As ± Au ± Ag) in magmatisch bis hydrothermalen hypo- und supergenen Ablagerungen durchgeführt. Der Murchison Greenstone Belt wird hierbei als orogene Goldlagerstätte interpretiert, die unter Herausbildung einer Hydrothermalalterationsparagenese in einer duktil-spröden Deformation vor dem Hintergrund von grünschieferfaziellen Bedingungen von 200-420 °C und unter Beteiligung eines CO2-reichen Fluides entstanden ist. Das die primäre Mineralisation herbeiführende vererzende Fluid in diesem System kann entweder durch ein granitoid-magmatisches oder durch ein metamorphes Devolatilisierungsmodel erklärt werden. Die untersuchten Phasenbeziehungen deuten klar auf eine Verschiebung von anfänglich niedrigen S2 und O2 Fugazitäten zu später deutlich erhöhten S2 bei gleichbleibend niedrigen O2 Fugazitäten hin. Die beobachteten metasomatischen Alterationsprozesse sind Folge einer Serpentinisierung und Listvenitisierung von Metaultramafiten sowie eines felsischen Protoliths. Die Ergebnisse dieser Untersuchungen implizieren, dass diese Art von metasomatischer Alteration ultramafischer Lithologien einen wirkungsvollen Mechanismus zur Anreicherung von Sb und potentiell weiteren Elementen wie As, Ag und Au darstellt. Die Anreicherungen von Sb, As, Ag und Au in volcanogenic massive sulfide (VMS) Lagerstätten am PACManus Hydrothermalfeld werden durch einen komplexe Reaktion aus magmatischen Entgasungsprozessen verstärkt. Diese werden zum einen durch tiefe, hypogene, ein sukzessives Zonerefining nach sich ziehende Meerwasser-Gesteins Wechselwirkungen beeinflusst und des Weiteren durch ein meeresbodennahe, supergene Sulfidanreicherung, die sich in einer fortgesetzten Umlagerung der primären Sulfidablagerung äußert. Optimal läuft letzterer Prozess bei Bedingungen nahe 270 °C und einem pH zwischen 2 und 3 ab.

Bei der Anreicherung von Antimon in diesen Hydrothermalsystemen dominiert für den Temperaturbereich von 250 bis 400 °C die oxidierte Sb(OH)3 Spezies, wohingegen unterhalb von 150 °C die dann dominierenden Bisulfid Sb-Komplexe den größten Einfluss auf die resultierende Antimonmineralisation haben. Von maßgeblicher Bedeutung ist außerdem eine festgestellte starke Korrelation zwischen dem geochemischen Verhalten von As-Ag und Sb-Au. Die Beobachtungen legen nahe, dass Antimon auch bei höheren Temperaturen noch in signifikanten Mengen in Hydrothermalsystemen auftreten und somit auch eine entscheidende Rolle bei der Bildung von Au-reichen hydrothermalen Lagerstätten spielen kann. Hierbei lässt sich die Komplexität des wechselseitigen geochemischen Verhaltens von Sb und Au durch das gegensätzliche Verhalten von reduzierten und oxidierten Sb und Au bzw. As und Ag Komplexen erklären.

Die vorliegende Arbeit zeigt auf, wie kleine Veränderungen in Temperatur, Sauerstofffugazität und pH des die Lithologie durchströmenden Trägerfluids in Kombination mit Variationen in der Pufferkapazität des infiltrierten Gesteins zu einer großen Vielfalt an Metall- und Metalloidspezies in Erzlagerstätten führen kann. Die Ergebnisse demonstrieren zudem wie eine detaillierte Charakterisierung von bestimmten untergeordneten Metallgruppen bei dem Verständnis solcher Systeme helfen kann und sie unterstreichen somit deren Bedeutung für das Feld der Lagerstättenpetrologie insgesamt.

Acknowledgements

I am sincerely thankful for the contribution and support during this thesis by my direct supervisor at the University of Bremen, Wolfgang Bach. I truly appreciate his help, feedback and the amount of time, he invested in me and this project. I am also very grateful to dr. Ulrich Schwarz-Schampera (BGR) for initiating this project and providing me with the opportunity to conduct this Phd project. Furthermore, I would like to thank Frank Lisker for being the second supervisor and reviewing this thesis. I am grateful for Andreas Klügel, Stephan Sopke and Niels Jöns for providing help with both LA-ICPMS and EMPA measurements. Additionally, I would like to thank is Michael Hentscher, for his contribution and discussions on various modeling prospects.

Also, I like to thank all my colleagues, Svenja, Karin, Basti, Christian, Janis, Alex, Andreas, Stefan, Wolf-Achim and Patrick for the pleasant time. Finally I would like to thank Dominik, for always believing in me and providing support wherever it was necessary as well as my friends and family for their impecable patience with me during this project.

Chapter 1

Introduction

1.1 Historical uses of antimony (Sb)

Humankind has known the element metal Sb for at least 6 centuries. Both stibium and antimonium have mutually been used as the name for the element for centuries, where antimonium comes from the Greek words anti (against) and monos (alone) (Wang, 1919; T. Li et al., 1992). Throughout the oldest parts of history the main uses of antimony has been medical and cosmetic. Even though nowadays, the scientific world acknowledges the health hazards like skin irritation when in contact with the skin and even to be lethal, similar to arsenic, when swallowed (Australian Drinking Water Guidelines), this seemed to not have bothered the ancient Egyptians. They used the mineral Stibnite (Sb_2S_3) as the main ingredient for kohl and smeared it on their eyes to create the characteristically known eye-make up. And the Greek recommended stibnite as a cure for skin ailments. The Egyptians used Sb also as plating on copper articles by the middle of the third millennium B.C. (Butterman and Carlin, 2004). From the Middle Ages on, medical uses to aid ulcers continue to exist. More procedures are being explored and antimony is started to be used to create the reflecting surface in mirrors and is added to bell metal to generate more tones (T. Li et al., 1992).

Even though the Chaldeans tought themselves the art of winning the Sb from its ores,

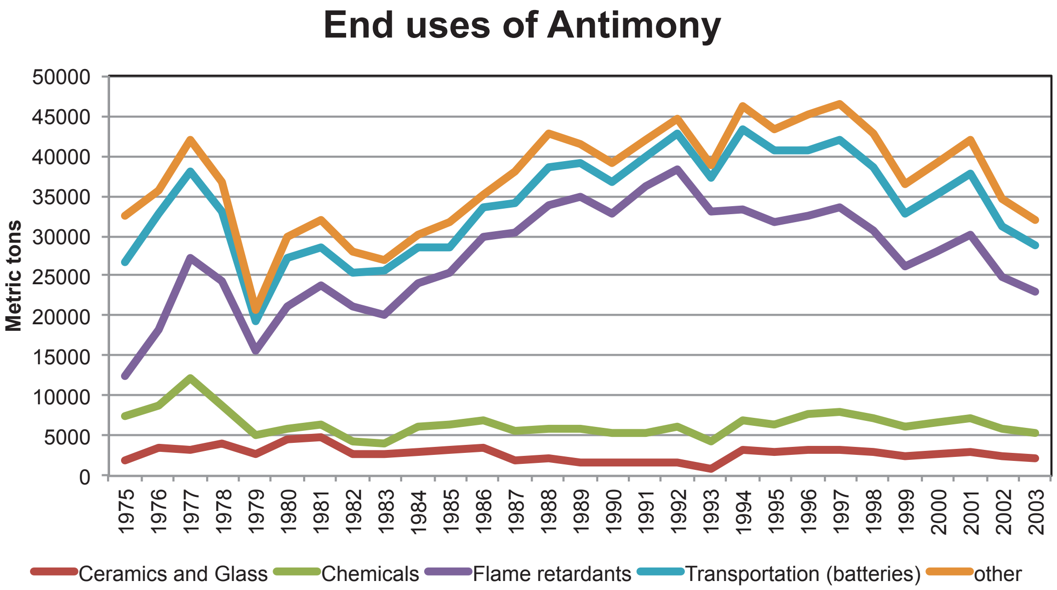

Figure 1.1: U.S. end uses of antimony. Other industrial meanings, such as ammunitions, cable coverings, fireworks, metal castings, paper, pigments, rubber products and sheet, pipe and type metal (USGS, 2015b).

Basil Valentile, an alchemist between 1350 and 1600 A.D., published his treatise “The Triumphal Chariot of Antimony”. Whereas he wrote for the first time the extraction of metallic antimony from its ore, he is known to be the one ‘discovered’ the element (K. Li, 1953).

Throughout the 19th century, the number of uses for antimony remained small. A brittle lead alloy was founded and been used for the spherical bullets contained used in both WWI and WWII (Butterman and Carlin, 2004). Furthermore, antimony-lead alloys were largely incorporated in batteries. Nowadays antimony is used for flame-retardant materials for metals and textiles, chemicals, glass, batteries and plastics (Figure 1.1).

In these applications, a large number of synthetic antimony compounds are being used in the industry. These are based on the trioxide (Sb_2O_3), for example pentoxide (Sb_2O_5), sodium antimonate ($NaSbO_3$), trisfulfide (Sb_2S_3), pentasulfide (Sb_2S_5) and the triacetate ($Sb(CH_3COO))_3$). These synthetics are applied as flame retardants,

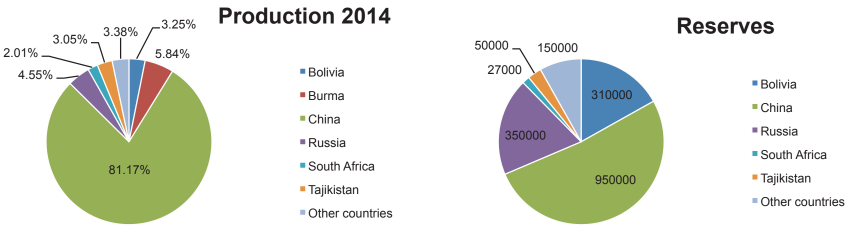

(a) Antimony world production. **(b)** Antimony world reserves

Figure 1.2: Antimony world production of a total 160,000 ton and reserves of 2014 (USGS, 2015a).

pigments, heat and radiation stabilizers for plastic and catalyst precursors (Butterman and Carlin, 2004; USGS, 2015b). Due to its hardness, brittleness and lack of malleability, antimony in native state has no commercial uses as material. Instead it is a minor component in many lead- and tin-based alloys (Butterman and Carlin, 2004).

1.2 Physicochemical properties and geochemical behavior of Sb

Antimony, with atomic number 51 and atomic weight 121.75, is located in period 5, group 11 of the periodic table and is a lustrous tin-white metalloid of the arsenic group. It naturally occurs in four oxidation states: +5, +3, 0, -3 and has two stable isotopes: ^{121}Sb (57.25 wt%) and ^{123}Sb (42.75 wt%). Additionally, around 35 radioactive isotopes of Sb are known.

Antimony is a poor conductor of heat and electricity. Moreover it is hard and brittle and easily crushed into powder. The melting temperature of Sb is 630.6 °C, and has a hardness of 3 to 3.5 on the Mohs scale and ±55 on the Brinell scale. Moreover, Sb crystallizes in the rhombohedral class of the hexagonal system. Oxidation of stibnite forms senarmontite (Sb_2O_3) as the most common phase.

Due to its position in the periodic table between the metals and nonmetals, Sb together with silicon, germanium, arsenic and tellerium has been classified as a semimetal or metalloid. Antimony is a chalcophile element, similar to As, Hg and Pb, and the geochemical behavior is intermediate between that of Hg and Pb (Pohl, 2011).

The average concentration of antimony in the Earth's crust is 0.15-1 ppm, which is less than tin, arsenic and REE though more than bismuth, mercury, or silver. It's abundance in lower in igneous rocks (around 0.2 ppm) when compared to pelitic sediments (ca. 2 ppm) (Pohl, 2011). Like mercury and arsenic, antimony is commonly concentrated in near-surface epizonal hydrothermal systems typically associated with volcanic-hydrothermal systems in convergent margin settings. The solubility of Sb in aqueous solution is governed by its complexation in hydrothermal fluids and ligands may be derived from water-rock reactions, degassing magma, or from pelites enriched in organic matter. Mobilization of antimony is mostly observed in contact metamorphism or of orogenic metamorphism (Pohl, 2011). On the other hand it seems to be immobilized by enriching iron oxy hydroxides. It has been thought that Sb solubility is mainly controlled by temperature, when looking at concentrations within fluids: ±10,000 ppm at 300 °C and ±1 ppm at 100 °C (Pohl, 2011).

1.3 Types of antimony deposits

Major producers of antimony are, in order of importance: China, Bolivia, Russia, South Africa and Tajikistan (Figure 1.2a) (Carlin, 2011; USGS, 2015b). The most common and economically most important antimony ore mineral are stibnite (Sb_2S_3) and jamesonite ($Pb_4FeSb_6S_{14}$), which may host traces of Au, Ag, Fe and Cu (Pohl, 2011). Other common Sb sulfides include berthierite ($FeSb_2S_4$) and gudmundite (FeSbS) as

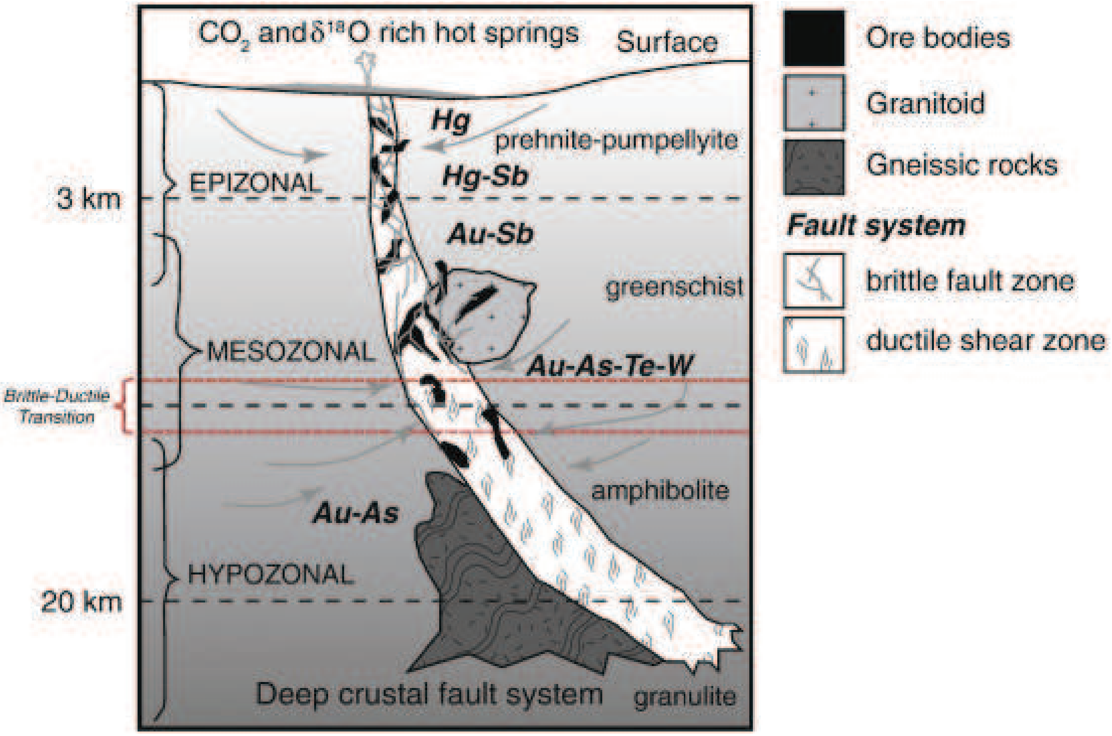
CO2 and δ18O rich hot springs
Surface
Hg
prehnite-pumpellyite
Hg-Sb
EPIZONAL
3 km
Au-Sb
greenschist
MESOZONAL
Au-As-Te-W
Brittle-Ductile Transition
amphibolite
Au-As
HYPOZONAL
20 km
Deep crustal fault system
granulite
Ore bodies
Granitoid
Gneissic rocks
Fault system
brittle fault zone
ductile shear zone

Figure 1.3: An overview of orogenic gold deposits at different depths, showing Au-Sb mineralization in the epizonal-mesozonal zone in greenschist facies (Goldfarb and Groves, 2015).

well as ullmannite (NiSbS). Important oxides of Sb are senarmontite (Sb_2O_3) and valentinite (Sb_2O_3), associated with arsenic, bismuth or silver in sulfide ores Pohl (2011).

Antimony is commonly distributed throughout many different types of mineral deposits and displays no evident affinity to any particular metallogenic period or province (Boyle and Jonasson, 1984). Antimony is one of the main ore-forming elements not only at antimony deposits, where it is present in ores as stibnite, berthierite, gudmundite, but also prominently present at more complex deposits, such as Au-Sb, Ag-Sb, Pb-Zn-Sb, Hg-Sb, Hg-Sb-W mineralizations. At these more complex settings, antimony will mineralize as both sulfides and sulfosalts containing Cu, Pb, Ag, Bi, Hg (Obolensky et al., 2007). Additionally, many of the stibnite deposits are related to deep-seated fracture systems often graben or uplifted orogenies (Boyle and Jonasson, 1984).

Several attempts have been made of grouping this extensive mineralization behavior of antimony into low temperature hydrothermal and metamorphogene-hydrothermal settings from solutions of different compositions and origins (Boyle and Jonasson, 1984; Obolensky et al., 2007; USGS, 2015a).

1. *(Low temperature) hydrothermal Sb deposits within plate rifting settings.* (e.g. volcanic massive sulfide ore (VMS); sedimentary exhalative deposits (SEDEX) and Carlin type gold deposits). These deposits form below 200 °C and 100-600 bars. The temperature gradient does not exceed 7-12 °C/100 m. The metal-enriched fluids range from diluted chlorite-carbonate composition and chloride-bicarbonate to highly concentrated chloride mixed with dissolved CO_2 and minor N_2 and H_2S gases (Obolensky et al., 2007). The hydrothermal-exhalative sedimentary deposits (SEDEX) are predominantly present within China and dominate the antimony mining industry and thus commercially consumed antimony (Figure 1.2a). The SEDEX sulfide formation forms in stratiform sequences, when hydrothermal fluids seep into a brine-type water reservoir like the ocean (Herzig, 2000). The Carlin-type gold deposits are epizonal hydrothermal (oxidized) replacements ore within sediments, predominantly limestone and dolomite (Boyle and Jonasson, 1984; Volkov et al., 2006)

2. *Sb and Sb-Hg deposits in subaerial volcanic belts on active continental margins.* These deposits form in subsurface conditions with a high vertical temperature gradient of 30-35 °C/100m. The temperatures decreases from early stage of mineralization to the final stage of mineralization. The mineral-forming fluids have low concentrations of salt and are originated from mixed fluid within recycling

hydrothermal settings. The dominant gas phases are CO_2 and N_2, with minor CH_4 and H_2S (Obolensky et al., 2007).

3. *Gold antimony metamorphogene-hydrothermal deposits.* These deposits form within orogenies with temperatures between 380-120 °C and varying pressures. The fluid composition is enriched in CO_2 (up to 60 wt.%) and varying amounts of sulfurous-chloride (Obolensky et al., 2007). The ore are located within gold-quartz veins, stockworks and carbonated silificied zones. The host rocks vary between greenstones, but also greywacke-slate sequences and granitic rocks (Boyle and Jonasson, 1984).

However, the last two deposits described can be considered two of the most important distinct settings for antimony enrichment: the (Archaean) gold deposits enriched both in antimony and arsenic and the gold deposits in greywacke-slate-graphitic schist assemblages (Boyle and Jonasson, 1984). The antimony ore deposits associated with orogenic gold systems (Figure 1.3) is more numerous in young orogenic belts, related to andesite and rhyolite volcanism, due to erosion resulting in loss of near-surface formations (Pohl, 2011). However, several orogenic gold deposits have been preserved within Archaean greenstone belt (Boyle and Jonasson, 1984; Powell et al., 1991), such as the Murchison Greenstone Belt (South Africa) which has been interpreted as an epizonal example of an orogenic gold system (Pohl, 2011; Jaguin et al., 2014). Here, komatiites have been altered into massive talc-carbonate rocks in greenschist facies by hydrothermal alteration along a shear zone that extends over 55 km (Davis et al., 1986).

1.4 Types of antimony deposits

Archaean greenstone belts

The first time the term ‘greenstone belt’ was mentioned when the Canadian Geological Survey attempted in the 1900’s to describe the geology of Northwestern, Canada, nowadays known as the Superior Craton (Figure 1.4). Following this event, the term ‘greenstone’ has never had an explicit description throughout time due to the complexity of the deformed and metamorphosed Archaean cratons and surroundings (Anhaeusser, 2014). Within this dissertation the term ‘greenstone belt’ will be used by the definition summarized by Anhaeusser (2014):

Deformed and metamorphosed volcano-sedimentary successions, generally enveloped by Archaean (>3600 to ±2500 Ma) granitic and gneissic rocks.

A distinction is made between these and Archaean volcano-sedimentary basins, which are developed on top of continental basement instead of intracratonic Archaeanic basins. Furthermore, the term has been used alternately with *schist belts* and *gold belts*, due to substantial amounts of gold deposits located within shear zones have been found (Powell et al., 1991; Anhaeusser, 2014).

Overall, the oldest rocks on Earth have been dated between >4.0-3.2 Ga (Hadean-Palaeoarchaean) and have been found in small crustal regions, called granite-greenstone terranes, within relics of Archaean (3200-2500 Ma) cratonic basement which have been tectonically stable since the Archean, spread out over the world (Figure 1.4) (Kusky and Polat, 1999; Anhaeusser, 2014). Archaean cratons encompass mainly three different domains, which can be characterized as a regional-metamorphosed stratigraphic sequence (Anhaeusser, 2014). These involve (1) low-grade volcano-sedimentary greenstone belts surrounded by (2) high-grade tonalitic gneisses or plutons and amphibolites and gener-

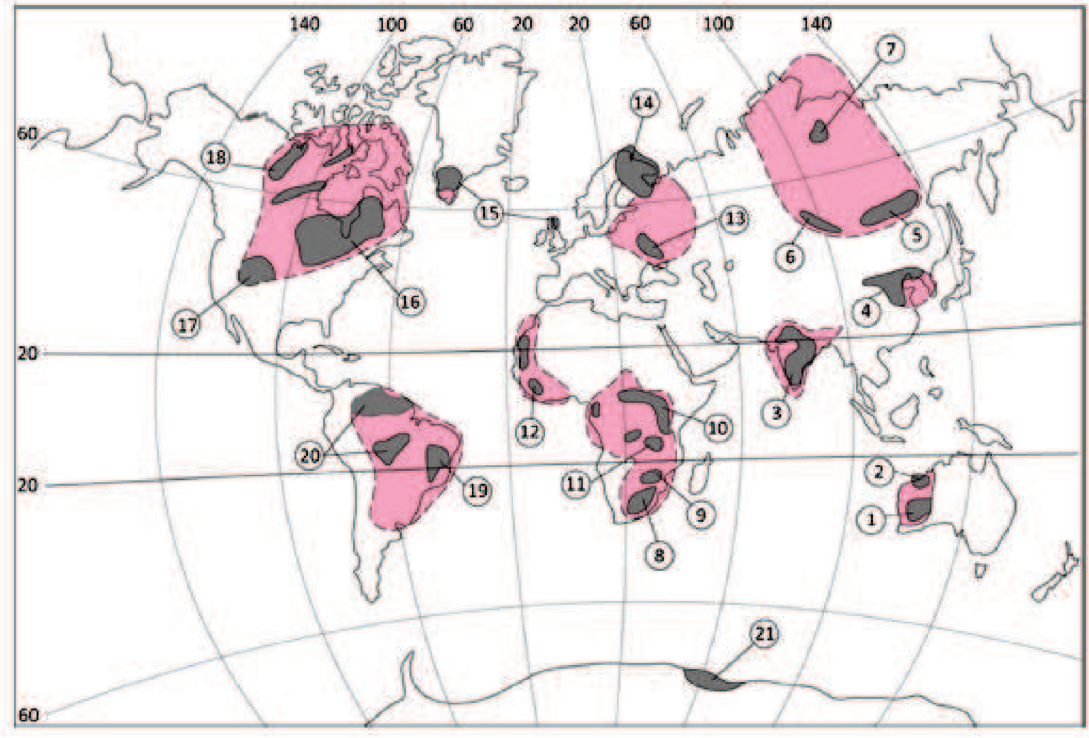
140
100
60
20
20
60
100
140
60
20
20
60
1
2
3
4
5
6
7
8
9
10
11
12
13
14
15
16
17
18
19
20
21

Figure 1.4: Overview Archaean cratons and greenstone belts. The areas shown in pink are poorly known, but are considered to be underlain mostly by Archaean-Proterozoic terranes. Key to major provinces: 1 = Yilgarn, 2 = Pilbara, 3 = Indian, 4 = North China, 5 = Aldan-Stanovik, 6 = Yenisei, 7 = Anabar, 8 = Kaapvaal, 9 = Zimbabwe, 10 = Central African (Tanzanian and northeastern Zaire), 11 = Kasai, 12 = West African (Liberia, Sierra Leone, Mauritania), 13 = Ukranian, 14 = Baltic-Svecofennian (Inari-Kola, Karelian), 15 = North Atlantic (Greenland, Scotland), 16 = Superior, 17 = Wyoming, 18 = Slave, 19 = São Francisco, 20 = Amazonian (Guiana, Guaporé), 21 = East Antarctica (Anhaeusser, 2014).

ally intruded by (3) later granitoids covered by sediments (Figure 1.5) (Gorman et al., 1978; K Condie, 1976; Anhaeusser, 2014).

The volcanic segments can be subdivided into an ultramafic group (Mg-rich, such as komatiite, komatiitic-basalt and tholeiite) and a greenstone group (containing a range from minor ultramafic rocks, tholeiite, to andesite and calc alkaline and felsic volcanics) (Anhaeusser, 2014).

These Archaean granite-greenstone terranes have further been metamorphosed in the course of a complex series of structural and magmatic events. First of all, buoyant slabs of Archaean oceanic lithosphere may have been underplating the simultaneously thinning crustal roots, causing LP-HT metamorphism. Dehydrated subducted slabs generated magmas of the sanukitoid suite, whereas the hydrated magmas, produced the TTG suite (Powell et al., 1991; Kusky and Polat, 1999). Secondly, eventual collision with continental blocks formed anatectic granites and thickened the crust to a point where gravitational collapse and triggered decompressional release of granitoids. Moreover fragments of mantle wedge were often trapped between the continental and oceanic crust. Thirdly, shear and suture zones provided pathways for fluids and granitoids to migrate into the mid- and upper crust, supposedly accountable for gold mineralization (Powell et al., 1991; Kusky and Polat, 1999).

Orogenic lode gold deposits, of Middle Archean to Tertiary age, are perhaps the largest gold deposit type existing in metamorphic belts, with several giants (>250 t Au) deposit examples (Figure 1.3) (Groves et al., 2003). These deposits are miscellaneous in means of age, geometry and structural control, though entailing different host rocks reaching upper greenschist facies (250-500 °C; 0.5-5 kbars), with carbonate-muscovite-biotite alterated wall rock associations with varying enrichments of Ag, As, B, Bi, Cu, Pb, Sb, Te, W and Zn (Groves et al., 2003).

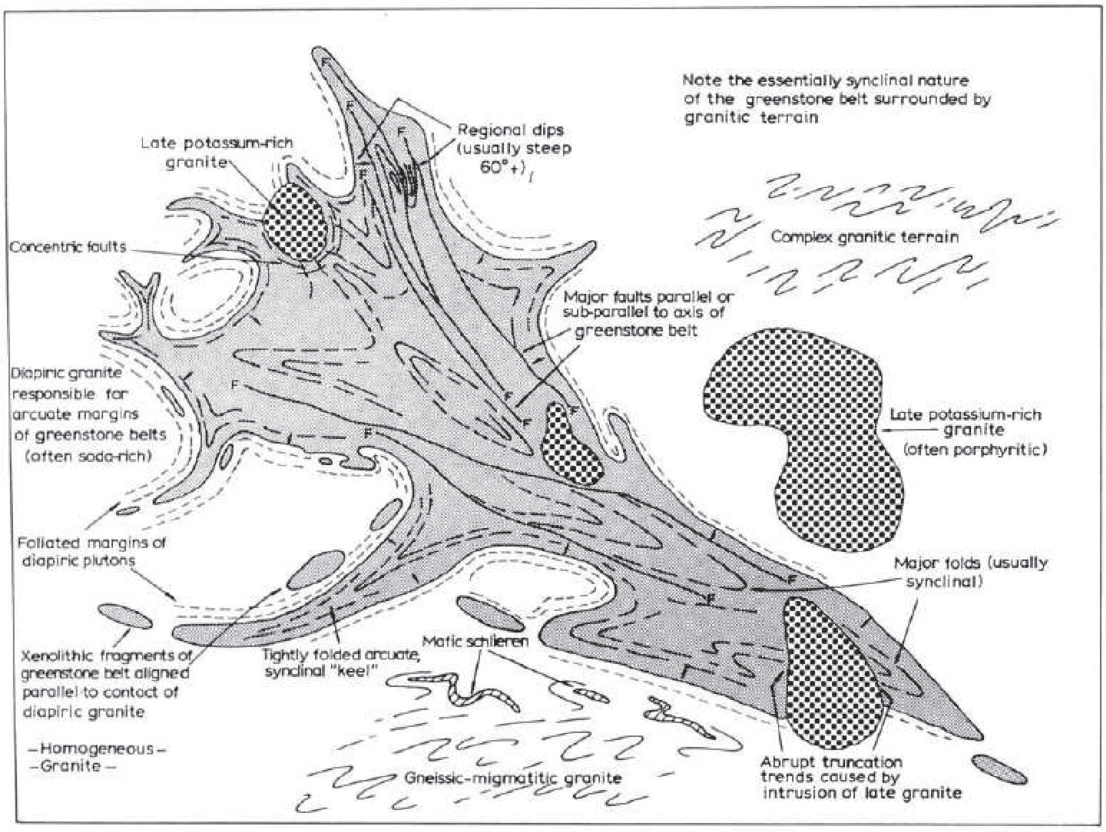
Note the essentially synclinal nature of the greenstone belt surrounded by granitic terrain
Late potassum-rich granite
Regional dips (usually steep 60°+)
Concentric faults
Complex granitic terrain
Major faults parallel or sub-parallel to axis of greenstone belt
Diapiric granite responsible for arcuate margins of greenstone belts (often soda-rich)
Late potassium-rich granite (often porphyritic)
Foliated margins of diapiric plutons
Major folds (usually synclinal)
Xenolithic fragments of greenstone belt aligned parallel to contact of diapiric granite
Tightly folded arcuate, synclinal "keel"
Mafic schlieren
–Homogeneous– –Granite–
Gneissic-migmatitic granite
Abrupt truncation trends caused by intrusion of late granite
F

Figure 1.5: Idealized sketch of a typical Archaean greenstone belt (K.C. Condie, 1981).

]

1.5 Archaean VMS-mineralization

Besides the orogenic lode gold deposits, VMS deposits are likewise widely acknowledged to be part of the oldest deposits on Earth (Anhaeusser, 2014; Hannington, 2014). Generally, two types of VMS deposits can be distinguished: the Ni-rich and Cu-Zn-rich deposits. The VMS (Ni-rich) deposits are best developed and preserved in the Canadian Shield and the Yilgarn Craton, W. Australia. The VMS (Cu-Zn-rich) deposits are well represented in the Abitibi Greenstone belt and to a lesser extent in the Superior Province. Smaller deposits of this type also occur in the Barberton and Murchison Greenstone belts in South Africa (Anhaeusser, 2014). The presence of the VMS deposits can defended by the geological setting of the Archaean greenstone belts which are considered to be spatially associated with convergent margins, (juvenile) island arcs, steep subduction zones, and rifted continental margins associated with early extension by back-arc development (Figure 1.6) (Kusky and Polat, 1999; Vearncombe and Kerrich, 1999; C. Scott et al., 2002).

The high-grade gneisses of the Archaean greenstone belts are believed to be originally thick crustal segments and the greenstone belts like shield volcanoes, which have been thrusted onto the crustal segments, together with seafloor sediments. This specific geological setting could be interpreted as an analogue with recent (back)-arc systems and thus an explanation for the Archaean VMS deposits (Gorman et al., 1978; C. Scott et al., 2002; Anhaeusser, 2014), due to the close proximity of back-arc basins with convergent plate boundaries (Martinez et al., 2007).

Volcanism plays a dominant role for VMS deposits and felsic volcanics are thought to be the principal hosts for about half of all VMS deposits (Boyle and Jonasson, 1984; Hannington, 2014), though a close link to bimodal basalt-rhyolite volcanism has been

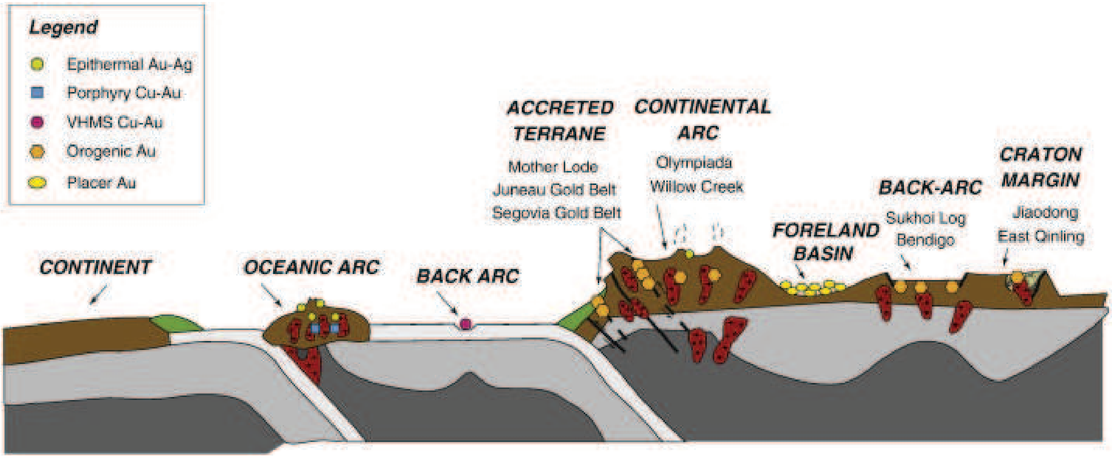
Legend
Epithermal Au-Ag
Porphyry Cu-Au
VHMS Cu-Au
Orogenic Au
Placer Au
ACCRETED TERRANE
Mother Lode
Juneau Gold Belt
Segovia Gold Belt
CONTINENTAL ARC
Olympiada
Willow Creek
CRATON MARGIN
Jiaodong
East Qinling
BACK-ARC
Sukhoi Log
Bendigo
FORELAND BASIN
CONTINENT
OCEANIC ARC
BACK ARC

Figure 1.6: Varying localities of epithermal, porphyry, VMS and orogenic gold deposits. Note the VMS deposit at back-arc settings (Goldfarb and Groves, 2015).

widely recognized (Anhaeusser, 2014). For the Cu-Zn-rich deposits, mafic volcanic rocks are the dominant volcanic host rocks, although felsic rocks are generally prominently present near most of the felsic volcanics and the corresponding deposits (Anhaeusser, 2014). Analogously, it is believed that the (Archaean) gold orogeny deposits are related to the recent-style volcanogenic massive sulfide (VMS) deposits (Figure 1.6) (Hannington, 2014; Goldfarb and Groves, 2015).

1.6 Modern arc and back arc basins

Back-arc basins are localities of extension and crustal accretion formed behind subduction zones (Martinez et al., 2007). Back-arc spreading zones can be interpreted as evolved island arc spreading systems, where arc volcanism can extend into back-arc volcanism, but typically has an abrupt trenchward limit and maximum subparallel to the trench. This process forms a chain of arc volcanoes, known as the arc volcanic front (AVF) (Martinez et al., 2007). The difference between back-arc basins and mid-ocean ridges is mainly based on the close proximity of back-arc basins to convergent plate boundaries (Martinez et al., 2007).

Back-arc basin basalts (BABB) are typically enriched in fluids, though less than the more hydrous arc volcanism nevertheless higher than open ocean ridge volcanism (Langmuir et al., 2006). The relative enrichment of fluids is caused by subducted lithosphere that releases water into the overlying mantle wedge through metamorphic breakdown of hydrated minerals at a range of depths down to 150-200 km (Martinez et al., 2007). Overall the BABB is known for its low FeO, MgO and TiO_2 and high Al_2O_3 + SiO_2 (Langmuir et al., 2006) contents

The island arc system can gradually evolve into mature back-arc spreading, due to changes in melt generations and modes of crustal accretion which affects the interaction of several subduction-related processes and conditions, like (Martinez et al., 2007):

1. Changes in mantle dynamics from flux-melting and buoyancy-driven upwelling at the arc volcanic front to decompression melting driven by plate separation at back-arc spreading centers;
2. Re-circulation of refractory material through arc and back-arc melting regimes by mantle wedge corner flow;
3. Changes in the locus of magmatic centers relative to the arc volcanic front;
4. Variable locus of initial rifting and breakup;
5. Spatially varying rheology attributable to mantle wedge hydration gradients with distance from the slab;
6. Slab subduction rate, dip and length.

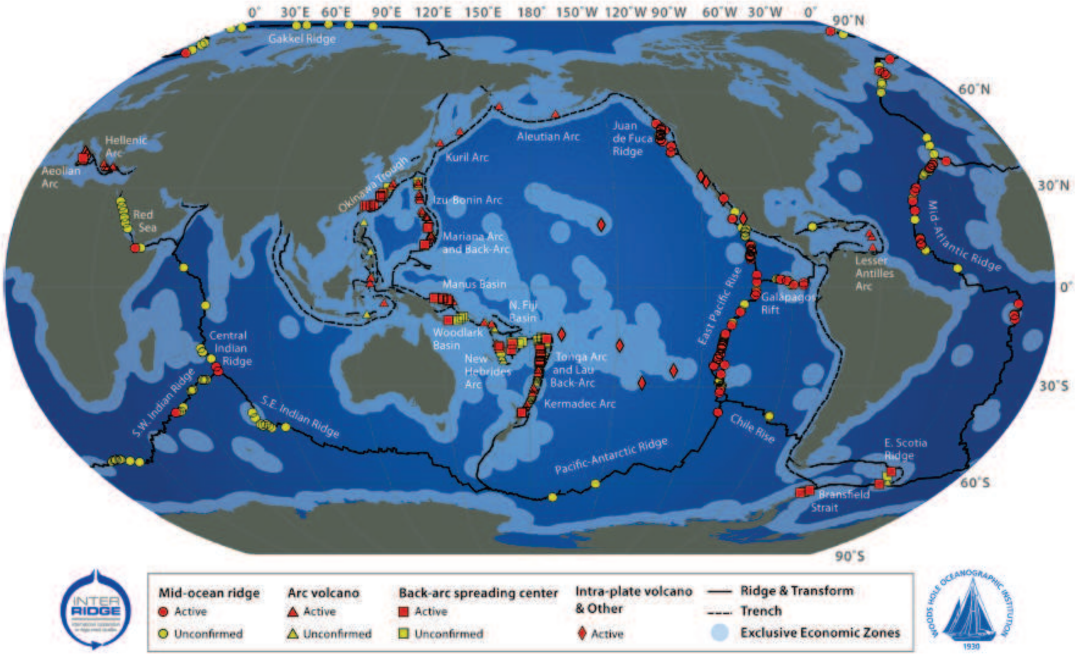
0°
30°E
60°E
90°E
120°E
150°E
180°
150°W
120°W
90°W
60°W
30°W
0°
90°N
60°N
30°N
0°
30°S
60°S
90°S
Gakkel Ridge
Hellenic Arc
Aeolian Arc
Red Sea
Okinawa Trough
Kuril Arc
Aleutian Arc
Juan de Fuca Ridge
Izu-Bonin Arc
Mariana Arc and Back-Arc
Manus Basin
N. Fiji Basin
Woodlark Basin
New Hebrides Arc
Tonga Arc and Lau Back-Arc
Kermadec Arc
Central Indian Ridge
S.W. Indian Ridge
S.E. Indian Ridge
Pacific-Antarctic Ridge
East Pacific Rise
Galápagos Rift
Chile Rise
Lesser Antilles Arc
Mid-Atlantic Ridge
E. Scotia Ridge
Bransfield Strait
Mid-ocean ridge
● Active
● Unconfirmed
Arc volcano
▲ Active
△ Unconfirmed
Back-arc spreading center
■ Active
□ Unconfirmed
Intra-plate volcano & Other
♦ Active
Ridge & Transform
Trench
Exclusive Economic Zones

Figure 1.7: Global distribution of hydrothermal systems (Hannington, Jamieson, et al., 2011).

1.7 Hydrothermal activity at back-arc basins

Hydrothermal activity at (back-)arc settings has long been known and studied (Hannington, De Ronde, et al., 2005; Martinez et al., 2007) (Figure 1.7). Modern fluid venting from seafloor hydrothermal fields, is predominantly seawater heated by underlying magmatic bodies and their corresponding magmatic fluids (Yang and S. D. Scott, 2006). Magmatic fluids are supercritical, mainly composed of CO_2 at the early stage magma degassing and of H_2O at a later stage. These fluids have unique chemical characteristics, due to various levels of mixing between the two fluids sources, and large variation of crustal chemistry (Yang and S. D. Scott, 2006; Martinez et al., 2007).

Generally, back-arc hydrothermal fluids have a pH of 2 to 3 (seawater is pH 7.8) and contain high CO_2 and CH_4 values. The low pH results from the removal of Mg from the heated seawater, due to the formation of Mg-OH-Si minerals and the release of protons. Volatile gases (SO_2 and HCl) can further decrease the pH of the venting fluids. Due to the unique characteristics of the hydrothermal fluids, various ore metals can be transported as chloride and sulfide complexes and are thus responsible for the distribution of various VMS deposit styles (Gamo et al., 1997; Hannington, De Ronde, et al., 2005; Yang and S. D. Scott, 2006; Martinez et al., 2007).

Although, a primary distinction can be made between mafic and felsic oceanic hydrothermal settings, due to the influence of fluids of subducted slabs in arc and back-arcs settings when comparing to MOR-like settings (Hannington, De Ronde, et al., 2005; Martinez et al., 2007). The influence of this extensive water-rock interaction can promote enrichments in metals (Cu, Au, Zn, Fe, Ag) and metalloids (Sb, As) (Hannington, De Ronde, et al., 2005; Patten et al., 2016). Several back-arc related hydrothermal vent areas at the East Manus basin, such as PACManus, North Pual, Desmos and SuSu Knolls have been discovered and studied. The hydrothermal fluids of the east Manus basin, expresses a large variability that corresponds with the complexity of a back-arc setting (Binns and S. Scott, 1993; J.-M. Auzende et al., 1996; Hashimoto et al., 1999; J. M. Auzende et al., 2000; Tivey et al., 2006; Bach et al., 2011; Reeves et al., 2011).

Bibliography

Anhaeusser, C.R. (2014). “Archaean greenstone belts and associated granitic rocks – A review”. In: *J. African Earth Sci.* 100, pp. 684–732. DOI: `10.1016/j.jafrearsci.2014.07.019`.

Auzende, Jean Marie et al. (2000). “Thinned crust in southwest pacific may harbor gas hydrate”. In: *Eos (Washington. DC).* 81.17, pp. 182–185. DOI: `10.1029/00EO00127`.

Auzende, Jean-Marie, Tetsuro Urabe, and Scientific Party (1996). “Cruise explores hydrothermal vents of the Manus Basin”. In: *Eos (Transactions, Am. Geophys. Union)* 77.26, p. 244.

Bach, W. et al. (2011). “Carbonate veins trace seawater circulation during exhumation and uplift of mantle rock: Results from ODP Leg 209”. In: *Earth Planet. Sci. Lett.* 311.3-4, pp. 242–252. DOI: `10.1016/j.epsl.2011.09.021`.

Binns, R.A. and S.D. Scott (1993). “Actively forming polymetallic sulfide deposits associated with felsic volcanic rocks in the Eastern Manus back-arc basin, Papua New Guinea”. In: *Econ. Geol.* 88, pp. 2226–2236.

Boyle, R.W. and I.R. Jonasson (1984). “The geochemistry of antimony and its use as an indicator element in geochemical prospecting”. In: *J. Geochemical Explor.* 20, pp. 223–302.

Butterman, W.C. and J.F. Carlin (2004). *Mineral Commodity Profiles - Antimony*. Tech. rep. U.S. Department of the interior and U.S. Geological Survey.

Carlin, J.F. (2011). *Mineral Commodity Summaries - Antimony*. Tech. rep. U.S. Geological Survey, pp. 18–19.

Condie, K (1976). “Trace-element geochemistry of archean greenstone belts”. In: *Earth-Science Rev.* 12.4, pp. 393–417. DOI: `10.1016/0012-8252(76)90012-X`.

Condie, K.C. (1981). *Archean greenstone belts*. Vol. 17. 3. Elsevier, p. 201. DOI: `http://dx.doi.org/10.1016/0301-9268(82)90029-8`.

Davis, D.R., D.B. Paterson, and D.H.C. Griffith (1986). “Antimony in South Africa”. In: *J. S. Afr. Inst. Min. Met.* 86.6, pp. 173–193.

Gamo, T. et al. (1997). “Acidic and sulfate-rich hydrothermal fluids from the Manus back-arc basin, Papua New Guinea”. In: *Geology* 25.2, pp. 139–142. DOI: `10.1130/0091-7613(1997)025<0139:aasrhf>2.3.co;2`.

Goldfarb, R.J. and D.I. Groves (2015). “Orogenic gold: Common or evolving fluid and metal sources through time”. In: *Lithos*. DOI: `10.1016/j.lithos.2015.07.011`.

Gorman, B.E., T.H. Pearce, and T.C. Birkett (1978). “On the structure of Archean Greenstone Belts”. In: *Precambrian Res.* 6, pp. 23–41.

Groves, D.I. et al. (2003). “Gold Deposits in Metamorphic Belts: Overview of Current Understanding,Outstanding Problems, Future Research, and Exploration Significance”. In: *Econ. Geol.* 98.1, pp. 1–29. DOI: `10.2113/gsecongeo.98.1.1`.

Hannington, M.D. (2014). “Volcanogenic Massive Sulfide Deposits”. In: *Treatise on Geochemistry*. 2nd ed. Elsevier Ltd. Chap. 13.18, pp. 463–488. DOI: `10.1016/0169-1368(95)00022-4`.

Hannington, M.D., C.E.J. De Ronde, and S. Petersen (2005). “Sea-Floor Tectonics and Submarine Hydrothermal Systems”. In: *Econ. Geol.* 100th Anni, pp. 111–141.

Hannington, M.D., J. Jamieson, et al. (2011). “The abundance of seafloor massive sulfide deposits”. In: *Geology* 39.12, pp. 1155–1158. DOI: 10.1130/G32468.1.

Hashimoto, J. et al. (1999). “Hydrothermal vent communities in the Manus Basin, Papua New Guinea: Results of the BIOACCESS cruises in ’96 and ’98.” In: *InterRidge News* 8, pp. 12–18.

Herzig, P.M. (2000). “Economic potential of sea-floor massive sulphide deposits : ancient and modern”. In: *R. Soc.* 357, pp. 861–875.

Jaguin, J. et al. (2014). “Stable isotopes (O, C) and fluid inclusion study of quartz-carbonate veins from the antimony line, Murchison Greenstone Belt”. In: *Am. J. Sci.* 314.7, pp. 1140–1170. DOI: 10.2475/07.2014.03.

Kusky, T.M. and A. Polat (1999). “Growth of granite–greenstone terranes at convergent margins, and stabilization of Archean cratons”. In: *Tectonophysics* 305.1-3, pp. 43–73. DOI: 10.1016/S0040-1951(99)00014-1.

Langmuir, C.H. et al. (2006). “Chemical systematics and hydrous melting of the mantle in back-arc basins”. In: *Back-arc spreading Syst. Geol. Biol. Chem. Phys. Interact.* Vol. 53. 9. Geophysical Monograph Series, AGU, pp. 87–146. DOI: 10.1017/CBO9781107415324.004. arXiv: arXiv:1011.1669v3.

Li, K.C. (1953). “Arsenic and antimony”. In: *Mod. uses nonferrous Met.* Ed. by C.H. Mathewson. 2nd. York, Pennsylvania: The Maple Press, pp. 40–53.

Li, T., G.F. Archer, and S.C. Jr. Carapella (1992). “Antimony and antimony alloys”. In: *Kirk-Othmer Encycl. Chem. Technol.* 4th. New York: John Wiley & Sons, pp. 367–381.

Martinez, F. et al. (2007). “Back-Arc Basins”. In: *Oceanography* 20.1, pp. 116–127. DOI: 10.5670/oceanog.2007.85.

Obolensky, A.A. et al. (2007). “Antimony in hydrothermal processes: solubility, conditions of transfer, and metal-bearing capacity of solutions”. In: *Russ. Geol. Geophys.* 48, pp. 992–1001. DOI: 10.1016/j.rgg.200.

Patten, C.G.C. et al. (2016). “Mobility of Au and related elements during the hydrothermal alteration of the oceanic crust: implications for the sources of metals in VMS deposits”. In: *Miner. Depos.* 51.2, pp. 179–200. DOI: 10.1007/s00126-015-0598-8.

Pohl, W.L. (2011). *Economic Geology Principles and Practice - Metals, minerals, coal and hydrocarbons - Introduction to formation and sustainable exploitation of mineral deposits*. Vol. 1. July. Wiley-Blackwell, pp. 1–699. DOI: `10.5962/bhl.title.18736`.

Powell, R., T.M. Will, and G.N. Phillips (1991). “Metamorphism in Archaean greenstone belts: calculated fluid compositions and implications for gold mineralization”. In: *J. Metamorph. Geol.* 9.2, pp. 141–150. DOI: `10.1111/j.1525-1314.1991.tb00510.x`.

Reeves, E.P. et al. (2011). “Geochemistry of hydrothermal fluids from the PACMANUS, Northeast Pual and Vienna Woods hydrothermal fields, Manus Basin, Papua New Guinea”. In: *Geochim. Cosmochim. Acta* 75.4, pp. 1088–1123. DOI: `10.1016/j.gca.2010.11.008`.

Scott, C.R., W.U. Mueller, and P. Pilote (2002). “Physical volcanology, stratigraphy, and lithogeochemistry of an Archean volcanic arc: evolution from plume-related volcanism to arc rifting of SE Abitibi Greenstone Belt, Val d’Or, Canada”. In: *Precambrian Res.* 115.1-4, pp. 223–260. DOI: `10.1016/S0301-9268(02)00011-6`.

Tivey, M. et al. (2006). *Cruise report R/V Melville MAGELLAN-06*. Tech. rep. Woods Hole Oceanographic Institution, pp. 1–67.

USGS (2015a). *Antimony*. Tech. rep. U.S. Geological Survey, pp. 18–19. DOI: `10.1017/CBO9781107415324.004`. arXiv: `arXiv:1011.1669v3`.

– (2015b). “Antimony — A Flame Fighter”. In: April, pp. 4–5.

Vearncombe, S. and R. Kerrich (1999). “Geochemistry and geodynamic setting of volcanic and plutonic rocks associated with Early Archaean volcanogenic massive sulphide mineralization, Pilbara Craton”. In: *Precambrian Res.* 98.3-4, pp. 243–270. DOI: `10.1016/S0301-9268(99)00052-2`.

Volkov, A.V. et al. (2006). “Volkov, A.V., Serafimosvki, T., Kochneva, N.T., Tomson, I.N., Tasev, G., 2006, The Alshar epithermal Au-As-Sb-Tl deposit, southern Macedonia. Geology of ore deposits, 48, p.175-192.” In: *Geol. Ore Depos.* 48, pp. 175–192.

Wang, C.Y. (1919). *Antimony: its History, Chemistry, Mineralogy, Geology, Metallurgy, Uses, Preparations, Analysis, Production, and Valuation; with complete Bibliographies for Students, Manufacturers, and Users of Antimony*, pp. 1–225. DOI: `10.1038/081068a0`.

Yang, K and S D Scott (2006). “Magmatic fluids as a source of metals in arc/back-arc hydrothermal systems: evidence from melt inclusions and vesicles”. In: *Back Arc Spreading Syst. Geol. Biol. Chem. Phys. Interact.* Geophysica.1, pp. 163–184.

Chapter 2

Motivation and outline

2.1 Motivation

This project was initiated by U. Schwarz-Schampera, BGR Hannover in order to give a better understanding of the exceptionally well developed Sb-As-Au-Hg mineralization within the Antimony Line (AL) in the Murchison Greenstone Belt (MGB), South Africa and the possible relationship to recent VMS deposits. The AL is located in a prominent suture zone within the MGB and is tied to metasomatically influenced metaultramafic rocks. Metasomatism of ultramafic rocks is a core subject of the Petrology of the Ocean Crust Group at the Universtität of Bremen. The principal goal of my PhD project was to (1) identify the role of metasomatism in the AL deposit formation, and (2) compare the AL deposit with modern back-arc massive sulfide mineralization systems. Goal (1) relates to the comprehension that a knowledge gap still exists in the field of ore petrology and geochemistry in regard to lode orogenic S-Au deposits within (Archaean) suture zones and their possible relationship to recent back-arc settings. Goal (2) concerns the Sb-As behavior in magmatic-hydrothermal hypogene and supergene deposits, which is related to Au-Ag mineralizations in way that are incompletely understood. To try to overcome these critical knowledge gaps, a comparison of Sb-As(-Au-Ag) mineralization of a greenstone belt is made with a recent back-arc system: PACManus, New

Guinea.

The MGB host an enrichment of Sb-As mineralization within the Antimony Line suture zone, which runs paralelle to a zone of of major Cu-Zn mineralization (the Cu line), which shows strong resemblance to modern seafloor massive sulfide mineralizations (Schwarz-Schampera et al., 2010). This relationship is less well established for the AL, although modern back-arc VMS deposits often show Sb-As enrichments, which are spatially and genetically related to Cu-Zn mineralizations. Schwarz-Schampera et al. (2010) hence speculated that the AL, like the Cu line, is related to seafloor magmatic-hydrothermal processes. Studying the MGB provides thus an exceptional insight in the geochemical behavior of Sb-As mineralization. Expeditions (in 2006 and 2011) to the PACManus hydrothermal system in the Manus Backarc Basin, Papua New Guinea, performed by W. Bach and others, has provided a detailed metal concentration dataset of both fluid and whole rock records. This dataset provides the uncommon opportunity to look at the geochemical behavior of Sb-As-(Au-Ag) in an active black smoker system.

The research for this dissertation was conducted within the Department of Geosciences of the University of Bremen and was in part funded by the BGR Hanover “Bundesanstalt für Geowissenschaften und Rohstoffen”. Additional funding was received through the MARUM “Center for Marine Environmental Sciences” as part of the research area GB4. This project was carried out from October 2012 until June 2016.

The samples used in this work were collected by myself during fieldwork in 2013 made possible by an introduction of Ulrich Schwarz-Schampera and Friedhelm Henjes-Kunst (BGR). This fieldwork has been preformed in cooperation with Blanka Sperner and George LÖwe (University of Freiberg), with the goal to combine their structural analyses with my geochemical analyses. Additionally samples have been provided by a previous fieldwork in 2006 by U. Schwarz-Schampera. Furthermore, fluid and whole rock data sets interpreted of the PACManus back-arc basin were collected during research cruise MGLN06MV in 2006 (Tivey et al., 2006) and the SO-216 Bambus in 2011 (Bach et al., 2011), both led by Wolfgang Bach. These data were in part provided by Sven Petersen (GEOMAR) (ref appendix) and Paul Craddock (WHOI/MIT) (Craddock, 2009).

2.2 Outline

The following two chapters present two geochemical studies at the Murchison Greenstone belt, where major, trace element and stable isotopic studies have been preformed on carbonated gangue material enriched with Sb-As as well as Sb-As sulfides to investigate the mobilizing and trapping mechanisms of a hydrothermal system and their interaction with the surrounding host rocks. Geochemical reaction path modeling with the use of Geochemical Workbench provided insights into the geochemical characteristics of these mechanisms. The fifth chapter presents fluid data and whole rock of the PACManus back-arc system, to provide insight the source, mobilization and precipitation of Sb-As-Au-Ag within an active hydrothermal setting. The thesis is completed by a conclusion and outlook.

Chapter 3: Geochemical model of the Sb-As mineralization at the Murchison Greenstone Belt, South Africa

Authors: Nikki Blaauwbroek, Ulrich Schwarz-Schampera, Wolfgang Bach

(Submitted at Journal of Geochemical Exploration)

In this study new mineral chemistry and stable isotopic data of carbonates, silicates and sulfides will be presented along with results of geochemical modeling of Sb-As mineralization within the MGB suture zone. The aim of this research is to comprehend the solubility of Sb and As in aqueous solutions from magmatic precursor rocks and the effect of later structural evolution of the greenstone belt and related alteration processes like serpentinization and listvenization. Collecting samples on the geochemical fieldwork of two weeks in 2013 has been made possible by a three-day introduction by U. Schwarz-Schampera. The rock sampling has been preformed individually, with local assistance navigating throughout the mines from the geologists working at Consolidated Murchison Limited (ConsMurch). Interpretation of the geological setting together with the collected dataset of the apparent enriched regions within carbonated and fuchsite-enriched regions has been discussed on multiple occasions with B. Sperner, U. Schwarz-Schampera and W. Bach. Geochemical analyses of both 2006 and 2013 sample sets of major and trace elements together with stable isotopes have been preformed independently. Reaction path modeling has been made possible by the new acquired database by the input of Moritz Wagner and Michael Hentscher. Modeling with the use of Geochemical Workbench has been preformed in continuous dialogue with W. Bach.

Chapter 4: On the phase relations of Sb-As mineralization within an Archean suture zone, Murchison Greenstone Belt, South Africa

Authors: Nikki Blaauwbroek, Wolfgang Bach, Niels Jöns

(Minerals, to be submitted)

In this study new petrography and mineralogy of the Sb-As mineralization will be presented along with results of geochemical modeling of Sb-As mineralization within the MGB. Extensive descriptions of this mineralization is made possible by XRF, XRD, EMPA and LA-ICPMS analyses. The focus of this research is to describe the major and trace metal concentrations of the Sb-As sulfides and gangue material hosting these minerals. The aim of this research is to comprehend the behavior and relationship of Sb and As mineralization amongst each other and correlate the behavior with the structurally active plus serpentinized and listvenized greenstone belt. Electron microprobe work was conducted at Universität Bremen and Universität Bochum by Niels Jöns and myself. For this research only the samples of the 2013 fieldwork has been taken into account, as described in the previous chapter. Interpretation of the geological setting together with the collected dataset of the apparent enriched regions within carbonated and fuchsite-enriched regions has been discussed on multiple occasions with B. Sperner and W. Bach. Geochemical analyses of major and trace metal concentrations have been preformed independently. XRD analyses on five samples have been preformed by T. Flathmann for his bachelor thesis, within the mainframe of this project. Modeling with the use of Geochemical Workbench has been preformed in continuous dialogue with W. Bach.

Chapter 5: Sb-As-Au-Ag mineralization in an active back-arc system, PACManus, New Guinea

Authors: Nikki Blaauwbroek, Michael Hentscher, Wolfgang Bach, Sven Petersen

(Mineralium Deposita, to be submitted)

In this study we represent geochemical characteristics of Sb, As, Ag and Au within an active hydrothermal setting. The aim of this research is to define geochemical interactions, connections and dependencies amongst these precious metals and whether they can be used as tracers to determine a magmatic input of hydrothermal systems. These relationships could be vital information for oceanic and continental mining prospects. Extensive descriptions of their behavior are made possible by fluid and whole rock datasets. Analyzes of these datasets have been preformed by P. Craddock and S. Petersen. Interpretation has been preformed in close dialogue with S. Petersen. Reaction path modeling is based on a new database made by M. Hentscher and has been preformed in close dialogue with M. Hentscher and W. Bach.

Chapter 6: Synthesis and outlook

This dissertation closes with a conclusion and outlook to emphasize the importance of geochemical analyses of non-prominent metal concentrations within the field of ore petrology. The importance of research on alteration processes such as serpentinization and listvenization with their influence on ore-forming mechanisms will be outlined. Finally, concepts for further investigations for understanding and defining Sb-As mineralization will be presented.

2.3 Scientific contributions

In the framework of this dissertation, comprehensive research activity resulted in three first-author manuscripts that are presented in chapter three, four and five. For chapter 3 and 4, I produced all data myself, assisted by the persons mentioned above. For chapter 5, I used existing data. In each of these chapters, I led the synthesis of data and model calculations and wrote the first drafts of manuscripts. I then edited the drafts with W. Bach, before other coauthors contributed.

Bibliography

Bach, W. et al. (2011). “Carbonate veins trace seawater circulation during exhumation and uplift of mantle rock: Results from ODP Leg 209”. In: *Earth Planet. Sci. Lett.* 311.3-4, pp. 242–252. DOI: `10.1016/j.epsl.2011.09.021`.

Craddock, P.R. (2009). “Geochemical traces of processes affecting the formation of seafloor hydrothermal fluids and deposits in the Manus Back-arc basin”. PhD thesis, pp. 1–370.

Schwarz-Schampera, U., H. Terblanche, and T. Oberthür (2010). “Volcanic-hosted massive sulfide deposits in the Murchison greenstone belt, South Africa”. In: *Miner. Depos.* 45, pp. 113–145. DOI: `10.1007/s00126-009-0266-y`.

Tivey, M. et al. (2006). *Cruise report R/V Melville MAGELLAN-06*. Tech. rep. Woods Hole Oceanographic Institution, pp. 1–67.

CHAPTER 3

A geochemical model of the Sb-As mineralization in the Murchison Greenstone belt

NIKKI BLAAUWBROEK[1], ULRICH SCHWARZ-SCHAMPERA[2], WOLFGANG BACH[1]

[1] Department of Geosciences and MARUM – Center for Marine Environmental Sciences,
University of Bremen, Klagenfurter Str., 28359 Bremen, Germany
[2] Bundesanstalt für Geowissenschaften und Rohstoffe (BGR),
Geozentrum Hannover, Stilleweg 2, 30655 Hanover, Germany

Submitted at Journal of geochemical exploration

Keywords: Antimony, stibnite, listvenite, suture zone, greenstone belt

Abstract

We present a petrological and geochemical re-assessment of the Sb-As dominated mineralizations of four mines from the Antimony Line (AL) in the Murchison Greenstone Belt (MBG), South Africa. The AL is a well-defined linear zone of carbonated-quartz alteration with striking Sb-As-Au mineralization. The mineralization comprises two principal types (i) arsenopyrite-chalcopyrite-gudmundite-ullmannite- berthierite-pyrite, and (ii) stibnite±pyrite±berthierite. Type I is bound to metasomatized chlorite and talc schists as well as listvenites, whereas type II occurs predominantly in completely quartz-carbonate altered varieties of these rocks. High Cr contents of chlorite, fuchsite, and dravite as well as the presence of Ni(Sb,As)S phases indicates that ultramafic precursor rocks where involved in the genesis of the deposits. Stable O isotope data of the carbonates (magnesite and dolomite) and quartz indicate, uncommonly high, formation temperatures between 350 and 400 °C. The field and geochemical data reveal a clear relationship between the mineralization and metasomatic reactions involving meta-ultramafic rocks and felsic protoliths. We propose that these lithologies represent a bimodal ultramafic-felsic magmatism, possibly in a subduction zone setting. Based on these observations, we developed hypotheses for the genesis of the Sb-As-Au mineralizations and tested them rigorously by thermodynamic modeling. The Sb-As-Fe-Cu-Au-S-O-H phase relations and solubilities were re-investigated in relationship to PTX relations using a tailor-made and up-to-date thermodynamic database. The general enrichment of Sb of the type I mineralization may have developed by water-rock interactions and mass transfer of Sb (and As) across the main lithologic units from the felsic into the ultramafic units. This mineralization took place during collision and isoclinal folding (D1) in the MGB as part of the Limpopo suture zone. The type II

stibnite-dominated deposit appears to be linked to later transtensional movement (D2) in this fault zone, during which tensional gashes allowed upwelling of deep crustal fluids that gave rise to the pronounced quartz-carbonate-stibnite mineralization. Reaction path modeling was also conducted to verify the petrological plausibility of the genetic models. These computational results corroborate the key role of bimodal, felsic and ultramafic, lithologies in turning the AL suture zone into a trap for Sb at fairly high temperatures.

3.1 Introduction

Sb-Au-As(-Hg)-mineralization within major orogenic suture zones such as Archaean greenstone belts and younger analogues have been described from all over the world (Table 3.1). The most prominent deposits that have been described are from the Archaean: the Ajjanahalli deposit at the Dharwar Craton (Bhattacharya et al., 2014), the Kwekwe (Buchholz and Oberthür, 2007) and Murchison Greenstone Belts (Vearncombe et al., 1992) in the Kaapvaal Craton, and the Abitibi Greenstone belt, Canada (Moritz, Crocket, and Dickin, 1990; Moritz and Crocket, 1991). But Phanerozoic occurrences, like the Snowbird deposit in the Canadian Cordillera (Madu et al., 1990), the Senator Antimony deposit in Turkey (Bernasconi et al., 1980), and the Tsugu Gold-Antimony vein deposit in Japan (Shikazono and Shimizu, 1988), also represent suture zones with Sb-As enrichments. Although these deposits may vary in age, they have in common that contrasting lithologies with ultramafic rocks were juxtaposed against quartz-feldspar-bearing sedimentary and magmatic rocks that were subsequently modified by silicification and carbonation processes. These consortia of rocks have witnessed deformation under greenschist-facies conditions which were accompanied by drastic metasomatic mass transfers in major shear zones fluxed with aqueous solutions low pressures at temperatures of 250-400 °C. Some have clear metasomatic fronts at the juxtaposed rocks, such as serpentinites at the Canadian Cordillera (Normand et al., 1996). In others intense carbonization and silicification has obscured the nature of the protoliths in the shear zones, but the common appearance of Cr-rich mica (fuchsite or mariposite) or tourmaline in listvenites and related rocks suggests that ultramafic rock types were commonly present. Next to Sb-As mineralization the deposits in these suture zones either have enrichments in Hg or Au(+Ag), and the relative enrichment of the various elements

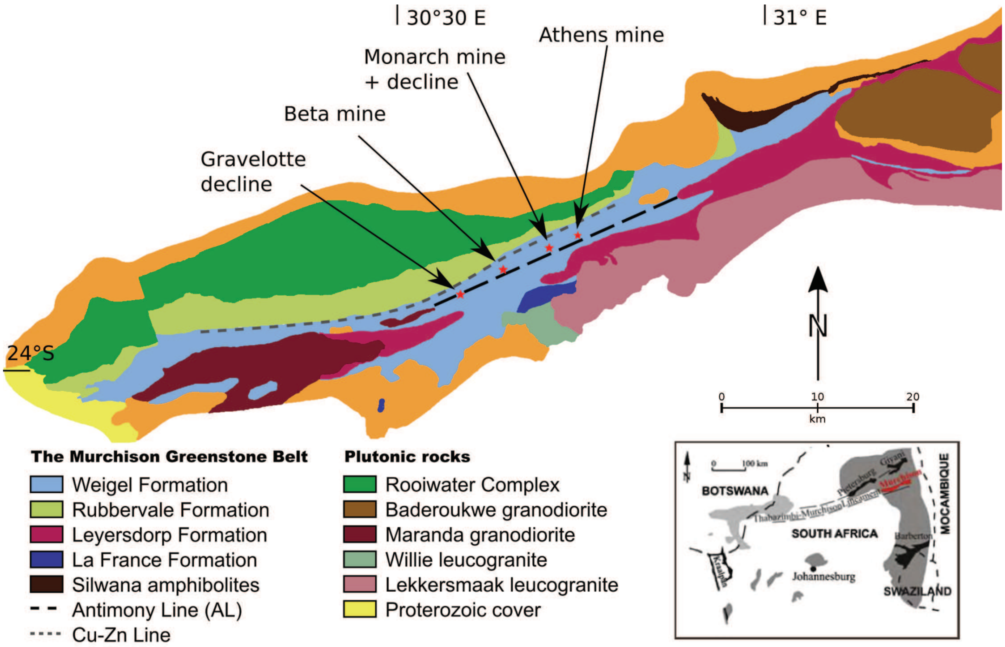
30°30 E
31° E
Athens mine
Monarch mine
+ decline
Beta mine
Gravelotte
decline
24°S
N
0
10
20
km
The Murchison Greenstone Belt
Weigel Formation
Rubbervale Formation
Leyersdorp Formation
La France Formation
Silwana amphibolites
Antimony Line (AL)
Cu-Zn Line
Plutonic rocks
Rooiwater Complex
Baderoukwe granodiorite
Maranda granodiorite
Willie leucogranite
Lekkersmaak leucogranite
Proterozoic cover
N
0
100 km
BOTSWANA
Thabazimbi-Murchison Lineament
Pietersburg
Giyani
Murchison
SOUTH AFRICA
Barberton
MOCAMBIQUE
Kraaipan
Johannesburg
SWAZILAND

Figure 3.1: Geological map of Murchison Greenstone Belt. The Antimony Line and Cu-Zn line have been marked and along the AL, together with the positions of the four mines (Athens, Beta, Gravelotte and Monarch). Adjusted after Vearncombe et al. (1992) and Schwarz-Schampera et al. (2010).

may reflect temperature and depth within the basement.

In the past 80 years, several observations were made that are relevant to Sb and As enrichments in these hypogene deposits associated with suture zones. Whitmore et al. (1946) was one of the first to observe that fuchsite (chromium muscovite) within Pre-Cambrian greenstone belts are typically found in Au-Sb-bearing districts. Anhaeusser (1976) stated that the mineralization is closely related to the presence of various volcanological subdivisions within an Archaean greenstone belt. Madu et al. (1990) thought that fluid fluxing within shear zones, caused precipitation of Sb-As minerals. Active shear zones are permeable and can facilitate upflow of ore-forming solutions (e.g. Buchholz and Oberthür (2007)). Others have pointed out similarities between greenstone belt-hosted copper and antimony deposits to active (back-)arc hydrothermal systems within a volcanic arc setting (Vearncombe, 1991; Schwarz-Schampera et al.,

Table 3.1: Summary of Sb-hosted Precambrian and younger suture zones.

Deposit and region	Mineral assemblage	Host rock related to mineral assemblage	Possible fluid regime
Ajjanahalli deposit. Dharwar Craton[a]	Au-As-Sb	Granite. metabasalt. greywacke	CO2/CH4 = 7.13; C=-5.81 to 1.14‰
Timmins Porcupine district. Abitibi Greenstone Belt[b]	Au-As-Sb	Carbonatized ultramafic rocks	Unknown
Kwekwe district. Midlands Greenstone belt[c]	Au-Sb-As	Quartz-carbonate vein between ultramafic and granitoid complexes	P =0.8 to 1.8 kbars; T=120 to 230°C; P=0.8 to 1.8 kbars
Coolgardie Goldfield. Yilgarn Craton[d]	Ag-As-Sb-W	Mafic rock. greenstone contact	O=4 to 8 ‰; P=2.3 - 3.8 kbar; T=490 - 525C
Noranda district. Canada[e]	Au-Sb	Listvenite+Carb. argillite+slate+chert	T=240°C
Quebec Antimony deposit. Appalachians[f]	Sb-As	Metasediments enclosed in the serpentinites	Shift in fluid from CO2-rich to CH4 rich
Wiluna lode-gold deposits. Australia[g]	Au-Sb	Komatiite juxtaposed with low-Mg basalt and dolerite	T=290±25°C; 0.2 and 23 eq. wt% NaCl
Canadian Cordillera[h]	Au-Sb	Listvenite grade into carbonaceous argillite. intruded by diorite-andesite	T=200-250°C; P=2.7 kbar;
Tsugu Gold-Antimony vein deposit. Japan[i]	Au-Hg-Sb-As	Green tuff juxtaposed with outer zone SW Japan	T=208-350°C. log aS2=-12 to -14
Senator Antimony deposit. Turkey[j]	Sb-As	Phyllites intruded by ophiolitic bodies (carbonaceous tuffs)	Oxidizing and fluid unmixing

*Comparison has been made between different suture zones. with emphasis on the host rock and fluid regime related hypothesis to Sb-mineral assemblages.

a: Sarangi et al.. 2013

b: Moritz and Crocket. 1991;

c: Buchholz and Oberthur. 2007

d: Knight et al.. 2000;

e: Beaudoin et al.. 1987;

f: Normand et al.. 1996

g: Hagemann and Lüders. 2003;

h: Madu and Nesbitt. 1996;

i: Shikazono and Shimizu. 1988;

j: Bernasconi et al.. 1980.

2010). These observations suggest a volcanic/metamorphic origin of the Sb-As mineralization in an active plate boundary setting. Furthermore, various trapping mechanisms have been discussed. Fluid mixing (and adiabatic cooling) as well as decompressional degassing, related cooling and changes in f S_2 and/or f O_2 have been identified as potential ore trap mechanisms (Hagemann and Lüders, 2003). Likewise, changes in f S_2 and/or f O_2 in the course of serpentinization in contact with the ore-hosting metasediments have been identified as possible trap for Sb-sulfides (Normand et al., 1996). Decreasing temperature (>300 °C) (Williams-Jones and Norman, 1997)and changes in fluid pH and redox-potential (Obolensky, Gushchina, Borisenko, Borovikov, and Nevol'ko, 2009) have also been suggested to play a major role in Sb-mineralization.

The Murchison Greenstone Belt (MGB) in South Africa is one of the Archaean greenstone belts along the Kaapvaal Craton. The MGB is known for the antimony enrichment along the Antimony Line (AL) (Figure 3.1), and has been mined since 1928 for antimony with gold as byproduct (Davis et al., 1986). The (primary) antimony mineralization has been related to the emplacement of Maranda granodiorite intrusions that occurred around 2.9 Ga (Poujol, 1996; Justine Jaguin et al., 2013) and that may be related to orogeny in the Limpopo Belt, north of the MGB (Block et al., 2013). These felsic intrusions have been interpreted by Schwarz-Schampera et al. (2010) to represent an Archaean back-arc system with the associated VMS deposits. J. Jaguin, Boulvais, M.-C. Boiron, et al. (2014) suggested the primary Sb-As mineralization is related to the formation of albitites that they view as the metasomatized equivalent of the Maranda granodiorite. The Sb-mineralization is mainly stibnite and hosted in listvenites and related quartz-carbonated veins, which formed 2 Ga in a deformation zone with NNE-SSW compression and isoclinal folding with steeply dipping stretching lineations and boudinage (Poujol, 1996; Block et al., 2013; J. Jaguin, Boulvais, M.- C. Boiron, et al., 2014). In this study new mineral chemistry and stable isotopic data will be presented along with results of geochemical modeling of Sb-As mineralization within the MGB suture zone will be presented. We pay particular attention to the solubility of Sb and As in aqueous solutions in the magmatic precursor rocks and during the later structural evolution of the greenstone belt and related alteration processes like serpentinization and listvenization.

3.1.1 Regional geology

The MGB is located in South Africa in the northwestern corner of the Kaapvaal Craton. The Kaapvaal Craton, 3.7-2.7 Ga (Schwarz-Schampera et al., 2010; Block et al., 2013) consists of several subdomains that were merged together at 2.97 Ga (McCourt and Reenen, 1992) and represents part of a collision zone of the Witwatersrand with the Pietersburg terrains (Block et al., 2013). Several tonalites, trondhjemites, and granodiorites (TTGs) had intruded the komatiite on multiple occasions, approximately 2.9 Ga ago (Poujol, 1996; Vearncombe et al., 1992), suggesting an (back-) arc-system (Poujol, 2001; Schwarz-Schampera et al., 2010). The MGB extends for 140 km ENE-WSW, 15-20 km N-S, is covered by the Neoarchaean to Palaeoproterozoic sediments and is located parallel to the Murchison-Thabazimbi Lineament (Block et al., 2013).

The sedimentary formations are made up of metapelites (La France Formation) and meta-arenites (MacKop Formation), whereas the volcanic formations vary between (ultra) mafic-sedimentary successions (Leydsdorp and Mulati Formations) to intermediate felsic lavas and tuffs (Rubbervale Formation), all ranging in age between 2.97 to 3.09 Ga (Vearncombe, 1991; Block et al., 2013; J. Jaguin, Boulvais, M.- C. Boiron, et al., 2014). Serpentinite lenses have been found in the southern part of the belt (Davis et al., 1986; Vearncombe, 1991), though not along the AL. Each formation has undergone unique contrasting metamorphic conditions, though in close proximity of each other (Block et al., 2013). The Weigel Formation has reached greenschist- to lower amphibolite facies grade, with P-T conditions from 1.30 to 2.8 kbar at 340-370 °C along the AL, whereas the Lekkersmaak granite has reached up to 5.6 kbar and 570 °C. The Silwana amphibolites, La France Formation and Rooiwater Complex have reached even higher metamorphic P-T conditions in the proximity of 8.7 kbar and 600-670 °C (Block et al., 2013). The AL is a locally discordant zone of brittle deformation within a zone of heterogeneous ductile shear with a length of 12 km (Figure 3.1) (Vearncombe, 1988), known for the enrichment in stibnite (Sb_2S_3) (Davis et al., 1986). The quartz-carbonate-rich AL has been isoclinally folded into a narrow elongated sequence of carbonated deformed rocks, which are prominent features within the topography (Block et al., 2013) and are locally cut by small-scale shear zones and breccias (Vearncombe et al., 1992). Most geological domains exhibit evidence for a poly-phased deformation (Vearncombe, 1988; Block et al., 2013). In total three deformation episodes have been recognized: The first deformation phase (D1) corresponds to the formation of isoclinal folding with a S1 cleavage trending ENE (Vearncombe, 1988; Vearncombe et al., 1992; Block et al., 2013). Along the AL, competent quartz-carbonate rocks are deformed by folding, by boudinage and by brittle tension fracturing (Vearncombe et al., 1992). The tension gashes are later filled by quartz, carbonate, stibnite and other ore minerals in smaller quantities (Vearncombe et al., 1992). Deformation phase D2 transposed these isoclinal folds by E-W trending asymmetrical S-shaped folds. The granitoid intrusions post-date D1 (Vearncombe, 1988). D3 encompasses D2 and D1 and principally comprises kink bands (Vearncombe et al., 1992); though found seldomly (Vearncombe, 1988). Overall fold structures are intradomainal, with major tectonic faults present between each geological domain (Vearncombe, 1988). Smaller-scale faults are found occasionally within the mines (Vearncombe et al., 1992). The carbonated rocks have been thought to be formed by hydrothermal alteration from an ultramafic rock type, based on their high Mg, Cr and Ni concentrations (Vearncombe, 1988). North of the Antimony Line lies the Cu-Zn line (Figure

3.2 Methods

Alternating quartz-carbonate veins and domains within Sb and As enriched zones have been sampled in 2006 and 2011 from four mines located in the MGB: Athens, Monarch, Gravelotte, Athens (Figure 3.1). Electron microprobe analyses were conducted on both silicates and sulfides from the AL. The silicates have been measured by a JEOL JXA-8900R, with 10 µm beamsize, 20 kV acceleration voltage, and 5 nA beam current at Kiel University. The sulfides were measured at Bochum University with a Cameca SXFiveFE, with fully focused beam, 20 kV acceleration voltage and 30 nA probe current. Carbonate and quartz samples have been obtained by micro-drilling or handpicking from crushed core material of veins (Figure 3.3h). While drilling, utmost care was taken to distinguish between pure carbonate veins and mixed carbonate-quartz veins. δ^{18}O and δ^{13}C isotopic compositions of both dolomite and magnesite samples were determined at MARUM in Bremen with a Finnigan MAT 252 and MAT 251, respectively. δ^{18}O values of quartz separates were determined in the Geoscience department of the University of Göttingen using CO_2-laser fluorination and a Thermo MAT253 Gas mass spectrometer (dual inlet mode). REE+Y+Sb concentrations and Mg# of the carbonates have been obtained by laser ablation ICP-MS using a Thermo Element2 mass spectrometer and a NewWave UP193ss laser at the Department of Geosciences in Bremen. Samples and standards were ablated with an irradiance of 1 GW/cm2 a beam diameter of typically 75 mm and a pulse rate of 5 Hz. For data quantification we used the Cetac GeoProTM software with Ca as internal standard, recalculated for both dolomite and magnesite. Std610 and Std612 was used as reference material. Uncertainties of the concentrations are <5%. Temperatures of dolomite-magnesite formation were computed according to the theoretical calibration of (Chacko and Deines, 2008), using the following formula:

$$10^3 \ln \alpha = \ln \beta(mgs) - 1000 \ln \beta(dol) \tag{3.1}$$

where β is based on internal vibrational frequencies and Debye temperatures of the two minerals. From the $\delta^{18}O$ composition of dolomite, we then calculated the $\delta^{18}O$ composition of water. Unfortunately, values for ΔDol-H_2O have not been devised by Chacko and Deines (2008) for temperatures higher than 373 K. To expand the temperature range, the ΔDol-H_2O fractionation data from Horita (2014) have been incorporated as well:

$$10^3 \ln \alpha(dol - \mathrm{H_2O}) = 3.140(\pm 0.022)x(10^6/T^2) - 3.14(\pm 0.011) \tag{3.2}$$

The Chacko and Deines (2008) and Horita (2014) data for ΔDol-H_2O correspond to each other within 0.7‰ for temperatures up to 100 °C, which validates the integration of both models to determine both temperature and $\delta^{18}O$ composition of the fluids (Table 3.2 and Figure 3.2). The average $\delta^{18}O$ composition of the fluid was then used to calculate temperatures from $\delta^{18}O$ compositions of quartz, using the Zhang et al. (1989) and

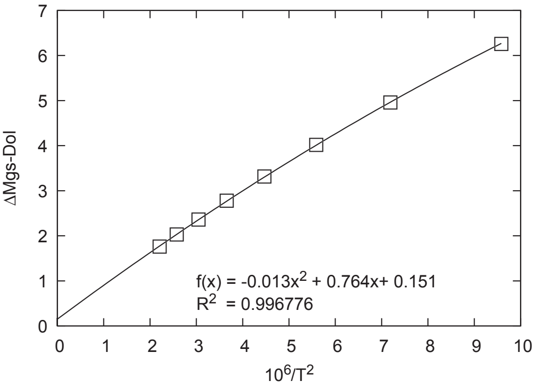

Figure 3.2: Linear relationship between temperature and ΔMgs-Dol based on data in Table 3.2 (a: Chacko and Deines (2008); b: Horita (2014)).

Sharp and Kirschner (1994) calibration.

Table 3.2: Integration of ΔDol-H_2O values of temperature range between 293-673 K.

(a) 106/T^2	T (K)	1000 ln ß Mgs	1000 ln ß Dol	ΔMgs-Dol	ΔDol-H_2O	(b) ΔDol-H_2O
11.7	293	113.4	106.1	7.285	**33.86**	**33.44**
9.59	323	97.06	90.80	6.257	**27.60**	**26.96**
7.19	373	76.59	71.63	4.959	**19.57**	**19.43**
5.59	423	61.87	57.85	4.017		14.41
4.47	473	50.94	47.62	3.315		10.89
3.66	523	42.62	39.84	2.779		8.340
3.05	573	36.15	33.79	2.361		6.424
2.58	623	31.03	29.00	2.029		4.950
2.21	673	26.90	25.14	1.761		3.793

* Temperature range of 293-373 K for ΔDol-H_2O of (a) Chacko and Deines (2008) based on 1000 ln α formula (2). in comparison with a temperature range from 293-673 K by (b) Horita (2014).

Reaction path modeling and activity-activity diagrams have been calculated using Geochemist's Workbench. There is no thermodynamic data for Sb-As-Au minerals and aqueous species in the default GWB database. We have hence built a new database for a pressure of 1 kbar and 25 to 600 °C, using SUPCRT92 (Johnson et al., 1992). The database includes 112 aqueous species and 110 minerals. Data for major rock-forming minerals were taken from Wolery and Jove-Colon (2004). Data for major solutes are from Sverjensky et al. (1997) and Schock et al. (1997).These data were supplemented by data for Sb, As and Au minerals as well as aqueous HS^-, OH^- and Cl^- species of these elements from various sources, while maintaining internal consistency (Yund, 1962; Lynch, 1982; Wagman et al., 1982; Krupp, 1988; Seal, Essene, et al., 1990; Seal, Robie, Barton, et al., 1992; Vink, 1996; Seal, Robie, Hemingway, et al., 1996; Williams-Jones and Norman, 1997; Welham, 2001; Kantar, 2002; Stefánsson and Seward, 2003b; Stefánsson and Seward, 2003a; Stefánsson and Seward, 2004; Castro and Baltierra, 2005; Pokrovski et al., 2006; Akinfiev and Zotov, 2010; Firdu and Taskinen, 2010).

3.3 Results

3.3.1 Fieldwork

Two fieldwork expeditions have been undertaken in 2009 and 2013. The focus of this paper will lie on the 2013 fieldwork, though samples of the 2009 fieldwork have been incorporated as well. The motivation of the 2013 fieldwork was to determine the relationship between host rock and vein system(s) in proximity to Sb and As enrichment. Samples have been taken from four different mines from east to west: Gravelotte, Beta, Athens, Monarch (Table 3.3). These mines lie along the AL, and are 1 to 8 km apart from each other (Figure 3.1). In each of these mines, samples were taken where the Sb-content was the highest. These are at different depths: Gravelotte decline from 0 to 20 m, Beta mine at 640-680 m, Athens at 1160-1240 m and Monarch decline from 0 to 1240 m depth.

Overall, we discriminated between chlorite schists, talc schists, variably mineralized quartz-carbonate veins and boudins (dolomite-quartz, magnesite-quartz), and fuchsite-bearing quartz-carbonate rocks (listvenite). This entire deposit-hosting unit is heavily metasomatized and deformed. Frequently, different rock types are juxtaposed to each

Table 3.3: Sample descriptions of 2006 and 2013 fieldwork expedition at Murchison. South Africa.

Mine	Sample name	Description	Depth	Near fuchsite?	Photo nr	Carbo?
Gravelotte	**Gr001**	Dyke of 5m thick (Carboon time)	0-20m	No	-	-
	Gr002	The surrounding rock of the dyke	0-20m	No	1	-
	Gr003	Schist + vein of quart/carbo alteration	0-20m	No	2	Mag + q
	Gr004	Schist + vein of quart/carbo alteration	0-20m	No	2	Large dol vein adjacent mag (red)
	Gr005	Schist + vein of quart/carbo alteration	0-20m	No	2	Large dol. cutting mag. recutted by small q
	Gr006	Green carbo vein in schist. same other q-veins	0-20m	?	3	mag matrix
	Gr007	Chlorite schist	0-20m	15m	4	mag matrix
	Gr008	Chlorite schist + red carbo	0-20m	15m	5	q + dol + redmag boudinaged veins
	Gr010	Car/q alteration with reddish dots (real or paint?)	0-20m	8m	6	matrix
	Gr014	Quartzite plus albite grains and sulfides. adjacent to fuchsite layer	0m	**at fuchsite**	9	albitized quartz
	SA0973	Carbonate alteration	0-20m	**at fuchsite**	-	mag matrix with small q veins + fuchsite
Beta quarry	**B020**	Samples located from W to E. sampled from different quartz veins	0m	No	10	none
	B021	Samples located from W to E. sampled from different quartz veins	0m	No	-	none
	B022		0m	No	-	none
	B023		0m	No	11	none
	B024	Samples located from W to E. sampled from different quartz veins	0m	No	12	none
	B025	Samples located from W to E. sampled from different quartz veins	0m	No	13	none
	B026	Samples located from W to E. sampled from different quartz veins; tension gashes	0m	No	-	none
	B028	Stibnite ore vein (maybe old q/carbo alteration?	0m	No	15	large dol vein
	B029	Stibnite ore vein crosscutting D2 -> different precipitation stage than B028	0m	No	16	-
	B030	1.5m alteration zone with q+car+stib+berthiriete	0m	No	-	lenses + fractures
	B031	hand sample from rubble with nice stibnite and carbonate and apy plus q	0m	No	17	-
	B032	car plus apy	0m	No	17	matrix + fracture
	B033	car plus apy	0m	No	-	lenses +brittle
Beta quarry	**Bm040**	Range of carbo's near stibnite ore. in large q-vein	640-680m	talc schist + albitized quartz		Large dol-mag vein
	Bm041	Range of carbo's near stibnite ore. in large q-vein	640-680m	talc schist + albitized quartz		Large Q-carbo veins
	Bm042	Range of carbo's near stibnite ore. in large q-vein	640-680m	talc schist + albitized quartz		Large Q-carbo veins
	Bm043	Range of carbo's near stibnite ore. in large q-vein	640-680m	talc schist + albitized quartz		Large Q-carbo veins
	Bm044	Range of carbo's near stibnite ore. in large q-vein	640-680m	talc schist + albitized quartz		Large Q-carbo veins
	Bm045	Range of carbo's near stibnite ore. in large q-vein	640-680m	talc schist + albitized quartz		Large Q-carbo veins
	Bm046	Range of carbo's near stibnite ore. in large q-vein	640-680m	talc schist + albitized quartz		Large Q-carbo veins
	Bm047	carbo plus albite plus py/apy next to q+stib vein	640-680m	talc schist + albitized quartz		Large Q-carbo veins
	Bm048	carbo plus albite plus py/apy next to q+stib vein	640-680m	talc schist + albitized quartz		Large Q-carbo veins. three different grain sizes
	Bm049	carbo plus apy veins	640-680m	talc schist + albitized quartz		Large Q-carbo veins
	Bm050	bt-carb/q schist	640-680m	**at fuchsite + biotite**		
	Bm052	Car+Q+apy in phylite	640-680m	**at fuchsite**		
	Bm053	yelow carbo vein croscutting fuchsite	640-680m	**at fuchsite**		siderite
	Bm054	yellow carbo vein croscutting fuchsite	640-680m	**at fuchsite**		siderite
	Bm055	chlorite-fuchite alteration	640-680m	**at fuchsite**		small veins in matrix
	Bm056	chlorite-fuchite alteration	640-680m	**at fuchsite**		small veins in matrix
	Bm057		640-680m	**at fuchsite**		small veins in matrix
	Bm058	the carbo related to to fuchsite -> occurred as blocks in quartz veins (large veins)	640-680m	**at fuchsite**		matrix + quartz vein
	Bm059	the carbo blocks in sulfide lenses in between fuchsite	640-680m	5m		mag matrix
	Bm060	carbo lenses of mafc material in fuch-q furhter away from fuchsite schist	640-680m	5m		-
	Bm061	carbo lenses of mafc material in fuch-q furhter away from fuchsite schist	640-680m	5m		-
	Bm062	carbo lenses of mafc material in fuch-q furhter away from fuchsite schist	440-480 m	No		-

Mine	Sample name	Description	Depth	Near fuchsite?	Photo nr	Carbo?
Beta quarry	SA0947	Contact biotite schist/ore body then stibnite ore with q-carb inclination very coarse grained surrounded by biotitic schist	440-480 m	**?**		
	SA0948	Stibnite-berthierite ore plus quartz and sulfides	440-480 m	**at fuchsite**		
	SA0950	Stibnite ore with brown + white quartz and some carbonate – 3rd unites. Quartz vein are Au-bearing and associated with arsenopyrite.	980	**at fuchsite**		
	SA0951	Talc schists with dolomaite/carbonate. 14th level. 3-4 unite. stibnite in talcose schists	980	?		
	SA0952	5m thick. Main beta ore enveloped by talc schists. stibnite-carbonate/qartz-talc. E-W Stibnite	980	?		
	SA0953	Recrystallized coarse grained carbonate in talc schist plus q-carb alteration north. High grade Au in quartz veins.	1160-1240m	No		
Athens	**A080**	apy+py at rim of quartz vein. adjacent to talc schist again with crenulation foliation	1160-1240m	No		dol.mag matrix
	A081	q+albite phenocrysts	1160-1240m	No		
	A082	sulfide ore (yellow ones are weathered Sb). in talc schist boudinaged together with Q with flinters of fuchsite	1160-1240m	No		dol.mag matrix
	SA0923	Southern country rock. More carbonate and talc towards ore zone.	1160-1240m	No		
	SA0924	Southern country rock. phyllitic with chlorite. carbonate and pyrite. Quartz-carb lenses along D1 foliaton	1160-1240m	No		
	SA0927	Quartz-carbonate remobilized. Folded with chloritic schist. Coarse grained.	1160-1240m	No		
Monarch mine	**Mm100**	Apy reef	1160-1240m	No		small veinlets in chlorite matrix
	Mm101	apy reef	1160-1240m	No		small veinlets in chlorite matrix
	Mm102	apy reef	-	No		small veinlets in chlorite matrix
	Mm103	flint of Sb-reef	-	No		
	Mm104	transition from apy to sb-reef	-	No		
	Mm105	transition from apy to sb-reef	0-40m	No		bt.
	Mm106	transition from apy to sb-reef	0-40m	No		
	Mm107	reaching talc schist near sb-reef	0-40m	No		
	Mm108	brown/green lenses in between q-veins (faultplane). near biotite	0-40m	No		
	SA0964	Apy ore recrystallized	0-40m	-		
	SA0968	Stibnite ore with quartz-carbonate	0-40m	?		
	SA0968_2	Stibnite ore with quartz-carbonate	0-40m	?		
Monarch decline	**M120**	small veins with Sb and carbo rich!	0-40m	**at fuchsite**		dol + mag + quartz veins. mag matrix
	M121	Q-carbo alteration veins inside fuchsite. Sb-poor (reef)	-	**at fuchsite**		
	M122A	Siderite-dolomite vein with py	-	**at fuchsite**		yellow and white carbo
	M122B	Siderite-dolomite vein with py	-	**at fuchsite**		yellow and white carbo
	M123	q-carbo vein with sulfide lenses. Talc schist	-	talc schist		
	M124	the green veins. prob chlorite within talc schist	-	talc schist		
	M125	talc schist with higher chloride content	-	talc schist		
	M126	apy-rich zone	-			
	SA0901	Qtz-carb alteration – freeslate zone – Close to S1 main shear zone. Shear zone mineralized with stibnite	10	?		
	SA0902	Late quartz-carbonate stibnite remobilization	-	?		
	SA0903	Late quartz-carbonate stibnite remobilization	-	?		
	SA0904	Stibnite ore	-	?		
	SA0906	Arsenopyrite ore body tightly folded area. Development towards the Monarch 'pipe' (main stibnite ore)	-	no		
	SA0907	Altered country talc. Chlorite-talc-carbonate schist envelope of the ore body southern end of the Monarch orebody.	-	no		
	SA0909	Apy zone	-	no		
	SA0911	carbonate-quartz remobiliazation	-	no		
	SA0914	Magnesite-quartz. No mineralization association.	-	no		Dol-quartz
	SA0915	Chesty pyritic ore. Pyrite bands in the past recrystallized pyrite. in parts the quartz as well but still cherty siliceous ore.	-	no		

*Footnote: All samples described per mine and depth of sampling. Special note has been made of approximity near fuchsite (listvenite) mineralization.

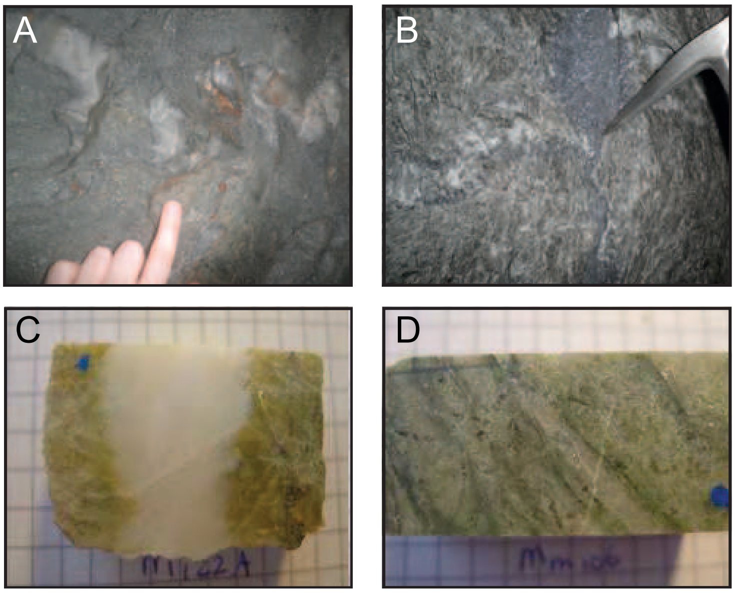

Figure 3.3: Photos of sample locations (A; B) and hand specimen (C; D) belonging to the metagranodiorite unit

other in zones of the most intense shearing, and some workers may term those domains listvenite (sensu lato). We use the term listvenite exclusively for rocks that contain noticeable amounts of fuchsite as identified by their bright green color. Chlorite schists are dark green and may grade into listvenite in carbonated domains. In these rocks with pronounced pressure-solution schistosity, quartz-carbonate (dolomite-magnesite) veins developed synkinematically as tension fractured and were folded and boudinaged. The quartz-carbonate veins were more competent than the surrounding schist and stibnite precipitated in pressure shadows around these microlithons as well as in brittle fractures within them (Vearncombe et al., 1992).

At **Gravelotte** we declined to 20m through chlorite-rich schists cut by carbonate veins

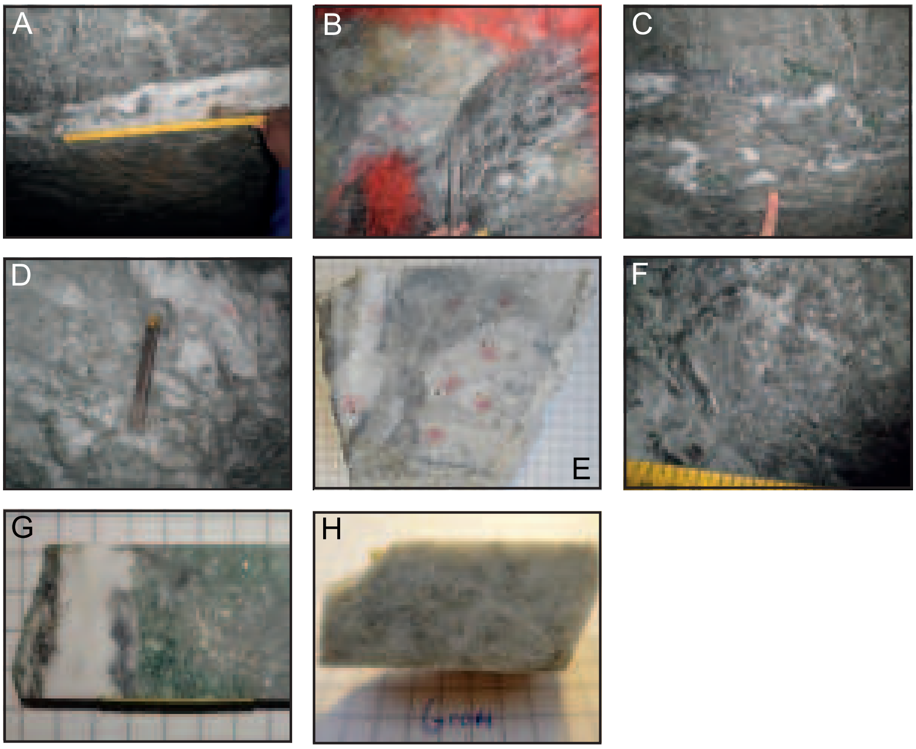

Figure 3.4: Photos of sample locations (A; B; C; D; F) and hand specimen (E; G; H) belonging to the listvenite unit.

of variable widths. Occasionally, quartz was the dominant matrix material biotite was found in the schists. Domains (cm-size) of fuchsite-rich rocks could be recognized within these chlorite-schists. At the bottom of the decline, the stibnite ore body was exposed; it is surrounded by large fuchsite-dolomite domains (m-size). At places in between the fuchsite-dolomite domains (Figure 3.4c), quartz-albite domains (m-size) were found (Figure 3.4h).

The focus of our sampling at the **Beta mine** was at the 16-17th level. Here we entered the stibnite mineralization, which is surrounded by large quartz veins and fuchsite mineralization. Stibnite mineralization is developed both along the margins of

the heavily deformed and stibnite-rich domains of type 1 (Figure 3.4a). These veins contain siderite and are free of stibnite away from the zones of major Sb mineralization. Additionally, rare quartz-stibnite veins are developed that crosscut the foliations and carbonate veins. These types have been grouped by paragenesis and appearance and they document a transition from ductile to brittle deformation processes and increasing abundance of quartz as vein fill.

3.3.2 Petrography and mineral chemistry

Chlorite, talc and fuchsite have undergone ductile to brittle deformation. Two types of chlorite-schists have been distinguished: biotite-rich quartz-chlorite schist and quartz-poor schist with chromium-rich chlorite. Dravite was sporadically found in the margins of carbonate veins of type 1, throughout the AL, with no apparent relationship between Sb-mineralization and dravite formation. Mineral formulas of fuchsite, chlorite and dravite are represented in Table 3.4, respectively. Fuchsite has high Cr-numbers (Cr# = Cr / (Cr+Al) at%), with Cr_2O_3 contents between 2.88 wt.% and 3.29 wt.% (Table 3.6). The Cr_2O_3 contents of chlorite are more variable, ranging between 0.0 and 2.69 wt.%. Dravite has the highest Cr contents though they vary between 0.8 and 6.9 wt.% (Figure 3.9). It is also apparent that both sulfides and silicates have low Mn contents. Microtextural observations show that the minerals formed during different mineralization stages, which are represented by specific mineral assemblages, grouped by the previously mentioned lithological units. These observations are summarized in the following paragenetic sequences (Figure 3.6 and 3.7).

As mentioned before, multiple carbonate minerals have been identified: dolomite, magnesite and siderite (Figure 3.8). The carbonate-matrix of chlorite and fuchsite is

Table 3.4: Average mineral formula of chlorite, fuchsite and dravite with Cr# and Mg#.

	Chlorite				***Dravite***		***Fuchsite***		
	Athens Mine	Monarch Decline	Beta Mine	S.Egypta	Monarch Mine	Beta Mine	Monarch Mine	Beta Mine	S.Egypta
	n = 23	n = 2	n = 19	n = 7	n=22	n=8	n = 23	n = 3	n = 5
SiO_2	26.50	27.02	28.71	29.09	37.83	37.66	47.34	49.67	49.56
TiO_2	0.06	0.07	0.06	0.03	0.86	0.15	0.35	0.29	0.13
Al_2O_3	22.15	22.51	19.27	17.84	36.22	30.86	33.39	24.20	33.43
Cr_2O_3	0.23	0.03	2.36	5.47	0.22	4.37	2.88	3.29	1.04
FeO	20.79	16.24	10.73	9.26	3.06	2.45	1.20	1.13	0.42
MnO	0.06	0.04	0.03	0.00	0.02	0.01	0.03	0.01	0.04
MgO	18.90	20.86	24.92	25.34	8.49	8.40	2.98	4.18	0.94
CaO	0.02	0.05	0.01	0.03	0.08	0.02	0.00	0.16	0.15
Na_2O	0.03	0.02	0.02	0.02	2.28	2.72	0.19	0.08	0.75
K_2O	0.01	0.00	0.00	0.03	0.01	0.01	9.66	11.52	6.66
Total	88.77	87.04	86.48	87.12	89.06	86.64	98.00	95.24	93.10
	Formula based on 14 anions				Formula based on 24.5 anions		Formula based on 11 anions		
Si	2.7	2.7	2.9	3.0	5.9	6.0	3.1	3.4	4.0
Ti	0.0	0.0	0.0	0.0	0.1	5.8	0.0	0.0	0.0
Al	2.7	2.7	2.3	2.1	6.5	0.0	2.6	1.9	3.2
Cr	0.0	0.0	0.2	0.2	0.0	0.6	0.2	0.2	0.0
Fe	1.8	1.4	0.9	0.8	0.3	2.0	0.1	0.1	0.0
Mn	0.0	0.0	0.0	0.0	0.0	0.3	0.0	0.0	0.0
Mg	2.8	3.1	3.7	3.9	2.0	0.0	0.3	0.4	0.1
Ca	0.1	0.0	0.0	0.0	0.0	0.0	0.0	0.0	0.0
Na	0.0	0.0	0.0	0.0	0.7	0.8	0.0	0.1	0.1
K	0.0	0.0	0.0	0.0	0.0	0.0	0.8	1.0	0.7
Total	10.1	9.9	9.9	10.0	15.6	15.7	7.0	7.1	8.1
Mg#	0.6	0.7	0.8	0.8	0.9	0.9	0.8	0.9	0.9
Cr#	0.0	0.0	0.1	0.1	0.0	0.1	0.1	0.5	0.0

* EMPA dataset of groups of chlorite. fuchsite and dravite minerals within the MGB in comparison with listvenites of the South Egypt ophiolite by (a) Emam and Zoheir (2013).

Cr# = (Cr / Cr+Al); Mg# = (Mg/ Mg+Fe)

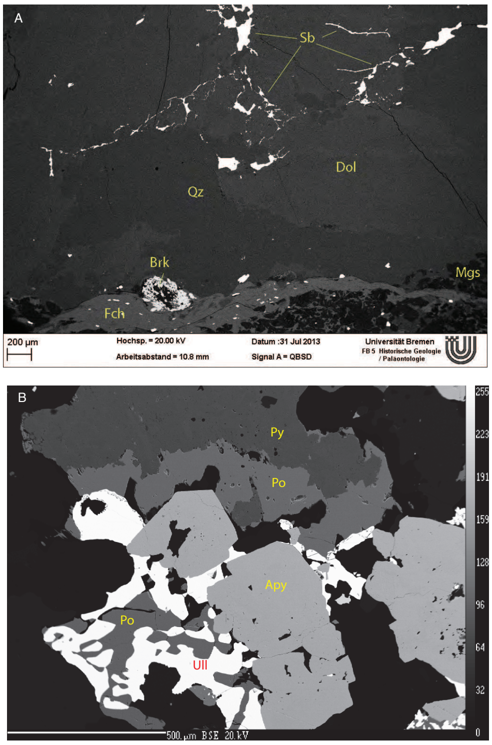
A
Sb
Dol
Qz
Brk
Mgs
Fch
200 µm
Hochsp. = 20.00 kV
Arbeitsabstand = 10.8 mm
Datum :31 Jul 2013
Signal A = QBSD
Universität Bremen
FB 5 Historische Geologie / Paläontologie
B
Py
Po
Apy
Po
Ull
255
223
191
159
128
96
64
32
0
500 µm BSE 20 kV

Figure 3.5: BSE Images of thin sections from an Sb-enriched listvenite (A) from the Monarch mine and an As-enriched granodiorite (B) from the Athens mine.

predominantly magnesite. Dolomite is mostly present within veins and/or fractures in varying grain size and contains the highest amount of stibnite intergrowths. Additionally, it appears that dolomite is the dominant host of Sb in the form of stibnite (Figure 3.10). Cogenetic magnesite-dolomite have highly variable Mg#'s and thus color. The carbonates selected for geochemical analyses include examples from quartz-magnesite and quartz-dolomite veins. Dolomite-magnesite-quartz veins and proximal to stibnite mineralization were also selected. In these veins, the carbonate phases appeared to be in textural equilibrium (cogenetic) with each other (Figure 3.4). Figure 3.8 depicts the large variation of Mg# of all the carbonates within the MGB system. The carbonates with high stibnite contents have the highest Mg#. The carbonates with the lowest Mg#

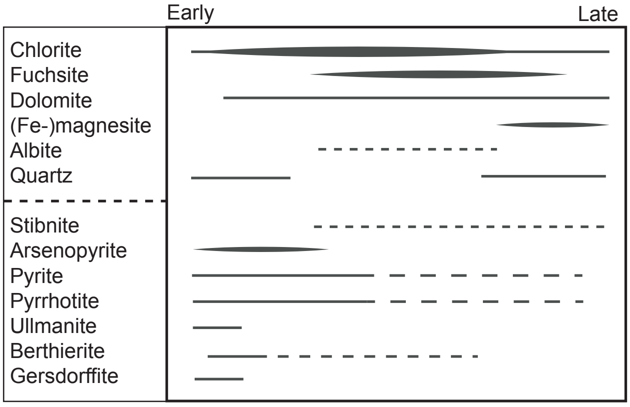

Figure 3.6: Paragenetic sequence of the lithological unit metagranodiorite. Chlorite within this unit has varying amounts of biotite and occasional chromium enrichments.

values, as well as the rare occurrences of siderite, are limited to the metagranodiorite lithological units. Sb-As minerals are disseminated within the silicates and are predominantly present within the metamorphic host rock. There are two types of Sb mineralization. The first type is an apparently primary assemblage of berthierite, ullmannite and gudmundite that co-occurs with pyrite, chalcopyrite and pyrrhotite. For instance, foliated chlorite schists contain arsenopyrite, pyrite and pyrrhotite, gudmundite, chalcopyrite and to lesser extents berthierite and ullmannite. These rock domains have not been affected by later-stage carbonate or quartz formation (Figure 3.5). A second type of Sb mineralization has stibnite as sole Sb-mineral, which is accompanied by rare berthierite, pyrite. In this apparently secondary formation, stibnite has been mobilized.and reprecipitated in tension gashes and pressure shadows.

The compositions of the dominant As and Sb minerals (arsenopyrite, berthierite, gudmundite, ullmannite and stibnite) are presented in Tables 3.5 and 3.6. The development of an arsenopyrite, pyrite, pyrrhotite assemblage allows for the application of the arsenopyrite geothermometer of Kretschmar and Scott (1976). Their calibration sug-

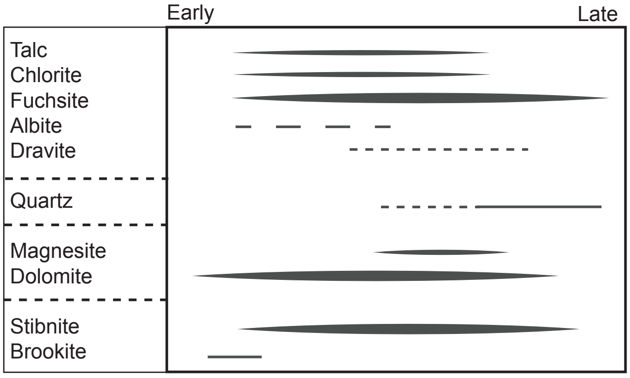

Figure 3.7: Paragenetic sequence of the lithological unit listvenite. Chlorite within this unit is predominantly chromium-rich.

gests that arsenopyrite with 30-32 at.% arsenic (Table 43.4) coexists with pyrite and pyrrhotite at temperatures between 300 and 400 °C (cf. Figure 3.7 in Kretschmar and Scott (1976)). Berthierite is present as main mineral or as rim of ullmannite within the chlorite schist. Ullmannite has only been found surrounded by berthierite. Gudmundite has been found adjacent to arsenopyrite, within the arsenopyrite-rich zone in the Monarch mine. Ullmannite and gudmundite lack in the carbonate-quartz metasomatized domains of the AL lithologies. In contrast, stibnite (and minor berthierite) is exclusively found within tension fractures, like boudins, boudinages or veins and is clearly related to isoclinal folding and subsequent episodes of deformation and veining.

3.3.3 Trace element compositions of carbonates

A distinction was made between pure carbonate and mixed carbonate-quartz veins in terms of both dolomite and magnesite compositions (Table 3.7). When comparing the different carbonate minerals, a clear difference in ΣREE+Y values between dolomite and magnesite is evident. Dolomite (Figure 3.12a, 3.12b) is enriched in both LREE and

Table 3.5: EMPA dataset of selected stibnite minerals.

Stibnite	M123	Bm048	Bm048	Bm048
S	28.26	28.23	28.17	28.26
Mn	0.02	0.01	0.01	0.03
Fe	0.13	0.00	0.02	0.00
Co	0.02	0.00	0.02	0.00
Ni	0.00	0.00	0.00	0.01
Zn	0.00	0.00	0.02	0.00
As	0.03	0.06	0.01	0.03
Cd	71.43	71.60	71.71	71.66
Sb	0.04	0.04	0.00	0.02
Cu	0.00	0.00	0.00	0.00
Total	99.94	99.95	99.96	100.01
S	59.87	59.88	59.82	59.90
Mn	0.03	0.01	0.01	0.04
Fe	0.16	0.00	0.02	0.00
Co	0.03	0.00	0.02	0.00
Ni	0.00	0.00	0.00	0.01
Zn	0.00	0.00	0.02	0.00
As	0.03	0.06	0.01	0.03
Cd	39.85	40.00	40.10	40.00
Sb	0.05	0.05	0.00	0.02
Cu	0.00	0.00	0.00	0.00
Total	100	100	100	100

Ullmanite	A080	B028a	B028b	M123a	M123b
S	15.34	15.32	15.29	15.42	15.22
Mn	0.01	0.02	0.01	0.02	0.00
Fe	0.15	0.04	0.07	0.14	0.12
Co	0.00	0.00	0.00	0.06	0.10
Ni	27.28	27.17	26.94	27.37	26.98
Zn	0.03	0.00	0.00	0.01	0.08
As	1.07	0.07	0.04	2.90	0.98
Sb	56.04	57.44	57.42	54.16	56.29
Cu	0.00	0.00	0.00	0.00	0.00
Total wt.%	99.93	100.06	99.81	100.10	99.78
S	33.66	33.78	33.82	33.51	33.55
Mn	0.02	0.02	0.01	0.03	0.00
Fe	0.19	0.05	0.09	0.18	0.16
Co	0.00	0.00	0.00	0.08	0.12
Ni	32.69	32.72	32.55	32.48	32.48
Zn	0.04	0.00	0.00	0.01	0.09
As	1.00	0.07	0.04	2.70	0.92
Sb	32.39	33.35	33.45	31.00	32.68
Cu	0.00	0.00	0.00	0.00	0.00
Total at.%	100	100	100	100	100

Gudmundite	A082a	A082b	A082c	A082d
S	15.60	15.53	15.45	15.61
Mn	0.04	0.00	0.00	0.00
Fe	26.46	26.57	26.13	26.97
Co	0.03	0.02	0.05	0.00
Ni	0.36	0.15	0.35	0.04
Zn	0.02	0.01	0.04	0.05
As	0.04	0.00	0.00	0.01
Sb	0.00	0.00	0.00	0.00
Cu	58.39	58.46	58.39	58.37
Ti	0.00	0.00	0.03	0.02
Total wt.%	100.94	100.74	100.42	101.07
S	33.59	33.57	33.54	33.56
Mn	0.05	0.00	0.00	0.00
Fe	32.72	32.96	32.55	33.28
Co	0.03	0.03	0.06	0.00
Ni	0.43	0.17	0.41	0.05
Zn	0.02	0.01	0.04	0.05
As	0.04	0.00	0.00	0.01
Sb	0.00	0.00	0.00	0.00
Cu	33.12	33.27	33.37	33.04
Ti	0.00	0.00	0.03	0.02
Total at.%	100	100	100	100

Berthierite	M126	M126	M124	B028	B028
S	30.05	30.01	29.93	30.10	29.88
Mn	0.00	0.00	0.00	0.02	0.01
Fe	12.95	12.84	12.85	12.88	13.00
Co	0.00	0.00	0.00	0.00	0.02
Ni	0.01	0.00	0.00	0.00	0.02
Zn	0.06	0.01	0.02	0.02	0.00
As	0.11	0.11	0.07	0.02	0.00
Sb	56.75	57.00	57.10	56.95	57.02
Cu	0.04	0.02	0.00	0.00	0.03
Ti	0.00	0.00	0.00	0.00	0.00
Total wt.%	99.97	99.98	99.97	100.00	99.98
S	57.21	57.22	57.14	57.30	57.03
Mn	0.00	0.00	0.00	0.02	0.02
Fe	14.15	14.06	14.08	14.08	14.24
Co	0.00	0.00	0.00	0.00	0.02
Ni	0.01	0.00	0.00	0.00	0.02
Zn	0.06	0.01	0.01	0.02	0.00
As	0.09	0.09	0.06	0.02	0.00
Sb	28.45	28.61	28.71	28.55	28.65
Cu	0.04	0.02	0.00	0.00	0.03
Ti	0.00	0.00	0.00	0.00	0.00
Total at.%	100	100	100	100	100

Table 3.6: EMPA dataset of selected arsenopyrite minerals.

Arsenopyrite	A082a	A082b	M126a	M126b	M126c
S	20.55	21.68	20.37	20.86	20.72
Mn	0.01	0.00	0.02	0.00	0.00
Fe	34.86	34.91	34.77	34.80	34.63
Co	0.00	0.00	0.00	0.00	0.03
Ni	0.05	0.15	0.01	0.03	0.23
Zn	0.06	0.00	0.07	0.00	0.00
As	44.26	43.01	44.72	44.12	44.24
Cd	0.00	0.00	0.04	0.09	0.07
Sb	0.14	0.08	0.00	0.01	0.00
Cu	0.00	0.00	0.00	0.00	0.00
Total wt.%	99.92	99.85	100.00	99.92	99.91
S	34.48	35.99	34.22	34.91	34.71
Mn	0.01	0.00	0.02	0.00	0.00
Fe	33.58	33.27	33.53	33.43	33.31
Co	0.00	0.00	0.00	0.00	0.03
Ni	0.05	0.13	0.01	0.03	0.21
Zn	0.05	0.00	0.06	0.00	0.00
As	31.78	30.55	32.14	31.59	31.72
Cd	0.00	0.00	0.02	0.04	0.03
Sb	0.06	0.03	0.00	0.01	0.00
Cu	0.00	0.00	0.00	0.00	0.00
Total at.%	100	100	100	100	100

*Five selected samples from Athens mine (A-sample nr) and Monarch decline (M-sample nr).

HREE, while magnesite is depleted in LREE. Dolomite associated with quartz (Figure 3.12) displays a greater overall variation in the contents of REE than pure dolomite veins (Figure 3.12). All dolomite associated with quartz shows positive Eu anomalies, which is most pronounced in samples with low REE contents. Pure dolomite veins show generally high REE contents with flat distribution patterns and a lack of Eu anomalies. Magnesite from both pure magnesite and magnesite-quartz veins show distinct LREE depletions with magnesite associated with quartz displaying very small positive Eu anomalies. Dolomite has an average Mg# value of 0.87, and is more magnesian than magnesite with an average Mg# of 0.71.

3.3.4 Stable isotope compositions and geothermometry

$^{13}C_{PDB}$ values of pure dolomite range from -4.5 to -6 ‰ and those of pure magnesite vary between -4 and 5.5 ‰ (Table 3.8). Another population of those carbonates,

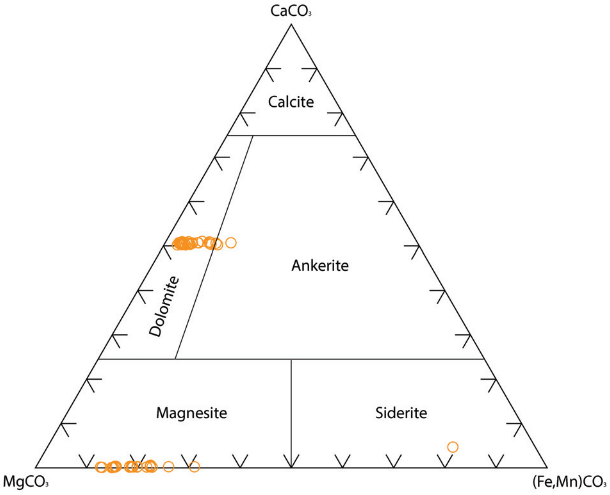

Figure 3.8: Compositional plot of dolomite, magnesite and siderite samples from the AL

however, has values indistinguishable from the ones presented here. $\delta^{18}O_{SMOW}$ values range between 12 to 13.5 ‰ for dolomite and 14 to 16 ‰ for magnesite (Figure 3.9a). The carbonate-quartz veins (Figure 3.9b) show similar C values, and slightly lighter $\delta^{18}O_{SMOW}$ values. Samples from the Beta mine are lighter in $\delta^{18}C_{PDB}$ values than samples from Gravelotte by about 1.5, while samples from Athens and Monarch are more variable (Figure 3.9d). $\delta^{18}O$ values of quartz range from 12.8 to 15.2 and average at 13.6+/-0.7‰ (n=13; Table 12).

Estimations of carbonate vein formation temperature and calculations of $\delta^{18}O$ compositions of the fluids ($\delta^{18}O_{H2O}$) were conducted. In these calculations it was assumed that dolomite and magnesite formed coevally. Textural evidence in support of this assumption has been found in a subgroup of the carbonate-altered rocks that feature large and intergrown grains of magnesite and dolomite (Figure 3.4f). Only two samples from the entire sample set exhibited this kind of texture and were suited for geothermometry using dolomite-magnesite. According to the data of Chacko and Deines (2008), the dolomite-magnesite fractionation has the following temperature dependence:

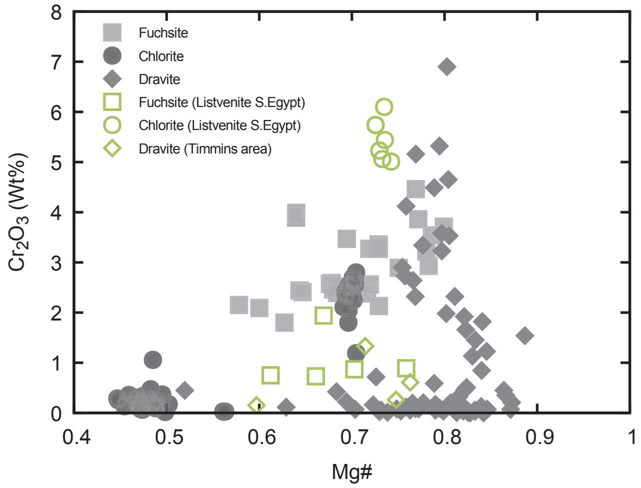

Figure 3.9: Cr_2O_3 vs Mg# of fuchsite, chlorite and dravite. For comparison fuchsite and chlorite compositions from (a) Emam and Zoheir (2013) and dravite from (b) Moritz and Crocket (1991) are also shown.

Table 3.3 presents the average calculation results for both locations, yielding temperatures of 357±19 °C for the Beta Mine and 402±24 °C for the Gravelotte decline. From these temperatures and average dolomite compositions, we have calculated $\delta^{18}O_{H2O}$ values of the carbonatizing fluids, using the Horita (2014) calibration of the dolomite-water system (3.2) of 8.7 and 9.1 ‰. With an average $\delta^{18}O_{H2O}$ composition of 8.9 ‰ and the quartz-water calibration from Sharp and Kirschner (1994)

$$\Delta qtz - H_20 = 3.65x10^6/T^2 - 2.9 \tag{3.3}$$

we get temperatures of 424+/-31 °C for the quartz data from all quartz-carbonate veins (Table 3.10). The calibration by Zhang et al. (1989)

Table 3.7: Average REE+Y values of four groups of carbonate.

Avg	**Dol-Q**	**Dol**	**Mgs-Q**	**Mgs**
La	7.04	4.80	0.05	0.02
Ce	10.46	6.86	0.04	0.02
Pr	11.16	7.59	0.04	0.03
Nd	11.40	8.53	0.05	0.04
Sm	14.27	12.14	0.11	0.13
Eu	15.20	21.36	0.14	0.14
Gd	17.25	14.71	0.17	0.26
Tb	16.34	15.49	0.32	0.53
Dy	15.15	12.64	0.49	2.25
Y	17.87	13.76	0.62	1.10
Ho	12.87	14.67	0.74	1.15
Er	11.83	14.31	1.17	1.65
Tm	10.80	12.73	1.87	2.31
Yb	10.44	12.71	2.85	3.04
Lu	27.29	11.42	3.64	3.66
ΣREE+Y	187.90	186.59	12.28	14.90
ΣLREE	87.97	75.93	0.59	0.65
ΣHREE	81.24	96.90	10.38	13.15
Mg#	0.85	0.88	0.70	0.73
n	15	79	16	27

*Chondrite normalised values of two sets of carbonates: dolomite(-quartz) and magnesite(-quartz).
Chondrite values of Sun and McDough (1995).

$$\Delta qtz - H_2O = 3.306x10^6/T^2 - 2.71 \tag{3.4}$$

for the same data yields 399+/-31 °C.

3.3.5 Geochemical calculations and reaction path model results

We conducted thermodynamic calculations to depict the Fe-Cu-Sb-O-H-S phase relations and computed equilibrium reaction paths to examine possible sources and traps for Sb, As, Au, Cu, and Fe in the specific setting of the AL in the MGB. The phase relations were examined in H_2(aq) vs. H_2S(aq) activity plane at 1 kbar and temperatures of 350 and 250 °C (3.13a and b), indicate that the transition from early native antimony and berthierite along with pyrrhotite to later stibnite and pyrite is consistent

Table 3.8: Stable isotope dataset of dolomite and magnesite in close approximation of Sb-enrichments.

Dolomite				**Magnesite**				**Quartz**	
	$\delta^{13}C_{PDB}$	$\delta^{18}O_{VMSOW}$	Comment		$\delta^{13}C_{PDB}$	$\delta^{18}O_{VMSOW}$	Comment	Sample	$\delta^{18}O$
SA0947	-5.84	12.77		Gr008	-3.94	15.50	red	B020	13.6
	-5.81	12.90			-4.01	14.74	red	B025A	13.2
	-5.81	12.91			-4.11	14.83	red	B026	13.5
	-5.90	13.17		Bm048	-5.06	15.31		B027	12.9
	-5.76	13.16			-4.95	15.42		B032	12.8
	-5.85	12.88		B026	-5.15	15.23		B033	13.3
	-5.82	13.04			-5.13	14.73		Bm040	14.5
SA0933	-5.28	13.00			-5.05	14.90		Bm053	13.2
	-5.42	12.57		Gr004	-4.12	14.61	red	Gr012	13.6
	-5.21	11.27			-4.38	14.77	red	M121	13.1
	-4.98	13.54			-4.14	14.57	red	M124	15.2
	-5.21	11.28			-4.22	14.83	red	M126	13.0
	-5.77	12.61		Bm040	-4.96	15.67			
	-5.77	13.29			-5.08	15.43			
Gr008	-4.58	12.58			-5.19	15.34			
	-4.61	12.38			-4.99	15.58			
	-4.69	13.00			-4.62	15.06	yellow		
Gr004	-4.66	13.05			-5.10	15.62			
	-4.66	12.58			-4.67	12.23			
	-4.69	12.85			-4.80	11.85			
	-4.60	12.74			-4.80	11.53			
	-4.59	12.55			-4.48	12.12			
Bm040	-5.53	13.29			-4.81	11.66			
	-5.53	13.47							
	-5.55	13.48							
	-5.42	13.47							
	-5.51	13.34							
	-5.54	13.36							
	-4.85	13.05							
Gr006	-4.28	12.60	yellow						
	-4.21	12.44	yellow						
	-4.36	12.46	yellow						
	-4.26	12.44	yellow						
M122	-4.15	13.23	yellow						
	-4.08	13.46	yellow						
	-4.22	13.32	yellow						
	-4.28	13.96							
	-4.71	12.22							
	-3.93	12.09	yellow						
	-4.44	13.22	yellow						
	-4.27	13.90	yellow						
Gr005	-4.56	12.52							
	-4.20	13.90							
	-4.63	12.56							
	-4.59	12.44							

Table 3.9: Temperature calculations from MGB quartz.

Sample	$\delta^{18}O_{qtz}$	$\delta^{18}O_{H_2O}$	T(K)^{a}	T(°C)	T(K)^{b}	T(°C)
Gr012	136	62	6432	3702	6680	3950
B020	136	62	6432	3702	6680	3950
B025A	132	58	6600	3870	6849	4119
B026	135	61	6473	3743	6721	3991
B027	129	55	6734	4004	6985	4255
B032	128	54	6781	4051	7033	4303
B033	133	59	6557	3827	6806	4076
Bm043	144	7	6133	3403	6375	3645
Bm044	145	71	6098	3368	6340	3610
Bm052	132	58	6600	3870	6849	4119
M121	131	57	6644	3914	6894	4164
M124	152	78	5871	3141	6109	3379
M126	13	56	6689	3959	6939	4209

*Based on $\delta^{18}O_{H_2O}$=8.32 ‰) and $\delta^{18}O_{qtz}$ and $\delta^{18}O_{H_2O}$ temperatures have been calculated based on geothermometers of (a) Zhang et al. (1989) and (b) Sharp and Kirschner (1994).

Samples taken from Gravelotte mine (Gr-sample nr), Beta quarry (B-sample nr), Beta mine (Bm-sample nr) and Monarch decline (M-sample nr).

Table 3.10: Temperature and ΔDol-H_2O calculation of MGB carbonates.

δ^{18}OMgs	δ^{18}ODol	1000 ln α	T(K)^{a}	T (°C)	ΔDol-H_2O^{b}	$\delta^{18}O_{H_2O}$
15.67	13.00	2.67	603	330	5.50	7.50
15.43	13.47	1.95	659	385	4.09	9.38
15.34	13.48	1.87	681	408	3.63	9.84
15.58	13.47	2.11	624	350	4.93	8.54
14.61	13.05	1.57	779	506	2.03	11.00
14.77	12.58	2.18	610	336	5.31	7.27
14.57	12.58	1.71	727	453	2.81	10.00
14.83	12.74	2.09	628	355	4.82	7.92

* Calcuation based on based on the linear relationship (Figure 3.2) of Chacko and Deines (2008) (a) and Horita (2014) (b).

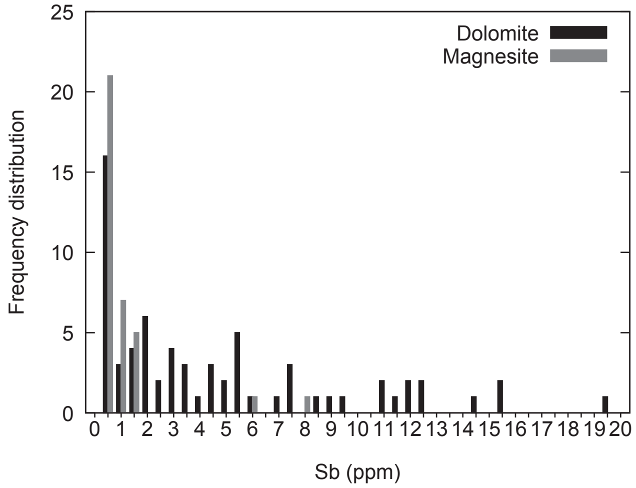

Figure 3.10: Histogram of the frequency distribution of Sb content within dolomite and magnesite, revealing dolomite to be the main host for Sb.

with a drop in the activity of aqueous dihydrogen, which causes an increase of sulfur fugacity, according to

$$S_2(g) + H_2(aq) = H_2S(aq) \tag{3.5}$$

Isopleths for sulfur fugacities were calculated using this reaction and are also shown in Figure 3.13. An increase or decrease in $H_2S(aq)$ activity can also cause the transition from berthierite to stibnite. A decrease in H_2S activity can explain the berthierite-stibnite transition only in the presence of magnetite, which is lacking in the AL assemblages. Likewise, degassive loss of both H_2 and H_2S in equal proportions would not affect sulfur fucacity, so the berthierite-stibnite phase boundary can only be crossed if magnetite were present. Because pyrite is commonly developed in the Sb-mineralized rocks from the AL, the replacement of berthierite by stibnite as dominant Sb phase can only be accomplished by decreasing a_{H2} or by increasing a_{H2S}, both leading to in-

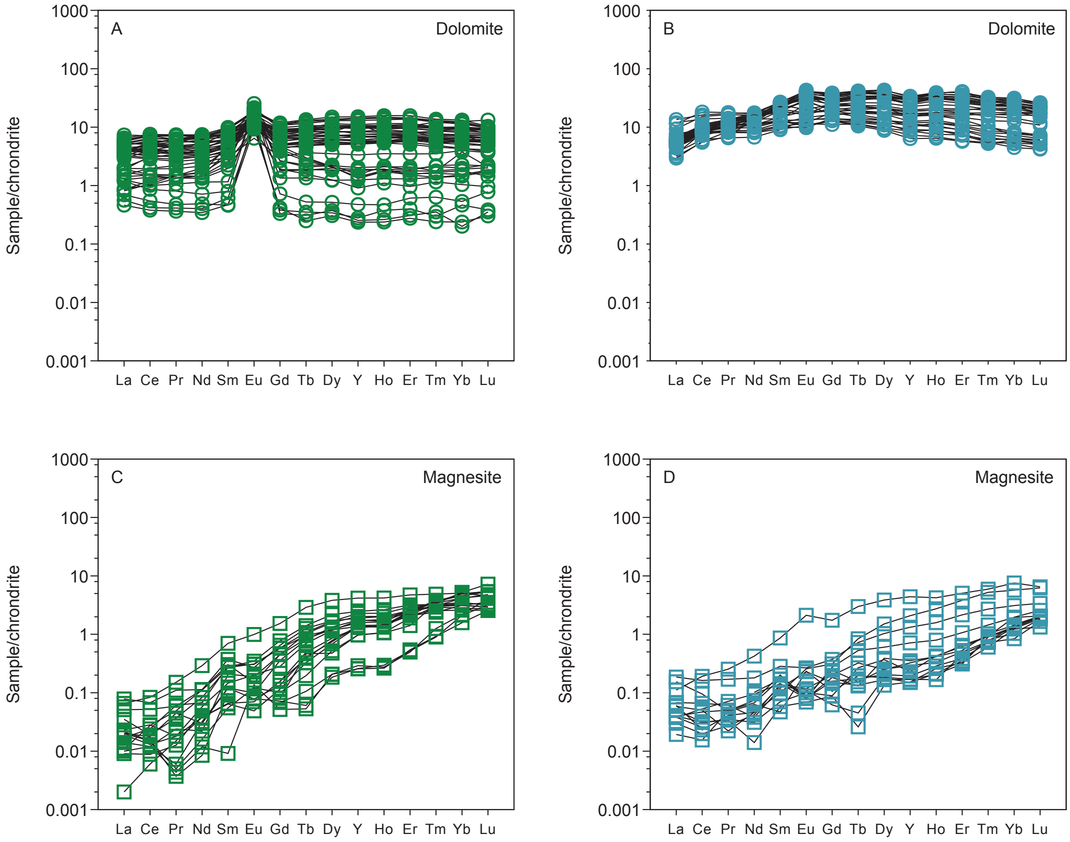

Figure 3.11: ΣREE+Y chondrite-normalized patterns of selected samples of dolomite veins (A), dolomite-quartz veins (B), magnesite veins and/or veinlets (C) and magnesite-quartz veins or veinlets (D). Chondrite values used for normalization are from McDonough and Sun (1995).

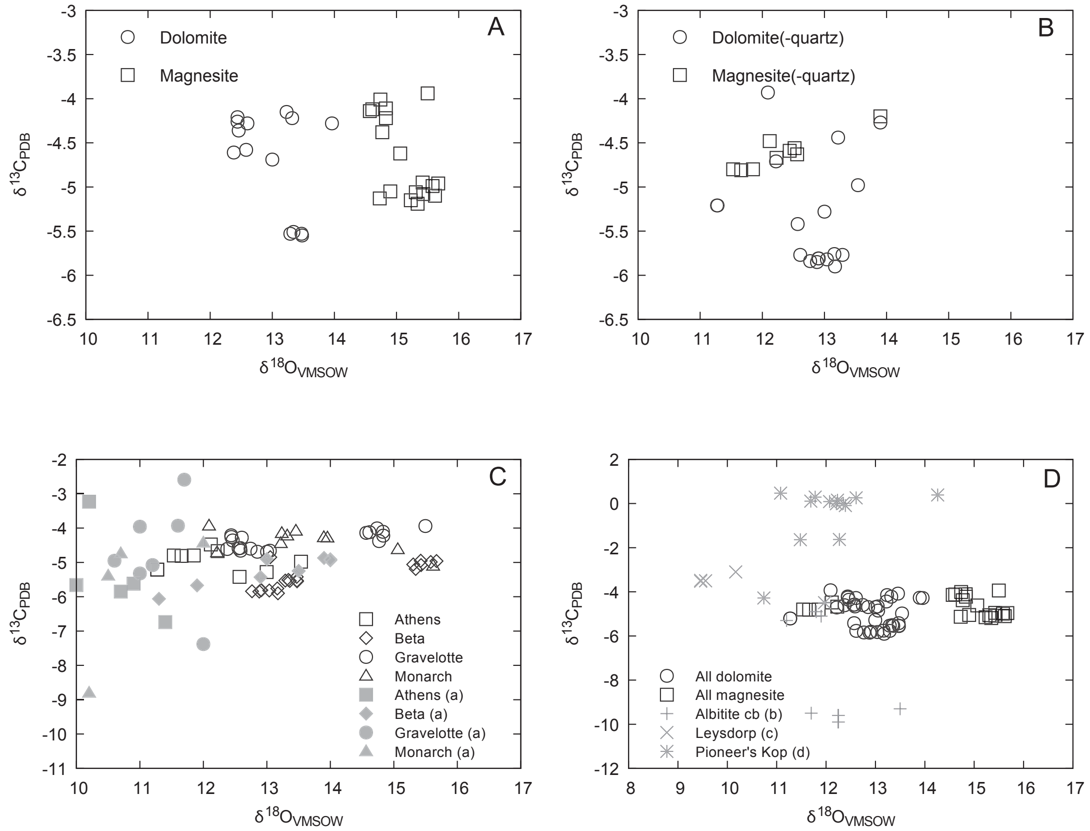

Figure 3.12: Stable isotopes A-D of four sets of chemically distinct carbonate-veins and fissures. A) pure dolomite, B) pure magnesite veins, C) dolomite-quartz veins and D) magnesite-quartz fissures. Comparisons have been made with (a) J. Jaguin, Boulvais, M.- C. Boiron, et al. (2014); (b) Justine Jaguin et al. (2013); (c) Schürmann et al. (2000); (d) Nesbitt et al. (1979) and (e) Ronde and Wit (1992).

creased sulfur fugacities. The compositional consequences of degassing do not explain the observed evolution of phase relations. The solubility of Sb (ppm) is contoured on top of the solid phase relations in Figure 3.13c. The diagram depicts that Sb solubility increases as a_{H2S} goes down. Boiling and removal of H_S will hence increase Sb solubility (cf. Hagemann and Lüders (2003)). The diagram also shows that increasing a_{H2} will decrease Sb solubility. Hence Sb is quite soluble at 1 kb and 400 °C in a fluid in which H_2 and H_2S are buffered by pyrite-hematite-magnetite. Fluids typical for serpentinization have much lower Sb solubility. For a fluid to precipitate Sb in the stability field of stibnite, increased a_{H2} at lowered a_{H2} would be ideal.

The reaction path model is set up to simulate the behavior of Sb, As, Fe, Cu, and Au in a scenario that is consistent with the geological evolution of the AL in the MGB (Vearncombe et al., 1992; J. Jaguin, Poujol, et al., 2013). In this scenario, intrusion of the Maranda granodiorite into basement composed of sediments and peridotitic komatiite gave rise to the primary Sb-mineralization in the tectonized and metasomatized contact between the two lithologies. In a first step, the model assesses the solubility of Sb, As, Fe, Cu, and Au within the granodiorite body (using average unmetasomatized granodiorite composition from J. Jaguin, Poujol, et al. (2013)), under temperatures up to 600 °C. The model results indicate that at intermediate temperatures of 250-350 °C, the solubility of Sb and As is greater than that of Fe and Cu (Figure 3.14a). In the following step, we computed the geochemical consequences of reactions between 350 °C fluids equilibrated with the granodiorite when such a fluid encounters ultramafic rock (using average MGB serpentinite compositions from Madisha (1996) along its flow path.

The results indicate that even small amounts of ultramafic rock reacting with the fluids would cause the solubilities of Sb and As (and Fe) to drop by 2-3 orders of magnitude, while the solubility of Cu and Au would not be decreased along the same reaction path

(Figure 3.14b). The levels of Fe that can be deposited are trivial compared to those of As and Sb. This result suggests that the lithological contact between granodiorite and komatiite would make an efficient trap for Sb and As, while Fe, Cu, and Au would not be trapped very efficiently. It is the reducing conditions imposed by the serpentinization of the komatiite that lowers the solubility of Sb. This relation is depicted in Figure 3.13c which indicates high Sb solubilities only under conditions of fairly low H_2 and high H_2S activities. Serpentinization environments, by contract are always characterized by high H_2 and low H_2S activities (Klein and Bach, 2009).

Figure 3.14c predicts a primary mineralization of arsenopyrite-pyrrhotite-chalcopyrite-gold-native antimony. In a second set of reaction path models, we reacted (1) fluid of seawater salinity with quartz, albite, K-feldspar, muscovite, biotite, and calcitet at 500 °C and (2) let this fluid react with metakomatiite and granodiorite (using the same rock compositions as above), while cooling the system from 500 to 300 °C (Figure 3.15). The initial fluid has an X(CO2) of 0.1, which is consistent with the compositions of fluid inclusions in quartz from the AL (J. Jaguin, Boulvais, M.-C. Boiron, et al., 2014). Initial As and Sb concentrations of 1000 ppm and a Au concentration of 1 ppm in the starting fluid were assumed. These values are lower than solubility values for these elements in the starting fluid at 1 kbar and 500 °C. The results of these model runs indicate that stibnite-rich quartz-magnesite rocks form from metakomatiite at high water-to-rock rations at T<400 °C (Figure 3.15a). The chalcopyrite-pyrrhotite- berthierite assemblage in this lithology is expected to be stable at lower water-to-rock ratios and higher temperatures (Figure 3.15b). Arsenopyrite is predicted to be stable throughout much of the reaction path. The granodiorite is predicted to form albite-quartz rich rocks with minor muscovite throughout much of the reaction path and quartz-stibnite rich rocks with abundant dolomite at the highest water-to-rock ratios (Figure 3.15c). These model run

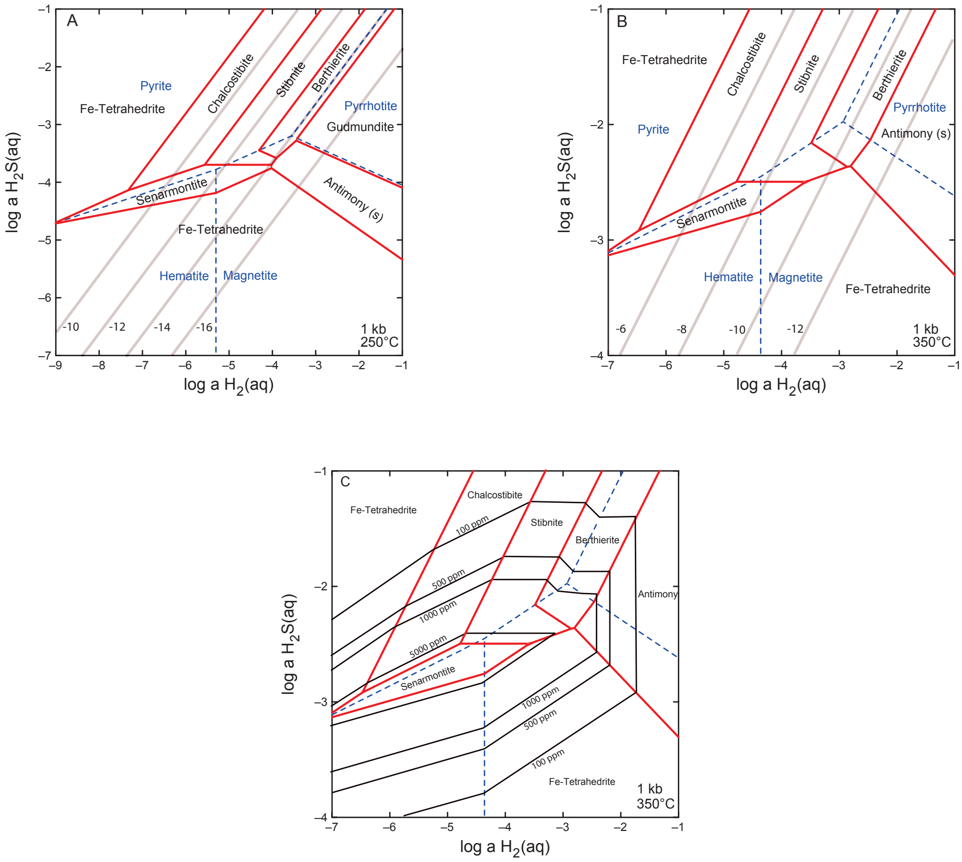

Figure 3.13: Activity-activity diagram for 250 (a) and 350 °C (b) and 1 kb, of Fe-S-O system in blue and the Fe-Sb-Cu-S-O-H system superimposed in red. Isopleths of sulfur fugacities are represented by the light grey lines. Figure c shows the 250 °C activity-activity diagram with Sb concentrations contours in ppm.

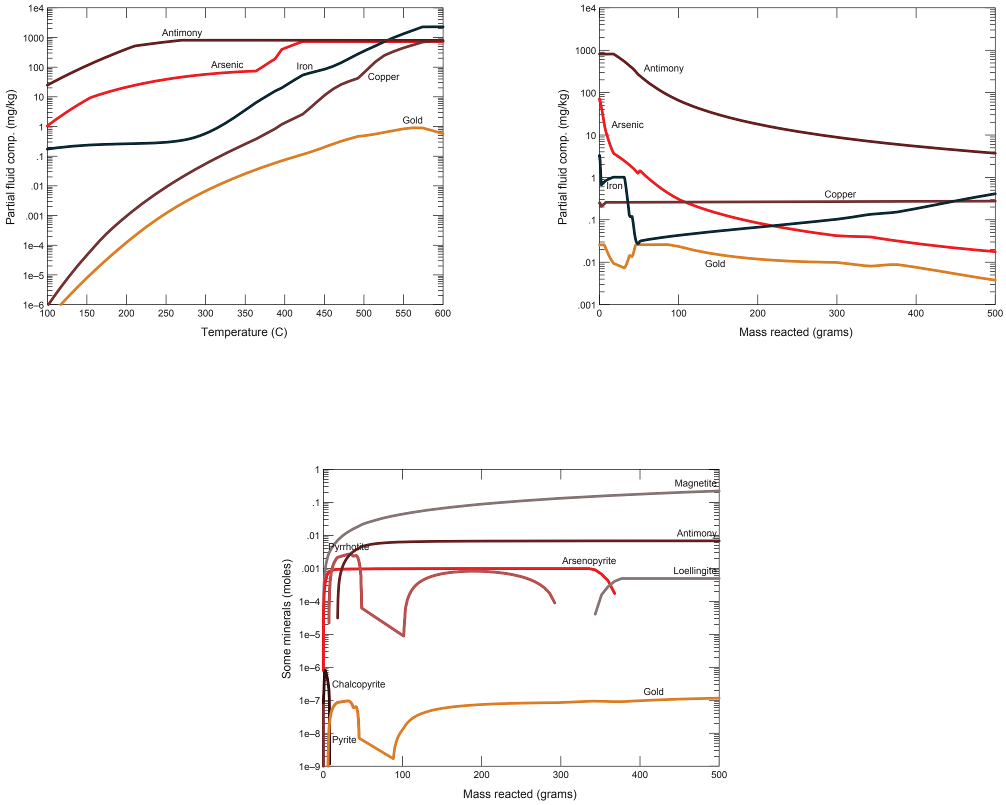

Figure 3.14: Reaction path modeling results revealing the compositions of fluids reacting with granodiorite, while being heated up to 600 °C (a). Figure b shows the composition change of a fluid that was initially equilibrated with granodiorite at 350 °C and then reacted with a metakomatiite. The concentrations of antimony, arsenic, iron, copper and gold are presented and show different behaviors (depletions in Sb and As vs. steady concentrations for Au and Cu). Figure c shows the sequences of mineral predicted to occur while titrating the metakomatiite into the granodiorite-equilibrated fluid. See text for further details.

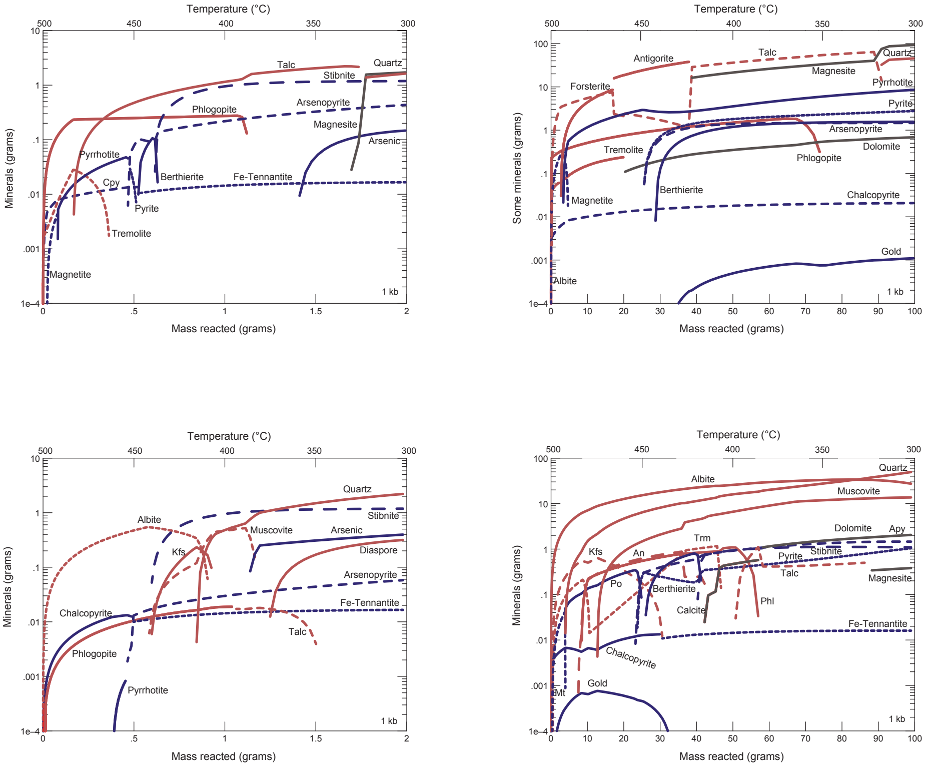

Figure 3.15: Results of reaction path models in which a model metamorphic fluid was reacted metakomatiite and granodiorite, while the system cooled from 500 to 300 °C. The compositions of the initial metamorphic fluid was calculated by reacting a fluid of seawater salinity with quartz, albite, K-feldspar, muscovite, biotite, and calcitet at 500 °C. The second paths shown depict two different final water-to-rock ratios (high w/r=500, and low w/r=10) for each of the two lithologies. In each of these, temperature correlates linearly with w/r, such that T=500 °C when w/r=0 and T=300 °C when w/r=final (i.e., 500 or 10, respectively). Note that common qz-mag and qz-dol with abundant As and Sb mineralization are predicted to form at T<400 °C. Also note that the grandiorite is predicted to alter to albitite.

results match the observed lithologies (listvenite and albitite) and mineralization (stibnite in quartz-carbonate rocks) remarkably well. Au enrichments on the order of up to 5-10 ppm are predicted to develop at intermediate and low water-to-rock rations in the granodiorites (Figure 3.15d) and metakomatiites, respectively.

3.4 Discussion

3.4.1 Fluid source and temperatures of mineralization

The AL represents a suture zone in an Archaean greenstone Belt that features TTG intrusions into the mafic-ultramafic/sedimentary basement. This suture zone has undergone multistage structural deformation and metasomatism (listvenitization) (2.0 Ga; J. Jaguin, Boulvais, M.-C. Boiron, et al. (2014)). The events have carbonatized and silicified the ultramafic host rock and deposited quartz-carbonate-stibnite veins that were folded and boudinaged. The source of the metasomatizing fluids can be characterized based on C and O isotopic compositions and fluid inclusions. Fluid inclusions have not been incorporated in this study, due to the poor quality of the fluid inclusions. The MGB has endured several deformation events over the 2.9 Ga that compromise the reliability of the information to be retrieved from the fluid inclusions present. The most recent published articles (J. Jaguin, Poujol, et al., 2013; J. Jaguin, Boulvais, M.-C. Boiron, et al., 2014) have similarly investigated the stable isotopes and fluid inclusions of the carbonates along the AL and have come with a more disperse isotope and temperature data set (Figure 3.10). Their main objective was to investigate all the carbonates along the AL, making no distinction which carbonates have been related to the Sb mineralization, which is attempted in this study. Our data indicate that both magnesite and dolomite have a fairly uniform $\delta^{13}C$ signature (≈ -5 ‰). J. Jaguin, Boulvais, M.-C. Boiron, et al. (2014) find a larger range (-4 to -11‰) in their more diverse set of carbonate samples from the AL. $\delta^{18}O$ of the carbonates from the AL range from 11.5 to 16 ‰ (J. Jaguin, Boulvais, M.-C. Boiron, et al. (2014) and this work). The dolomite is uniformly around 13 ‰. Magnesite from Athens mine is lighter than magnesite from the other mines. The discrepancy of $\delta 18O_{VMSOW}$ between the different mines may reflect the distance between sample locations: Gravelotte and Athens mine lie ≈ 10 km apart (Figure 3.1). Additionally, the Sb ore zones visited and sampled in every mine lie in significantly different depths, from 0 to 1240 m (Table 3.2). $\delta^{18}O$ of quartz associated with the carbonates ranges from 12.9 to 15 ‰ in our data set, similar to the 11.9 to 14.3 ‰ range reported by J. Jaguin, Boulvais, M.-C. Boiron, et al. (2014). These data are generally similar to values retrieved for other mineralized Archaean greenstone belts. Ronde and Wit (1992)has found slightly lighter $\delta^{13}C$ (-4.4 to -2.2 ‰) values for Au-Sb associated carbonates from similar fuchsite-carbonate-quartz or sericitet-carbonate-quartz alteration zones and veins in the Barberton Greenstone belt. Their $\delta^{18}O$ values (12-13.5 ‰) overlap with those found in the AL (Figure 3.9). Likewise, Phanerozoic Sb-Au deposits bound to quartz-carbonate veined listvenites show similarly heavy δ18O (4-16 ‰) and $\delta^{13}C$ values (-5 to -7 ‰) reconstructed for the metasomatizing fluids (Madu et al. (1990) and references therein).

Schürmann et al. (2000) reports similar compositions of $\delta^{13}C$ (-3.7 to -4.9 ‰) and $\delta^{18}O$ (12.8 to 13.2 ‰) from altered carbonatite dykes from the Barberton Greenstone belt. If those dykes preserved the mantle signatures, their similarity in the $\delta^{13}C$ and $\delta^{18}O$ signatures to the quartz-carbonate veins in the MGB and AL may indicate that the latter are also derived from a mantle-derived fluid. But the larger range in $\delta^{13}C$ reported by J. Jaguin, Boulvais, M.-C. Boiron, et al. (2014) is more difficult to reconcile with a mantle origin. A perhaps more common hypothesis is that deep-seated fluids derived from devolatilization of metavolcanic and metasedimentary rocks released upon collision and shearing from deeper crustal zones within the greenstone belt (McCuaig and Kerrich (1998) and references therein). The calculated $\delta^{18}O_{H2O} \approx 9$ ‰ isotopic signature is heavier than of modern hydrothermal vent fluids of 0.4-2.11 ‰ (De Ronde et al., 1997). Jaffrés et al. (2007) calculated that Archaean seawater had $\delta 18O_{VMSOW}$ of -13 to -17 ‰ value at 2-3 Ga. Assuming a similar (2 ‰) fractionation during heating a reaction with basement, Archaean seawater-derived hydrothermal solutions would have $\delta 18O_{VMSOW}$ values of -11 to -15 ‰, which is >20 ‰ lighter than the reconstructed fluid signature. We can hence exclude a marine source of the water that gave rise to the precipitation of the MGB carbonate-quartz veins. In the Barberton GB, Ronde and Wit (1992) noted a 100 Ma hiatus between deformation and Sb-Au mineralization and ruled out devolatization as a source for the ore-forming fluids. They argue that external fluids originating from the contact of intruded tonalite underwent phase separation, which caused Sb-Au mineralization to occur. Similarly, J. Jaguin, Poujol, et al. (2013) suggested a relation between the intrusion of a TTG body (the Maranda and Baderoukwe intrusion) and the antimony mineralization in the AL. However, the relation between the intrusion and Sb-mineralization is more difficult to establish in the AL, because Sb-mineralization took place synchronous with deformation and fuchsite-quartz-carbonate alteration 2 billion years ago (J. Jaguin, Boulvais, M.-C. Boiron, et al., 2014). We suggest that the most plausible source for water enriched in δ18O in low-grade mineralizations is metamorphic fluids or connate waters from sedimentary basins (cf., Wagner et al. (2010)). This interpretation is in line with the fact that the regional carbonated schists away from the mineralized zones and contact with granitoids show similar isotopic characteristics (Kedda, 1992). The flat REE+Y patterns with the small positive Eu anomalies are consistent with a metamorphic origin of the fluids (Kontak and Jackson, 1999). The variations in total abundance may be due to variable fluid-to-rock ratios (Lottermoser, 1992) or temperature (Kontak and Jackson, 1999). In addition, the positive Eu anomaly of the inferred hydrothermal fluids could imply a low oxygen fugacity (Bau, 1991), although this would be at odds with the presumed H_2O-CO_2 nature of the fluids. REE patterns of replacive magnesite resemble those of ultramafic rocks, which confirms that magnesite is an alteration product of komatiite. A clear distinction of REE+Y patterns can be seen between dolomite and magnesite, as the distribution patterns of dolomite are flatter, with higher ΣREE contents and positive Eu anomalies in a subset of the samples. It is to be expected that a Ca-bearing mineral will be much more accommodating to incorporation of REE (and Eu^{+2} in particular) than a Mg-Fe phase. The fact that magnesite has much lower ΣREE and light REE depleted patterns does therefore not indicate a different source. The stable isotope data actually suggest that dolomite and magnesite formed from the same fluid that also precipitated quartz. This can be concluded from the consistent temperatures and reconstructed $\delta^{18}O$ values of fluids we calculated using different approaches. Also, the carbon isotopic composition of magnesite and dolomite are virtually identical to each other. We estimated the temperatures of the carbonatizing fluids to be in the 350-400 °C range based on oxygen isotope magnesite-dolomite thermometry of carefully selected samples (Chacko and Deines, 2008; Horita, 2014). Magnesite and dolomite have fractionation factors for exchange with water that are different enough to make a useful thermometer. The concept of combining multiple mineralization pairs to estimate temperatures of listvenitization has been used before by Beinlich et al. (2012), who deduced temperature of around 280 °C and then calculated $\delta^{18}O$ of H_2O of around 6-7 ‰. Our temperature estimates in the 350-400 °C range are generally consistent with, although somewhat lower than, those estimated by J. Jaguin, Boulvais, M.-C. Boiron, et al. (2014) based on fluid inclusion work and phase relations (400-450 °C). J. Jaguin, Boulvais, M.-C. Boiron, et al. (2014) presented δ^{18}O data for pairs of calcitet and quartz from the Malati pump location within the AL, that we used to calculate temperatures between 340 and 380 °C using the Sharp and Kirschner (1994) calibration. In summary, our mineral chemistry and geothermometry results suggest that metasomatic reactions between metakomatiite and metagranodiorites (with the possible involvement of sediments) took place in the AL at temperatures roughly between 350 and 400 °C. The lack of tremolite within the quartz-dolomite rocks of the AL confirms the geothermometry results, indicating that the AL has not been exposed to amphibolite facies in the past 2.9 Ga (cf. Block et al. (2013)). At a temperature of 400 °C and 200 MPa pressure, the X(CO2) of the fluid must have been >0.1 to account for the predominance of the dolomite-quartz assemblage and the lack of talc-calcitet and tremolite-calcitet-quartz, respectively. These moderate to high contents of CO_2 in the fluid are consistent with the compositions of fluid inclusions reported by J. Jaguin, Boulvais, M.-C. Boiron, et al. (2014). These carbonic acid-rich fluids can be expected to be quite oxidizing, which may seem at odds with the small positive Eu anomalies found in the dolomite-quartz veins. However, at temperatures >250 °C and at high solution pH, fluids don't have to be particularly reduced to have dissolved Eu in its divalent redox state (Sverjensky, 1984).

3.4.2 Paragenetic constraints on metasomatic mass transfers in the different lithological units

The exceedingly high Cr contents of chlorite, fuchsite, and dravite in the host rocks of the quartz-carbonate-stibnite mineralization provide strong evidence for an ultramafic precursor lithology. Pearton (1980) suggested that these precursor rocks were peridotitic komatiites, with low Ca and Al contents. Likewise, Madisha (1996) reported whole rock and mineral chemical data of serpentinites from locations 25 and 33 km ENE of the Gravelotte mine (Pike's Kop and Pioneer Kop, respectively) indicative of a peridotitic protolith composition. These komatiites are believed to have undergone serpentinization, and locally carbonation, in a seafloor setting. This interpretation is supported by the δ13C compositions of the carbonates, which are seawater-like (-2 to 1 ‰; Madisha (1996)) and clearly distinct from the carbonates in the Sb-mineralized quartz-carbonate-fuchsite rocks in the main AL (-4.5 to -5.5 ‰). The serpentinites show indications of prograde metamorphism (antigorite replacing lizardite) and deformation (D1). They are not affected by the later deformation and Sb-mineralization events developed in the AL in the west. It is very likely, that these serpentinites represent the ultramafic precursor rocks indicated by the Cr-enrichment of the chlorite and the abundance of fuchsite in the AL. The high Cr contents suggest a relative mobile setting for both Cr and Al, comparable to the listvenite in an ophiolite in S. Egypt (Emam and Zoheir, 2013). Emam and Zoheir (2013) have found zonations of Cr within chlorite, surrounding Cr-spinels. Likewise, Madisha (1996) reported the occurrence of Cr-rich chlorite in association with partially altered Cr-spinel in serpentinites from the Pioneer location. In the intensely quartz-carbonate altered metakomatiites in the main AL, Cr-spinel has not been found, suggesting a complete alteration of spinel to chlorite (and fuchsite). Conceivably, chromite was more pervasively altered during the severe fluxing by H_2O-CO_2 fluids that caused the quartz-carbonate-fuchsite alteration than during serpentinization. However, at least on spatial scales greater than meters, Cr was apparently immobile, which allows us to use it as tracer of an ultramafic protolith lithology. Another indication of ultramafic precursors in the lithologies hosting the AL are the common appearance of Ni-bearing phases, like ullmannite and gersdorffite. Whereas many of the dravite and chlorite analyses suggest very high Cr contents (and hence point to an ultramafic precursor rock), an equally large population of the dataset shows very low Cr contents, which are inconsistent with the concept of an ultramafic precursor (Figure 3.9). We propose that the low Cr contents are due to the involvement of other, metasedimentary or metagranodioritic lithologies that were in contact with the metakomatiite. It is well established that pronounced metasomatic zonations, including monomineralic zones of chlorite and talc, will develop by diffusional metasomatism at the contact between ultramafic and felsic lithologies (e.g., Bach et al. (2013)).

We suggest that the common and spatially close relationship of chlorite and talc schist represent such a lithological contact. It is likely that the diffusional metasomatism took place during the prograde metamorphism that is preserved in the serpentinites in the ENE extension of the AL (Madisha, 1996). During the main deformation (D1), the talc-rich domains may have acted as lubricant and localized much of the strain, while allowing ductile deformation to prevail under greenschist facies conditions. The ultramafic rock unit was likely dismembered and intermingled with felsic lithologies, which greatly enhanced the extent of metasomatic replacement. Later transtensional deformation allowed large quantities of deeply rooted H_2O-CO_2 fluids to rise up and cause fluid-infiltration-driven metasomatism of talc –> talc+dolomite –> magnesite+quartz. The formation of fuchsite appears to be related to the alteration of chlorite, based on textural relations in rocks that contain both phases (Madisha, 1996). The formation of fuchsite was assisted by metasomatic mass transfers of K, Al, Si into and Mg as well as Fe out of the fuchsite-bearing domains. Again, these mass transfers could be related to the presence of felsic materials.

3.4.3 Trapping mechanisms of Sb enrichment in the AL – the role of metasomatic reactions

As mentioned before, most Sb-enriched deposits within orogenies are found within suture zones where geochemically different rocks are juxtaposed against each other (Table 3.1). These juxtaposed rocks differ in acidity and/or reducing capacity. The intruded granodiorites within the komatiite at the AL of the MGB are predominantly TTG suites, which are known for their H_2O-rich composition (Vearncombe, 1991; Condie, 2005; Martin et al., 2005). Felsic volcanic / volcaniclastic rocks, such as the ones in the Weigel formation that hosts the AL, are enriched in Sb (Boyle and Jonasson, 1984). The metavolcaniclastic rocks of the Weigel formation host small TTG intrusive bodies, with are in part albitized in particular in proximity to the Sb-mineralized quartz-carbonate rocks (J. Jaguin, Boulvais, M.-C. Boiron, et al., 2014). As we discussed in the previous section, the massive quartz-carbonate rocks that host the stibnite mineralization represent metasomatized komatiites, which were probably peridotitic in composition (cf. Vearncombe et al. (1992)). The original komatiites that were part of the volcanic / volcaniclastic sequence of the Weigel formation were probably not enriched in Sb (Boyle and Jonasson, 1984). However, the metasomatosed and veined metakomatiites are always associated with Sb mineralizations in the AL. This observation may indicate that there is a relation between the Sb mineralization and the metasomatic events that affected the komatiites and particularly the interfaces of komatiitic and felsic units. This idea is corroborated by the results of the geochemical reaction path models (Section 3.5) indicating the solubilities of Sb drop by two orders of magnitude when percolating fluids move across a lithologiy boundary from felsic into ultramafic rocks. Likewise the solubility of As (and Au) will drop along the same reaction path. These reactions could have been taking place in the course of hydrothermal alteration in the original geotectonic setting of the MGB, which is likely an arc/backarc setting (Vearncombe, 1991). A submarine back-arc-related origin is indeed what Schwarz-Schampera et al. (2010) proposed as most plausible setting in which the Cu-Zn line formed. This interpretation of the Cu-Zn line in terms of synvolcanic VMS deposits put a firm age constraint on this mineralization event: the Rubbervale volcanics were age-dated at 2.97±0.02 Ga (Poujol, 1996). The Cu-Zn line runs parallel to the AL and follows the contact between the felsic Rubbervale formation and the nearby Weigel formation (felsic-mafic-ultramafic). It is conceivable, then, that hydrothermal circulation of seawater mobilized Sb and As from the enriched felsic extrusives (modern felsic-rock hosted hydrothermal vents are enriched in these elements; Douville et al. (1999)). The initial Sb-As-Fe-S mineralization in the AL (with gudmundite, berthierite, pyrrhotite, pyrite, and arsenopyrite being the main phases) may have formed in this type of seafloor setting, similar to the Cu-Zn line. The volcanic and volcaniclastic rocks forming the Weigel formation are 3.09±0.01 Ga in age (Poujol, 1996), so apparently older than the Rubbervale volcanics. The two might still be related as arc/back-arc systems do have lifetimes on the order of 10s of millions of years. Potential traps of this original mineralization could have been the seafloor (in analogy to the Cu-Zn line) or the lithologic boundary between felsic and ultramafic rocks. The former scenario would correspond to the well-established concept of mixing between hot, reducing, and acidic hydrothermal solutions with seawater and cooling, neutralization and oxidation as trapping mechanism. Our modeling shows the other trapping mechanism affective in lowering metalloid solubility by neutralization and reduction may be related to serpentinization of the komatiite units. We are not the first ones to propose this sort of trapping mechanism. In fact, Normand et al. (1996) suggested that serpentinization would lead to the reduction of dissolved trivalent Sb and the precipitation of Sb as gudmundite or native Sb. The rationale behind Normand et al.'s model is that the dominant Sb species in solution is probably $Sb(OH)_0^3$ (Williams-Jones and Norman, 1997) and during serpentinization the oxygen fugacity will drop so much that native Sb is expected to form according to:

$$Sb(OH)_3^0 = Sb(s) + 3/2H_2O + 3/4O^2 \tag{3.6}$$

Our model calculations fully support this idea. It is noteworthy in this context to point out that it is not the consumption of oxygen but the release of dihydrogen by serpentinization that generates the driving force for this reaction:

$$2Sb(OH)_3^0 + 3H_2(aq) = 2Sb(s) + 6H_2O \tag{3.7}$$

Only serpentinites will provide this type of trap, because the amounts of dihydrogen produced during serpentinization are orders of magnitude higher than during alteration of mafic or felsic rocks (e.g., McCollom and Bach (2009). In contrast to the Cu-Zn line mineralizations and also the arsenopyrite-dominated mineralization within the Weigel formation, the main Sb-mineralization in the AL is clearly structurally bound and formed coevally with the carbonation and silicification event (listvenitzation). This carbonation/silicification event took place during D2 and was caused by fluxing of the shear zone by CO_2-rich fluids. Stibnite is closely associated with the quartz-carbonate altered rocks and veins. The D2 event has been associated with a tectono-thermal event that affected the MGB roughly 2.75 Ga (Block et al., 2013). The 2.97-2.90 Ga old

TTG intrusions were hydrothermally altered during this event; the albitites in the AL are product of this alteration and have been assigned a key role in the Sb enrichment (J. Jaguin, Poujol, et al., 2013). The occurrence of the stibnite in the AL (concentrated in tension gashes of and in pressure shadows behind boudins) indicates that it is heavily dynamically recrystallized during the D2 event. It is uncertain how the Sb enrichment came about. A number of options appear plausible:

(1) Sb enrichment was already developed along with As and Fe (as in the submarine hydrothermal scenario) and the reduced assemblage was later altered to stibnite, while Fe and As were mobilized. This hypothesis is plausible from a phase etrology point of view, because the intense fluxing by fluids would lead to an expected increase in the variance of the system (i.e. a decrease in the number of phases stable). Another possibility (2) is that the Sb was delivered by the fluxing fluids, like it is assumed in the formation of typical orogenic Sb-Au deposits (Goldfarb and Groves, 2015). Within this conceptual model, numerous different geochemical processes have been proposed, invoking various fluid regimes, to be responsible of trapping economically important Sb deposits, with stibnite as dominant phase (Davis et al., 1986). It has been established that Sb is mostly associated with other elements (Au, As, Hg) within hypogene deposits in brittle faults of orogenic suture zones (Goldfarb and Groves, 2015). Adding H_2S decreases Sb solubility at temperatures >250 °C, but solubility of Sb is generally high at these temperatures regardless of the sulfide concentration in the system (Hagemann and Lüders, 2003; Obolensky, Gushchina, Borisenko, Borovikov, and Pavlova, 2007). Adding or removing H_2S were hence likely not involved in the trapping mechanisms that led to the Sb enrichment in the AL. At these temperatures, both oxidizing and reducing fluids can cause Sb mineralization. Fluids in which CO_2 is the dominant carbon species will favor stibnite, whereas more reducing CH_4–bearing fluids will have

native antimony and gudmundite form (Normand et al., 1996; Obolensky, Gushchina, Borisenko, Borovikov, and Pavlova, 2007). We have shown that conditions under which pyrrhotite is stable favour those reduced Sb minerals at 350 °C (Figure 3.14a). Both CO_2 and CH_4 dominant fluids could have been present in the AL, as CO_2 is converted into CH_4 by during serpentinization favoring reduced and sulfur poor mineral assemblages assemblages (Normand et al., 1996). Normand et al. (1996) suggested that stibnite can form by alteration of gudmundite caused by acidic and/or iron poor fluids. One trapping mechanims proposed is adiabatic cooling in these shear zones causes a drop in Sb solubility (Williams-Jones and Norman, 1997).

Other (more efficient) cooling mechanisms include degassing of CO_2 (2.5 °C / $\%CO_2$ degassing; Hagemann and Lüders (2003)) and isoenthalpic boiling (Obolensky, Gushchina, Borisenko, Borovikov, and Pavlova, 2007). Adiabatic cooling may drive CO_2 vand related cooling along fault zone movement lowering antimony saturation (Hagemann and Lüders, 2003). This process is expected to play a role at temperatures <300 °C, where there is a clear solvus in the CO_2-H_2O-NaCl system at pressures between 1 and 3 kbar (Dubacq et al., 2013).

This study and earlier work (J. Jaguin, Boulvais, M.-C. Boiron, et al., 2014) have shown that the temperatures of formation of the AL mineralization are much greater than 300 °C, so it appears unlikely that cooling by CO_2 unmixing played a major role as antimony trap. There are two types of Sb mineralization in the AL. An apparently primary assemblage of berthierite, ullmannite and gudmnudite that co-occurs with pyrite, chalcopyrite and pyrrhotite (Figure 3.5). A second type of Sb mineralization has stibnite as sole Sb-mineral, which is accompanied by rare berthierite and pyrite. In this apparently secondary formation, stibnite has been mobilized. and reprecipitated in tension gashes and pressure shadows. This low variance assemblage essentially indicates rock-buffered conditions, and this mineralization is indeed developed in metamorphosed and weakly metasomatized host rocks. In contrast, the other type of Sb mineralization has stibnite as sole Sb-mineral, which is accompanied by pyrite-pyrrhotite. This high-variance assemblage indicates open system fluid-dominated conditions of recrystallization and is indeed developed only in the most heavily metasomatized listvenite and albitite units and in carbonate-quartz veins. The type I assemblage is preserved in less intensely carbonated domains, such as chlorite and talc schists. It has been shown before, that dropping $f\,O_2$ and $f\,S_2$ fugacities decreases the Sb solubility by two orders of magnitude (Obolensky, Gushchina, Borisenko, Borovikov, and Nevol'ko, 2009). Our model calculations fully supports this notion. Thus, precipitation of Sb from such a fluid is expected to occur close to a serpentinization metasomatic front (Normand et al., 1996). Again, our model calculations suggest that serpentinization environments do make for an efficient trap for Sb. CO_2-rich fluid will radically change the redox conditions and acidity, increasing the oxygen fugacity ($f\,O_2$) and sulfur fugacity ($f\,S_2$) (Klein and Garrido, 2011) and recrystallizing pure Sb to berthierite and then stibnite within the quartz-carbonate alteration veins (Hagemann and Lüders, 2003; Obolensky, Gushchina, Borisenko, Borovikov, and Nevol'ko, 2009). This second mineralization stage involves the input of deeply rooted H_2O and CO_2. CO_2 enriched fluids are expected to oxidize H_2S, HS^- and Sb-Au species within the fluid and solubilize Sb (Kerrich and Fyfe, 1981; Boyle and Jonasson, 1984; Normand et al., 1996; Phillips and Evans, 2004; Obolensky, Gushchina, Borisenko, Borovikov, and Nevol'ko, 2009). In the AL apparently this mobilization of Sb has not taken place. Instead stibnite is enriched in quartz-carbonate veins that are invariably associated with metakomatiite. This relation is manifest by the enrichment of Cr within chlorite and muscovite (fuchsite) in the AL. Similar associations between metal enrichment of Au-Co-Sb has been linked to carbonation in the contact between felsic and ultramafic protoliths (Hansen et al., 2005; Emam and Zoheir, 2013). The carbonization of the reduced komatiite, prevents the sulfide in the fluids from becoming oxidized and maintains a trap for Sb. Apparently this trap is efficient even at temperatures of 350-400 °C, where cooling by CO_2 exsolution does not take place. Albitization has been linked to the CO_2 fluxing and, thus, to listvenization (J. Jaguin, Boulvais, M.-C. Boiron, et al., 2014; Halls and Zhao, 1995). Thus, the abundance of (albitized) quartz veins, within the metagranodiorite, reveals that silica (including Sb and K) has been mobilized in the system (J. Jaguin, Poujol, et al., 2013) by the same fluid that has been responsible for listvenization of the ultramafic protolith (Halls and Zhao, 1995). This idea is entirely consistent with the results of our model calculations, indicating that albitization of granodiorite and quartz-carbonate-stibnite alteration of the metakomatiite in the AL could have been caused by the same CO_2-rich metamorphic fluid. Albitization has been dated at 2.8 Ga with an overprinting event at 2.0 Ga (J. Jaguin, Boulvais, M.-C. Boiron, et al., 2014). As fuchsite clearly formed during this listvenitization event, which has been dated at roughly 2.0 Ga (J. Jaguin, Boulvais, M.-C. Boiron, et al., 2014; Sperner and Pfänder, n.d.). In fact, a very large number of fuchsite separates from different mines in the AL gives ages that fall in a very tight range between 2.00 and 2.04 Ga. Regardless of whether the age of the Sb mineralization in the AL is 2.0 or 2.8 Ga, the MGB has undergone multiple extensive structural events, causing dominant ductile and brittle deformation. The Sb enrichment is clearly related to the D2 deformation and associated carbonation and silicification.

3.5 Summary and conclusions

We assign a key role in the origin, trapping and (re)mobilizing of the Sb-species and minerals to the presence of ultramafic rocks in the AL. The Sb enrichment is likely due to suprasubduction-related submarine hydrothermal systems that were active contemperanously with the volcanic construction of the Weigel formation. The deeply rooted CO_2-rich fluids wiped out much of the primary mineral association and led to a uniform stibnite-carbonate-quartz association. The high variance of this association is indicative of major fluid-assisted metasomatic mass transfers. Those fluids were most likely released from deep-seated prograde metamophic reactions releasing a H_2O-CO_2-rich fluid phase that could migrate up the suture zone in which the AL is developed. Below temperatures of around 400 °C, the ultramafic rocks were listvenitized and impregnated by stibnite. The model calculations presented also help explain the origin of the albitites that are also developed in the AL. The same fluid that turns metakomatiite into listvenite is predicted to replace granodiorite by albitite, which is mineralized weakly by stibnite and arsenopyrite. We propose that metasomatic reactions involving ultramafic rocks may make for efficient traps of Sb and likely other elements (As, Ag, Hg, Au). They may play a general role in the formation of many orogenic lode deposits.

3.6 Acknowledgements

The authors thank the management and acting geologists of Consolidated Murchison Limited (ConsMurch) for their assistance and cooperation during our fieldwork in 2013. Stephan Sopke, Andreas Klügel, Patrick Monien from the Universität Bremen are thanked for their assistance in conducting the geochemical measurements. Moritz Wagner and

Michael Hentscher helped with assembling the thermodynamic databases. We thank Chris Heinrich (ETH Zurich) for making his compilation of aqueous Au-species available to us. We thank Dr. Sperner (Freiberg University) for the numerous insightful discussions. Furthermore, we would like to thank Barbara Mader (Universität Kiel) and Dr. Jöns (Universität Bochum) for their extensive help with the EMPA.

Bibliography

Akinfiev, N.N. and A.V. Zotov (2010). "Thermodynamic description of chloride, hydrosulfide, and hydroxo complexes of Ag(I), Cu(I) and Au(I) at temperatures of 25-500°C and pressures of 1-2000 bar". In: *Geochemistry Int.* 39.10, pp. 990–1006. DOI: `10.1134/S0016702910070074`.

Anhaeusser, C.R. (1976). "Archean Metallogeny in Southern Africa". In: *Econ. Geol.* 71, pp. 16–43.

Bach, W., N. Jöns, and F. Klein (2013). "Metasomatism of the ocean crust". In: *Metasomatism Metamorph.* Ed. by D.E. Harlov and H. Austrheim. Springer, pp. 253–288. DOI: `10.1007/978-3-642-28394-9_8`.

Bau, M. (1991). "Rare-earth element mobility during hydrothermal and metamorphic fluid-rock interaction and the significance of the oxidation state of europium". In: *Chem. Geol.* 93.3-4, pp. 219–230. DOI: `10.1016/0009-2541(91)90115-8`.

Beinlich, A. et al. (2012). "Massive serpentinite carbonation at Linnajavri, N-Norway". In: *Terra Nov.* 24.6, pp. 446–455. DOI: `10.1111/j.1365-3121.2012.01083.x`.

Bernasconi, A, N. Glover, and R.P. Viljoen (1980). "The Geology and Geochemistry of the Senator Antimony Deposit- Turkey". In: *Miner. Depos.* 15, pp. 259–274.

Bhattacharya, S. et al. (2014). "Oxygen isotope ratio of quartz veins from the auriferous Ramagiri–Penakacherla schist belt and surrounding granitoids in the Eastern Dharwar craton: A case for a possible link between gold mineralization and granite magmatism". In: *Ore Geol. Rev.* 63, pp. 201–208. DOI: `10.1016/j.oregeorev.2014.04.023`.

Block, S. et al. (2013). “The Murchison Greenstone Belt, South Africa: Accreted slivers with contrasting metamorphic conditions”. In: *Precambrian Res.* 227, pp. 77–98. DOI: 10.1016/j.precamres.2012.03.005.

Boyle, R.W. and I.R. Jonasson (1984). “The geochemistry of antimony and its use as an indicator element in geochemical prospecting”. In: *J. Geochemical Explor.* 20, pp. 223–302.

Buchholz, P. and T. Oberthür (2007). “Multistage Au-As-Sb Mineralization and Crustal-Scale Fluid Evolution in the Kwekwe District , Midlands Greenstone Belt , Zimbabwe : A Combined Geochemical , Mineralogical , Stable Isotope , and Fluid Inclusion Study”. In: *Econ. Geol.* 102.1994, pp. 347–378.

Castro, S.H. and L. Baltierra (2005). “Study of the surface properties of enargite as a function of pH”. In: *Int. J. Miner. Process.* 77.2, pp. 104–115. DOI: 10.1016/j.minpro.2005.03.002.

Chacko, T. and P. Deines (2008). “Theoretical calculation of oxygen isotope fractionation factors in carbonate systems”. In: *Geochim. Cosmochim. Acta* 72.15, pp. 3642–3660. DOI: 10.1016/j.gca.2008.06.001.

Condie, K.C. (2005). “TTGs and adakites: are they both slab melts?” In: *Lithos* 80.1-4, pp. 33–44. DOI: 10.1016/j.lithos.2003.11.001.

Davis, D.R., D.B. Paterson, and D.H.C. Griffith (1986). “Antimony in South Africa”. In: *J. S. Afr. Inst. Min. Met.* 86.6, pp. 173–193.

De Ronde, C.E.J. et al. (1997). “Fluid chemistry of Archean seafloor hydrothermal vents: Implications for the composition of circa 3.2 Ga seawater”. In: *Geochim. Cosmochim. Acta* 61.19, pp. 4025–4042. DOI: 10.1016/S0016-7037(97)00205-6.

Douville, E. et al. (1999). “Le comportement de I’arsenic (As) et de I’antimoine (Sb) dans les fluides provenant de diffkents systgmes hydrothermaux océaniques”. In: *Earth Planet. Sci.* 328.2, pp. 97–104.

Dubacq, B. et al. (2013). “An activity model for phase equilibria in the H2O-CO2-NaCl system”. In: *Geochim. Cosmochim. Acta* 110, pp. 229–252.

Emam, A. and B. Zoheir (2013). “Au and Cr mobilization through metasomatism: Microchemical evidence from ore-bearing listvenite, South Eastern Desert of Egypt”. In: *J. Geochemical Explor.* 125, pp. 34–45. DOI: 10.1016/j.gexplo.2012.11.004.

Firdu, F.T. and P. Taskinen (2010). “Thermodynamics and phase equilibria in the (Ni, Cu, Zn)–(As, Sb, Bi)–S systems at elevated temperatures (300–900 C)”. In: *Espoo Aalto Univ. Publ. Mater. . . .* Pp. 1–59.

Goldfarb, R.J. and D.I. Groves (2015). "Orogenic gold: Common or evolving fluid and metal sources through time". In: *Lithos*. DOI: 10.1016/j.lithos.2015.07.011.

Hagemann, S.G. and V. Lüders (2003). "P-T-X conditions of hydrothermal fluids and precipitation mechanism of stibnite-gold mineralization at the Wiluna lode-gold deposits, Western Australia: conventional and infrared microthermometric constraints". In: *Miner. Depos.* 38.8, pp. 936–952. DOI: 10.1007/s00126-003-0351-6.

Halls, C. and R. Zhao (1995). "Listvenite and related rocks: perspectives on terminology and mineralogy with reference to an occurrence at Cregganbaun, Co. Mayo, Republic of Ireland". In: *Miner. Depos.* 30.3-4, pp. 303–313. DOI: 10.1007/BF00196366.

Hansen, L.D. et al. (2005). "Carbonated serpentinite (listwanite) at Atlin, British Columbia: A geological analogue to carbon dioxide sequestration". In: *Can. Mineral.* 43.1, pp. 225–239. DOI: 10.2113/gscanmin.43.1.225.

Horita, J. (2014). "Oxygen and carbon isotope fractionation in the system dolomite – water – CO2 to elevated temperatures". In: *Geochemica Cosmochim.* 129, pp. 111–124.

Jaffrés, J.B.D., G.A. Shields, and K. Wallmann (2007). "The oxygen isotope evolution of seawater: A critical review of a long-standing controversy and an improved geological water cycle model for the past 3.4 billion years". In: *Earth-Science Rev.* 83, pp. 83–122. DOI: 10.1016/j.earscirev.2007.04.002.

Jaguin, J., P. Boulvais, M.- C. Boiron, et al. (2014). "Stable isotopes (O, C) and fluid inclusion study of quartz-carbonate veins from the antimony line, Murchison Greenstone Belt". In: *Am. J. Sci.* 314.7, pp. 1140–1170. DOI: 10.2475/07.2014.03.

Jaguin, J., P. Boulvais, M.-C. Boiron, et al. (2014). "Stable isotopes (O, C) and fluid inclusion study of quartz-carbonate veins from the antimony line, Murchison Greenstone Belt". In: *Am. J. Sci.* 314.7, pp. 1140–1170. DOI: 10.2475/07.2014.03.

Jaguin, J., M. Poujol, et al. (2013). "Albitization in the Antimony Line, Murchison Greenstone Belt (Kaapvaal Craton): A geochemical and geochronological investigation". In: *Lithos* 168-169, pp. 124–143. DOI: 10.1016/j.lithos.2013.01.010.

Jaguin, Justine et al. (2013). "Albitization in the Antimony Line, Murchison Greenstone Belt (Kaapvaal Craton): A geochemical and geochronological investigation". In: *Lithos* 168-169, pp. 124–143. DOI: 10.1016/j.lithos.2013.01.010.

Johnson, J.W., E.H. Oelkers, and H.C. Helgeson (1992). *SUPCRT92: A software package for calculating the standard molal thermodynamic properties of minerals, gases, aqueous species, and reactions from 1 to 5000 bar and 0 to 1000°C*. Vol. 18. 7. Pergmamon Press Ltd, pp. 899–947. DOI: `10.1016/0098-3004(92)90029-Q`.

Kantar, Cetin (2002). "Solution and flotation chemistry of enargite". In: *Colloids Surfaces A Physicochem. Eng. Asp.* 210.1, pp. 23–31. DOI: `10.1016/S0927-7757(02)00197-8`.

Kedda, S.W. (1992). "Geochemical and stable isotope studies of gold bearing granitoids in the Murchison Schist Belt, North Eastern Transvaal". Dissertation. University of the Witwatersrand, Johannesburg.

Kerrich, R. and W.S. Fyfe (1981). "The gold-carbonate assocation: Source of CO2 and CO2 fixation reactions reactions in Archaean lode deposits". In: *Chem. Geol.* 33, pp. 265–294.

Klein, F. and W. Bach (2009). "Fe-Ni-Co-O-S Phase Relations in Peridotite-Seawater Interactions". In: *J. Petrol.* 50.1, pp. 37–59. DOI: `10.1093/petrology/egn071`.

Klein, F. and C.J. Garrido (2011). "Thermodynamic constraints on mineral carbonation of serpentinized peridotite". In: *Lithos* 126.3-4, pp. 147–160. DOI: `10.1016/j.lithos.2011.07.020`.

Kontak, D.J. and S.J. Jackson (1999). "Documentation of variable trace- and Rare Earth Element abundances in carbonates veins from quartz in Meguma lode-gold Nova Scotia deposits". In: *Can. Mineral.* 37, pp. 469–488.

Kretschmar, U. and S.D Scott (1976). "Phase relations involving arsenopyrite in the system Fe-As-S and their application". In: *Can. Mineral.* 14, pp. 364–386.

Krupp, E (1988). "Solnbility of stibnite in hydrogen sulfide solutions, speciation, and equilibrium constants, from 25 to 350 ° C". In: *Geochemica Cosmochim.* 52, pp. 3005–3015.

Lottermoser, B.G. (1992). "Rare earth elements and hydrothermal ore formation processes". In: *Ore Geol. Rev.* 7.1, pp. 25–41. DOI: `10.1016/0169-1368(92)90017-F`.

Lynch, D C (1982). "Standard Free Energy of Formation of NiAsS". In: *Metall. Mater. Trans. B* 13.June, pp. 285–288.

Madisha, M.E. (1996). "Carbonate alteration of serpentinite in the Murchison Greenstone Belt, Kaapvaal Craton: Implication for gold mineralization". PhD thesis. Rand Afrikaans University.

Madu, B. E., B.E. Nesbitt, and K. Muehlenbachs (1990). "A mesothermal gold-stibnite-quartz vein occurence in the Canadian Cordillera". In: *Econ. Geol.* 85, pp. 1260–1268.

Martin, H. et al. (2005). “An overview of adakite, tonalite–trondhjemite–granodiorite (TTG), and sanukitoid: relationships and some implications for crustal evolution”. In: *Lithos* 79.1-2, pp. 1–24. DOI: `10.1016/j.lithos.2004.04.048`.

McCollom, T.M. and W. Bach (2009). “Thermodynamic constraints on hydrogen generation during serpentinization of ultramafic rocks”. In: *Geochim. Cosmochim. Acta* 73.3, pp. 856–875. DOI: `10.1016/j.gca.2008.10.032`.

McCourt, S. and D. van Reenen (1992). “Structural geology and tectonic setting of the Sutherland Greenstone Belt, Kaapvaal Craton, South Africa”. In: *Precambrian Res.* 55, pp. 93–110.

McCuaig, T.C. and R. Kerrich (1998). *P—T—t—deformation—fluid characteristics of lode gold deposits: evidence from alteration systematics*. Vol. 12. 6, pp. 381–453. DOI: `10.1016/S0169-1368(98)80002-4`.

McDonough, W.F. and S.-s. Sun (1995). *McDonough_Sun(CG_95).pdf*.

Moritz, R.P. and J.H. Crocket (1991). “Hydrothermal Wall-rock alteration and formation of the gold-bearing quartz-fuchsite vein at the Dome Mine, Timmins Area, Ontario, Canada”. In: *Econ. Geol.* 86, pp. 620–643.

Moritz, R.P., J.H. Crocket, and A.P. Dickin (1990). “Source of lead in the gold-bearing quartz-fuchsite vein at the Dome mine , Timmins area , Ontario , Canada”. In: *Miner. Depos.* 280, pp. 272–280.

Nesbitt, R W, S.-S. Sun, and A.C. Purvis (1979). “Komatiites: Geochemistry and genesis”. In: *Can. Mineral.* 17, pp. 165–186.

Normand, C., M. Gauthier, and M. Jébrak (1996). “The Québec Antimony deposit: An example of gudmundite - native antimony mineralization in the Ophiolitic mélange of the Southeastern Québec appalachians”. In: *Econ. Geol.* 91.1, pp. 149–163. DOI: `10.2113/gsecongeo.91.1.149`.

Obolensky, A.A., L.V. Gushchina, A.S. Borisenko, A.A. Borovikov, and P.A. Nevol’ko (2009). “Computer thermodynamic modeling of the transport and deposition of Sb and Au during the formation of Au-Sb deposits”. In: *Russ. Geol. Geophys.* 50.11, pp. 950–965. DOI: `10.1016/j.rgg.2009.10.004`.

Obolensky, A.A., L.V. Gushchina, A.S. Borisenko, A.A. Borovikov, and G.G. Pavlova (2007). “Antimony in hydrothermal processes: solubility, conditions of transfer, and metal-bearing capacity of solutions”. In: *Russ. Geol. Geophys.* 48, pp. 992–1001. DOI: `10.1016/j.rgg.200`.

Phillips, G.N. and K.A. Evans (2004). “Role of CO2 in the formation of gold deposits”. In: *Nat. Publ. Gr.* 429, pp. 860–863. DOI: `10.1038/nature02672.1.`.

Pokrovski, G.S. et al. (2006). “Antimony speciation in saline hydrothermal fluids: A combined X-ray absorption fine structure spectroscopy and solubility study”. In: *Geochim. Cosmochim. Acta* 70.16, pp. 4196–4214. DOI: `10.1016/j.gca.2006.06.1549`.

Poujol, M. (1996). “3.07-2.97 Ga Greenstone Belt formation in the northeastern Kaapvaal Craton: Implications for the origin of the Witwatersrand Basin”. In: *Econ. Geol.* 91, pp. 1455–1461.

– (2001). “U-Pb isotopic evidence for episodic granitoid emplacement in the Murchison greenstone belt, South Africa”. In: *J. African Earth Sci.* 33.1, pp. 155–163.

Ronde, C.E.J. de and M.J. de Wit (1992). “Shear Zone-Related , Au Quartz Vein Deposits in the Barberton Greenstone Africa : Field and Petrographic Characteristics , Fluid Properties , and Light Stable Isotope Geochemistry”. In: 87, pp. 366–402.

Schock, E.L. et al. (1997). “Inorganic species in geologic fluids: correlations among standard molal thermodynamic properties of aqueous ions and hydroxide complexes.” In: *Geochemica Cosmochim.* 61.5, pp. 907–950. DOI: `10.1017/CBO9781107415324.004`. arXiv: `arXiv:1011.1669v3`.

Schürmann, L.W. et al. (2000). “Carbonate dykes associated with Archaean lode-Au mineralisation, Barberton greenstone belt, South Africa”. In: *J. African Earth Sci.* 30.2, pp. 249–266.

Schwarz-Schampera, U., H. Terblanche, and T. Oberthür (2010). “Volcanic-hosted massive sulfide deposits in the Murchison greenstone belt, South Africa”. In: *Miner. Depos.* 45, pp. 113–145. DOI: `10.1007/s00126-009-0266-y`.

Seal, R.R., E.J. Essene, and W.C. Kelly (1990). “Tetrahedrite and tennantite: Evaluation of thermodynamic data and phase equilibria”. In: *Can. Mineral.* 28, pp. 725–738.

Seal, R.R., R.A. Robie, P.B. Barton, et al. (1992). “Superambient heat capacities of synthetic stibnite, berthierite, and chalcostibite; revised thermodynamic properties and implications for phase equilibria”. In: *Econ. Geol.* 87.7, pp. 1911–1918. DOI: `10.2113/gsecongeo.87.7.1911`.

Seal, R.R., R.A. Robie, B.S. Hemingway, et al. (1996). “Heat capacity and entropy at the temperatures 5 K to 720 K and thermal expansion from the temperatures 298 K to 573 K of synthetic enargite (Cu3AsS4)”. In: *J. Chem. Thermodyn.* 28.4, pp. 405–412. DOI: `10.1006/jcht.1996.0040`.

Sharp, Z.D. and D.L. Kirschner (1994). “Quartz-calcite oxygen isotope thermometry: A calibration based on natural isotopic variations”. In: *Geochim. Cosmochim. Acta* 58.21, pp. 4491–4501.

Shikazono, N. and M. Shimizu (1988). “Mercurian gold from the tsugu gold-antimony vein deposit in japan”. In: *Can. Mineral.* 26, pp. 423–428.

Sperner, B. and J.A. Pfänder. “Insights into evolution and ore mineralisation of the Murchison Greenstone Belt (South Africa) from 40 Ar / 39 Ar dating”. In: pp. 39–40.

Stefánsson, A. and T.M. Seward (2003a). “Stability of chloridogold(I) complexes in aqueous solutions from 300 to 600°C and from 500 to 1800 bar”. In: *Geochim. Cosmochim. Acta* 67.23, pp. 4559–4576. DOI: `10.1016/S0016-7037(03)00391-0`.

– (2003b). “The hydrolysis of gold(I) in aqueous solutions to 600°c and 1500 bar”. In: *Geochim. Cosmochim. Acta* 67.9, pp. 1677–1688. DOI: `10.1016/S0016-7037(02)01131-6`.

– (2004). “Gold(I) complexing in aqueous sulphide solutions to 500°C at 500 bar”. In: *Geochim. Cosmochim. Acta* 68.20, pp. 4121–4143. DOI: `10.1016/j.gca.2004.04.006`.

Sverjensky, D.A. (1984). “Europium redox equilibria in aqueous solution ’ n t”. In: *Earth Planet. Sci. Lett.* 67, pp. 70–78.

Sverjensky, D.A., E.L. Shock, and H.C. Helgeson (1997). “Prediction of the thermodynamic properties of aqueous metal complexes to 1000 degrees C and 5 kb.” In: *Geochim. Cosmochim. Acta* 61.7, pp. 1359–1412. DOI: `10.1016/S0016-7037(97)00009-4`.

Vearncombe, J.R. (1988). “Structure and metamorphism of the Archean Murchison belt, Kaapvaal Craton, South Africa”. In: *Tectonics* 7.4, pp. 761–774.

– (1991). “A possible Archaean Island Arc in the Murchison Belt , Kaapvaal Craton , South Africa”. In: *J. African Earth Sci.* 13.3, pp. 299–304.

Vearncombe, J.R. et al. (1992). *Geology, Geophysics and mineralisation of the Murschison Schist Belt, Rooiwater Complex and Surrounding granitoids*. Geological. Department of Mineral and Energy affairs.

Vink, B.W. (1996). “Stability relations of antimony and arsenic compounds in the light of revised and extended Eh-pH diagrams”. In: *Chem. Geol.* 130.1-2, pp. 21–30. DOI: `10.1016/0009-2541(95)00183-2`.

Wagman, D.D. et al. (1982). *The NBS Tables of Chemical Thermodynamic Properties*.

Wagner, T., A.J. Boyce, and J. Erzinger (2010). “Fluid-rock interaction during formation of metamorphic quartz veins: A REE and stable isotope study from the Rhenish Massif, Germany”. In: *Am. J. Sci.* 310.7, pp. 645–682. DOI: `10.2475/07.2010.04`.

Welham, N J (2001). “Mechanochemical processing of enargite (Cu3AsS4)”. In: *Hydrometallurgy* 62, pp. 165–173.

Whitmore, D.R.E., L.G. Berry, and J.E. Hawley (1946). “Chrome Micas”. In: *J. Am. Mineral.* 31.1-2, pp. 1–21.

Williams-Jones, A.E. and C. Norman (1997). “Controls of mineral parageneses in the system Fe-Sb-S-O”. In: *Econ. Geol.* 92.3, pp. 308–324. DOI: `10.2113/gsecongeo.92.3.308`.

Wolery, T.J. and C.F. Jove-Colon (2004). *Qualification of Thermodynamic Data for Geochemical Modeling of Mineral-Water Interactions in Dilute Systems*. Tech. rep. November. Bechtel SAIC, pp. 1–212. DOI: `10.2172/850412`.

Yund, R.A. (1962). “The system NiAsS phase relations and mineralogical significance.pdf”. In: *Am. J. Sci.* 260, pp. 761–782.

Zhang, L. et al. (1989). “Oxygen isotope fractionation in the quartz–water–salt system”. In: *Econ. Geol.* 84, pp. 1643–1650.

CHAPTER 4

Sb-As-Au mineralization at the Murchison Greenstone Belt, South Africa

NIKKI BLAAUWBROEK[1], NIELS JÖNS[2], WOLFGANG BACH[1]

[1] Department of Geosciences and MARUM – Center for Marine Environmental Sciences,
University of Bremen, Klagenfurter Str., 28359 Bremen, Germany
[2] Department of Geology, Mineralogy and Geophysics,
Ruhr-University Bochum, Universitaetsstrasse 150, 44801 Bochum, Germany

Keywords: Antimony, stibnite, listvenite, greenstone belt

Abstract

The Murchison Greenstone Belt (MGB) is an Archaean orogenic gold deposit, where the primary mineralization is connected to an ore fluid originating from a granitoid magmatic or a metamorphic devolatization model (Chapter 3). The Antimony Line (AL) in the MGB is enriched in stibnite and is typified by stibnite-arsenopyrite-pyrite-pyrrhotite-berthierite-ullmanite-gudmundite(-chalcopyrite) mineralization, which is dominantly disseminated within the carbonated domains. Three generations of Sb mineralization have been identified in this study: 1) gudmundite found adjacent to arsenopyrite; 2) berthierite-ullmannite outside dolomite-carbonation veins, in close proximity to arsenopyrite domains and finally 3) berthierite-stibnite mobilization within carbonatized domains. Various trapping mechanisms for Sb, like fluid mixing, adiabatic cooling as well as decompressional degassing and related cooling and changes in $f\,S_2$ and/or $f\,O_2$ have been suggested to be responsible for Sb enrichment within orogenic gold deposits. The phase relations of this study clearly indicate that the system transitioned from low $f\,S_2$ and low $f\,O_2$. Primary mineralization is As-Sb-Ni-Cu, and shifted towards As-Sb-Fe-Cu, visibly the loss of ullmanite and enrichment of berthierite which was followed by the alteration of berthierite into stibnite with high $f\,S_2$ and $f\,O_2$. However, Sb solubility, $(Sb(OH)_3)(aq)$, remains low at high temperatures up to 350°C and corresponding acidity range, even as $f\,O_2$ and $f\,S_2$ creep up. These effects can be explained by both pyritization and oxidation by carbonization lead to increased sulfur fugacities, a common explanation for the genesis of orogenic gold deposits and serpentinization environments.

4.1 Introduction

Sb-Au-As(-Hg)-mineralizations within major orogenic suture zones such as Archaean greenstone belts and younger analogues have been described from all over the world. In the past 80 years, several observations were made that are relevant to Sb and As enrichments in hypogene deposits associated with suture zones. Whitmore et al. (1946) was one of the first to observe that fuchsite (chromium muscovite) within Pre-Cambrian Greenstone belts are typically found in Au-Sb-bearing districts. Anhaeusser (1976) stated that Sb-Au mineralization is closely related to the presence of various volcanological subdivisions within an Archaean greenstone belt. Madu et al. (1990) thought that fluid fluxing within shear zones, caused precipitation of Sb-As minerals. Active shear zones are permeable and can facilitate upflow of ore-forming solutions (e.g. McCuaig and Kerrich (1998), Hagemann and Lüders (2003), and Buchholz and Oberthür (2007)) and causing precipitation of ore minerals changes in the lithospheric pressure gradient by the so-called *fault valve model* (Goldfarb, Groves, and Gardoll, 2001; Hagemann and Lüders, 2003).

Although these deposits may vary in age, they have in common that contrasting lithologies with ultramafic rocks were juxtaposed against quartz-feldspar-bearing sedimentary and magmatic rocks that were subsequently modified by silicification and carbonation processes. These consortia of rocks have witnessed deformation under greenschist-facies conditions which were accompanied by drastic metasomatic mass transfers in major shear zones fluxed with aqueous solutions at low pressures and temperatures of 250-400 °C. Some have clear metasomatic fronts at the juxtaposed rocks, such as the serpentinites at the Canadian Cordillera (Normand et al., 1996).

Others have pointed out similarities between greenstone belt-hosted gold, copper and antimony deposits to VMS deposits of active (back-)arc hydrothermal systems (Vearncombe, 1991; McCuaig and Kerrich, 1998; Schwarz-Schampera et al., 2010; Goldfarb and Groves, 2015). These observations suggest a volcanic/metamorphic origin of the Sb-As mineralization in an active plate boundary setting.

Various trapping mechanisms have been discussed. Fluid mixing (and adiabatic cooling) as well as decompressional degassing and related cooling and changes in $f\,S_2$ and/or $f\,O_2$ have been identified as potential ore trap mechanisms (Hagemann and Lüders, 2003). Likewise, changes in $f\,S_2$ and/or $f\,O_2$ in the course of serpentinization in contact with the ore-hosting metasediments have been identified as possible trap for Sb-sulfides (Normand et al., 1996). Decreasing temperature (>300 °C) (Williams-Jones and Norman, 1997) and changes in fluid pH and redox-potential (Obolensky, Gushchina, Borisenko, Borovikov, and Nevol'ko, 2009) have also been suggested to play a major role in Sb-mineralization.

Antimony is used for many industrial products, such as: flame retardant, catalyst in plastic production, pigment in paints and lacquers, additive in glassware and ceramics, and hardening agent in alloys for the production of batteries, ammunitions and brake pads (Ashley et al., 2003; USGS, 2015). The need of antimony in these industrial applications makes antimony the ninth most mined metal worldwide (Ashley et al., 2003).

4.1.1 The Murchison Greenstone Belt

The Murchison Greenstone Belt (MGB) in South Africa is one of the Archaean greenstone belts along the Kaapvaal Craton. The MGB is known for the antimony enrichment along the Antimony Line (AL) and is believed to be the largest Archaean economic stibnite deposit in the world (Boyle and Jonasson, 1984; Davis et al., 1986), and has been mined since 1928 for antimony with gold as byproduct (e.g. Davis et al. (1986)).

The (primary) antimony mineralization in the AL has been proposed to relate to the emplacement of Maranda granodiorite intrusions that occurred around 2.9 Ga (Poujol, 1996; Jaguin, Poujol, et al., 2013) and that may be related to orogeny in the Limpopo Belt, north of the MGB (Block et al., 2013). The MGB hosts an Archaean suture zone between a back-arc system and continental terrain (proto-Kaapvaal Craton) (Schwarz-Schampera et al., 2010; Zeh et al., 2013). The primary suture zone hosts a VMS-type deposit, responsible for the Cu-Zn line north of the AL (Schwarz-Schampera et al., 2010) and probably accountable for the Au found in the Pietersberg greenstone belt (Zeh et al., 2013). Jaguin, Boulvais, et al. (2014) suggested the primary Sb-As mineralization in the AL is related to the metasomatic alteration of the Maranda grandiorites to albitites.

The principal Sb-mineralization in the AL is stibnite and is hosted in listvenites and related quartz-carbonated veins, which formed 2 Ga ago in a deformation zone with NNE-SSW compression and isoclinal folding with steeply dipping stretching lineations and boudinage (Davis et al., 1986; Jaguin, Boulvais, et al., 2014).

Stibnite can be found as disseminations, with local (re)concentrations along the cleavage planes of the gangue minerals, being the richest in the core of the ore body. Fe-rich antimony minerals, in contrast, can be found more at the margins of the ore body (Davis et al., 1986). Gold is a byproduct of mining and occurs as coarse visible gold, as finer disseminations or in close association as sub-microscopic intergrowths within the sulphides. Gold has been found associated with the arsenopyrite mineralization, in variable distances from the antimony mineralization (Davis et al., 1986). For this study we preformed ore petrology and geochemical analyses with the focus on sulfide mineralogy on samples from six locations along the AL at the MGB.

4.2 Methods

Table 4.1: Sample summary and methods employed.

	Sample	XRD	SEM	EMPA	ICPMS
Athens	A080	X	X	X	X
	A081				X
	A082	X	X	X	
Monarch	M112A				X
	M112B			X	X
	M121	X	X		X
	M123	X	X	X	X
	M124			X	
	M126			X	
Monarch mine	Mm107			X	
Beta quarry	B028			X	
	B032	X	X		
	B033			X	
Beta mine	Bm048			X	X

Bulk mineralogy, together with major and trace elements have been varying and intensively measured on selected samples enriched with Sb-As-sulfide mineralogy (Table 4.1), collected from Sb-enriched regions as well as As-enriched regions from the Athens, Beta, Gravelotte and Monarch mine, Murchison, South Africa (Figure 4.1).

Four hand specimen with varying end-member mineralogy has been picked for XRD measurements and have been pulverized to grain sizes < 50 µm. SEM analyses have been preformed as preparation for XRD measurements at Bremen University with a 20 kV acceleration voltage. Bulk rock mineralogy has been determined by X'pert Pro by Panalytical X'Celerator at the University of Bremen. Data interpretation has been preformed by the use of X'pert High Score with the ICSD database.

Major elements of the sulfides were measured at Bochum University with a Cameca SXFiveFE, with fully focused beam, 20 kV acceleration voltage and 30 nA probe cur-

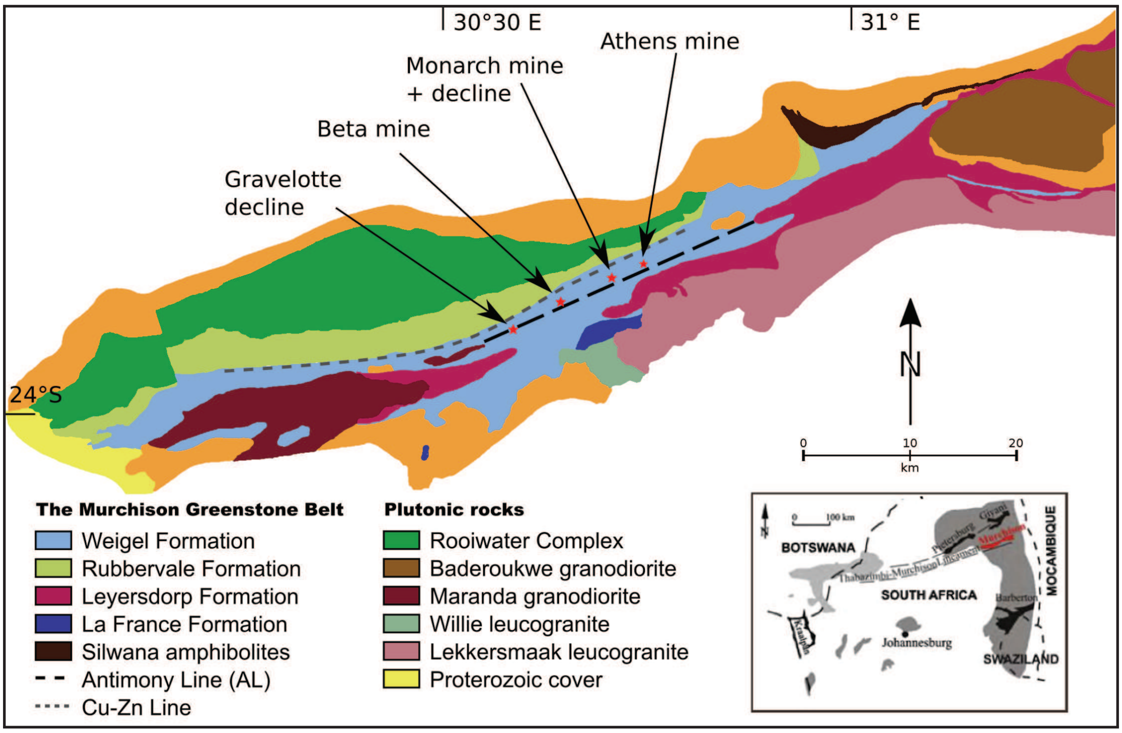
30°30 E
31° E
Athens mine
Monarch mine
+ decline
Beta mine
Gravelotte
decline
24°S
N
0
10
20
km
The Murchison Greenstone Belt
Weigel Formation
Rubbervale Formation
Leyersdorp Formation
La France Formation
Silwana amphibolites
Antimony Line (AL)
Cu-Zn Line
Plutonic rocks
Rooiwater Complex
Baderoukwe granodiorite
Maranda granodiorite
Willie leucogranite
Lekkersmaak leucogranite
Proterozoic cover
0
100 km
N
BOTSWANA
Thabazimbi-Murchison Lineament
Pietersburg
Giyani
Murchison
SOUTH AFRICA
Barberton
Kraalpan
Johannesburg
SWAZILAND
MOCAMBIQUE

Figure 4.1: Geological map of Murchison Greenstone Belt. The Antimony Line and Cu-Zn line have been marked and along the AL, together with the positions of the four mines (Athens, Beta, Gravelotte and Monarch). Ld: Leydsdorp; Gr: Gravelotte; Pp: Pike's Kop; Pnp; Pioneer's Kop. The map has been adjusted after Vearncombe et al. (1992) and Schwarz-Schampera et al. (2010).

rent. Trace metal concentrations of the sulfides have been obtained by laser ablation ICP-MS using a Thermo Element2 mass spectrometer and a NewWave UP193ss laser at the Department of Geosciences in Bremen. Samples and standards were ablated with an irradiance of 1 GW/cm^2 a beam diameter of typically 50-75 µm and a pulse rate of 5 Hz. For data quantification we used the Cetac GeoProTM software with Fe and S for Fe-(As)S minerals and S for Sb-minerals as an internal standard. Mass-1 standard has been used as reference material, for the measurement of ^{60}Ni, PGE-Ni standard has been used. Uncertainties of the concentrations are less than 5 %.

Reaction path modeling and stability diagrams have been calculated using Geochemist's Workbench. There is no thermodynamic data for Sb-As-Au minerals and aqueous species in the default GWB database, which goes up to 300 °C along the steam curve of water. We have hence built a new database for a pressure of 1 kbar and 25 to 600 °C, using SUPCRT92 (Johnson et al., 1992) (Tables 4.2 to 4.5. The database includes 112 aqueous species and 110 minerals. Data for major rock-forming minerals were taken from Wolery and Jove-Colon (2004). Data for major solutes are from Sverjensky et al. (1997) and Schock et al. (1997). These data were supplemented by data for Sb, As and Au minerals as well as aqueous HS^-, OH^- and Cl^- species of these elements from various sources, while maintaining internal consistency (Yund, 1962; Lynch, 1982; Wagman et al., 1982; Krupp, 1988; Seal, Essene, et al., 1990; Seal, Robie, Barton, et al., 1992; Vink, 1996; Seal, Robie, Hemingway, et al., 1996; Williams-Jones and Norman, 1997; Welham, 2001; Kantar, 2002; Stefánsson and Seward, 2003b; Stefánsson and Seward, 2003a; Stefánsson and Seward, 2004; Bessinger and Apps, 2005; Castro and Baltierra, 2005; Pokrovski et al., 2006; Padilla et al., 2008; Akinfiev and Zotov, 2010; Firdu and Taskinen, 2010).

Table 4.2: Overview Log K values Sb-species.

T (°C)	Log K1	Log K2	Log K3	Log K4	Log K5	Log K6	Log K7	Log K8
25	-	-	-	-	10.029	-58.151	4.737	14.137
100	-	-	-	-	10.237	-47.871	4.742	12.857
200	-	-	-	-	11.122	-40.418	5.06	12.597
300	-1.446	0.298	-	-	12.254	-36.886	5.541	13.16
400	-4.481	0.106	-5.748	-8.772	13.514	-35.936	6.184	14.337
500	-6.095	-0.028	-	-	14.908	-37.615	7.154	16.397
600	-	-	-	-	16.384	-42.082	8.858	19.578

*Corresponding reactions:		References:	Remarks
1	$H^+ + Cl^- + Sb(OH)_3 = H_2O + \mathbf{Sb(OH)_2Cl}$	Pokr+06	
2	$\mathbf{Sb(OH)_3CL^-} = Sb(OH)_3 + Cl^-$	Pokr+06	
3	$2H^+ + 2Cl^- + Sb(OH)_3 = 2H_2O + Sb(OH)Cl_2$	Pokr+06	600 bar
4	$Sb(OH)_3 + 3H^+ + 3Cl^- = 3H_2O + \mathbf{SbCl_3}$	Pokr+06	600 bar
5	$Sb(OH)_3 = H^+ + \mathbf{H_2SbO_3}$	SSW+97	
6	$2Sb(OH)_3 + 4HS^- + 4H^+ = 6H_2O + \mathbf{H_2Sb_2S_4}$	Bes05	
7	$HSb_2S_4{}^- + H^+ = \mathbf{H_2Sb_2S_4}$	Bes05	
8	$H_2SbS_4 = 2H^+ + \mathbf{Sb_2S_4}{}^{2-}$	Bes05	

Table 4.3: Overview Log K values As-species.

T (°C)	Log K1	Log K2	Log K3	Log K4	Log K5	Log K6	Log K7
25	23.78	-76.825	8.336	19.445	3.548	11.259	8.83
100	18.221	-62.625	9.103	19.908	2.898	9.739	8.275
200	13.308	-52.927	10.51	21.626	2.999	8.62	8.209
300	9.925	-48.734	12.195	24.018	1.881	8.143	8.558
400	7.366	-48.177	14.134	26.88	1.554	8.235	9.187
500	5.198	-51.484	16.528	30.337	1.242	9.199	10.155
600	3.167	-58.996	19.496	34.346	0.914	11.284	11.519

*Corresponding reactions:		References:
1	$\mathbf{As(OH)_3}$ + 1/2 O_2 =$AsO(OH)_3$	PPB-08
2	3 $As(OH)_3$ + 6 HS^- + H^+ = $\mathbf{H_3AsS_6}$ + 9 H_2O	Bes05
3	$\mathbf{HAsO_4}$ + H^+ = $AsO(OH)_3$	PPB+08
4	$\mathbf{AsO_4}^{--}$ + 2 H^+ = $AsO(OH)_3$	??
5	$\mathbf{H_2As_3S_6}^-$ + H^+ = $H_3As_3S_6$	Bes05
6	$\mathbf{HAs_3S_6}^{--}$ +2H^+ = H_3AsS_6	Bes05
7	$\mathbf{H_2AsO_3}^-$ + H^+ = $As(OH)_3$	SW+97

Table 4.4: Overview log K Au-species (From Heinrich (2005)).

T (°C)	Log K1	Log K2	Log K3	Log K4	Log K5	Log K6
25	-17.45	-16.50	-9.23	-11.06	-7.26	6,53
100	-14.07	-12.86	-7.96	-8.38	-5.72	6.25
200	-10.35	-8.51	-7.13	-5.65	-4.27	6,32
300	-7.34	-4.61	-7.11	-3.64	-3.32	6.81
400	-4.83	-1.02	-7.69	-2.10	-2.67	7.64
500	-2.64	2.41	-8.68	-0.76	-2.14	8.71
600	-0.55	5.82	-9.85	0.63	-1.53	9,93

*Corresponding reactions:

1 AuHs - H^+ = H_2S(aq) + Au^+

2 - $Au(HS)_2^-$ - 2 H^+ = 2 H_2S(aq) + Au^+

3 - $AuCl_2^-$ = 2 Cl^- + Au^+

4 - Au(OH) - 2 H^+ = Au_2^+ + H_2O

5 - Au(s) - H^+ - 1/4 O_2(aq) = 1/2 H_2O + Au^+

6 - HS_2^- - H^+ = H_2S

Table 4.5: Overview log K values of Sb-As minerals

T (°C)	Arsenolite	Claedetite	Orpiment	Arsenic	Realgar	Loellingite	Arsenopyrite	Valentinite
25	-1.229	-1.362	-46.162	-17.569	-22.001	149.636	-12.284	-8.836
100	0.051	-0.118	-37.04	-13.379	-17.375	117.909	-9.814	-6.39
200	1.108	0.912	-30.428	-9.522	-13.755	90.477	-4.275	-4.275
300	1.787	1.578	-27.182	-6.765	-11.682	72.009	-2.792	-2.792
400	2.192	1.982	-26.123	-4.641	-10.576	58.46	-1.738	-1.738
500	3.303	2.099	-27.258	-2.872	-10.332	47.737	-1.025	-1.025
600	2.1	1.91	-30.695	-1.291	-10.925	38.812	-0.601	-0.601

T (°C)	Senarmontite	Stibnite	Chalcostibnite	Berthierite	Antimony	Fe-Tennantite	Fe-tetrahedrite	Enargite
25	-9.817	-55.844	-51.954	-60.187	-16.738	-375.169	-361.34	-64.628
100	-7.314	-45.406	-42.851	-50.086	-13.041	-312.111	-302.324	-54.723
200	-4.882	-37.362	-35.553	-42.674	-9.431	-261.797	-254.758	-47.446
300	-3.182	-33.07	-31.368	-39.201	-6.776	-232.856	-227.403	-44.024
400	-1.967	-31.195	-29.079	-38.283	-4.383	-216.465	-211.994	-42.99
500	-1.13	-31.604	-28.224	-39.766	-2.879	-208.24	-204.289	-43.761
600	-0.608	-34.318	-28.432	-43.528	-1.192	-204.076	-200.236	-45.62

*Corresponding reactions:

1 $As(OH)_3 = \mathbf{As_2O_3} + H_2O$
2 $As(OH)_3 = \mathbf{As_2O_3} + H_2O$
3 $As(OH)_3 + 3HS^- + 3H^+ = 6H_2O + \mathbf{As_2S_3}$
4 $As(OH)_3 + 1.5\ H_2 = 3H_2O + \mathbf{As}$
5 $As(OH)_3 + H^+\ 0.5H_2 = 3H_2O + \mathbf{AsS}$
6 $2As(OH)_3 + Fe^{++} = 2H_2O + \mathbf{FeAs_2}$
7 $As(OH)_3 + Fe + H_2 = 3H_2O + H_2 + FeAs$
8 $Sb(OH)_3 = Sb_2O_3 + H_2O$
9 $Sb(OH)_3 = Sb_2O_3 + H_2O$
10 $2Sb(OH)_3 + 3HS^- + H^+ = 6H_2O + \mathbf{Sb_2S_3}$
11 $Sb(OH)_3 + 2HS^- + Cu^{++} + 0.5H_2 = \mathbf{CuSbS_2} + H_2O$
12 $2\ Sb(OH)3 + 4HS^- + Fe^{++} + 2H^+ = 6\ H_2O + \mathbf{FeSbS_4}$
13 $Sb(OH)_3 + 0.5H_2 = Sb\ (s) + H_2O$
14 $4\ As(OH)_3 + 13HS^- + 10Cu^{++} + 5\ H_2 + Fe^{++} = \mathbf{Cu_{10}Fe_2As_4S_{13}} + 12\ H_2O + H^+$
15 $4\ Sb(OH)3 + 13HS^- + 10Cu^{++} + 5\ H_2 + Fe^{++} = \mathbf{Cu_{10}Fe_2Sb_4S_{13}} + 12\ H_2O + H^+$
16 $As(OH)_3 + 4HS^- + 3\ Cu^{++} + 0.5H_2 = 3\ H_2O + H^+ + \mathbf{Cu_3AsS_4}$

4.3 Results

4.3.1 Fieldwork

The focus of this paper lies on the interpretation of phase relations observed in rock samples collected during a 2013 field expedition to the AL. The motivation of this fieldwork was to determine the relationship between host rock and vein system(s) in proximity to Sb and As mineralization. Samples have been taken from four different mines from east to west: Gravelotte, Beta, Athens, Monarch. These mines lie along the AL, and are 1 to 8 km apart from each other (Figure 4.1). In each of these mines, samples were taken where the Sb- and As-content were the highest. These locations are at different depths per mine: Gravelotte decline from 0 to 20 m, Beta mine at 640-680m, Athens at 1160-1240m and Monarch decline from 0 to 1240m depth.

This entire deposit-hosting unit has been heavily metasomatized (serpentinized and carbonatized) and is heavily structurally deformed (Chapter 3). Chlorite schists are dark green and may grade into listvenite, light bright green, within carbonated domains. In these rocks with pronounced pressure-solution schistosity, quartz-carbonate (dolomite-magnesite) veins developed synkinematically as tension fractured and were folded and boudinaged.

The quartz-carbonate veins were more competent than the surrounding schist and stibnite precipitated in pressure shadows around these dolomite-dominant microlithons as well as in brittle fractures within them (Vearncombe et al., 1992). These dolomite-quartz veins were most present in quantity and size within and in close approximation of the listvenite. Dolomite appears to be the main host of stibnite (Chapter 3). However in several locations and without clear association with these dolomite-rich regions, highly schistose chlorite-magnesite-quartz rocks contain abundant pyrite-pyrrhotite-arsenopyrite(-

berthierite) mineralization.

Sb and As-reefs in the mines

Overall two distinct lithological units have been recognized in close proximity and/or in contact with each other: 1) metagranodiorite and 2) listvenite. At the contact between these two lithologies, chromium-rich chlorite schist is enriched with fuchsite and cut by deformed networks of stibnite-rich carbonate veins. In contrast, the arsenopyrite-rich domains were found notably outside the dolomite(-quartz) veins and within the schistose chlorite-magnesite-quartz domains (cm-m scale). No direct relationship between the Sb- and As-reef was perceived.

Dolomite-veins can be recognized as large veins or zones (meter scale), or smaller fractures or fissures (mm scale). Dolomite(-quartz) veins are boudinaged or foliated and surrounded by either chlorite, talc, or fuchsite. Fine-grained magnesite (often associated with quartz) is disseminated within the chlorite-schist or in selvages of dolomite veins.

4.3.2 Petrography and bulk mineralogy

Table 4.6 presents a petrological overview and comparison of the different samples that have been used for geochemical analyses, presented in Table 4.1. A distinction has been made between Sb- and As-reefs and samples where both Sb and As mineralization was recognized. Furthermore, gangue material was depicted in varying combinations of dolomite, magnesite and quartz. Arsenopyrite is concentrated in varying amounts throughout the AL, though most prominent present with magnesite(-quartz) mineralization. Stibnite is predominantly found along with dolomite (Chapter 3). However, both enrichments can be developed in regions where both stibnite and arsenopyrite occur, and possibly represent different generations of mineralization (samples M124 and M121). Also, the results listed in table 4.6 indicate that pyrite-pyrrhotite(-chalcopyrite) mineralization is related to the arsenopyrite mineralization. Sb-mineralization is prevailing monomineralic (stibnite), with rare accounts of berthierite.

Two samples have been chosen as representatives of end member situations for stibnite and arsenopyrite mineralization. Both have been characterized by x-ray diffraction studies and the diffractograms are plotted in (Figures 4.2 and 4.3). These samples are A080, from the Athens mine and M121 from the Monarch decline. Figure 4.2 shows arsenopyrite, together with pyrite, surrounded by dolomite-magnesite-quartz and chlorite in sample A080. Sample M121 differs in that fuchsite and gersdorffite present and pyrite is not. This result is in line with the observations made within the mine and the petrographic results in table 4.6.

Table 4.6: Petrological overview of most prominent sulfide minerals.

	Sample	Sb/As reef?	Gangue material	FeS_2	$Fe_{(1-x)}S$	$CuFeS_2$	FeAsS	$FeSb_2S_4$	FeSbS	NiSbS	Sb_2S_3	Sulfo
Athens	A080	As-reef	mgs-q	A	M	T	A	-	-	M	-	T
	A081	As-reef	mgs-q near dol vein	-	-	-	D	-	-	-	-	-
	A082	-	mgs-q	C	C	T	C	-	M	M	-	-
Monarch decline	M121	As-reef	dol-mgs-q	-	-	-	M	-	-	-	C	-
	M122A	Sb-reef	dol	-	-	-	-	-	-	-	C	-
	M122B	Sb-reef	dol	-	-	-	M	-	-	-	C	-
	M123	-	dol and mgs	-	-	-	-	T	-	C	A	-
	M124	-	mgs-q	-	-	-	M	C	-	C	A	-
	M126	As-reef	mgs-q and dol	M	-	-	-	C	-	-	-	T
Monarch mine	Mm107	As-reef	mgs-dol-q	T	C	T	C	-	-	-	-	-
Beta quarry	B028	-	dol-q	M	-	-	-	C	-	T	T	-
	B032	-	q	-	-	-	C	-	-	-	-	-
	B033	-	q-mgs	M	-	-	C	-	-	-	M	-
Beta mine	Bm048	Sb-reef	dol	-	-	-	-	-	-	-	D	-

* Ore mineral abundances at different sampling sites.

Abbreviations:

T = trace (< 1%), M = minor (1-5%), C = common (5-25%), A = abundant (25-50%), D = dominant (> 50%)

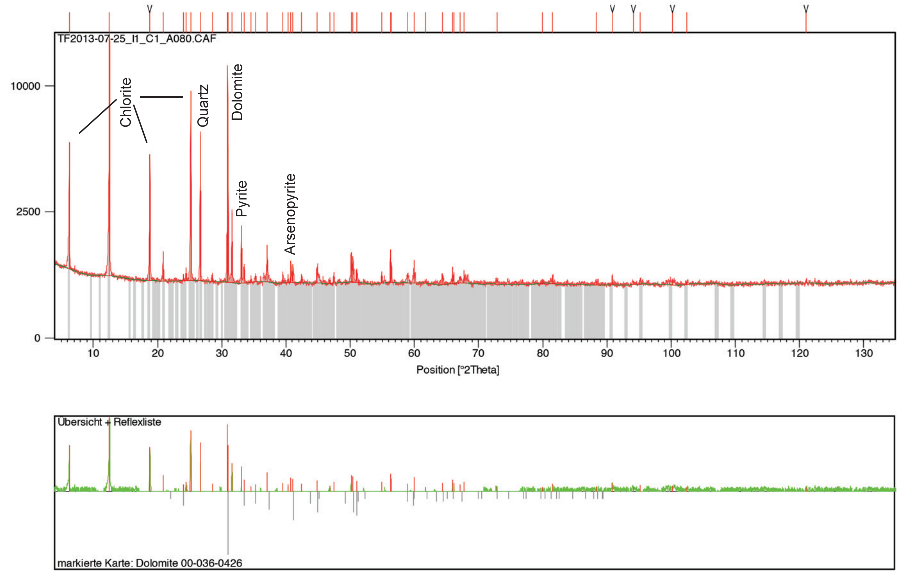

Figure 4.2: XRD results of sample A080, showing arsenopyrite, pyrite together with chlorite, quartz and dolomite.

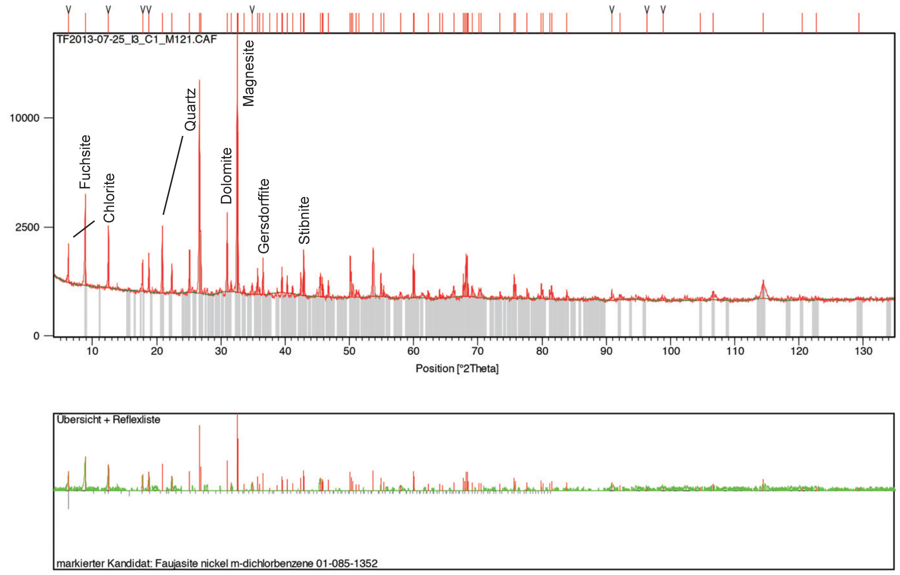

Figure 4.3: XRD results of sample M121, showing stibnite and gersdorffite together with fuchsite, chlorite, quartz and carbonates.

Figure 4.4 to 4.13 are plates, where 9 samples are represented by 3 to 5 BSE images each in addition to a photograph of each thin section billets cut from the handspecimen as well as a scan of the entire thin section. In the thin section scans, pink square boxes represent the locations of the EMPA measurements and the corresponding BSE plots.

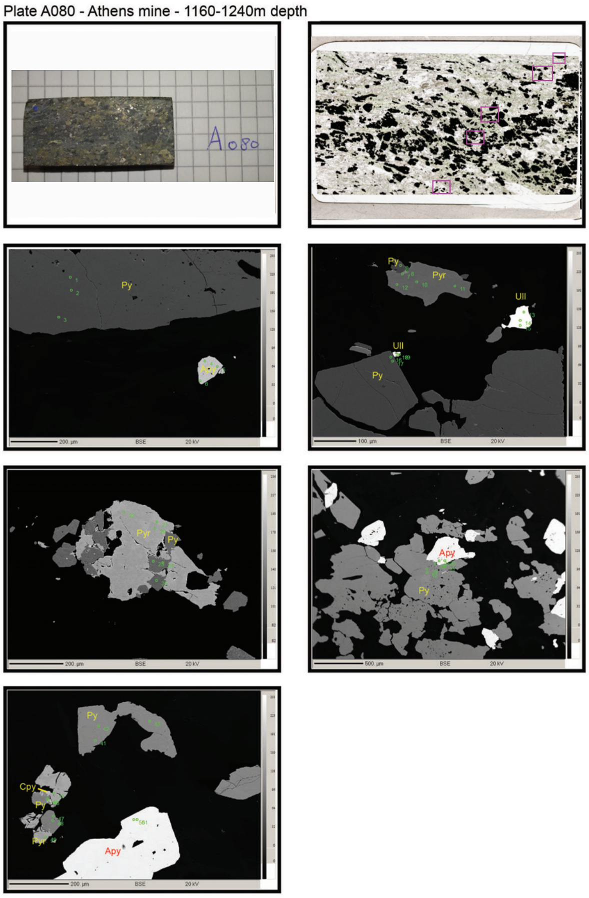
Plate A080 - Athens mine - 1160-1240m depth
A080
Py
Py
Pyr
Ull
Ull
Py
Pyr
Py
Apy
Py
Py
Cpy
Py
Pyr
Apy

Figure 4.4

Figure 4.4 - plate A080 represents an arsenopyrite-mineralized rock domain. Both the billet and the thin section show clearly the sulfide mineralization within a chlorite schist, surrounded by only minor amounts of magnesite and quartz. The dominant mineral here is pyrite, with smaller amounts of pyrrhotite-chalcopyrite-ullmannite and

arsenopyrite. Arsenopyrite is clearly recognized by its bright white reflection color in comparison to the pyrrhotite (grey) and pyrite (darker grey). Different generations of pyrite can be recognized; for example euhedral shaped as in box nr 5 (bottom left) or disseminated in pyrrhotite in box 3 (middle left).

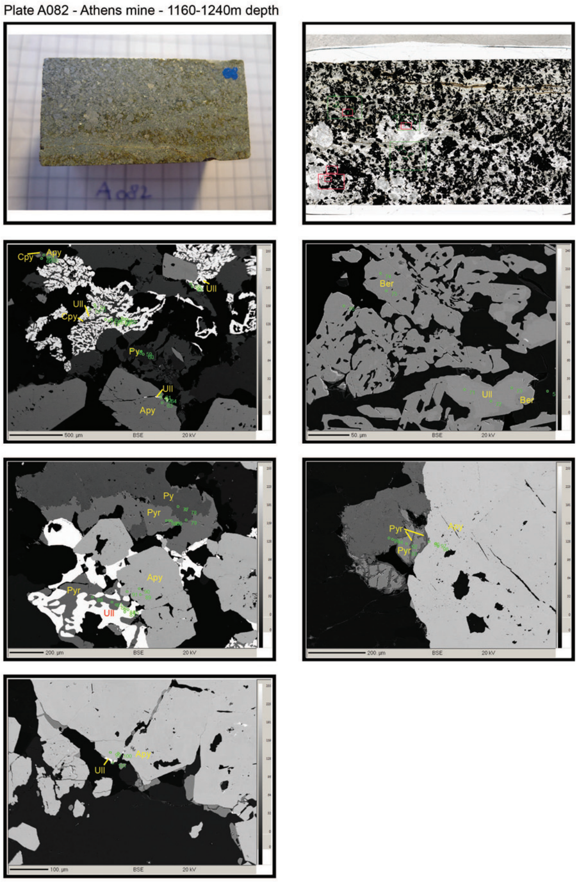
Plate A082 - Athens mine - 1160-1240m depth
A082
Cpy
Apy
Ull
Cpy
Py
Ull
Apy
Ber
Ull
Ber
Py
Pyr
Apy
Pyr
Ull
Pyr
Pyr
Ull
Apy

Figure 4.5

Figure 4.5 - plate A082 evidently shows the dominant sulfide mineralization in comparison to the surrounded chlorite schist (on plate A080). Here only small amounts of chlorite are present, and larger amounts of (rounded) magnesite and quartz. Sb-mineralization is manifest as myrmekitic ullmannite intergrown with chalcopyrite (box

1; upper left) and pyrrhotite (box 3; middle left); and ullmannite as replacement of berthierite (box 2; upper right). The rim of ullmannite on berhierite in box 2, could indicate a local change in chemical conditions to low sulfur fugacities and high Ni availability, both of which may be related to the presence of ultramafic rock. This ullmannite mineralization is different from the intergrowths of pyrrhotite-ullmannite and chalcopyrite-ullmannite, which are proximal to arsenopyrite. Box 1 and 5 even show a varying amounts of ullmannite at the rim of and within arsenopyrite, together with pyrrhotite. This suggests two different generations of ullmannite mineralization; 1) berthierite-ullmannite mineralization and 2) mobilization of Ni and reminalization of ullmannite in intergrowths of pyrite-pyrrhotite. Arsenopyrite remains dominantly euhedral, revealing that conditions were never outside the arsenopyrite stability field.

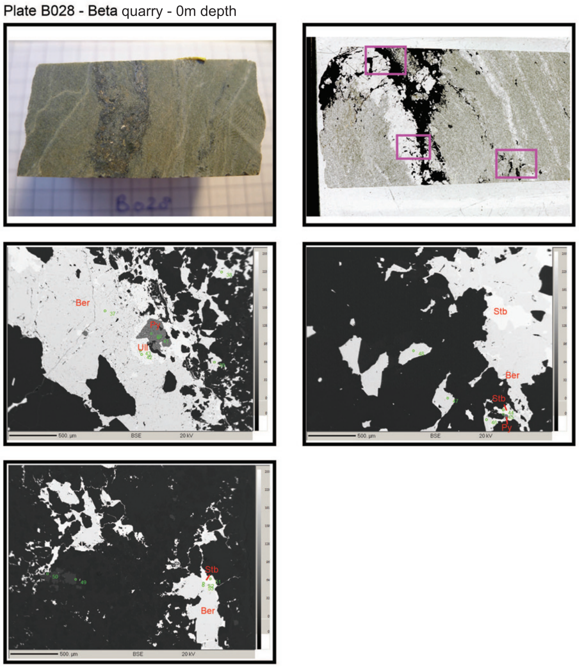

Figure 4.6

Figure 4.6 - plate B028 also shows a berhierite-ullmannite intergrowth in box 1 (upper left) and a berthierite-stibnite intergrowth in box 2 (upper right). The dominant gangue material is quartz, therefore lacking the dolomite-mineralization common for the dominance of stibnite. This intergrowth, however, may reveal that stibnite was not remobilized here by carbonization events, but may represent altered berthierite, which therefore possibly represents the first generation of stibnite within the AL.

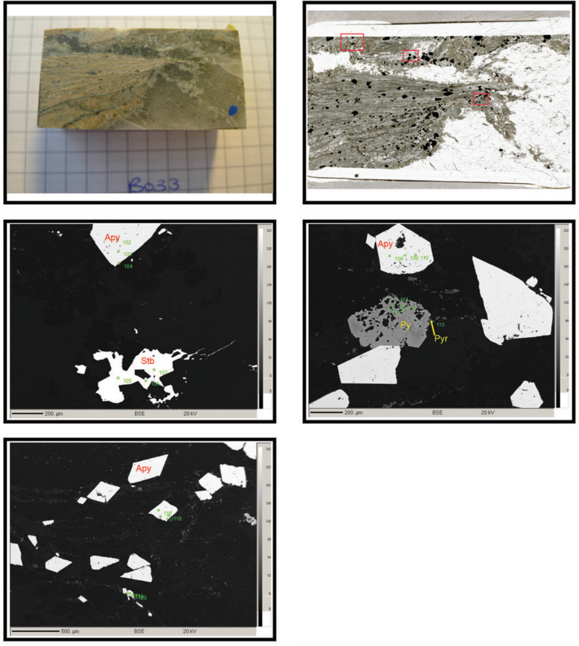
Plate B033 - Beta quarry - 0m depth

Figure 4.7

Figure 4.7 - plate B033 is one of the rare locations where arsenopyrite and stibnite are found in close proximity of one another (box 1). Disseminated pyrite-pyrrothite are found in close relationship with euhedral arsenopyrite (box 2).

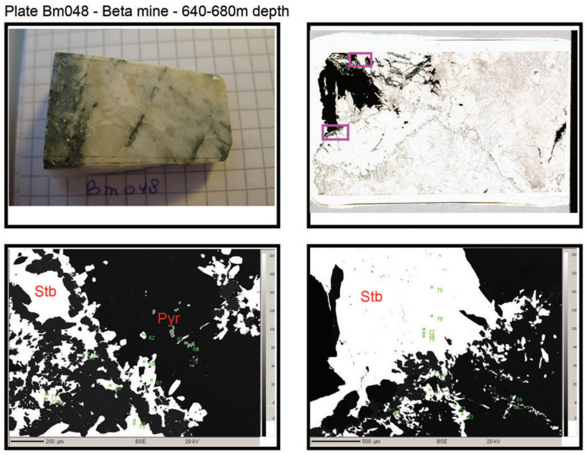
Plate Bm048 - Beta mine - 640-680m depth

Figure 4.8

Figure 4.8 - plate Bm048 has been sampled within a Sb-reef. The dominant mineralization is dolomite-quartz-stibnite with scattered occurrences of pyrite within quartz. Box 1 and box 2 noticeably show the different regrowth of stibnite into smaller branches within the dolomite. Box 2 in particular shows the dissolution of large stibnite grains and remineralization into smaller stibnite minerals within the dolomite. This feature is indicative of Sb immobility during dynamic recrystallization and carbonation of the rocks in the AL.

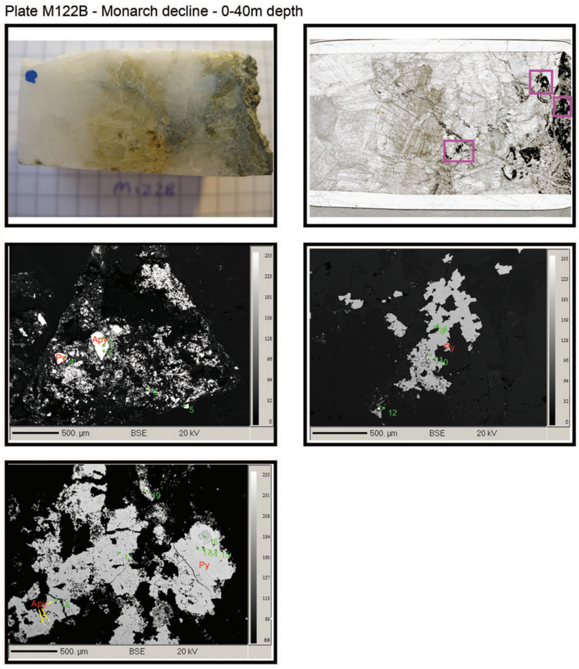
Plate M122B - Monarch decline - 0-40m depth
M122B
Apy
Py
500 µm
BSE
20 kV

Figure 4.9

Figure 4.9 - plate M122B is a sample of both dolomite and siderite (yellow in hand specimen), together with the common sulfide mineralization. Anhedral pyrite is the main sulfide in this sample, with small inclusions of arsenopyrite (box 3; middle left). Occasionally, anhedral arsenopyrite grains can be found, too (box 1; upper left). No Sb-minerals have been detected in this sample.

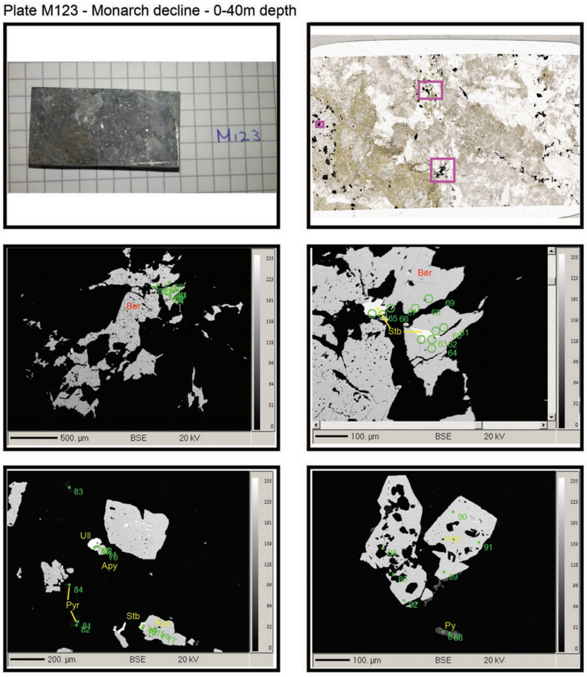
Plate M123 - Monarch decline - 0-40m depth
M123
Ber
500. µm BSE 20 kV
Ber
Stb
65 66 67 68 69
60 61
63 62
64
100. µm BSE 20 kV
83
Ull
70
Apy
84
Pyr
81
82
Stb
Apy
200. µm BSE 20 kV
90
Apy
91
86
85
89
92
Py
100. µm BSE 20 kV

Figure 4.10

Figure 4.10 - plate M123 represents another example for a rock in which stibnite-berthierite and arsenopyrite are found in close proximity of one another. The Sb-dominated sulfide mineralization is developed within dolomite (two larger pink boxes on thin section). In contrast, the sulfide mineralization within the chlorite-magnesite domain (left part thin section), contains arsenopyrite. The euhedral shapes of arsenopyrite can even be recognized with the naked eye in the thin section. In box 3 (down; left) ullmannite is found also as inclusions of arsenopyrite. Moreover, later stibnite mineralized on top of several arsenopyrite crystals.

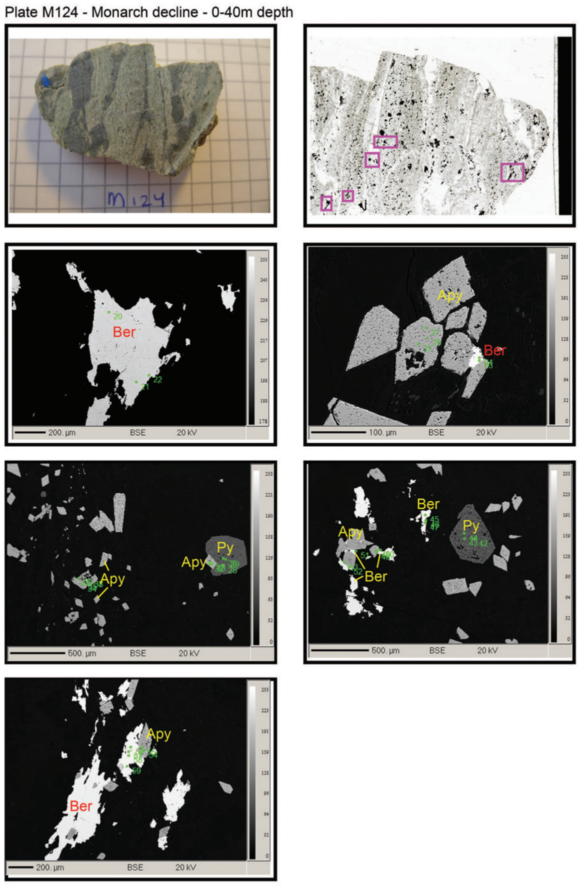
Plate M124 - Monarch decline - 0-40m depth
M124
Ber
200 µm BSE 20 kV
Apy
Ber
100 µm BSE 20 kV
Py
Apy
Apy
500 µm BSE 20 kV
Ber
Apy
Py
Ber
500 µm BSE 20 kV
Apy
Ber
200 µm BSE 20 kV

Figure 4.11

Figure 4.11 - plate M124 is a sample directly from a highly schistose chlorite-quartz rock, which has only been minimally carbonatized. Arsenopyrite and berthierite are the main sulfide mineralization within this sample, where berthierite appears to precipitate during a later stage, as it fills void space between arsenopyrite grains.

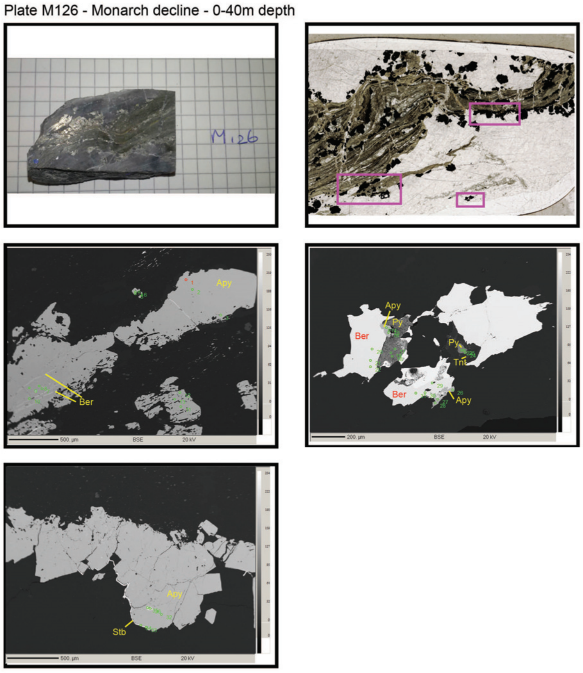
Plate M126 - Monarch decline - 0-40m depth
M126
Apy
Ber
500. µm
BSE
20 kV
Apy
Py
Ber
Py
Tnt
Ber
Apy
200. µm
BSE
20 kV
Apy
Stb
500. µm
BSE
20 kV

Figure 4.12

Figure 4.12 - plate M126 reveals overgrowth of stibnite and berthierite on arsenopyrite (filling and rimming) in a chlorite schist adjacent to a dolomite-rich vein (Box 1 and 3). Box 2 reveals a pyrite aggregate, adjacent to arsenopyrite and berthierite.

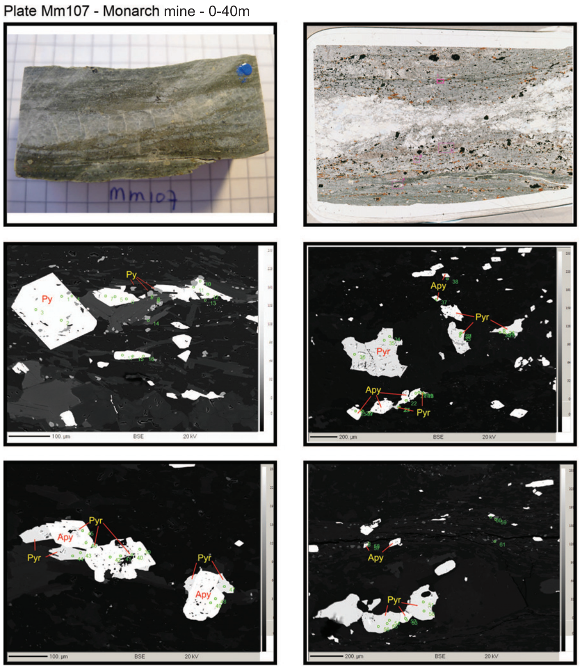
Plate Mm107 - Monarch mine - 0-40m
mm107
Py
Py
Apy
Pyr
Pyr
Apy
Pyr
Pyr
Apy
Pyr
Pyr
Apy
Apy
Pyr
100 µm
200 µm
BSE
20 kV

Figure 4.13

Figure 4.13 - plate Mm107 is pyrite-pyrrhotite rich and reveals pyrrhotite as inclusions of pyrite and arsenopyrite.

Overall Sb-As minerals are dominantly disseminated within the carbonated domains and are predominantly present within the metagranodiorite. Stibnite is clearly mobile on small spatial scales as it can be found mineralized throughout the carbonized system in different grain sizes and as fillings between dolomite grains or as newly mineralized rims on arsenopyrite or other sulfides. Foliated chlorite schists, with enrichments of magnesite(-quartz) contain arsenopyrite, pyrite and pyrrhotite, gudmundite, chalcopyrite and to lesser extents berthierite and ullmannite. These rock domains have not been affected by later-stage carbonate (dolomite) or quartz formation. T Different generations of berthierite occur: 1) berthierite-stibnite mobilization and 2) berthierite-ullmannite outside dolomite-carbonation veins, in close proximity to arsenopyrite domains. Berthierite is present as main mineral or as rim of ullmannite within the chlorite schist. Ullmannite (NiSbS) has been surrounded by berthierite ($FeSb_2S_4$). Gudmundite (FeSbS) has been found sporadically adjacent to arsenopyrite, within the arsenopyrite-rich zone in the Monarch mine. All these phases lack in the carbonate-quartz metasomatized domains of the AL lithologies. Tennantite is found as inclusions within pyrite and arsenopyrite. In contrast, stibnite is exclusively found within tension fractures, like boudins, boudinages or veins and is clearly related to isoclinal folding and subsequent episodes of deformation and veining.

4.3.3 Major and minor metal concentrations

Table 4.7 to 4.9 show selected mineral formulas of pyrite, pyrrhotite and chalcopyrite. Mineral formulas of arsenopyrite and Sb-minerals can be found in chapter 3 and Apppendices.

Table 4.7 shows mineral formulas of twelve distinct pyrite grains from samples described in previous section. Roughly, five types of pyrite can be distinguished. Older generations of pyrite within A080 contain low enrichments of As, whereas A082 has only ‘pure pyrite’, with minor traces of other metals. From the other mines, besides ‘pure’ pyrite, several enrichments stand out: B028 has a slight enrichment of Ni, reflecting the high amount of ullmannite adjacent to the pyrite. Pyrite measured in M126 and M122B shows an enrichment in Sb, although no Sb-mineralization is present within M122B. Cu-values are generally low, only in some Sb-enriched pyrites can a moderate Cu-content be detected. Figure 14A represents all the pyrite measured with As# (As/(Sb+As+Ni)), Sb# (Sb/(Sb+As+Ni)) and Ni# (Ni/(Sb+As+Ni)) values calculated.

Table 4.7: EMPA dataset of selected pyrite minerals

Pyrite	A080_37	A080_1	A080_2	A082a	B028	Mm107	Mm107_2	M122B_6	M122B_7	M122B	M126_23	M126
S	54.27	53.84	54.05	53.30	51.22	52.88	53.09	52.85	52.79	50.85	52.45	48.04
Mn	0.03	0.01	0.03	0.00	0.01	0.03	0.02	0.01	0.02	0.02	0.00	0.01
Fe	46.19	46.05	46.08	46.42	45.59	45.93	46.36	46.75	47.03	45.38	44.65	45.38
Co	0.00	0.00	0.01	0.00	0.09	0.01	0.00	0.01	0.01	0.00	0.05	0.00
Ni	0.02	0.04	0.03	0.01	**1.14**	0.01	0.03	0.00	0.00	0.00	**0.46**	0.10
Zn	0.07	0.03	0.01	0.00	0.00	0.02	0.05	0.00	0.00	0.02	0.05	0.00
As	**0.31**	**0.66**	**0.46**	0.00	0.05	**0.34**	**0.28**	0.13	0.05	0.04	0.08	**0.38**
Cd	0.00	0.00	0.00	0.00	-	-	-	-	-	-	-	-
Sb	0.00	0.00	0.00	0.18	0.02	0.00	0.00	0.00	0.00	**3.02**	**0.81**	**3.56**
Cu	0.05	0.00	0.06	0.05	0.00	0.02	0.01	0.00	0.02	0.00	**0.81**	0.16
Total wt.%	100.94	100.64	100.73	99.97	98.12	99.24	99.84	99.75	99.92	99.33	99.35	97.63
S	66.99	66.80	66.91	66.60	65.59	66.56	66.46	66.26	66.13	65.41	66.36	63.77
Mn	0.02	0.01	0.02	0.00	0.01	0.02	0.01	0.00	0.01	0.01	0.00	0.01
Fe	32.74	32.80	32.75	33.30	33.51	33.19	33.32	33.65	33.82	33.52	32.43	34.58
Co	0.00	0.00	0.01	0.00	0.06	0.00	0.00	0.01	0.01	0.00	0.03	0.00
Ni	0.02	0.03	0.02	0.01	**0.80**	0.01	0.02	0.00	0.00	0.00	**0.32**	0.07
Zn	0.04	0.02	0.00	0.00	0.00	0.01	0.03	0.00	0.00	0.02	0.03	0.00
As	**0.16**	**0.35**	**0.24**	0.00	0.03	**0.18**	**0.15**	0.07	0.03	0.02	0.04	**0.22**
Cd	0.00	0.00	0.00	0.00	-	0.00	0.00	0.00	0.00	-	-	-
Sb	0.00	0.00	0.00	0.06	0.01	0.01	0.01	0.00	0.01	**1.02**	**0.27**	**1.25**
Cu	0.03	0.00	0.04	0.03	0.00	0.01	0.01	0.00	0.00	0.00	**0.52**	0.11
Total at.%	100.00	100.00	100.00	100.00	100.00	100.00	100.00	100.00	100.00	100.00	100.00	100.00

*Twelve selected samples, representative with their distinct enrichments of Sb, Ni or As from Athens mine (A-sample nr), Monarch decline (M-sample nr),Beta mine (B-sample nr) and the Monarch mine (Mm-sample nr).

Overall it can be stated that pyrites from the AL have high As# values, with variable Sb# and Ni# values. These variable compositions could indicate different generations of pyrite, or postdepositional trace element remobilization.

Table 4.8: EMPA dataset of selected pyrrhotite minerals.

Pyrrhotite	A082a	A082b	A082_4	Mm107_19	Mm107a	Mm107b	A080	A080_10
S	40.17	39.95	40.12	38.02	39.87	39.17	39.94	40.06
Mn	0.00	0.02	0.00	0.02	0.02	0.00	0.00	0.00
Fe	58.68	59.83	59.54	58.16	58.60	58.68	58.75	58.55
Co	0.00	0.00	0.00	0.00	0.00	0.00	0.02	0.00
Ni	**0.59**	0.01	0.02	**0.30**	**0.31**	**0.36**	**0.62**	0.58
Zn	0.04	0.00	0.02	0.00	0.00	0.01	0.00	0.01
As	0.03	0.04	0.02	**1.08**	**0.51**	**0.49**	0.01	0.01
Cd	0.00	0.00	0.00	0.01	-	-	-	0.00
Sb	0.00	0.02	0.05	0.04	0.00	0.00	0.00	0.01
Cu	0.00	0.02	0.01	0.00	0.00	0.04	0.00	0.00
Total wt.%	99.51	99.88	99.79	97.63	99.31	98.75	99.34	99.21
S	54.13	53.74	53.96	52.76	53.94	53.44	53.95	54.14
Mn	0.00	0.01	0.00	0.01	0.01	0.00	0.00	0.00
Fe	45.40	46.20	45.97	46.33	45.52	45.96	45.56	45.42
Co	0.00	0.00	0.00	0.00	0.00	0.00	0.02	0.00
Ni	0.43	0.00	0.02	0.23	0.23	0.27	0.46	0.42
Zn	0.03	0.00	0.02	0.00	0.00	0.01	0.00	0.01
As	0.02	0.02	0.01	0.64	0.30	0.29	0.01	0.00
Cd	0.00	0.00	0.00	0.00	-	-	-	0.00
Sb	0.00	0.01	0.02	0.03	0.00	0.00	0.00	0.00
Cu	0.00	0.01	0.01	0.00	0.00	0.03	0.00	0.00
Total at.%	100.00	100.00	100.00	100.00	100.00	100.00	100.00	100.00

*Eight selected samples based on their representative enrichment of Ni and As from Athens mine (A-sample nr) and the Monarch mine (Mm-sample nr).

Table 4.8 shows mineral formulas of eight distinct pyrrhotite grains. Pyrrhotite is in general ‘cleaner’ than pyrite. Sb is absent and only small amounts of Ni and As can be traced. This has been made visible within Figure 14B. In contrast to the pyrite, no pyrrhotite with a dominant As# is measured, though from the three samples where pyrrhotite has been measured varying amounts of Ni# must be noted.

Chalcopyrite compositions are presented in Table 4.9 with only small enrichments of As. The concentrations of both Ni and Sb are below detection limit.

A larger set of trace elements has been analyzed by LA-ICPMS (Figure 4.14). Trace elements have been measured in arsenopyrite, pyrrhotite, pyrite, stibnite and berthierite.

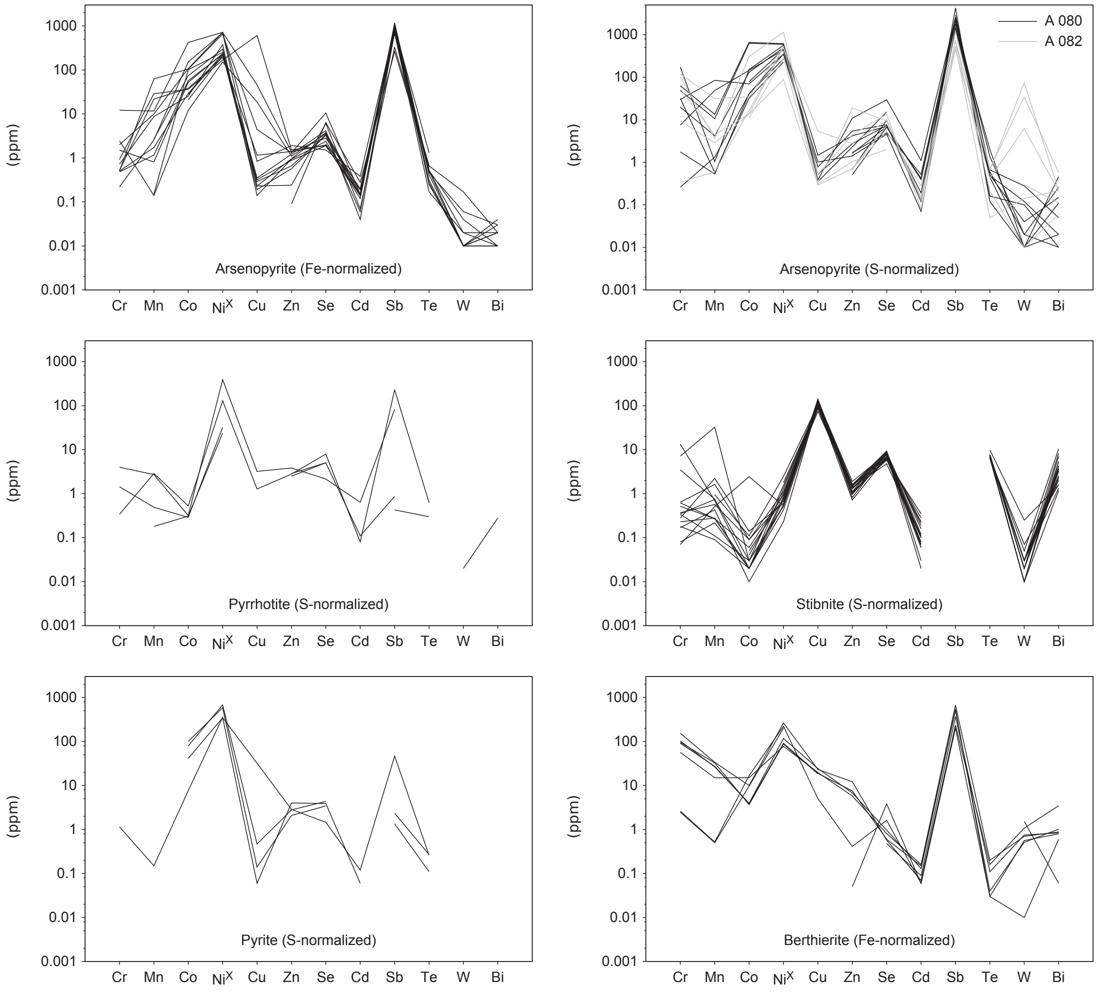

Figure 4.14: LA-ICPMS results showing metal trace content of stibnite, arsenopyrite, pyrite, pyrrhotite.

Table 4.9: EMPA dataset of five chalcopyrite minerals.

Chalcopyrite	A080	A082a	A082b	Mm107a	Mm107b
S	34.82	34.64	34.79	34.60	34.67
Mn	0.00	0.00	0.00	0.00	0.01
Fe	30.45	29.61	29.46	30.37	29.89
Co	0.00	0.00	0.00	0.00	0.02
Ni	0.00	0.00	0.00	0.00	0.02
Zn	0.00	0.03	0.00	0.06	0.00
As	0.00	**0.47**	**0.39**	0.02	0.04
Cd	0.00	0.00	0.00	-	-
Sb	0.00	0.03	0.06	0.00	0.00
Cu	33.62	34.27	33.99	33.93	34.18
Total wt.%	98.90	99.04	98.68	98.98	98.84
S	50.27	50.09	50.40	50.01	50.16
Mn	0.00	0.00	0.00	0.00	0.01
Fe	25.24	24.58	24.50	25.20	24.82
Co	0.00	0.00	0.00	0.00	0.02
Ni	0.00	0.00	0.00	0.00	0.02
Zn	0.00	0.02	0.00	0.04	0.00
As	0.00	0.29	0.24	0.01	0.03
Cd	0.00	0.00	0.00	-	-
Sb	0.00	0.01	0.02	0.00	0.00
Cu	24.49	25.00	24.84	24.74	24.95
Total at.%	100.00	100.00	100.00	100.00	100.00

**Five samples from Athens mine (A-sample nr) and Monarch mine (Mm-sample nr).

It was difficult to select grains for measurements, due to quality differences between the thin sections and small sizes of sulfide grains. The results presented here are mostly multiple grains from one specific sample (Table 4.10). It must be taken into account that the results plotted can thus not be seen as a representative for the overall sulfide mineralization. But the data collected help developing an understanding of the trace element chemistry of these different minerals.

When looking at arsenopyrite (both Fe- and S-normalized), the enrichments in Sb and Ni contents are most prominent. Also, there is considerable incorporation of gersdorffite (NiAsS) (e.g., Klemm (1965)) and likely gudmundite (FeSbS) components in arsenopyrite solid solution. Both pyrite and pyrrhotite plots are difficult to read, due to their relative low abundance of trace metals, though small enrichments of Sb-Ni are also visible as expected by the EMPA measurements (Table 4.7 and 4.8).

Table 4.10: Metal trace contents of arsenopyrite, pyrite, pyrrothite, stibnite and berhierite.

Mineral		Sample	Cr	Mn	Co	Nix	Cu	Zn	Se	Cd	Sb	Te	W	Bi
apy	Fe normalized	A082	9.97	-	20.97	210.03	-	-	2.05	0.19	684.03	0.17	0.02	0.02
apy		A082	1.99	9.97	107.56	711.88	45.60	1.38	1.97	0.12	774.84	0.52	0.01	0.04
apy		A082	0.22	2.58	151.86	700.05	0.23	0.96	3.76	0.15	1108.73	0.42	0.01	0.02
apy		A082	-	0.15	100.92	251.64	0.35	1.22	4.16	0.04	715.89	0.57	0.00	0.04
apy		A082	2.46	0.14	12.11	151.44	18.72	1.10	3.54	0.19	860.21	0.31	0.01	0.03
apy		A082	1.50	0.81	52.23	235.09	0.29	0.66	3.39	0.14	704.10	0.44	0.00	0.01
apy		A082	0.92	28.81	36.30	168.41	605.49	1.53	1.88	0.15	1037.15	0.25	0.01	0.02
apy		A082	0.50	1.73	29.21	229.74	0.19	0.57	3.27	0.06	706.63	0.27	0.01	0.01
apy		A082	0.66	-	27.79	224.64	-0.07	0.09	6.38	0.28	262.66	0.66	0.17	0.02
apy		A082	0.72	8.69	25.41	374.62	0.14	0.94	2.38	0.14	1167.99	0.52	0.01	0.01
apy		A082	-	2.66	74.08	296.75	0.23	0.24	6.07	0.07	328.20	0.68	0.00	0.01
apy		A082	0.51	62.49	105.02	649.87	4.42	1.31	10.56	0.15	930.88	0.47	0.06	0.03
apy		A082	0.48	1.16	57.15	227.02	0.32	0.88	1.90	0.14	816.34	0.49	0.02	0.01
apy		A082	0.52	21.72	38.16	193.43	1.15	1.40	2.83	0.20	921.27	0.52	0.04	0.01
apy		A082	12.16	11.68	422.62	715.10	0.84	1.91	1.51	0.38	914.76	1.31	0.00	0.08
apy	S normalized	A082	2.75	-	78.14	451.53	0.00	0.69	9.72	0.13	4259.39	0.12	0.01	0.11
apy		A082	1.75	0.53	40.83	271.69	0.00	0.51	6.73	0.42	2528.24	0.60	0.02	0.26
apy		A082	19.81	4.19	130.55	494.49	0.00	1.69	4.91	0.52	2190.51	0.49	0.12	0.02
apy		A082	31.76	0.58	32.29	226.70	0.00	1.63	6.90	0.39	1796.38	0.45	0.01	0.02
apy		A082	48.54	10.58	624.34	593.10	0.39	10.91	29.42	1.10	2564.60	0.50	0.04	0.15
apy		A082	7.51	48.70	145.23	438.51	0.52	2.75	7.31	0.19	2198.44	1.36	0.02	0.01
apy		A082	30.11	84.40	69.46	350.10	0.78	5.42	7.66	0.12	2414.27	0.16	0.10	0.01
apy		A082	0.26	1.32	40.68	353.40	1.02	1.41	4.57	0.07	1459.58	0.42	-	0.00
apy		A082	173.77	1.04	151.95	562.47	0.35	2.31	15.29	-	2919.45	0.66	0.28	0.05
apy		A082	63.30	13.42	661.34	614.74	1.46	4.19	7.01	-	1422.95	2.01	0.01	0.46
pyr		A082	1.44	0.49	0.29	32.41	-	2.51	5.05	0.11	0.87	-	0.00	0.04
pyr		A082	-	0.18	0.31	23.88	-	2.87	5.05	-	0.43	0.30	0.00	0.03
pyr		A082	4.00	2.73	0.32	393.08	3.22	3.85	2.16	0.64	82.73	0.00	0.02	0.28
pyr		A082	0.34	2.89	0.53	129.65	1.28	2.80	7.94	0.08	230.45	0.63	0.00	0.08
stb		Bm048	-	-	0.05	0.79	86.73	1.11	5.82	0.35	-	7.16	0.03	2.04
stb		Bm048	0.35	0.74	0.00	0.64	105.14	1.04	6.32	0.11	-	6.41	0.07	1.62
stb		Bm048	-	-	-	1.79	97.74	0.98	6.54	0.06	-	6.79	0.03	1.34
stb		Bm048	-	-	0.02	1.32	112.97	1.31	5.99	0.10	-	6.74	0.01	1.18
stb		Bm048	-	0.95	0.11	2.47	105.61	1.51	7.02	0.23	-	6.57	0.03	3.70
stb		Bm048	0.64	1.63	0.09	1.11	107.35	1.35	6.73	0.22	-	6.82	0.03	3.38
stb		Bm048	0.62	0.27	0.06	0.94	120.36	1.55	6.25	0.08	-	7.73	0.03	3.69
stb		Bm048	1.29	-	0.04	1.02	74.39	1.39	4.79	0.10	-	6.31	0.01	3.63
stb		Bm048	13.31	0.70	0.02	0.43	91.98	1.53	7.99	0.19	-	7.49	0.02	2.49
stb		Bm048	3.50	0.75	0.03	0.52	98.64	0.72	6.69	0.28	-	9.87	0.25	1.58
stb		Bm048	0.08	0.22	0.02	0.73	129.25	1.90	8.17	-0.05	-	7.00	0.01	4.28
stb		Bm048	0.07	0.51	2.45	0.53	131.74	1.62	8.69	0.16	-	7.54	0.02	3.21
stb		Bm048	0.28	2.24	0.14	0.61	139.18	1.34	7.56	0.07	-	7.49	0.03	2.31
stb		Bm048	0.34	0.11	0.03	0.54	133.51	1.12	8.91	0.07	-	6.65	0.03	2.57
stb		Bm048	0.37	0.57	0.09	0.72	104.54	1.58	9.33	0.07	-	7.26	0.03	8.26
stb		Bm048	0.17	0.43	0.01	0.23	110.35	1.46	9.03	0.03	-	7.53	0.02	7.07
stb		Bm048	0.23	0.28	0.02	0.85	129.05	0.82	8.24	0.12	-	7.72	0.02	5.33
stb		Bm048	7.17	32.45	0.03	1.54	98.58	1.60	7.82	0.10	-	6.96	0.05	10.49
stb		Bm048	0.18	0.09	0.02	0.56	141.78	0.97	8.91	0.06	-	7.75	0.02	4.21
stb		Bm048	0.52	0.27	0.02	0.00	135.63	1.30	8.15	0.02	-	6.99	0.01	5.34
py		A080	1.53	0.00	41.43	347.87	32.07	2.86	1.46	0.12	46.77	0.26	0.00	0.24
py		A080	0.01	-	79.68	675.31	0.47	2.79	4.35	-0.01	1.35	0.11	0.00	0.09
py		A080	1.15	0.15	7.59	354.60	0.06	4.01	3.91	0.06	-0.55	0.00	0.00	0.01
py		A080	0.52	-	100.77	586.95	0.14	2.08	3.44	0.00	2.35	0.27	0.00	0.17
apy		A080	52.76	4.39	13.70	508.92	5.40	2.77	9.66	0.15	445.19	0.42	6.17	0.21
apy		A080	0.34	0.60	16.50	516.49	-	0.71	5.38	0.28	526.76	0.05	0.14	0.22
apy		A080	103.13	3.62	306.44	1144.57	0.52	4.40	13.52	0.08	744.67	0.66	73.30	0.22
apy		A080	120.01	31.51	34.46	530.89	0.34	18.83	9.43	0.13	1169.64	0.70	34.70	0.57
apy		A080	9.43	2.85	13.62	87.08	0.31	1.04	2.00	0.00	1.35	-	0.30	0.11
apy		A080	0.20	-0.25	11.05	284.44	0.29	0.71	7.22	0.00	689.38	0.21	0.01	0.06
py	Fe normalized	M122	102.87	26.48	3.96	117.28	24.36	6.79	0.97	0.13	541.25	0.03	0.56	0.80
py		M122	91.49	27.35	3.84	91.26	18.91	7.50	0.60	0.15	510.63	0.04	0.51	1.02
py		M122	56.69	14.97	15.09	77.83	19.70	5.77	0.81	0.16	670.93	0.20	0.70	0.88
py		M122	95.84	32.62	3.68	88.29	18.37	0.00	0.48	0.09	368.45	0.11	0.75	0.84
py		M122	154.23	33.66	10.05	265.01	23.20	12.20	0.57	0.07	236.11	0.16	1.08	3.48
py		M122	2.48	0.50	9.68	201.81	-0.63	0.05	3.83	0.06	214.01	-	1.54	0.06
py		M122	2.61	0.52	16.80	223.13	5.06	0.41	1.62	0.06	204.10	0.03	0.01	0.60

*Metal trace contents on four samples, selected on their premisice to the Sb/As reefs.
X: normalised with PGE-Ni standard.
All values are in ppm.

When comparing arsenopyrite and stibnite, it is prominent that the quantity of trace elements is greater in arsenopyrite. This could be a reflection of the refractory character of arsenopyrite. Stibnite reveals higher quantitites of Cu and Ni. Only slight differences can be observed between different stibnite grains. The input of Cu, while lacking in arsenopyrite, could also indicate a change in fluid type that is responsible for the mobilization of stibnite. Element variability plots have been used to provide a more detailed look at the relationship between the trace elements of arsenopyrite and stibnite. Due to low quantities measured in pyrite and pyrrhotite, these minerals were not taken into account in this step.

The elemental plots show the relationship and R^2 of different elements with S within that specific mineral. The green band reflects the standard deviation. The elemental plots of arsenopyrite (Figure 4.15) show little to no relationship of S with the metal elements, except Cr (R^2: 0.38). One exception must be noted; a sample (marked by the red cross at all elements) has an unusual high Cu-content, changing the R^2 value radically. When this sample is not taken into account, a high relationship would also be detected with Cu. Overall, up to 100's ppm of Sb and Ni must be noted.

Figure 4.16 of stibnite on the contrary, shows high relationships of Ni, Cu and Se with S. A negative correlation for Cd is also present.

Overall, when combining both major and trace metal elements an affinity and relationship conjointly of As-Ni-Sb is noteworthy within the AL mineralogy. Wavering amounts of Cu-content within the solid and aqueous species is also apparent.

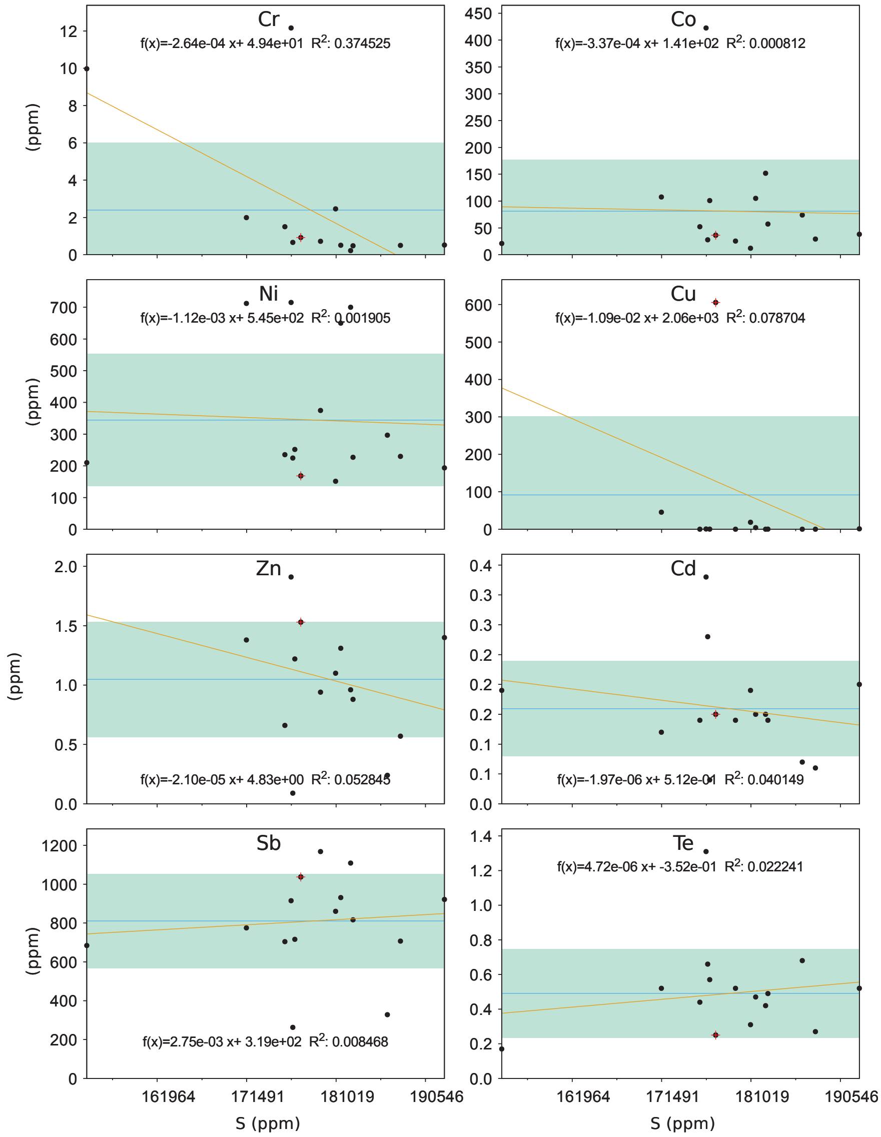

Figure 4.15: Elemental map of arsenopyrite, with calculated correlations (R^2) between the different metal concentrations.

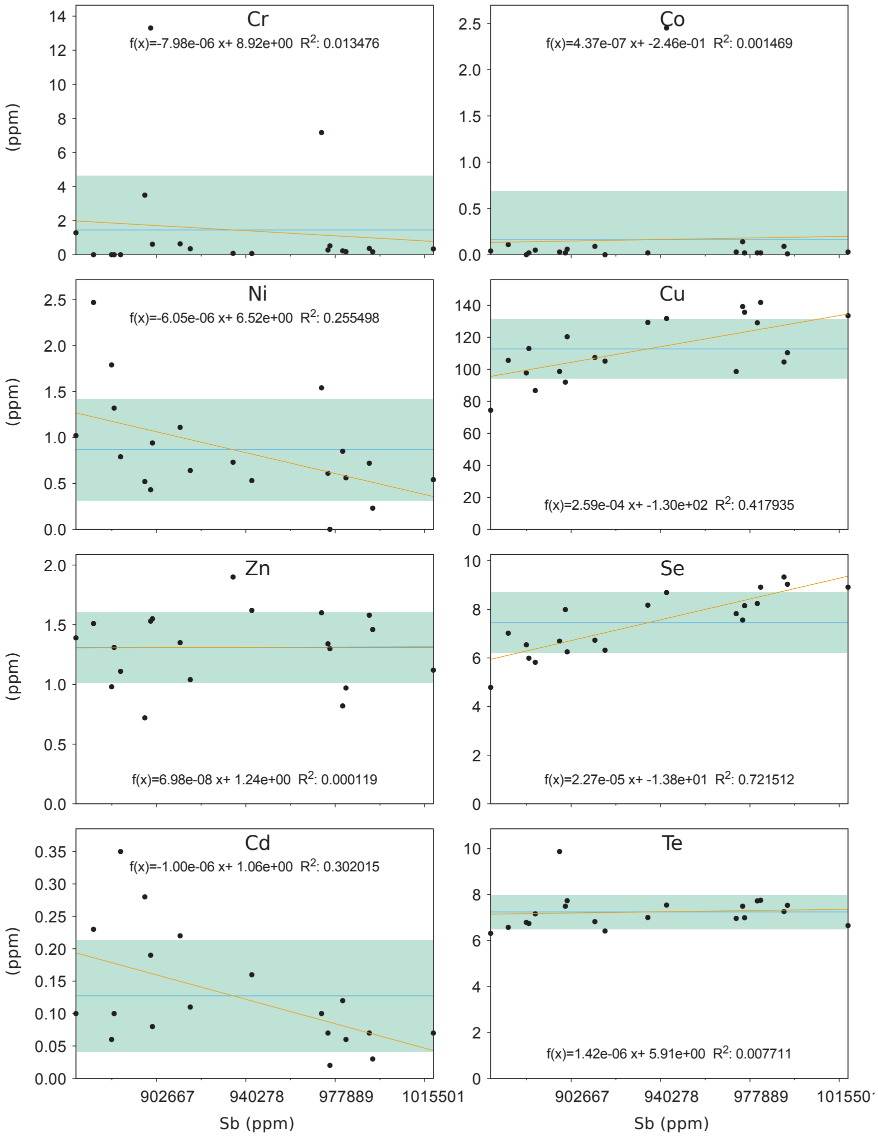

Figure 4.16: Elemental map of stibnite, with calculated correlations (R^2) between the different metal concentrations.

4.3.4 Geochemical modelling

We conducted thermodynamic calculations to depict the Fe-Cu-Sb-O-H-S and Fe-Cu-As-O-H-S phase relations. Furthermore we focused on computing the solubilities of As, Sb, and Au. The phase relations were examined in H_2(aq) vs. H_2S(aq) activity plane (Figure 4.17 and 4.18) and in pH vs log f O_2 plane (Figure 20-26) for a pressure of 1 kbar and temperatures of 350 and 250 °C.

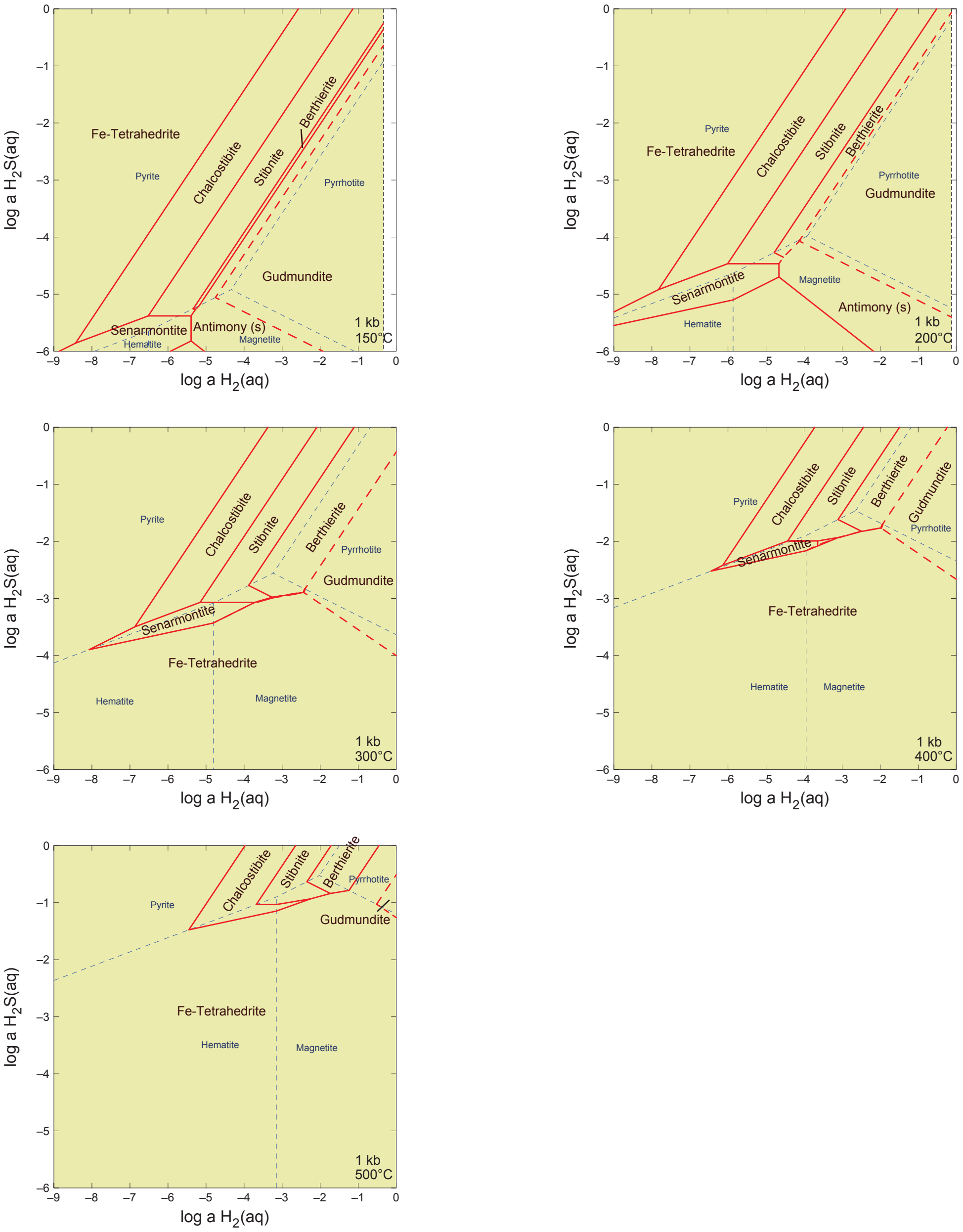

Figure 4.17: Activity diagram Fe-Sb-S-O at 1kb ranging from 150-500 °C.

The activity diagrams for Sb-phases (Figure 4.17) show that the stibnite-berthierite phase boundary in the H_2-H_2S plane runs parallel and close to the pyrite-pyrrhotite binary. It is hence likely that pyrite-pyrrhotite control H_2-H_2S activities in the system, and that the stibnite-berthierite assemblage is a reflection of this control mechanism. Additionally, it indicates that the transition from early native antimony and berthierite along with pyrrhotite to later stibnite and pyrite is consistent with a drop in the activity of aqueous dihydrogen, which causes an increase of sulfur fugacity, according to S_2(g) + H_2(aq) = H_2S(aq) (Hagemann and Lüders, 2003). An increase or decrease in H_2S(aq) activity can also cause the transition from berthierite to stibnite. A decrease in H_2S activity, by for example boiling, can explain the berthierite-stibnite transition only in the presence of magnetite, which is lacking in the AL assemblages. Likewise, degassive loss of both H_2 and H_2S in equal proportions would not affect sulfur fugacity, so the berthierite-stibnite phase boundary can only be crossed if magnetite were present.

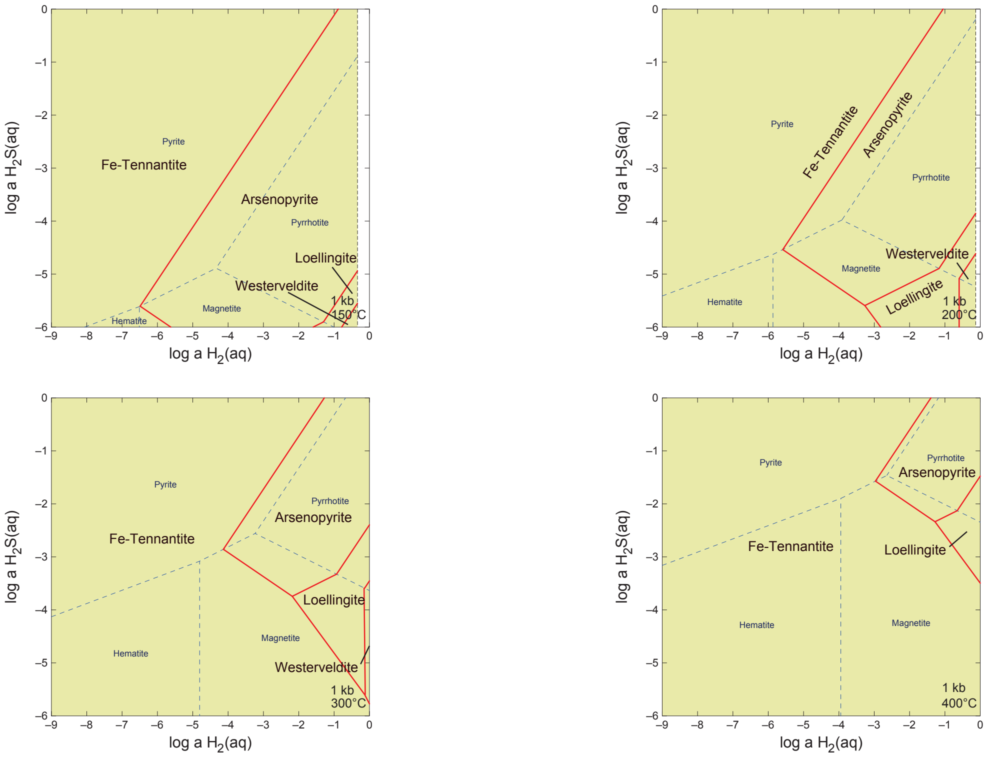

Figure 4.18: Activity diagram Fe-As-S-O at 1kb ranging from 150-400 °C.

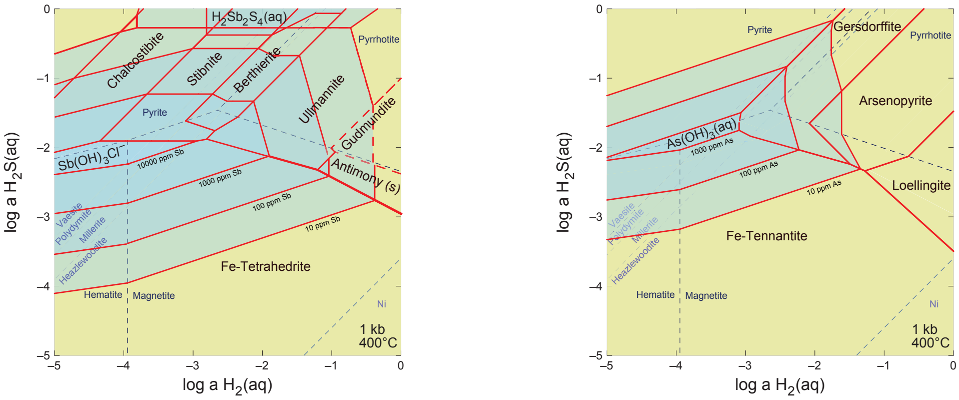

Figure 4.19: Activity diagram of a) Sb and b) As phases with varying Sb and As concentrations at 1kb and 400 °C, with contourlines of Ni+ plotted in the background.

Figure 4.19 emphasizes the activity diagrams for both Sb and As phase relations at 400 °C, based on the primary mineralization temperature deduction around 380-400

°C calculated by Jaguin, Boulvais, et al. (2014) and chapter 3. The red lines indicate variable Sb (10-10000 ppm) and As (10-1000 ppm) solubilities. In calculating these phase relations, Ni was included as component (in addition to Cu-Fe-O-S-H-As/Sb), and Fe-Ni-S phase relations are plotted in light blue. This treatment allows the inclusion of gersdorffite and ullmannite (both are common in the AL) in the phase relation analyses.

A different approach of deducing stability of Sb and As-solubilities and phase relations in multicomponent space is to focus on acidity in relationship to oxygen fugacity, as seen in Figure 4.20 - 4.25.

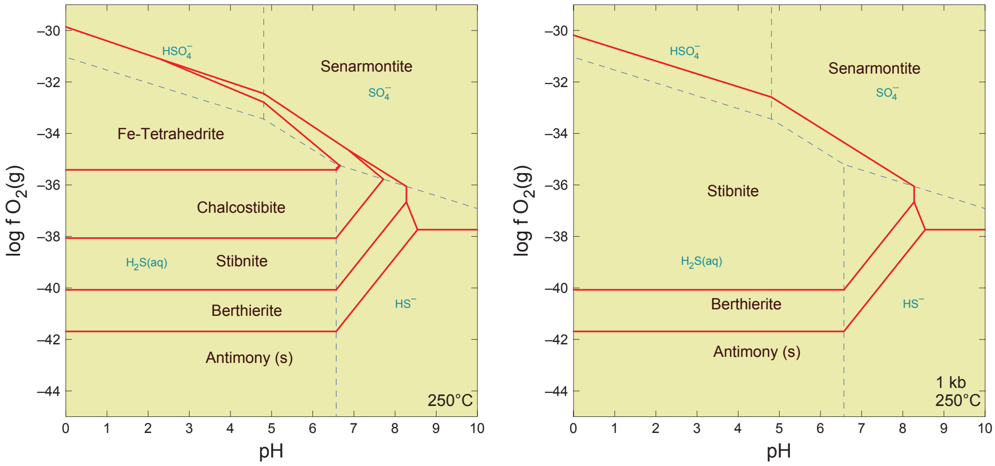

Figure 4.20: Activity diagram of Sb-minerals a) with Cu-content and b) without Cu-content at 250 °C and 1kb.

Figure 4.20 shows the stability fields of the solid minerals with and without Cu in the system. The stibnite-berthierite-chalcostibite group is dominantly dependent on the oxygen fugacity within the acidic to neutral regimes. In the presence of sulfate, the setting is too oxidized to form Sb-sulfides and only senarmontite (Sb_2O_3) will be present.

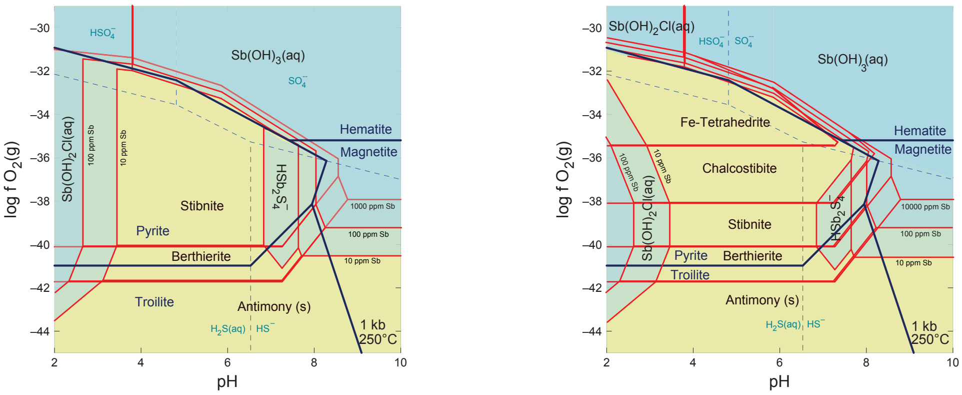

Figure 4.21: Activity diagram of Sb-species a) with Cu-content and b) without Cu-content at 250 °C and 1kb.

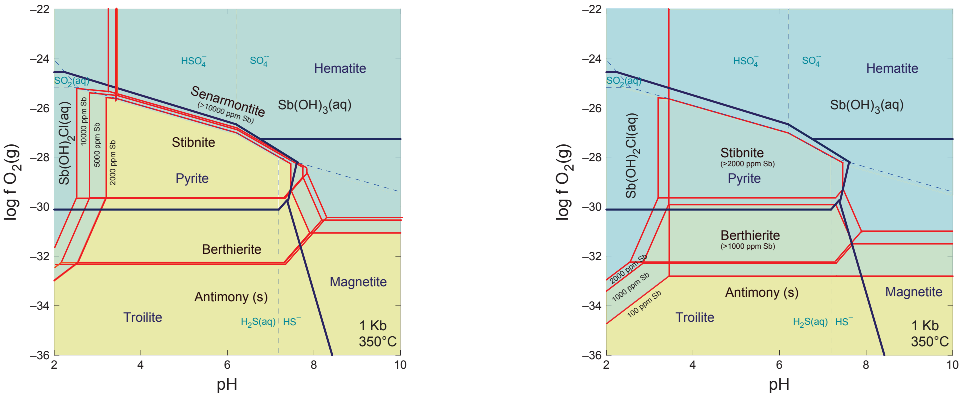

Figure 4.22: Activity diagram of Sb-minerals without Cu-content at 350 °C and 1kb.

Figure 4.21 and 4.22 examine the deposition of Sb(-Cu) minerals and Sb solubilities at 1 kb and 250 °C and 350 °C, respectively, under varying f O_2 and pH conditions. When focusing on stibnite(-berthierite), the mineralization will be promoted under reducing and acidic to neutral conditions, within the pyrite field. Native antimony will only be deposited at fairly reducing conditions. The $(OH)_2Cl$ complex is dominant in acidic conditions and prefers at 250 °C a more reducing setting, though slightly less reduced at 350 °C. In contrast hydroxo-complexes are dominant in the more neutral to basic conditions. Phase transitions between stibnite-berthierite-native antimony are dominantly controlled by oxygen fugacity. The acidity plays a major role in the precipitation of Sb-minerals as indicated by the strong pH-dependency of Sb solubility. Adding Cu to the phase relation analyses will effect the stability of stibnite at high f O_2 by introducing the sulfosalts chalcostibite and tetrahedrite.

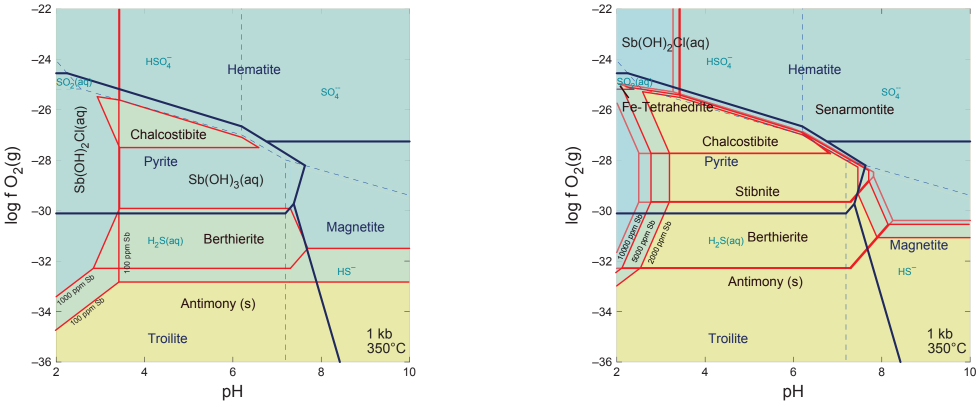

Figure 4.23: Activity diagram of Sb-minerals with Cu-content at 350 °C and 1kb.

Figure 4.23 displays the same setting at 350 °C with Cu-content. Figure 24a displays the isopleths for 100 ppm and 1000 ppm Sb, while Figure 24b displays a range of isopleths from 2000 to to 5000 to 10000 ppm Sb. A two-step visualization has been chosen due to an increase in readability of the plot. The diagrams show that a mineralizing fluid would need at least 2000 ppm dissolved Sb in order to precipitate stibnite at 350 °C. Berthierite and chalcostibite, in contrast, may occur already at 1000 ppm Sb. Overall, $Sb(OH)_3$ (aq) is the dominant aqueous Sb-species in solution.

Figure 4.24 examines the deposition of As(-Cu) minerals and As3+ species at 350 °C and 1kb, under varying f O_2 and pH conditions. Arsenopyrite + sulfosalt are stable under acidic and reducing conditions inside the H_2S(aq) predominance field. Under more oxidizing and alkaline conditions, westerveldite ((Fe,Ni)As) is expected to mineralize. $As(OH)_3$ (aq) is the dominant aqueous Sb-species in solution.

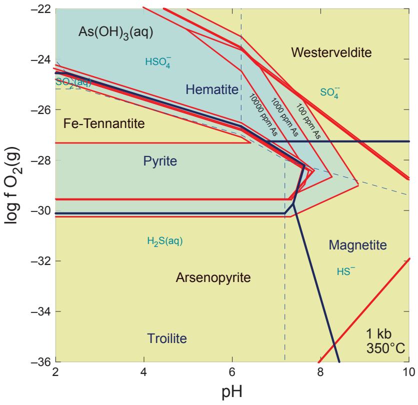

Figure 4.24: Activity diagram of As-minerals with Cu-content at 350 °C and 1kb.

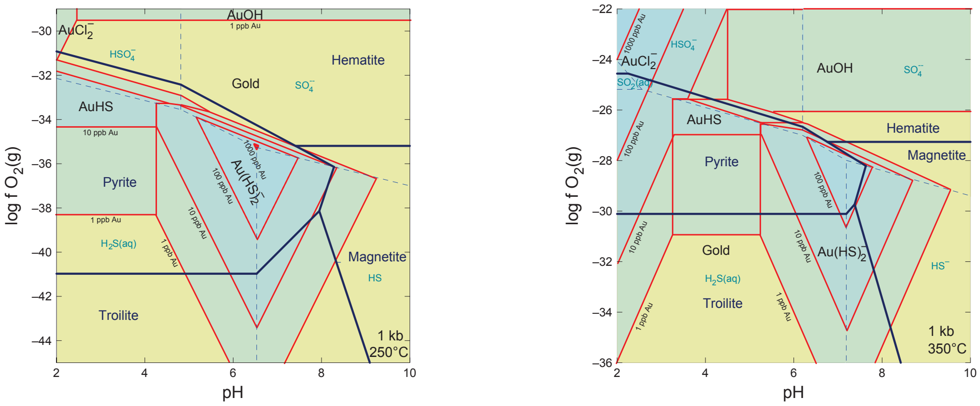

Figure 4.25: Activity diagram of Au at a) 250 °C and b) 350 °C at 1kb.

Similar computations were conducted to investigate the solubility of gold considering the stability of various Au-species at 250 °C (Figure 4.25a) and 350 °C (Figure 4.25b). Gold is preferably transported as Au(HS)$_2^-$ (c.f. e.g. Williams-Jones and Norman (1997)) in fairly reducing settings at both temperatures. Its solubility is actually greater at 250 °C than at 350 °C. The Au(HS)$_2^-$ is destabilized by either taking H_2S out of the system or by adding sulfate and acidifying the solution. This can be understood in terms of reaction

$$8\mathrm{Au(HS)}_2^- + \mathrm{SO}_4^{2-} + 15\,\mathrm{H}^+ = 8Au(s) + 4\,\mathrm{H_2O} + 15\,\mathrm{H_2S}. \tag{4.1}$$

At both temperatures the maxima of gold concentrations and major drops of its solubility lie within the pyrite stability field (and the stibnite stability field, cf. Figure 4.22.).

4.4 Discussion

4.4.1 Orogenic gold deposit style

The Murchison Greenstone Belt (MGB) in South Africa is one of the Archaean greenstone belts along the Kaapvaal Craton and hosts the largest Archaean economic stibnite deposit in the world (Boyle and Jonasson, 1984; Davis et al., 1986). The (primary) antimony mineralization in the AL has been proposed to relate to the emplacement of Maranda granodiorite intrusions that occurred around 2.9 Ga (Poujol, 1996; Jaguin, Poujol, et al., 2013) and that may be related to orogeny in the Limpopo Belt, north of the MGB (Block et al., 2013). The MGB hosts an Archaean suture zone with a VMS-type deposit, responsible for the Cu-Zn line north of the AL (Schwarz-Schampera et al., 2010) and probably accountable for the Au found in the Pietersberg greenstone belt (Zeh et al., 2013).

The dominant mineralogy is stibnite-arsenopyrite-berthierite-ullmannite-pyrite-pyrrhotite, with minor occurences of ullmannite, gersdorfite and chalcopyrite (Davis et al., 1986; Vearncombe et al., 1992). It has been widely accepted that stibnite, tetrahedrite and a great variety of other sulphosalts (e.g. berthierite) are the principal antimony minerals in gold-quartz veins within carbonated silificied zones like greenstone belts (Boyle and

Jonasson, 1984). Gold has not been found within scope of this paper, though is has been recognized by others as visible and invisible gold in varying distances from the dominant antimony mineralization (Davis et al., 1986; Vearncombe et al., 1992). The invisible gold has been determined to occur as fine disseminations or as sub-microscopic intergrowths in arsenopyrite-pyrite mineralization (Davis et al., 1986). Due to the Sb-As-Au mineralogy (Hagemann and Lüders, 2003), together with geological setting of a (back)-arc convergent plate setting within an in accretionary and collisional orogeny (Groves et al., 1998), the AL is interpreted to be a unique example of an Archaean orogenic gold deposit (Foster and Piper, 1993), also conform by the definition set up by Hagemann and Cassidy (2000). Furthermore, most orogenic gold deposits formed under greenschist facies conditions with hydrothermal alteration assemblages developed in ductile to brittle deformation, with temperatures around 200-420 °C and CO_2-rich fluids (Hutchinson, 1993; McCuaig and Kerrich, 1998) of granitoid magmatic or metamorphic origin (Ridley and Diamond, 2000), which all agrees to the temperature and fluid regime determined by Jaguin, Boulvais, et al. (2014) and chapter 3. Jaguin, Poujol, et al. (2013) and Jaguin, Boulvais, et al. (2014) assigned a major role in the formation of the Sb-mineralization to the albititzation of the Maranda granite. Chapter 3 presented a comprehensive geochemical model that accounts for the formation of listvenite and albitite in the contact between granodiorite and komatiited in the AL suture zone. These authors furthermore suggested that the metasomatic reactions forming the deposit-hosting lithologies acted as trap for Sb (and As and Au). The earlier Ni-As-Sb-Cu-Fe-S mineralization, however, could have formed prior to metasomatic replacement of the host lithologies. We present here solubility calculations and additional phase relations that support the idea that the AL represents a special type of orogenic lode deposit, in which metasomatic reactions rather than pressure-release and fluid boiling played a major role in the mineralization.

4.4.2 Sb-As-Au mineralization

Mineralization in the AL in the MGB is typified by stibnite-arsenopyrite-pyrite-pyrrhotite-berthierite-ullmanite-gudmundite(-chalcopyrite) dominantly disseminated within the carbonated domains, with stibnite being the most dominant economic important mineral. Different generations of Fe-Sb-S(-Cu) mineralization can be recognized throughout the AL. Stibnite is clearly mobile on small spatial scales as it can be found mineralized throughout the carbonatized system in different grain sizes and as fillings between dolomite grains or as newly mineralized rims on arsenopyrite or other sulfides.

Three generations of Sb-mineralization occur: 1) gudmundite found adjacent to arsenopyrite; 2) berthierite-ullmannite outside dolomite-carbonation veins, in close proximity to arsenopyrite domains and finally 3) berthierite-stibnite mobilization within carbonatized domains. Additionally, arsenopyrite-mineralization is not restricted to the carbonization event and dolomite-mineralization, though dominantly found within extensively deformed and schistosed regions, and is thus interpreted to be from a generation before the carbonization-event(s). A prominent Sb-As mineralization event is confirmed by the Sb-enrichment within arsenopyrite and pyrite and may be an indication of relatively high Sb-content in the primary sulfide forming fluids or reconcentration of Sb due do its ability to re-enter the arsenopyrite lattice when considering the FeAsS-FeSbS solid solution (Cook et al., 2013). Pyrite-pyrrhotite is additionally developed in the Sb-mineralized within the carbonized rocks from the AL, therefore the replacement of gudmundite to berthierite by stibnite in the presence of pyrite as dominant Sb phase can be accomplished by decreasing aH_2 or by increasing aH_2S (Figure

4.17) (Lambert, 1998; Craig, 1993). Both pyritization and oxidation by carbonization lead to increased sulfur fugacities, a common explanation for the genesis of orogenic gold deposits (Williams-Jones, Bowell, et al., 2009) and serpentinization environments (Klein and Bach, 2009).

Arsenian pyrite, with As contents greater than 100 ppm and minor contents of Sb and Ni, has been shown to be an economically important host for Au in epithermal gold deposits (Reich et al., 2005) and in greenschist facies orogenic lode deposits (Cook et al., 2013). Temperature changes plus alteration by hydrothermal fluids (Deditius et al., 2014) and the decrease in H_2S (Reich et al., 2005) additionally control incorporation of Au and As quantity within pyrite at orogenic gold deposits.

Low content of chalcopyrite, though varying Cu-concentrations can be explained the low amount of chalcopyrite in the primary mineralization event or the soft, non-refractory, behavior of chalcopyrite. Presumably chalcopyrite has been remobilized through the system, during the carbonization event and has not been redeposited due to lower temperatures within the carbonization regime and hence mostly was lost from the AL.

The high Ni contents can be explained by being a remnant of ultramafic precursor rock (komatiite).

4.4.3 Model results

Though the AL is known for its unique enrichment of antimony, it’s uniqueness stands out when compared with other (orogenic gold deposits) Archaean greenstone belts where berthierite-gudmundite(-native antimony) are the dominant Sb-minerals within their system instead of stibnite: Kwekwe district (Buchholz and Oberthür, 2007); Hemlo

Archaean gold deposit (Pan and Fleet, 1995); Flin Flon greenstone belt (Healy and Petruk, 1990); Barberton greenstone belt (Ronde and Wit, 1992); Abitibi greenstone belt (Normand et al., 1996). The lack of native antimony and the reduced amount of berthierite-gudmundite could be explained by higher f O_2 conditions at the MGB (Figure 4.22).

Though greenschist facies conditions have been thought responsible for the Au content in these deposit styles, a controversy arrives when looking at antimony separately within these settings. Goldfarb, Groves, and Gardoll (2001) summarized the geochemical characteristics of antimony to be likely soluble as bisulfide complexes at relative low temperatures (<200 °C). These results are disputed by our modeling results (Figure 4.21-4.22), showing that $Sb(OH)_3$ is the dominant aqueous species, and mineralization to be possible at higher temperature regimes (up to 350 °C) depending on pH and redox conditions (cf. Obolensky, Gushchina, Borisenko, Borovikov, and Pavlova (2007) and Obolensky, Gushchina, Borisenko, Borovikov, and Nevol'ko (2009)).

4.5 Conclusions

The Murchison Greenstone Belt is an Archaean orogenic gold deposit, where the primary mineralization is connected to an ore fluid originating from a granitoid magmatic or a metamorphic devolatization model (Ridley and Diamond, 2000) (Chapter 3). The phase relations clearly indicate that the system transitioned from low f S_2 and low f O_2. Primary mineralization is As-Sb-Ni-Cu, and shifted towards As-Sb-Fe-Cu, visibly the loss of ullmanite and enrichment of berthierite which was followed by the alteration of berthierite into stibnite with high f S_2 and f O_2. These transitions are a consequence of carbonation and silicification. The rock's buffering capacities become eventually overwhelmed. However, as the phase diagrams show, Sb solubility remains low at these temperature and acidity range even as f O_2 and f S_2 creep up.

4.6 Acknowledgments

The authors thank the management and acting geologists of Consolidated Murchison Limited (ConsMurch) for their assistance and cooperation during our fieldwork in 2013. Andreas Klügel and Patrick Monien from the Universität Bremen are thanked for their assistance in conducting the geochemical measurements at the LA-ICPMS at the University of Bremen. Moritz Wagner and Michael Hentscher helped with assembling the thermodynamic databases. We thank Chris Heinrich (ETH Zurich) for making his compilation of aqueous Au-species available to us.

Bibliography

Akinfiev, N.N. and A.V. Zotov (2010). “Thermodynamic description of chloride, hydrosulfide, and hydroxo complexes of Ag(I), Cu(I) and Au(I) at temperatures of 25-500°C and pressures of 1-2000 bar”. In: *Geochemistry Int.* 39.10, pp. 990–1006. DOI: `10.1134/S0016702910070074`.

Anhaeusser, C R (1976). “Archean Metallogeny in Southern Africa”. In: *Econ. Geol.* 71, pp. 16–43.

Ashley, P.M. et al. (2003). “Environmental mobility of antimony around mesothermal stibnite deposits, New South Wales, Australia and southern New Zealand”. In: *J. Geochemical Explor.* 77.1, pp. 1–14. DOI: `10.1016/S0375-6742(02)00251-0`.

Bessinger, B. and J.A. Apps (2005). *The Hydrothermal Chemistry of Gold, Arsenic, Antimony, Mercury and Silver*. Tech. rep. Office of Science U.S. Department of Energy, pp. –52.

Block, S. et al. (2013). “The Murchison Greenstone Belt, South Africa: Accreted slivers with contrasting metamorphic conditions”. In: *Precambrian Res.* 227, pp. 77–98. DOI: `10.1016/j.precamres.2012.03.005`.

Boyle, R.W. and I.R. Jonasson (1984). “The geochemistry of antimony and its use as an indicator element in geochemical prospecting”. In: *J. Geochemical Explor.* 20, pp. 223–302.

Buchholz, P. and T. Oberthür (2007). “Multistage Au-As-Sb Mineralization and Crustal-Scale Fluid Evolution in the Kwekwe District , Midlands Greenstone Belt , Zimbabwe : A Combined Geochemical , Mineralogical , Stable Isotope , and Fluid Inclusion Study”. In: *Econ. Geol.* 102.1994, pp. 347–378.

Castro, S.H. and L. Baltierra (2005). “Study of the surface properties of enargite as a function of pH”. In: *Int. J. Miner. Process.* 77.2, pp. 104–115. DOI: `10.1016/j.minpro.2005.03.002`.

Cook, N. et al. (2013). “Arsenopyrite-Pyrite Association in an Orogenic Gold Ore : Tracing mineralization history from textures and trace elements”. In: *Econ. Geol.* 108, pp. 1273–1283.

Craig, J.R. (1993). “The Metamorphism of pyrite and pyritic ores: An overview”. In: *Mineral. Mag.* 57.386, pp. 3–18. DOI: `10.1180/minmag.1993.057.386.02`.

Davis, D.R., D.B. Paterson, and D.H.C. Griffith (1986). “Antimony in South Africa”. In: *J. S. Afr. Inst. Min. Met.* 86.6, pp. 173–193.

Deditius, A.P. et al. (2014). “The coupled geochemistry of Au and As in pyrite from hydrothermal ore deposits”. In: *Geochemica Cosmochim.* 140, pp. 644–670. DOI: `10.1016/j.gca.2014.05.045`.

Firdu, F.T. and P. Taskinen (2010). “Thermodynamics and phase equilibria in the (Ni, Cu, Zn)–(As, Sb, Bi)–S systems at elevated temperatures (300–900 C)”. In: *Espoo Aalto Univ. Publ. Mater. . . .* Pp. 1–59.

Foster, R.P. and D.P. Piper (1993). “Archaean lode gold deposits in Africa: Crustal setting, metallogenesis and cratonization”. In: *Ore Geol. Rev.* 8, pp. 303–347.

Goldfarb, R.J. and D.I. Groves (2015). “Orogenic gold: Common or evolving fluid and metal sources through time”. In: *Lithos*. DOI: `10.1016/j.lithos.2015.07.011`.

Goldfarb, R.J., D.I. Groves, and S. Gardoll (2001). “Orogenic gold and geologic time: A global synthesis”. In: *Ore Geol. Rev.* 18.1-2, pp. 1–75. DOI: `10.1016/S0169-1368(01)00016-6`.

Groves, D.I. et al. (1998). “Orogenic gold deposits: A proposed classification in the context of their crustal distribution and relationship to other gold deposit types”. In: *Ore Geol. Rev.* 13.1-5, pp. 7–27. DOI: `10.1016/S0169-1368(97)00012-7`.

Hagemann, S.G. and K.F. Cassidy (2000). “Archean orogenic lode gold deposits”. In: *Econ. Geol.* 13.i, pp. 382–384.

Hagemann, S.G. and V. Lüders (2003). “P-T-X conditions of hydrothermal fluids and precipitation mechanism of stibnite-gold mineralization at the Wiluna lode-gold deposits, Western Australia: conventional and infrared microthermometric constraints”. In: *Miner. Depos.* 38.8, pp. 936–952. DOI: 10.1007/s00126-003-0351-6.

Healy, R.E. and W. Petruk (1990). “Petrology of Au-Ag-Hg alloy and invisible gold in the Trout lake massive sulfide deposit, Flin Flon Manitoba”. In: *Can. Mineral.* 28.2, pp. 189–206.

Heinrich, C.A. (2005). “The physical and chemical evolution of low-salinity magmatic fluids at the porphyry to epithermal transition: A thermodynamic study”. In: *Miner. Depos.* 39.8, pp. 864–889. DOI: 10.1007/s00126-004-0461-9.

Hutchinson, R. W. (1993). “A multi-stage, multi-process genetic hypothesis for greenstone-hosted gold lodes”. In: *Ore Geol. Rev.* 8.3-4, pp. 349–382. DOI: 10.1016/0169-1368(93)90022-Q.

Jaguin, J., P. Boulvais, et al. (2014). “Stable isotopes (O, C) and fluid inclusion study of quartz-carbonate veins from the antimony line, Murchison Greenstone Belt”. In: *Am. J. Sci.* 314.7, pp. 1140–1170. DOI: 10.2475/07.2014.03.

Jaguin, J., M. Poujol, et al. (2013). “Albitization in the Antimony Line, Murchison Greenstone Belt (Kaapvaal Craton): A geochemical and geochronological investigation”. In: *Lithos* 168-169, pp. 124–143. DOI: 10.1016/j.lithos.2013.01.010.

Johnson, J.W., E.H. Oelkers, and H.C. Helgeson (1992). *SUPCRT92: A software package for calculating the standard molal thermodynamic properties of minerals, gases, aqueous species, and reactions from 1 to 5000 bar and 0 to 1000°C*. Vol. 18. 7. Pergmamon Press Ltd, pp. 899–947. DOI: 10.1016/0098-3004(92)90029-Q.

Kantar, Cetin (2002). “Solution and flotation chemistry of enargite”. In: *Colloids Surfaces A Physicochem. Eng. Asp.* 210.1, pp. 23–31. DOI: 10.1016/S0927-7757(02)00197-8.

Klein, F. and W. Bach (2009). “Fe-Ni-Co-O-S Phase Relations in Peridotite-Seawater Interactions”. In: *J. Petrol.* 50.1, pp. 37–59. DOI: 10.1093/petrology/egn071.

Klemm, D.D. (1965). “Synthesen und Analysen in den Dreiecksdiagrammen FeS - CoAsS - NiAsS und FeS2 - CoS2 - NiS2”. In: *Neues Jahrb. Miner.* 103, pp. 205–255.

Krupp, E (1988). “Solnbility of stibnite in hydrogen sulfide solutions, speciation, and equilibrium constants, from 25 to 350 ° C”. In: *Geochemica Cosmochim.* 52, pp. 3005–3015.

Lambert, J.M. (1998). “Kinetics and mechanism of the pyrite to pyrrhotite transformation”. In: *Metall. Mater. Trans. B.*

Lynch, D C (1982). "Standard Free Energy of Formation of NiAsS". In: *Metall. Mater. Trans. B* 13.June, pp. 285–288.

Madu, B. E., B.E. Nesbitt, and K. Muehlenbachs (1990). "A mesothermal gold-stibnite-quartz vein occurence in the Canadian Cordillera". In: *Econ. Geol.* 85, pp. 1260–1268.

McCuaig, T.C. and R. Kerrich (1998). *P—T—t—deformation—fluid characteristics of lode gold deposits: evidence from alteration systematics*. Vol. 12. 6, pp. 381–453. DOI: `10.1016/S0169-1368(98)80002-4`.

Normand, C., M. Gauthier, and M. Jébrak (1996). "The Québec Antimony deposit: An example of gudmundite - native antimony mineralization in the Ophiolitic mélange of the Southeastern Québec appalachians". In: *Econ. Geol.* 91.1, pp. 149–163. DOI: `10.2113/gsecongeo.91.1.149`.

Obolensky, A.A., L.V. Gushchina, A.S. Borisenko, A.A. Borovikov, and P.A. Nevol'ko (2009). "Computer thermodynamic modeling of the transport and deposition of Sb and Au during the formation of Au-Sb deposits". In: *Russ. Geol. Geophys.* 50.11, pp. 950–965. DOI: `10.1016/j.rgg.2009.10.004`.

Obolensky, A.A., L.V. Gushchina, A.S. Borisenko, A.A. Borovikov, and G.G. Pavlova (2007). "Antimony in hydrothermal processes: solubility, conditions of transfer, and metal-bearing capacity of solutions". In: *Russ. Geol. Geophys.* 48, pp. 992–1001. DOI: `10.1016/j.rgg.200`.

Padilla, R., C.A. Rivas, and M.C. Ruiz (2008). "Kinetics of Pressure Dissolution of Enargite in Sulfate-Oxygen Media". In: *Metall. Mater. Trans. B* 39.3, pp. 399–407. DOI: `10.1007/s11663-008-9151-9`.

Pan, Y. and M.E. Fleet (1995). "The late Archean Hemlo gold deposit, Ontario, Canada: a review and synthesis". In: *Ore Geol. Rev.* 9.6, pp. 455–488. DOI: `10.1016/0169-1368(95)00003-K`.

Pokrovski, G.S. et al. (2006). "Antimony speciation in saline hydrothermal fluids: A combined X-ray absorption fine structure spectroscopy and solubility study". In: *Geochim. Cosmochim. Acta* 70.16, pp. 4196–4214. DOI: `10.1016/j.gca.2006.06.1549`.

Poujol, M. (1996). "3.07-2.97 Ga Greenstone Belt formation in the northeastern Kaapvaal Craton: Implications for the origin of the Witwatersrand Basin". In: *Econ. Geol.* 91, pp. 1455–1461.

Reich, M. et al. (2005). "Solubility of gold in arsenian pyrite". In: *Geochim. Cosmochim. Acta* 69.11, pp. 2781–2796. DOI: `10.1016/j.gca.2005.01.011`.

Ridley, J.R. and L.W. Diamond (2000). *Fluid chemistry of orogenic lode gold deposits and implications for genetic models.*

Ronde, C.E.J. de and M.J. de Wit (1992). “Shear Zone-Related , Au Quartz Vein Deposits in the Barberton Greenstone Africa : Field and Petrographic Characteristics , Fluid Properties , and Light Stable Isotope Geochemistry”. In: 87, pp. 366–402.

Schock, E.L. et al. (1997). “Inorganic species in geologic fluids: correlations among standard molal thermodynamic properties of aqueous ions and hydroxide complexes.” In: *Geochemica Cosmochim.* 61.5, pp. 907–950. DOI: `10.1017/CBO9781107415324.004`. arXiv: `arXiv:1011.1669v3`.

Schwarz-Schampera, U., H. Terblanche, and T. Oberthür (2010). “Volcanic-hosted massive sulfide deposits in the Murchison greenstone belt, South Africa”. In: *Miner. Depos.* 45, pp. 113–145. DOI: `10.1007/s00126-009-0266-y`.

Seal, R.R., E.J. Essene, and W.C. Kelly (1990). “Tetrahedrite and tennantite: Evaluation of thermodynamic data and phase equilibria”. In: *Can. Mineral.* 28, pp. 725–738.

Seal, R.R., R.A. Robie, P.B. Barton, et al. (1992). “Superambient heat capacities of synthetic stibnite, berthierite, and chalcostibite; revised thermodynamic properties and implications for phase equilibria”. In: *Econ. Geol.* 87.7, pp. 1911–1918. DOI: `10.2113/gsecongeo.87.7.1911`.

Seal, R.R., R.A. Robie, B.S. Hemingway, et al. (1996). “Heat capacity and entropy at the temperatures 5 K to 720 K and thermal expansion from the temperatures 298 K to 573 K of synthetic enargite (Cu3AsS4)”. In: *J. Chem. Thermodyn.* 28.4, pp. 405–412. DOI: `10.1006/jcht.1996.0040`.

Stefánsson, A. and T.M. Seward (2003a). “Stability of chloridogold(I) complexes in aqueous solutions from 300 to 600°C and from 500 to 1800 bar”. In: *Geochim. Cosmochim. Acta* 67.23, pp. 4559–4576. DOI: `10.1016/S0016-7037(03)00391-0`.

– (2003b). “The hydrolysis of gold(I) in aqueous solutions to 600°c and 1500 bar”. In: *Geochim. Cosmochim. Acta* 67.9, pp. 1677–1688. DOI: `10.1016/S0016-7037(02)01131-6`.

– (2004). “Gold(I) complexing in aqueous sulphide solutions to 500°C at 500 bar”. In: *Geochim. Cosmochim. Acta* 68.20, pp. 4121–4143. DOI: `10.1016/j.gca.2004.04.006`.

Sverjensky, D.A., E.L. Shock, and H.C. Helgeson (1997). “Prediction of the thermodynamic properties of aqueous metal complexes to 1000 degrees C and 5 kb.” In: *Geochim. Cosmochim. Acta* 61.7, pp. 1359–1412. DOI: `10.1016/S0016-7037(97)00009-4`.

USGS (2015). “Antimony — A Flame Fighter”. In: April, pp. 4–5.

Vearncombe, J.R. (1991). “A possible Archaean Island Arc in the Murchison Belt , Kaapvaal Craton , South Africa”. In: *J. African Earth Sci.* 13.3, pp. 299–304.

Vearncombe, J.R. et al. (1992). *Geology, Geophysics and mineralisation of the Murschison Schist Belt, Rooiwater Complex and Surrounding granitoids*. Geological. Department of Mineral and Energy affairs.

Vink, B.W. (1996). “Stability relations of antimony and arsenic compounds in the light of revised and extended Eh-pH diagrams”. In: *Chem. Geol.* 130.1-2, pp. 21–30. DOI: `10.1016/0009-2541(95)00183-2`.

Wagman, D.D. et al. (1982). *The NBS Tables of Chemical Thermodynamic Properties*.

Welham, N J (2001). “Mechanochemical processing of enargite (Cu3AsS4)”. In: *Hydrometallurgy* 62, pp. 165–173.

Whitmore, D.R.E., L.G. Berry, and J.E. Hawley (1946). “Chrome Micas”. In: *J. Am. Mineral.* 31.1-2, pp. 1–21.

Williams-Jones, A.E., R.J. Bowell, and A.A. Migdisov (2009). “Gold in solution”. In: *Elements* 5.5, pp. 281–287. DOI: `10.2113/gselements.5.5.281`.

Williams-Jones, A.E. and C. Norman (1997). “Controls of mineral parageneses in the system Fe-Sb-S-O”. In: *Econ. Geol.* 92.3, pp. 308–324. DOI: `10.2113/gsecongeo.92.3.308`.

Wolery, T.J. and C.F. Jove-Colon (2004). *Qualification of Thermodynamic Data for Geochemical Modeling of Mineral-Water Interactions in Dilute Systems*. Tech. rep. November. Bechtel SAIC, pp. 1–212. DOI: `10.2172/850412`.

Yund, R.A. (1962). “The system NiAsS phase relations and mineralogical significance.pdf”. In: *Am. J. Sci.* 260, pp. 761–782.

Zeh, A. et al. (2013). “Juvenile crust formation in the northeastern Kaapvaal Craton at 2.97Ga—Implications for Archean terrane accretion, and the source of the Pietersburg gold”. In: *Precambrian Res.* 233, pp. 20–43. DOI: `10.1016/j.precamres.2013.04.013`.

CHAPTER 5

Geochemical modeling insight into Sb-As-Au-Ag mineralization at the PacManus basin, Papua New Guinea

NIKKI BLAAUWBROEK[1], MICHAEL HENTSCHER[1], SVEN PETRERSEN[2], WOLFGANG BACH[1]

[1] Department of Geosciences and MARUM – Center for Marine Environmental Sciences,
University of Bremen, Klagenfurter Str., 28359 Bremen, Germany
[2] Geomar Helmholtz-Zentrum für Ozeanforschung Kiel,
Wischhofstrasse 1-3, 24148 Kiel, Germany

Keywords: auriferous VMS, back-arc basin, antimony, PACManus

Abstract

The tectonic and petrological characteristics of the East Manus Basin (EMB), and the PACManus hydrothermal area on the dacitic Pual Ridge make it a useful analog for land-based auriferous VMS ore mineralizations. Unlike black smoker systems on mid-ocean ridges, these arc- and back-arc-systems are influenced strongly be magma degassing, which has major consequences for the transport of elements like Sb, As, Ag, and Au. In this study, geochemical data of solids and fluids from the PACManus hydrothermal area in the Manus back-arc basin are used to examine the controls of host rock composition, magma degassing, zone refining, and supergeneous processes in the distribution of these elements in the massive sulfide. Geochemical modeling has been employed to assess the consequences of fluid mixing, conductive cooling/heating, and zone refining. The model results are compared with the variability observed in the compositions of vent fluids and solids to identify common processes in subseafloor fluid mixing and fluid-rock interactions and investigate their importance for seafloor massive sulfide deposits. This study contributes robust geochemical constraints related to enrichments of Sb, As, Au and Ag, in relation to other metals, like Zn and Cu, and thus provides a start for understanding geochemical behavior between different metals and their corresponding relationship between the (altered) oceanic crust and active hydrothermal venting.

5.1 Introduction

Volcanogenic massive sulphide (VMS) deposits are commonly enriched in Cu, Zn and Pb and can also be variably enriched in Au, As, Sb and Ag (Herzig and Hannington, 1995; Patten et al., 2016). Although the apparent diversity and corresponding complexity, the gold-enriched VMS deposits was not in the least short in attention throughout the past from for instance mining companies (e.g. Hannington, De Ronde, et al. (2005) and Mercier-Langevin et al. (2011)). Gold-rich VMS deposits are important targets for the mining industry (Mercier-Langevin et al., 2011) and are found on a diverge range of oceanic and continental geological settings; from fast to slow spreading mid ocean ridges; in sedimented rifts adjacent to continental margins and in subduction related back-arc environments (Herzig and Hannington, 1995). (Auriferous) VMS deposits are known for their complex mineral paragenesis, commonly associated with Cu-Zn-Pb mineralization (Hannington, Poulsen, et al., 1999; Mercier-Langevin et al., 2011), and at back-arc environments at high temperatures includes pyrrhotite, pyrite/marcasite, sphalerite/wurzite, chalcopyrite, bornite and may contain galena, Pb-As-Sb sulfosalts, realgar, orpiment and locally native gold with trace element enrichments of As, Sb, Ba, Te and In (Herzig and Hannington, 1995; Moss and S. Scott, 2001; Patten et al., 2016).

Understanding the geochemical behavior of Au, Ag, As and Sb is interesting and increasingly important for both oceanic and continental mining prospects, while precious metal contents of seafloor sulfides are well within range of those found in land based deposits (Herzig and Hannington, 1995; Moss and S. Scott, 2001; Mercier-Langevin et al., 2011). However, until recently, no specific attention has been given to this specific group within these a range of gold deposits and their possible relationship with one another and one can conclude that the geochemical behavior is thus not well understood

(Douville et al., 1999; Craddock, 2009; Patten et al., 2016). Nevertheless, recent published studies, such as Patten et al. (2016) and Dekov et al. (2016) indicate an increase in interest and consequently an increased necessity in understanding the geochemical behavior of polymetallic mineralization.

5.1.1 Sb, As, Au and Ag enrichment in arc and back-arc settings

The coupling between magmatic and hydrothermal processes is perhaps most impressive in suprasubduction systems, where volatile-rich melts are segregated from a mantle wedge that is heavily flux-modified by slab-derived fluids (Hedenquist and Lowenstern, 1994; Richards, 2011). Degassing of magmatic fluids has been demonstrated to take place in these systems and strongly affect the geochemical processes in hydrothermal vents hosted in the arc volcanoes (Ronde, 1995; Ronde et al., 2001) and in the PACManus system in the Manus back-arc basin (Kamenetsky et al., 2001; K.H. Yang and S. Scott, 1996; K Yang and S. D. Scott, 2006). On a global scale, arc systems are responsible for about 10% of the hydrothermal fluid flux, the remainder being associated mostly with mid-ocean ridge processes (Baker et al., 2008). But because fluids venting from arc volcanoes are enriched in elements such as As, Sb, Tl, Al, Ag, Au, Zn, Pb, Bi and gases (in particular SO_2 and CO_2), the suprasubduction zone systems play an important, yet largely unconstrained, role in global mass transfers between lithosphere and the oceans. Fluid inclusion studies indicate high levels of metals in trapped magmatic vapors and support the idea that magma degassing can deliver metals directly to the overlying hydrological system (Heinrich, Günther, et al., 1999; Heinrich, Driesner, et al., 2004).

Thus far, studies laying the empirical (field) and theoretical (modeling) foundation of this hypothesis are missing, in particular for submarine volcano-hosted hydrothermal systems. Au, Au, As and Sb exhibit a wide range of (geo)chemical behavior(s) that could provide important constraints in subseafloor hydrothermal processes (Craddock, 2009). However previous studies have mainly focused on hydrothermal systems along basalt-dominated MOR spreading centers (Craddock (2009) and references therein; Patten et al. (2016)), despite the fact that increased concentrations of precious metals like Au and Ag, and metalloids like As and Sb at back-arc spreading centers have been observed, relative to their mid-ocean ridge (MOR) vent deposit counterparts (Herzig and Hannington, 1995; Douville et al., 1999; Hannington, Poulsen, et al., 1999; Moss and S. Scott, 2001; Craddock, 2009). Although the overall enrichments of Zn, Pb, As, As, Ag Au and Ba have been generally attributed to seawater-rock interaction within felsic host rock (S. Scott and Binns, 1995), a magmatic origin for these elements has also been proposed (Gamo et al., 1997; Douville et al., 1999). It was realized that some of the extreme enrichments in these elements relative to the felsic host rocks (Stanton, 1994) are unlikely to result from leaching from host rocks alone (Ishibashi et al., 2008; Hannington, Jonasson, et al., 1995; M. Tivey, 2007). It has even been suggested that Sb, together with As, Pb and Zn, could be used as a (felsic) magmatophile trace element (Boyle and Jonasson, 1984; Binns, 2004; Henley and Berger, 2013).

This paper focuses on the PACManus hydrothermal vent area, in the Manus back-arc basin, Bismarck-Sea, Papua New Guinea (Figure 1) where As and Sb contents have been measured in the vent fluids that are 10 to 100 fold higher than in typical MOR fluids (Douville et al., 1999). Likewise, the VMS accumulations at PACManus are enriched in As, Sb, Ag, and Au (Binns and S. Scott, 1993; Moss and S. Scott, 2001), but details of the trapping mechanisms for these metals are unknown. Sulfides chimneys are often zoned and mineralogically complex due to highly variable processes of conductive cooling of hydrothermal vent fluids, conductive heating of seawater, and mixing of the two fluids with variable extents of concomitant cooling or heating (e.g., Hannington, Jonasson, et al. (1995)). These structures collapse with time and hydrothermal sulfide mounds build up. Within these mounds, previously formed sulfides react with mixed seawater-vent fluids that undergo conductive cooling. This process of zone refining leads to precipitation of some minerals (e.g., pyrite) and dissolution of others (e.g., sphalerite) (M.K. Tivey, 1995). Finally, supergeneous enrichment of As, Sb, Ag, and Au are commonly observed and are explained by remobilization of these elements inside the mound followed by precipitation of them in the topmost part of the mound, where seawater-derived fluids reside within the void spaces of the rubbly pile.

We are using geochemical modeling to systematically examine the behavior of As, Ab, Ag, and Au in these different processes. We will attempt to identify the roles of subseafloor entrainment of seawater and mixing with upwelling hydrothermal fluids under different extents of conductive heating and cooling to identify which scenarios lead to an enrichment in these elements in the primary sulfide structures. We will furthermore investigate the role of zone refining and supergenous processes in causing some of the specific replacement textures and element enrichments observed in the VMS materials from the PACManus hydrothermal area. The main motivation for this study is to try to understand the geochemical behavior of Au, Ag, Sb and As in hydrothermal seafloor settings, through a in depth comparison between fluid samples and whole rock samples, taken at several PACManus hydrothermal vent sites, with a reaction path model. The goal of this study is to demonstrate that these elements can provide important limitations on subseafloor hydrothermal processes in general and for auriferous VMS deposits. Due to the constrained tectonic characteristics of the East Manus Basin (EMB), the PACManus hydrothermal field can be considered as a rough analogy for a land-based VMS ore body, hence increasing knowledge of the PACManus hydrothermal system could play an important role in understanding and assessing VMS prospects.

5.2 Regional background hydrothermal system PACManus

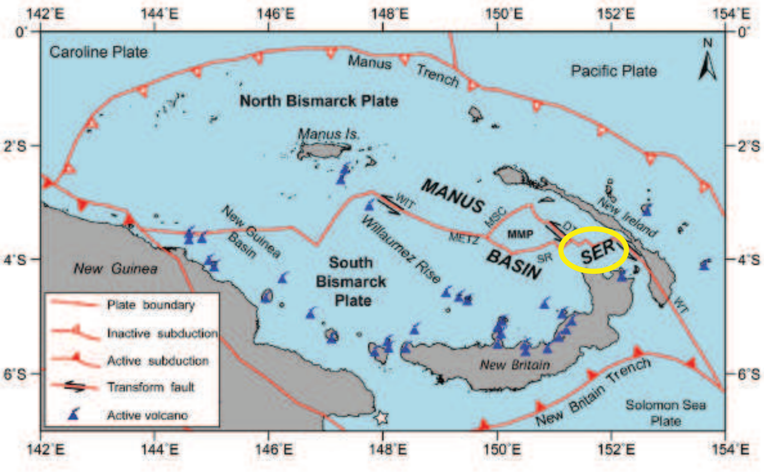
142°E
144°E
146°E
148°E
150°E
152°E
154°E
0°
2°S
4°S
6°S
Caroline Plate
Manus Trench
Pacific Plate
North Bismarck Plate
Manus Is.
MANUS
BASIN
WIT
MSC
METZ
MMP
DT
SER
SR
New Ireland
WT
New Guinea Basin
Willaumez Rise
South Bismarck Plate
New Guinea
New Britain
New Britain Trench
Solomon Sea Plate
Plate boundary
Inactive subduction
Active subduction
Transform fault
Active volcano
N

(a) Tectonics at the Manus Basin, Papua New Guinea (Thal et al., 2014). Abbreviations: WT= Weitin Transform; DT= Djaul Transform; WIT= Willaumez Transform; METZ= Manus Extensional Transform Zone; SR= Southern Ridges; MMP= Manus Microplate; SER= Southeast Ridges; MSC= Manus Spreading Centre; Star= Absolute Pole of South Bismarck Plate Rotation.

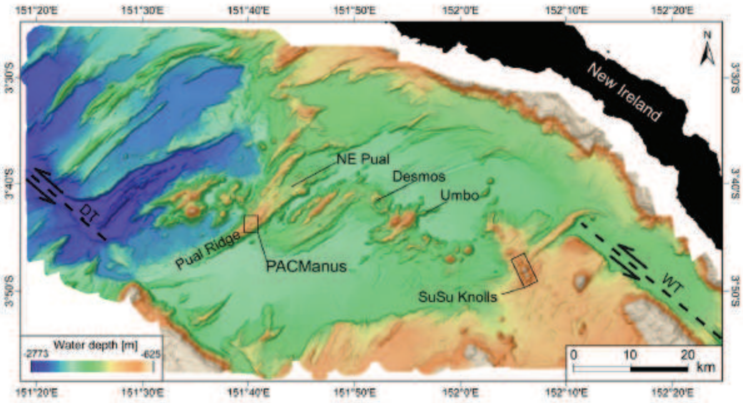
151°20'E
151°30'E
151°40'E
151°50'E
152°0'E
152°10'E
152°20'E
3°30'S
3°40'S
3°50'S
New Ireland
NE Pual
Desmos
Umbo
DT
Pual Ridge
PACManus
SuSu Knolls
WT
Water depth [m]
-2773
-625
0
10
20
km
N

(b) Multibeam bathymetry map of South Eastern Ridges (SER) region in the Eastern Manus Basin (EMB), showing PACManus on top of the Pual Ridge. WT = Weitin Transform; DJ = Djaul Transform. SuSu Knolls = South Su and North Su Knolls. Data recorded on BAMBUS - R/V Sonne 216 Cruise 2011 (Thal et al., 2014)

Figure 5.1:

fig:chpt5$_{f}ig1$

The Manus basin is located in the Bismarck Sea and is a fast oblique opening back-arc basin, associated by subduction of the Solomon Sea Plate at the New Britain Trench (Figure 5.1a) (Binns and S. Scott, 1993; Martinez and Taylor, 1996; Thal et al., 2014). Crustal rifting and spreading occurs along the Extensional Transform Zone (ETZ), Manus Spreading Center (MSC) and the EMB (Martinez and Taylor, 1996). The EMB, a pull apart basin, is located along the South Eastern Ridges (SER), a series of en echelon volcanic ridges that are bounded by two transform faults, Weitin Transform (WT) and Djaul Transform (DT) (Binns and S. Scott, 1993; Martinez and Taylor, 1996). The arc-volcanism is characterized by volcanic cones, with basalt and (acidic) andesite-to-rhyolitie composition (Binns and S. Scott, 1993; Hannington, De Ronde, et al., 2005). The PACManus hydrothermal field, which lies at the height of the Pual Ridge (Figure 5.1b) (Binns and S. Scott, 1993), an elongated ridge of 35 km composed of stacked lava flows of dacite with basaltic andesite and rhyodacite composition that stands 500-700 m above the surrounding seafloor (Binns and S. Scott, 1993; Binns, Barriga, et al., 2007; Beier et al., 2015). The PACManus hydrothermal system is distinguished by elevated Au, Ag, Pb, As, Sb contents within polymetallic sulfides (Douville et al., 1999; Moss and S. Scott, 2001; Binns, Barriga, et al., 2007; Craddock, 2009). The Sb-As-Ag-Au enrichment has been interpreted as a result of deep-seated seawater-rock interaction, magmatic input and near seafloor sulfide deposition and reworking (Douville et al., 1999; Craddock, 2009), and shows a positive correlation with Au within sulfur-rich samples (Moss and S. Scott, 2001). Gold occurs in copper-rich chimneys as inclusion in chalcopyrite associated with sulfosalts, bornite and covellite. And in zinc-rich chimneys as in inclusions in tennantite associated with chalcopyrite and Fe-poor sphalerite (Moss and S. Scott, 2001).

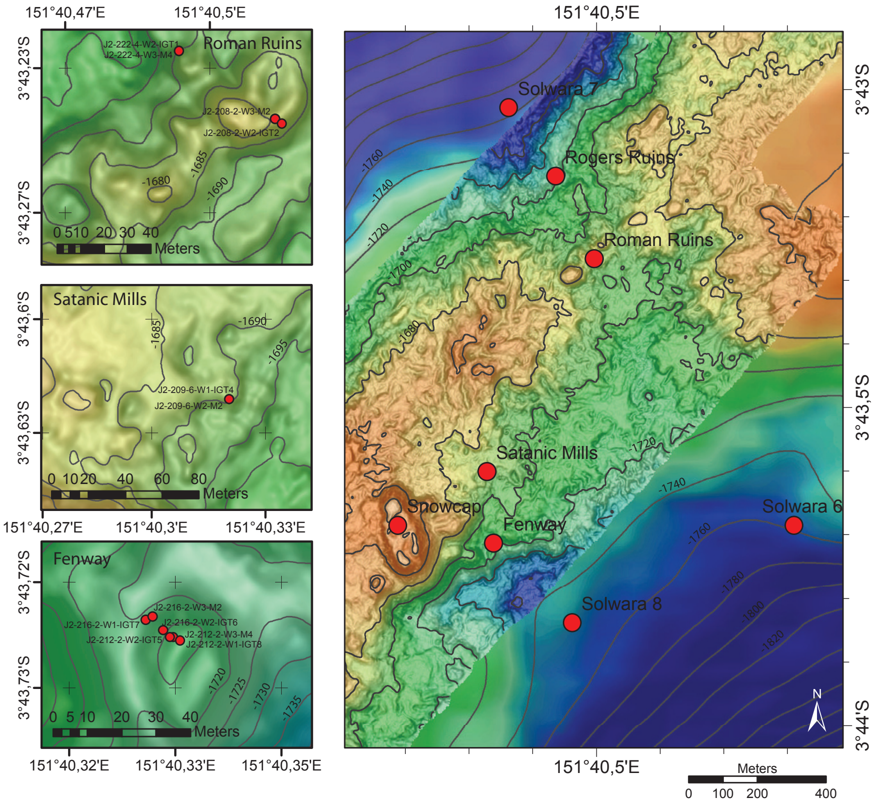
151°40,47'E
151°40,5'E
3°43,23'S
3°43,27'S
Roman Ruins
J2-222-4-W2-IGT1
J2-222-4-W3-M4
J2-208-2-W3-M2
J2-208-2-W2-IGT2
-1680
-1685
-1690
0 510 20 30 40
Meters
Satanic Mills
3°43,6'S
3°43,63'S
-1685
-1690
-1695
J2-209-6-W1-IGT4
J2-209-6-W2-M2
0 10 20 40 60 80
Meters
151°40,27'E
151°40,3'E
151°40,33'E
Fenway
3°43,72'S
3°43,73'S
J2-216-2-W3-M2
J2-216-2-W1-IGT7
J2-216-2-W2-IGT6
J2-212-2-W3-M4
J2-212-2-W2-IGT5
J2-212-2-W1-IGT8
-1720
-1725
-1730
-1735
0 5 10 20 30 40
Meters
151°40,32'E
151°40,33'E
151°40,35'E
151°40,5'E
3°43'S
3°43,5'S
3°44'S
Solwara 7
Rogers Ruins
Roman Ruins
Satanic Mills
Snowcap
Fenway
Solwara 6
Solwara 8
-1760
-1740
-1720
-1700
-1680
-1720
-1740
-1760
-1780
-1800
-1820
N
Meters
0 100 200 400

Figure 5.2: Detailed AUV ABE multibeam bathymetry map of Pual Ridge. The fluid samples are presented as red dots on the primary PACManus hydrothermal fields Fenway, Satanic Mills and Roman Ruins.

5.2.1 Prominent vent sites located at PACManus site

Several principal areas of hydrothermal venting have been identified at the PACManus site on the Pual Ridge in a 2.5 km^2 area centered in 1640 to 1780 m water depth (Figure 5.2) (Bach, Rosner, et al., 2011): Romain Ruins, Roger Ruins, Satanic Mills, Fenway, Snowcap, Solwara 6-8 and Tsukushi (Binns, Barriga, et al., 2007; Bach, Rosner, et al., 2011; Reeves et al., 2011). They consist of active and inactive black smoker chimneys and spires on sulfide mounds, where fluids escape as acid (pH between 2.5-3.8) and temperatures up to 341 °C (Reeves et al., 2011). We refer to Thal et al. (2014) for a detailed account of the vent fields and potential structural and magmatic controls of the different vent sites in the PACManus hydrothermal area.

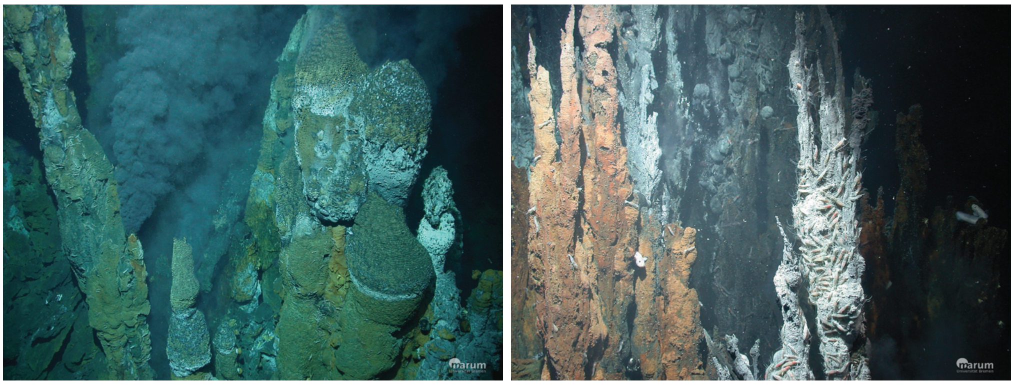

(a) PACManus, Fenway **(b)** PACManus, Roman Ruins

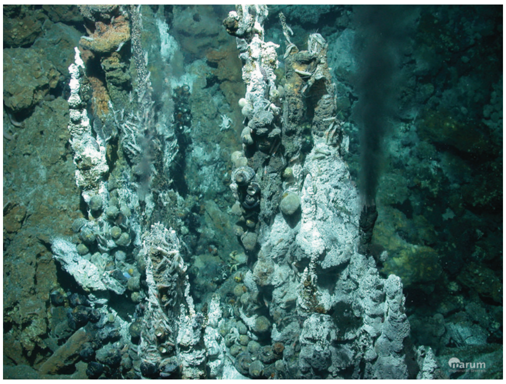

(c) PACManus, Satanic Mills

Figure 5.3: Photographs at the Bambus cruise (2011) (Bach et al., 2011).

Fenway The hydrothermal field Fenway has been newly discovered in 2006 and is comprised of an anhydrite-hosted black smoker complex, called Big Papi, two small chimney clusters and diffuse venting on the flanks of the mound (Bach, Rosner, et al., 2011; Reeves et al., 2011). At the summit of Fenway a black smoker chimney complex was found with temperatures up to 358 °C (Figure 5.3a) (Reeves et al., 2011). Fenway is Au poor, and low in magma-volatile elements, with some traces of Ag within the sulfides (See Appendix X).

Roman Ruins The Roman Ruins site is a long-lived system with a large sulfide mound, made up of large (up to 20 meters and 3 in diameter) predominantly inactive chimneys (Figure 5.3b) (Moss and S. Scott, 2001; Bach, Rosner, et al., 2011), and is classified together with Roger Ruins as a ‘pure beehive’ system (Bach, Rosner, et al., 2011). The central part is covered in sulfide chimney rubble, while on the south side predominantly volcanic rock talus with moderate hydrothermal activity with low H_2S contents is present. Fe-oxyhydroxide deposits that occasionally form chimneys are found in the Roman Ruins area (Bach, Rosner, et al., 2011). Overall low values of Au, Ag, Sb and As were detected in the sulfides, mainly due to absence of tennantite (As-sulfosalt). Au is predominantly located in sphalerite (See Appendix X).

Satanic Mills Abundant clusters of sulfide chimneys characterize Satanic Mills, where they are growing directly on top of fresh dacitic block lava (Thal et al. 2014). Fluids have high temperatures, between 339-345 °C and overcritical venting CO_2 fluid is observed (Figure 5.3c) (Moss and S. Scott, 2001; Bach, Rosner, et al., 2011). Overall high, though varying, Cu-grade is measured (Moss and S. Scott, 2001). Magmatic elements such as Bi, In and Te as well as high As, Hg, Sb and Sn are detected (See Appendix X).

Snowcap The hydrothermal activity at Snowcap mostly comprises low temperature diffuse venting through volcaniclastic sediments (Moss and S. Scott, 2001; Bach, Rosner, et al., 2011; Reeves et al., 2011). The chimney’s are variably Cu- and Zn-rich, although vent hydrothermal fluids reach only a maximum 224 °C. On top of the Snowcap knoll, countless diffuse fluid seepage is observed (Bach, Rosner, et al., 2011). As, Bi, Sn and Te are barely present, however In, Sb and Au are remarkably enriched within the sulfides. Gold is dominantly associated with chalcopyrite, primary bornite and secondary veins of digenite (See Appendix X).

Solwara 8 The Solwara 8 vent site lies southeast of Big Papi and is build up of chimney clusters up to 12 m high. Two sets of chimneys are distinguished: the first one being spiry (2-3 cm in diameter) and Cu-rich (up to 40 wt.%); the second one porous, larger in diameter and Zn-rich (Bach, Rosner, et al. (2011); See Appendix X). Cu-enrichment is mainly represent by primary bornite-digenite-tennantite formation together with primary chalcopyrite. Au, As and Ag concentrations are high (See Appendix X).

5.3 Materials and Methods

The fluid and solid compositions used in this study come from multiple sources. The sample materials were retrieved during R/V Melville cruise MGLN06MW (July to September, 2006) and R/V Sonne cruise SO216 (June-August, 2011). In both cruises, the samples were retrieved from the seafloor by remotely operated vehicles (ROVs): WHOI's Jason2 ROV in 2006 and MARUM's Quest4000 ROV in 2011. The cruise reports M. Tivey et al. (2006) and Bach, Rosner, et al. (2011) give detailed information about the goals and initial results of the cruises. Fluid compositions from the 2006 cruise were analyzed by Eoghan Reeves, Paul Craddock, and Jeff Seewald and are published in Reeves et al. (2011), Craddock (2009), Craddock and Bach (2010) and Seewald, Reeves, et al. (2015).

The samples were collected in 755 ml Ti–syringes samplers (Damm et al., 1985) and in 160 ml isobaric gas–tight samplers (Seewald, Doherty, et al., 2002). In all cases, fluids were sampled in triplicate allowing an assessment of uncertainties and calculation of end–member fluid compositions (i.e., extrapolated to zero Mg (Damm et al., 1985)). For the fluids from the PACManus hydrothermal area, these triplicates gave consistent Mg concentrations that were significantly above zero. We did hence not extrapolate fluid end-member compositions to zero Mg, which is commonly done for vent fluids from mid-ocean ridges (Damm et al., 1985). This was avoided for the acidic fluids from the Manus back-arc basin, because the assumption of minimal Mg-solubility in vent fluids is not valid form pH<3 fluids. Venting temperatures were measured with either the ROV T–probe or with a thermocouple mounted directly on the sampler. Solid samples were collected during both cruises by ROV operations in water depths between 1600 and 1800 m water depth. The rocks were rinsed in fresh water, dried and cut by a tile saw. Aliquots of the cut slabs were used for the preparation of thin sections, while opposite pieces were crushed in an agate shatter box for whole rock analyses. The rock powders were analyzed by ACTLAB, a commercial lab that has specialized in whole rock analyses of ore materials, including sulfides. The data is reported by Craddock (2009) and Sven Petersen at GEOMAR (unpublished report to Nautilus Minerals (Appendix)). Elements analyzed comprise Fe, Mn, Cu, Zn, Pb, S, Ba, Sr, Si, Co, Se, Mo, Cd, As, Sb, Ag, and Au. From the total sulfur contents, sulfate concentrations were calculated by assuming that all Ca and Ba in the rocks are tied to anhydrite and barite, respectively. Sulfide concentrations were then calculated from the difference between total S and S tied to sulfate. The data was used to calculate the mineralogical mode of the sulfide samples, assuming that they are composed of pyrite, anhydrite, barite, amorphous silica, sphalerite, galena, chalcopyrite, bornite, digenite, hematite, tennantite. The EXCEL Solver was used to solve these mass balance problems. All data are listed in the electronic appendix of this thesis.

Thermodynamic modeling was conducted using the Geochemist's Workbench software package and tailor-made (SUPCRT92; Johnson et al. (1992)) thermodynamic databases for 250 bar and temperatures between 0 and 350 °C. The database is otherwise identical in structure to the 1kbar-database used in chapters 3 and 4. It includes

112 aqueous species and 110 minerals. Data for major rock-forming minerals were taken from Wolery and Jove-Colon (2004). Data for major solutes are from Sverjensky et al. (1997) and Schock et al. (1997). These data were supplemented by data for Sb, As and Au minerals as well as aqueous HS^-, OH^- and Cl^- species of these elements from various sources, while maintaining internal consistency (Yund, 1962; Lynch, 1982; Wagman et al., 1982; Krupp, 1988; Seal, Essene, et al., 1990; Seal, Robie, Barton, et al., 1992; Vink, 1996; Seal, Robie, Hemingway, et al., 1996; Williams-Jones and Norman, 1997; Welham, 2001; Kantar, 2002; Stefánsson and Seward, 2003b; Stefánsson and Seward, 2003a; Stefánsson and Seward, 2004; Bessinger and Apps, 2005; Castro and Baltierra, 2005; Pokrovski et al., 2006; Padilla et al., 2008; Akinfiev and Zotov, 2010; Firdu and Taskinen, 2010).

The goal of the modeling was threefold:

1. Construct T-X sections for the major vent sites at PACManus to map out which phase assemblages are thermodynamically stable in specific regimes of seawater entrainment and mixing with upwelling hydrothermal fluids.

2. Calculate speciation and solubilities for Sb, As, Ag, and Au along specific mixing paths to examine the potential reasons behind similar or dissimilar geochemical behavior of these elements in the PACManus mineralization system.

3. Execute complex reaction path models to simulate the evolution of seafloor massive sulfide deposits in the critical stages of (i) mound-building, (ii) zone refining within the mound, and (iii) supergeneous enrichment of certain elements in the outmost parts of the mound.

A common workflow of modeling the VMS forming processes starts with the speciation of the measured vent fluid compositions (from Reeves et al. (2011) and Craddock and Bach (2010)) using the pH values measured after sampling in the laboratory (pH at 25 °C). This speciated fluid was then heated up to in situ temperatures, measured upon sampling of the fluids (M. Tivey et al., 2006; Bach, Rosner, et al., 2011). This step will speciate the fluid to ambient conditions inside the vent orifice from which it was collected. The pH of the fluid determined in this step is the in situ pH. Determining this in situ pH is critical for assessing element solubility in vent fluids. Likewise, it is critical to know the redox conditions of the fluids. Concentrations of dihydrogen (H_2,aq) from Reeves et al. (2011) were used to compute the fugacity of oxygen in the fluids. These fluids were then mixed with ambient seawater, while assuming different extents of conductive cooling or heating, respectively, to map out phase relations in T-X plane for the three main vent sites at PACManus: Roman Ruins, Fenway, and Satanic Mills. The speciation and solubilities of As, Sb, Ag, and Au were examined along two specific mixing/cooling paths (isenthalpic cooling of the vent fluid by mixing with seawater, and pure conductive cooling without mixing with seawater). In the complex reaction modeling, we use the fluid end-member with seawater (4 °C) (Table 5.2) in a 1 to 9 ratio to produce the minerals that make the chimney mound material. We then mix the vent fluid end-member with seawater in a 1 to 0.1 ratio, while cooling the system to 275 °C A temperature of 275 °C was chosen because it is commonly observed in PACManus vent fluids that show geochemical evidence of subseafloor entrainment of seawater (Reeves et al., 2011). In the following step, this 275 °C fluid is reacted with the precipitate produced in the earlier run, while keeping the temperature at 275 °C. This step simulates the mobilization of elements upon mixing between vent fluid and entrained seawater within the mound (zone refining). The resulting fluid is then mixed with seawater in a 1 to 9 ratio to simulate what should get precipitated on top of the mound upon mixing between the zone-refined fluid and seawater. This last step simulates the precipitation of minerals in the supergeneous zone and examines the enrichment of Sb, As, Ag, and Au in these processes.

5.4 Results

Increased contents of Sb, As, Au and Ag are restricted to black smoker systems from felsic basement in the Manus basin: PACManus and South Su (Figure 5.1b). Acid-sulfate vents (DESMOS and North Su) and the basalt-hosted Vienna Woods vent field have, by comparison, exceedingly low Sb and As contents (Craddock, 2009). Therefore the main focus will lie on the hydrothermal sites of PACManus for fluid samples and modeling results.

5.4.1 Fluids samples

The hydrothermal venting sites of Fenway, Roman Ruins and Satanic Mills were repeatedly sampled in 2006 and there are complete analyses of several fluid and solid samples available from each of these sites. The location of the fluid samples is shown in Figure 5.2 and they will be the main point of focus for the reaction path modeling, the methods of which were outlined in Section 5.3. Those three sites were selected, based on their prominent character in the PACManus area; additionally they represent the wide spectrum of fluid compositions of the PACManus, interpreted by Reeves et al. (2011). Overall the fluids measured at these sites are between 241 and 380 °C and they range from 2.6 to 3.9 in pH at 25 °C (Table 5.1), with one exception at Fenway (5) where 78 °C and pH of 4.9. The concentration of Sb, As, Au and Ag as well as Fe, Cu and Zn are plotted against temperature and in situ pH in Figure 5.4. Overall As is dominantly enriched within the fluid samples, with concentrations of Sb, Ag and Au in the order

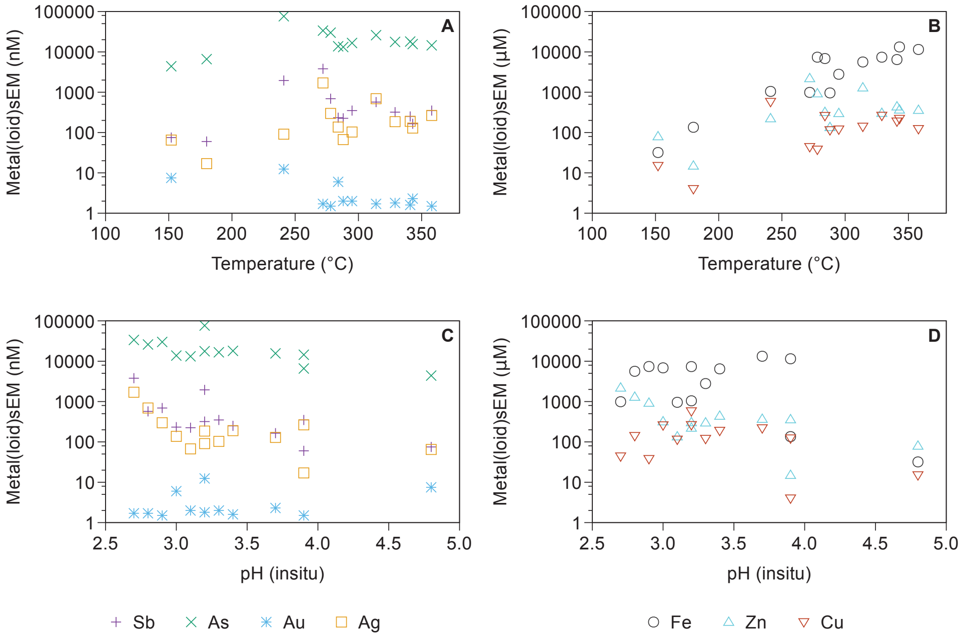

Figure 5.4: In situ Sb, As, Au and Ag, as well as Fe, Zn and Cu concentrations in fluid samples of Fenway, Roman Ruins, Snowcap and Satanic Mills (Craddock, 2009).

of decreasing abundance. Au contents in the fluids lie for Fenway, Satanic Mills and Roman Ruins between 1.5 and 12.4 nM; those of Ag span from 25 to 1700 nM, Sb concentration are between 99 and 3800 nM and As from 132 to 336 µM. It is apparent in Figure 5.4a and c, that two different peaks can be recognized: a primary peak for all elements at 270 °C and a secondary peak at 310 °C. Fe, Cu and Zn show a general trend of increasing concentrations with increasing temperatures. However, a small peak could be discriminated around 270 °C, in particular for Zn. A coinciding peak for Sb, As, Au and Ag can also be recognized in Figure 5.4c, at a pH of 2.7, which is also noticeable for Zn, though not for Fe and Cu (Figure 5.4d). The tight relationships between the four elements are surprisingly strong; when one element is enriched within a fluid sample, the concentration of the other three are conjointly high.

Table 5.1: Fluid samples from Craddock (2009) with the focus on precious metals and metalloids Sb, As, Au and Ag.

					Mg	**Fe**	**Zn**	**Cu**	**Sb (nM)**	**As (nM)**	**Au (nM)**	**Ag (nM)**
	Sample	Temperature (°C)	pH (25°C)	pH (in situ)	mM	µM	µM	µM	nM	µM	nM	nM
RMR1	J2-208-1-W2-IGT5	314	2,3	2,8	8,0	5619	1300	141	570	26,0	1,7	690
RMR2	J2-208-2-W2-IGT2	272	2,3	2,7	16,5	990	2200	44	3800	33,6	1,7	1700
RMR3	J2-213-3-W1-IGT7	278	2,5	2,9	6,4	7385	927	38	690	30,0	1,5	298
RMR4	***J2-222-4-W2-IGT1***	***341***	***2,6***	***3,4***	***3,2***	***6468***	***440***	***190***	***250***	***18,0***	***1,6***	***190***
S.M.1	***J2-209-1-W1-IGT6***	***295***	***2,6***	***3,3***	***8,8***	***2790***	***300***	***120***	***350***	***16,6***	***2,0***	***103***
S.M.2	J2-209-6-W1-IGT4	241	2,4	3,2	17,4	1045	223	580	1950	76,5	12,4	91
S.M.3	J2-214-3-W2-IGT5	288	2,5	3,1	10,1	960	135	115	225	13,2	2,0	67
SC1	J2-210-1-W2-IGT5	152	4,6	4,8	31,0	32	80	15	75	4,4	7,5	65
SC2	J2-211-9-W1-IGT4	180	3,4	3,9	24,0	135	15	4	60	6,6	0,4	17
FW1	J2-210-7-W2-M4	329	2,5	3,2	5,8	7373	304	263	320	17,7	1,8	186
FW2	***J2-212-2-W2-IGT5***	***343***	***2,7***	***3,7***	***4,7***	***13263***	***368***	***220***	***165***	***15,6***	***2,3***	***129***
FW3	J2-212-6-W1-IGT2	358	2,7	3,9	4,5	11500	360	123	350	14,5	1,5	265
FW4	J2-216-2-W2-IGT6	284	2,4	3,0	9,4	6850	320	260	233	13,8	6,0	137
FW5	J2-216-5-W1-IGT4	78	5,0	4,9	44,7	600	50	9	99	-	-	25

*Abbrevations: RMR: Roman Ruins; SM: Satanic Mills; FW: Fenway.

The bold and italic marked rows are end-member vent sites and are therefor used as input for the reaction path modeling.

Aqueous species are extrapolated to in situ Mg.

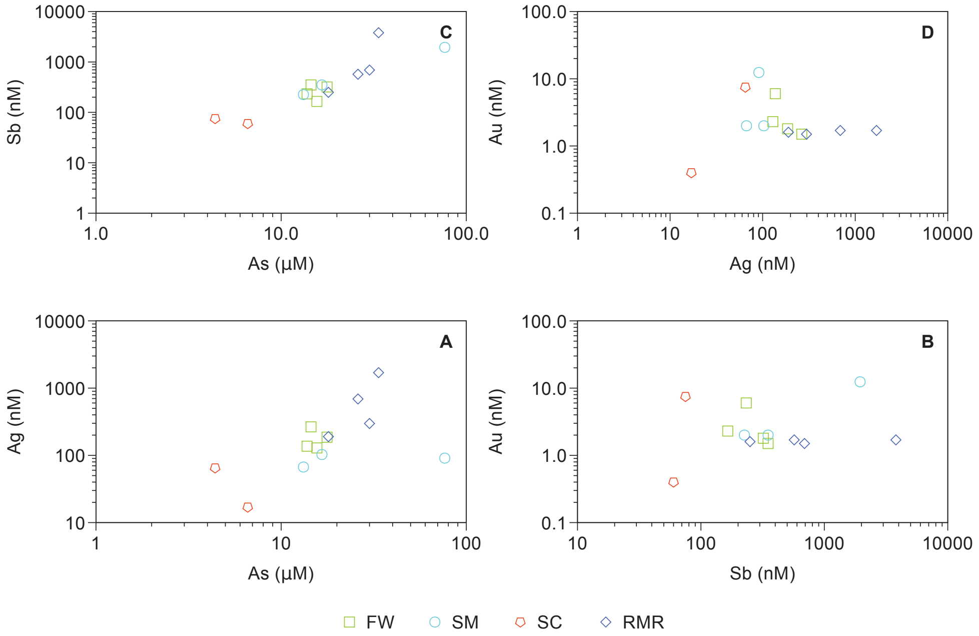

Figure 5.5: Fluid samples of Vienna Woods (VW), Roman Ruins+Roger Ruins (RMR), Satanic Mills (SM), Snowcap (SC) and Fenway (FW) showing positive correlations between Ag and As, Au and Sb in comparison with the positive correlations of Sb and As as well as Au and Ag (Craddock, 2009).

This strong relationship between Sb, As, Au and Ag is also recognizable in Figure 5.2, where their contents from fluid samples of Fenway (FW), Roman Ruins (RMR), Satanic Mills (SM) and Snowcap (SC) are plotted against each other. A clear positive correlation, among every site separately and combined, can be observed between Sb with Au and Ag with As. These correlations are comparable to the acknowledged related Sb-As and Au-Ag. Additionally, every element is separately plotted versus temperature in Figure 5.6 and Figure 5.7 to provide a more detailed synopsis. Figure 5.6a shows a positive correlation between pH and temperature at Roman Ruins, Fenway and Satanic Mills and not at Snowcap. Roman Ruins system shows an increase in Zn as T and pH drop (Figure 5.6b). At Fenway and Satanic Mills, Zn is not mobilized. Fenway shows some increase in Cu and Satanic Mills shows strong enrichment in Cu in one instance.

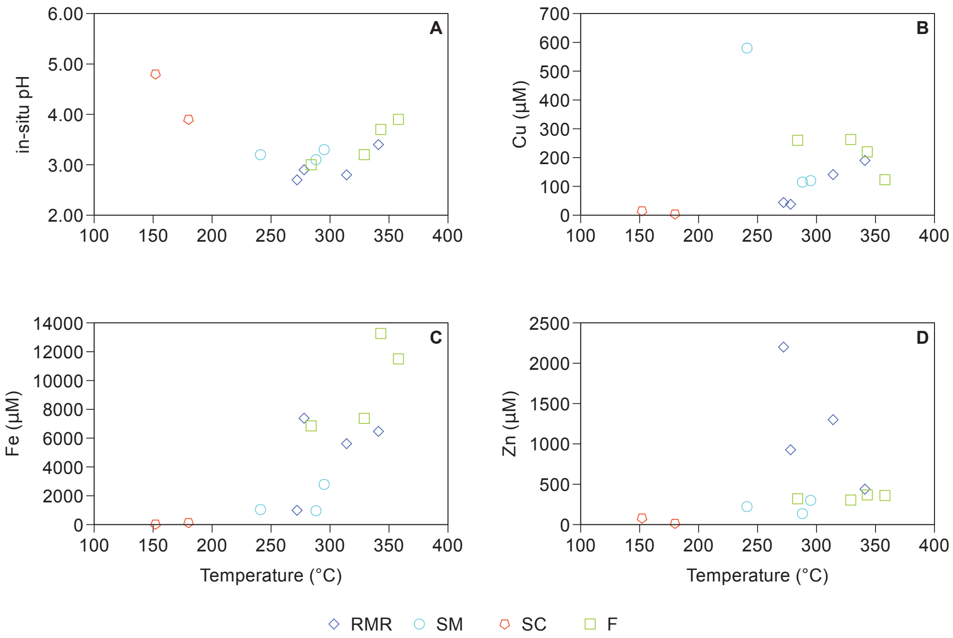

Figure 5.6: pH and in situ Fe, Zn and Cu concentrations in fluid samples of Fenway, Roman Ruins, Snowcap and Satanic Mills versus temperature (Craddock, 2009).

In comparison, Cu shows strong decoupling from Zn (Figure 5.6d).

This increased Cu concentration in the Satanic Mills fluid is matched by an equally strong increase in As (Figure 5.7a). Arsenic is somewhat enriched at Roman Ruins. Likewise, Ag is enriched in the zone refined fluids from Roman Ruins (Figure 5.7e). Sb and Au show enrichments in some, but not all sites (Figures Figure 5.7a and d). Au is mobilized in the Satanic MIlls and Snowcap sites (triangles in Figure 5.7d), though not at the Roman Ruins site. The coldest of the four fluids from Fenway, on the other hand, does show some Au enrichment. Sb is markedly enriched in two fluids, one from Satanic Mills and one from Roman Ruins.

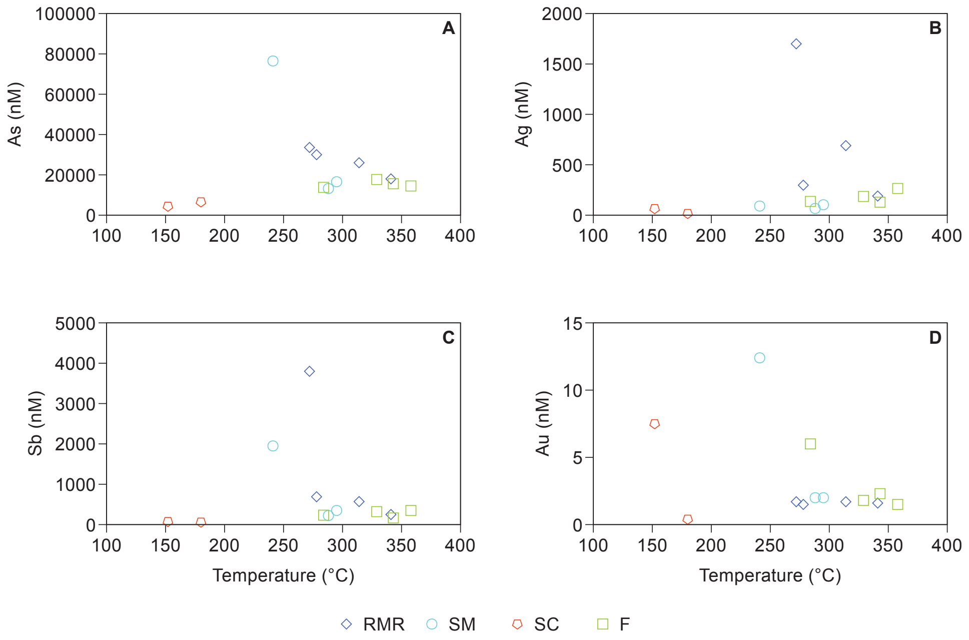

Figure 5.7: In situ Sb, As, Au and Ag concentrations in fluid samples of Fenway, Roman Ruins, Snowcap and Satanic Mills versus temperature (Craddock, 2009).

5.5 Whole rock dataset

The whole rock samples retrieved from the seafloor by remotely operated vehicles (ROVs): WHOI's Jason2 ROV in 2006 and MARUM's Quest4000 ROV in 2011 have been sorted to location and local chimney type (diffuser, massive sulfide/talus, open conduit and inactive) for Fenway, Satanic Mills, Roman Ruins, Snowcap and Solwara 6-8 (Figure 5.2 and Table 5.2). A quick overview is provided of the different mineralization phases in Figure 5.8. Native gold is primarily found within Cu-rich, secondary digenite and digenite-bornite intergrowths (Figure 5.8a, b and f), and occasionally within As-sulfosalt; tennantite (Figure 5.8b) at Satanic Mills. Figure 5.8a is a thin section from a sample taken from Snowcap. At this specific site oxidation of primary chalcopyrite-bornite mineralization into digenite + gold is visible, fitting the moderate temperature of maximum 224 °C. Figure 5.8b and 5.8f are from samples taken at Solwara 8, where Cu-mineralization is represented by primary chalcopyrite overgrown by digenite-bornite intergrowths (Figure 5.8b); and primary bornite-digenite-tennantite formation (Figure 5.8f). Gold is found within primary and secondary Cu-rich mineralization. In Figure 5.8d the gold flake is captured within a secondary tenanntite rim of chalcopyrite, and not in a Cu-rich mineral as described from the other samples. Fenway is in general Au poor, though Cu-rich with chalcopyrite overgrowing bornite (Figure 5.8e), with covelite growth within the fractures of bornite.

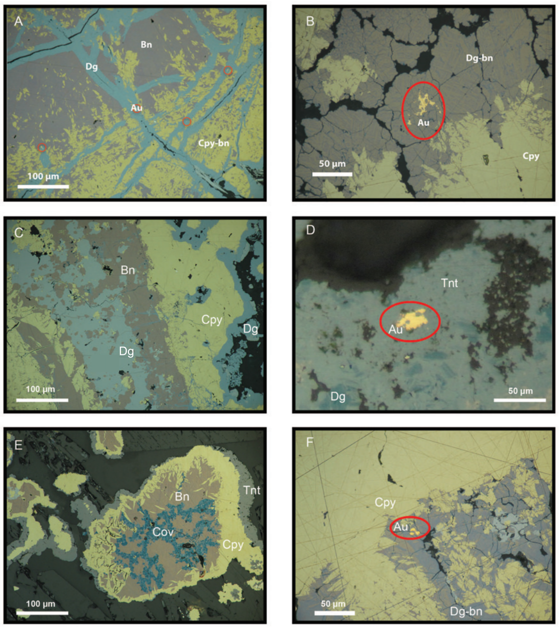

Figure 5.8: *Snowcap*; Oxidation of primary chalcopyrite-bornite intergrowth altered into digenite with finegrained gold flakes. b: *Solwara 8*; Primary bornite-digenite intergrowth overgrowing chalcopyrite, with native gold. c: *Satanic Mills*; different generations of chalcopyrite and digenite. d: *Satanic Mills*; Gold flake and present within outskirt and digenite within innerskirt of tennantite. e: *Fenway*; Chalcopyrite overgrowing fractured bornite, with covelite growing within fractures. f: *Solwara 8*; Primary bornite-digenite intergrowth overgrowing chalcopyrite, with native gold.

A first comparison between (trace) element content of the whole rock samples is made between Fenway, Satanic Mills+Snowcap, Solwara 6-8 and Roman Ruins (Figure 5.9) and chimney style (Figure 5.10). The plots represent the tightest positive correlation with another: the well established Sb-As and Au-Ag, though these relations are not inferior to the positive correlations between As-Ag and Sb-Au (Figure 5.9c and d),

Table 5.2: Overview of categorized whole rock samples of hydrothermal vent sites of 2006 and 2011 expedition.

type	Sample	Location	type	Sample	Location	type	Sample	Location	type	Sample	Location
diffuser chimney	J2-208-1-R3	RMR.	inactive chimney	J2-208-1-R2	RMR.	massive sulfide/talus	J2-212-4-R1	FW.	open conduit chimney	J2-213-2-R1	RMR.
	J2-208-2-R3	RMR.		J2-208-1-R4	RMR.		J2-212-5-R1	FW.		J2-222-4-R1	RMR.
	J2-208-9-R1	RMR.		J2-208-2-R4	RMR.		J2-212-7-R1	FW.		J2-209-1-R1	S.M.
	J2-208-10-R1	RMR.		J2-208-2-R4	RMR.		J2-216-7-R1	FW.		J2-209-7-R1	S.M.
	J2-213-3-R1	RMR.		J2-208-4-R2	RMR.		J2-216-8-R1-GC	FW.		J2-214-3-R1	S.M.
	J2-222-7-R1	RMR.		J2-222-4-R2	RMR.		J2-216-9-R1-GC	FW.		J2-212-1-R1	FW.
	J2-222-8-R2	RMR.		J2-222-8-R1	RMR.		49ROV-05	FW.		J2-212-2-R1	FW.
	J2-209-5-R1	S.M.		J2-209-1-R2	S.M.		34GTV-1	FW.		J2-212-6-R1	FW.
	J2-209-6-R1	S.M.		J2-209-6-R2	S.M.		41ROV-12B	FW.		J2-216-15-R1	FW.
	J2-211-4-R2	SC.		J2-209-6-R3	S.M.		41ROV-12C	FW.		J2-216-16-R1	FW.
	J2-212-3-R1	FW.		J2-209-7-R2	S.M.		41ROV08	FW.		27ROV-08	SC.
	J2-212-9-R2	FW.		J2-209-7-R5	S.M.		31ROV-17	S.M.		25ROV-03	FW.
	J2-212-misc	FW.		J2-210-1-R1	SC.		33GTV-1A	Solwara 8		53ROV-06	RMR.
	J2-216-2-R1	FW.		J2-211-7-R1	SC.		33GTV-1B	Solwara 8		39ROV-01	RMR.
	27ROV-01	SC.		J2-210-4-R1	FW.		33GTV-01C	Solwara 8			
	27ROV-06	SC.		J2-210-7-R1	FW.		33GTV-2A	Solwara 8			
	27ROV-07	SC.		J2-210-7-R2	FW.		33GTV-2B	Solwara 8			
	41ROV-05	FW.		J2-210-7-R3	FW.		33GTV-2C	Solwara 8			
	41ROV-12A	FW.		J2-210-8-R3	FW.		33GTV-2E	Solwara 8			
	31ROV-10	S.M.		J2-212-9-R1	FW.		33GTV-3A	Solwara 8			
				J2-212-10-R1	FW.		33GTV-3B	Solwara 8			
				29ROV-16	FW.		33GTV-3C	Solwara 8			
				29ROV-15	FW.		33GTV-4A	Solwara 8			
				31ROV-13A	S.M.		33GTV-4B	Solwara 8			
				31ROV-13B	S.M.		37ROV-05	Solwara 7			
				31ROV-13C	S.M.		53ROV-01	Solwara 6			
				49ROV-03	Solwara 8		53ROV-02	Solwara 6			
				37ROV-02	Solwara 7						

*Samples from R/V Melville cruise MGLN06MW and R/V Sonne cruise SO216.

In both cruises, the samples were retrieved from the seafloor by remotely operated vehicles (ROVs): WHOI's Jason2 ROV in 2006 and MARUM's Quest4000 ROV in 2011

Abbrevations: FW: Fenway; SC: Snowcap; S.M.: Satanic Mills; RMR: Roman Ruins.

Table 5.3: Whole rock dataset based on unpublished data from S. Petersen and Craddock (2009).

Sample	Location	Fe wt%	Cu wt%	Zn wt%	Pb wt%	As wt%	SO4 wt%	Sulfide wt%	Ca wt%	Ba wt%	SiO2 wt%	Sb mg/kg	Ag mg/kg	Au mg/kg
J2-212-3-R1	FW.	8.23	5.74	33.4	0.61	0.39	15.88	21.70	0.5	21.1	N.A.	869	363	41.1
J2-212-9-R2	FW.	10.95	20.1	11.5	0.37	1.07	0.14	15.50	0.06	0	0.12	430	126	9
J2-212-misc	FW.	14.2	10.4	14.05	0.4	0.26	1.37	19.50	0.57	0	0.22	237	141	8.7
J2-216-2-R1	FW.	10.16	26.6	6.62	0.15	1.49	9.60	16.00	0.23	13	N.A.	1050	98	50.4
41ROV-05	FW.	26.2	20.4	3.7	0.3	0.282	2.9	35.0	0	4.1		332	58	10.6
41ROV-12A	FW.	32.5	11	0.9	0.1	0.104	4.4	40.3	0.1	6	0.1	30		1.8
J2-210-4-R1	FW.	9.35	19.6	13.2	0.37	2.18	0.12	17.50	0.05	0	0.39	82	203	10.9
J2-210-7-R1	FW.	18.25	38.2	5.35	0.21	0.81	1.73	20.00	0.14	2	N.A.	797	95	17.4
J2-210-7-R2	FW.	25	29.3	0.83	0.06	0.16	6.12	20.90	2.55	0	0.11	236	40	7.4
J2-210-7-R3	FW.	10.49	22.5	1.45	0.01	0.65	9.91	13.40	0.07	14	N.A.	530	82	10.3
J2-210-8-R3	FW.	4.74	0.64	57.8	0.48	0.24	0.07	26.90	0.03	0	0.01	924	534	10.5
J2-212-9-R1	FW.	7.31	18.1	12.3	0.18	1.12	7.80	14.70	0.06	11	N.A.	499	127	13
J2-212-10-R1	FW.	1.65	0.51	55.9	0.75	0.57	0.07	25.50	0.03	0	0.03	338	611	15.4
29ROV-16	FW.	9	15.7	15.1	0.6	0.579	9.3	23.8	0	13.3	0.2		278	7.4
29ROV-15	FW.	11.1	30	11.8	0.5	2.7	5.6	26.4	0.2	7.3	0.3		352	16.8
J2-212-4-R1	FW.	20.3	20.6	4.36	0.08	0.1	0.05	17.15	0.02	0.01	0.15	90	58	3.7
J2-212-5-R1	FW.	34	9.09	1.22	0.06	0.11	0.10	34.50	0.04	0	0.15	57	31	5.4
J2-212-7-R1	FW.	22.5	15.5	0.19	0.01	0.02	20.88	21.00	0.96	26.7	N.A.	25	7	3.4
J2-216-7-R1	FW.	32.9	4.56	3.78	0.15	0.25	0.12	35.30	0.05	0	0.64	75	57	3.5
J2-216-8-R1-GC	FW.	2.63	0.24	32.3	1.61	0.69	0.07	17.45	0.03	0	4.46	1065	297	7.7
J2-216-9-R1-GC	FW.	38.3	1.48	0.8	0.1	0.27	6.03	37.80	0.16	8.11	N.A.	21	15	4.2
49ROV-05	FW.	41.8	1	0.7	0.3	0.0822	0.6	51.2	0	0.8	0.2	16		1.8
34GTV-1	FW.	15.7	0.1	22.7	3	0.818	6.1	32.4	0.1	8.4	4.9	376	216	0.8
41ROV-12B	FW.	18.7	13.7	7.5	0.2	0.0995	9.4	27.5	0.1	13		139	47	5.1
41ROV-12C	FW.	8.3	1.1	35.4	1.2	0.166	7.3	27.3	0.2	9.8	0.4	558	265	9.9
41ROV08	FW.	2.6	0.6	0.1	0	0.0085	66.4	2.0	27.6	0.2	0.1	5		0.2
J2-212-1-R1	FW.	9.15	5.07	0.5	0.03	0.05	32.42	21.60	13.35	0.55	N.A.	24	8	1.2
J2-212-2-R1	FW.	14.5	7.01	1.26	0.04	0.06	31.76	20.00	13	0.81	N.A.	31	16	1.7
J2-212-6-R1	FW.	9.28	5.96	0.41	0.02	0.04	38.74	23.10	16	0.49	N.A.	24	8	1.2
J2-216-15-R1	FW.	7.29	5.67	0.86	0.03	0.03	37.16	17.30	15.4	0.29	N.A.	44	14	2.2
J2-216-16-R1	FW.	11	8.93	0.11	0.01	0.02	33.73	19.70	14	0.18	N.A.	14	10	1.1
25ROV-03	FW.	8.4	4.3	0.2	0	0.0174	52.2	11.4	21.7	0.2		7	7	0.7
J2-208-1-R3	RMR.	8.37	15.2	31.5	1.23	2.03	0.14	21.50	0.06	0	0.07	871	267	13.7
J2-208-2-R3	RMR.	0.32	0.66	39.5	33	0.66	0.54	24.20	0.05	0.61	N.A.	5370	756	
J2-208-9-R1	RMR.	0.43	0.13	53.2	2.11	0.53	3.62	17.80	0.06	5	N.A.	209	111	
J2-208-10-R1	RMR.	19.9	3.61	21.4	6.39	0.52	5.21	30.40	0.03	7.38	N.A.	779	278	5
J2-213-3-R1	RMR.	7.79	7.54	17.9	0.42	0.12	25.04	20.00	10	1.5	N.A.	597	143	67.9
J2-222-7-R1	RMR.	0.7	0.73	59.8	3.5	0.6	4.34	28.70	0.05	6.07	N.A.	612	785	10.1
J2-222-8-R2	RMR.	10.6	14.5	27.9	2.82	1.23	10.18	24.20	2.49	6.04	N.A.	2910	428	69.9
J2-208-1-R2	RMR.	1.44	0.72	53.1	2.02	0.82	0.10	24.70	0.04	0	0.31	1280	632	15.4
J2-208-1-R4	RMR.	4.61	1.66	4.45	0.25	0.12	2.17	4.66	0.9	0.01	55.2	159	56	5.4
J2-208-2-R4	RMR.	1.3	2.14	56.1	1.34	0.24	5.33	26.30	0.06	7.46	N.A.	4100	910	118
J2-208-2-R4	RMR.	0.19	0.84	52.7	13.05	0.76	2.38	27.20	0.46	1.84	N.A.	2580	1005	2.1
J2-208-4-R2	RMR.	0.47	0.37	45.8	8.97	1.07	0.10	21.70	0.04	0	1.79	1120	567	3.3

Sample	Location	Fe wt%	Cu wt%	Zn wt%	Pb wt%	As wt%	SO4 wt%	Sulfide wt%	Ca wt%	Ba wt%	SiO2 wt%	Sb mg/kg	Ag mg/kg	Au mg/kg
J2-222-4-R2	RMR.	13.35	13.3	26.2	1.08	0.62	0.19	24.10	0.08	0	1.81	731	340	50.9
J2-222-8-R1	RMR.	2.48	5.53	52.2	5.84	1.4	3.70	26.20	0.04	5.18	N.A.	262	577	2.5
J2-213-2-R1	RMR.	21.2	29.4	4.14	0.24	0.05	10.44	20.50	4.2	0.52	N.A.	111	76	5.1
J2-222-4-R1	RMR.	23	37.5	0.42	0.03	0.01	3.61	19.40	1.42	0.29	N.A.	8	8	1.2
53ROV-06	RMR.	25.6	20.9	0.7	0	0.0436	11.9	30.9	4.8	0.6	0.7	49	22	2
39ROV-01	RMR.	25.4	37.6	0.1	0	0.0597	1.2	32.0	0.1	1.3	1.1	74	34	3.9
J2-209-5-R1	S.M.	3.52	14.1	29	1.61	1.69	14.96	20.30	0.03	21.4	N.A.	35	333	17.2
J2-209-6-R1	S.M.	16.8	28.7	5.49	0.13	1.64	0.19	19.70	0.08	0	0.1	919	87	26.9
31ROV-10	S.M.	25.8	17.5	13.9	0.8	0.42	0.5	37.3	0	0.7	0.2	468	111	8
J2-209-1-R2	S.M.	20.8	14.9	19.8	1.22	0.64	2.86	29.20	1.19	0	0.48	541	154	13.8
J2-209-6-R2	S.M.	23.3	19.9	7.22	0.21	1.01	0.05	27.20	0.02	0	0.24	688	79	8.7
J2-209-6-R3	S.M.	6.03	20.6	22	0.49	3.19	0.12	22.20	0.05	0	0.6	687	175	16.1
J2-209-7-R2	S.M.	27.1	26.9	3.85	0.29	0.32	2.77	22.10	0.36	2.74	N.A.	453	67	10.2
J2-209-7-R5	S.M.	27.5	34.7	0.99	0.08	0.29	0.71	21.40	0.02	0.95	N.A.	626	30	12.8
31ROV-13A	S.M.	5.6	6.8	39.4	1.1	0.835	4.5	27.6	0.2	5.7	0.1	1660	336	7.6
31ROV-13B	S.M.	27.2	32.6	1.9	0.1	0.102	1.7	34.6	0.3	1.4	0.2	184	46	6
31ROV-13C	S.M.	31.8	30.4	0	0	0.0312	0.3	38.2	0	0.4		127		2.2
31ROV-17	S.M.	10.9	27.7	0.1	0	0.291	26.8	16.6	11	0.5	0.1	413	61	18
J2-209-1-R1	S.M.	22.38	32.9	0.38	0.03	0.09	6.79	20.00	2.79	0.14	N.A.	475	13	3.5
J2-209-7-R1	S.M.	22.63	30.1	0.17	0.01	0.04	9.29	20.00	3.8	0.25	N.A.	133	8	3
J2-214-3-R1	S.M.	13.5	40.3	0.25	0.03	0.34	9.24	19.00	3.77	0.28	N.A.	519	54	18.8
J2-211-4-R2	SC.	10.75	32	8.87	0.69	2.19	11.69	19.70	0.09	16.5	N.A.	2610	234	97.8
27ROV-01	SC.	12.3	20.5	26.4	1.1	0.367	2.4	27.2	0.1	3.1	0.1	2150	431	16.7
27ROV-06	SC.	3.9	1.9	55.1	1.9	0.0473	2.0	32.4	0.6	0.8		1150	490	10.1
27ROV-07	SC.	1.6	1.4	59.9	2.4	0.148	1.0	30.9	0.1	1.1		1540	317	9.7
J2-210-1-R1	SC.	5.36	18.45	19.35	0.53	1.22	0.12	16.65	0.05	0	0.34	38	310	3.9
J2-211-7-R1	SC.	0.3	1.9	59.2	2.02	0.72	0.05	24.20	0.02	0	0.04	11	516	1.8
27ROV-08	SC.	27.8	39.7	0.1	0	0.0399	0.4	35.1	0.1	0.2	0.2	172	28	11.9
53ROV-01	Solwara 6	4.7	5.6	15.7	1.1	0.14	16.1	18.1	0.1	22.6	1.1	7	214	7.9
53ROV-02	Solwara 6	9.8	25.7	5.3	0.4	3.16	9.2	22.7	0.1	12.8	0.3	415	328	7.4
37ROV-02	Solwara 7	26.3	27.4	5	0.2	0.0962	1.8	35.1	0	2.6	0.1	122	132	4.4
37ROV-05	Solwara 7	25.2	7.2	11.8	0.6	0.201	4.4	37.0	0.1	6	2.7	189	96	2.2
49ROV-03	Solwara 8	1.6	2.5	45.5	2	1.085	5.2	26.9	0	7.4	0.05	116	455	5
33GTV-1A	Solwara 8	20.6	43.3	0.3	0	0.1982	0.6	29.4	0	0.8	0.4	161	76	22
33GTV-1B	Solwara 8	27.2	32.6	1.9	0.1	0.102	1.7	34.6	0.3	1.4	0.2	184	46	6
33GTV-01C	Solwara 8	27.4	35.9	0.2	0	0.0627	0.6	32.2	0	0.9	0.6	88	16	3.3
33GTV-2A	Solwara 8	6.2	41	7.4	0.2	1.56	5.0	22.8	0.1	6.8	0.9	1030	358	17
33GTV-2B	Solwara 8	2.6	36.2	13.9	0.9	1.58	6.3	21.8	0	9		838	438	40.8
33GTV-2C	Solwara 8	14.4	29.1	3.1	0.1	0.618	7.3	25.9	0.1	10.1	0.1	531	221	18.6
33GTV-2E	Solwara 8	6	48.5	4.6	0.3	1.37	3.3	24.3	0	4.7	0.2	888	465	17.8
33GTV-3A	Solwara 8	14.3	32.1	10.1	0.4	1.14	3.4	28.0	0	4.8	0.3	706	322	70.9
33GTV-3B	Solwara 8	14.4	36.6	1.3	0.1	0.925	4.9	23.6	0.1	6.7	0.4	756	311	65
33GTV-3C	Solwara 8	19.6	39.6	1.7	0.1	0.521	1.3	29.6	0	1.8	0.3	435	229	56.9
33GTV-4A	Solwara 8	5.9	10.3	29.9	1	1.65	6.1	26.7	0.1	8.3	0.1	602	414	5.6
33GTV-4B	Solwara 8	6.1	0	31.9	0.8	1.39	6.3	27.3	0	9	0.1	514	436	7.2

Table 5.4: Mineral mode calculations based on whole rock dataset based on unpublished data from S. Petersen and Craddock (2009).

type	Sample	Location	Cpy	Pyrite	Sphalerite	Galena	Digenite	Barite	Anhydrite	Tennantite	Bornite	Sum	bor+dig/bor+dig+cpy
diffuser chimney	J2-208-1-R3	RMR.	0.15	0.00	0.45	0.01	0.00	0.00	0.00	0.02	0.13	0.76	0.47
	J2-208-2-R3	RMR.	0.00	0.00	0.58	0.38	0.00	0.01	0.00	0.01	0.00	0.99	-
	J2-208-9-R1	RMR.	0.00	0.00	0.74	0.01	0.00	0.08	0.00	0.00	0.00	0.84	-
	J2-208-10-R1	RMR.	0.10	0.32	0.31	0.07	0.00	0.13	0.00	0.00	0.00	0.93	0.00
	J2-213-3-R1	RMR.	0.00	0.17	0.27	0.00	0.09	0.03	0.34	0.01	0.00	0.90	1.00
	J2-222-7-R1	RMR.	0.00	0.00	0.88	0.04	0.00	0.10	0.00	0.01	0.00	1.03	1.00
	J2-222-8-R2	RMR.	0.29	0.00	0.40	0.03	0.00	0.10	0.08	0.02	0.05	0.98	0.16
	J2-209-5-R1	S.M.	0.06	0.00	0.42	0.02	0.06	0.36	0.00	0.06	0.07	1.06	0.68
	J2-209-6-R1	S.M.	0.40	0.00	0.06	0.00	0.00	0.00	0.00	0.01	0.22	0.70	0.35
	J2-211-4-R2	SC.	0.17	0.00	0.12	0.01	0.00	0.28	0.00	0.07	0.36	1.01	0.67
	J2-212-3-R1	FW.	0.17	0.03	0.49	0.00	0.00	0.36	0.02	0.00	0.00	1.06	0.00
	J2-212-9-R2	FW.	0.24	0.00	0.15	0.00	0.03	0.00	0.00	0.00	0.14	0.57	0.41
	J2-212-misc	FW.	0.30	0.07	0.20	0.00	0.00	0.00	0.02	0.00	0.00	0.59	0.00
	J2-216-2-R1	FW.	0.18	0.00	0.09	0.00	0.00	0.22	0.01	0.03	0.29	0.82	0.62
	27ROV-01	SC.	0.33	0.00	0.39	0.01	0.00	0.05	0.00	0.00	0.14	0.92	0.30
	27ROV-06	SC.	0.01	0.07	0.82	0.02	0.01	0.01	0.02	0.00	0.00	0.99	0.52
	27ROV-07	SC.	0.03	0.01	0.89	0.03	0.01	0.02	0.01	0.00	0.00	0.98	0.18
	41ROV-05	FW.	0.24	0.38	0.05	0.00	0.04	0.07	0.00	0.02	0.12	0.93	0.41
	41ROV-12A	FW.	0.25	0.54	0.02	0.00	0.00	0.10	0.00	0.03	0.01	0.97	0.07
	31ROV-10	S.M.	0.27	0.34	0.20	0.01	0.00	0.01	0.00	0.01	0.12	0.96	0.30
inactive chimney	J2-208-1-R2	RMR.	0.00	0.00	0.78	0.02	0.00	0.00	0.00	0.00	0.00	0.81	0.74
	J2-208-1-R4	RMR.	0.05	0.04	0.06	0.00	0.00	0.00	0.03	0.00	0.00	0.18	0.00
	J2-208-2-R4	RMR.	0.00	0.00	0.82	0.01	0.01	0.13	0.00	0.00	0.01	0.99	1.00
	J2-208-2-R4	RMR.	0.00	0.00	0.78	0.15	0.00	0.03	0.02	0.01	0.00	0.99	1.00
	J2-208-4-R2	RMR.	0.00	0.00	0.67	0.10	0.00	0.00	0.00	0.00	0.00	0.77	-
	J2-222-4-R2	RMR.	0.38	0.00	0.38	0.01	0.00	0.00	0.00	0.00	0.00	0.77	0.00
	J2-222-8-R1	RMR.	0.01	0.00	0.76	0.06	0.02	0.09	0.00	0.01	0.04	1.00	0.84
	J2-209-1-R2	S.M.	0.43	0.12	0.28	0.01	0.00	0.00	0.04	0.00	0.00	0.89	0.00
	J2-209-6-R2	S.M.	0.57	0.09	0.10	0.00	0.00	0.00	0.00	0.00	0.00	0.77	0.00
	J2-209-6-R3	S.M.	0.13	0.00	0.32	0.00	0.05	0.00	0.00	0.11	0.12	0.73	0.56
	J2-209-7-R2	S.M.	0.75	0.00	0.02	0.00	0.00	0.05	0.01	0.00	0.00	0.83	0.00
	J2-209-7-R5	S.M.	0.67	0.00	0.00	0.00	0.00	0.02	0.00	0.00	0.16	0.85	0.19
	J2-210-1-R1	SC.	0.10	0.00	0.28	0.00	0.09	0.00	0.00	0.02	0.11	0.60	0.67
	J2-211-7-R1	SC.	0.00	0.00	0.85	0.02	0.01	0.00	0.00	0.00	0.00	0.88	1.00
	J2-210-4-R1	FW.	0.21	0.00	0.18	0.00	0.01	0.00	0.00	0.07	0.12	0.61	0.39
	J2-210-7-R1	FW.	0.34	0.00	0.05	0.00	0.00	0.03	0.00	0.00	0.40	0.83	0.54
	J2-210-7-R2	FW.	0.67	0.00	0.00	0.00	0.00	0.00	0.09	0.00	0.08	0.83	0.11
	J2-210-7-R3	FW.	0.24	0.00	0.01	0.00	0.00	0.24	0.00	0.00	0.22	0.71	0.48
	J2-210-8-R3	FW.	0.02	0.02	0.84	0.00	0.00	0.00	0.00	0.00	0.00	0.89	0.00
	J2-212-9-R1	FW.	0.13	0.00	0.17	0.00	0.00	0.19	0.00	0.02	0.19	0.71	0.59
	J2-212-10-R1	FW.	0.00	0.00	0.82	0.01	0.00	0.00	0.00	0.00	0.00	0.83	0.00
	29ROV-16	FW.	0.00	0.19	0.23	0.01	0.15	0.23	0.00	0.04	0.03	0.88	1.00
	29ROV-15	FW.	0.12	0.11	0.17	0.01	0.14	0.12	0.01	0.13	0.14	0.96	0.69
	31ROV-13A	S.M.	0.05	0.08	0.58	0.01	0.02	0.10	0.01	0.04	0.03	0.92	0.47
	31ROV-13B	S.M.	0.51	0.19	0.03	0.00	0.00	0.02	0.01	0.00	0.24	1.00	0.32
	31ROV-13C	S.M.	0.59	0.26	0.00	0.00	0.00	0.01	0.00	0.00	0.16	1.01	0.21
	49ROV-03	Solwara 8	0.00	0.04	0.68	0.02	0.00	0.13	0.00	0.06	0.00	0.93	1.00
	37ROV-02	Solwara 7	0.39	0.25	0.07	0.00	0.00	0.04	0.00	0.00	0.22	0.98	0.36

type	Sample	Location	Cpy	Pyrite	Sphalerite	Galena	Digenite	Barite	Anhydrite	Tennantite	Bornite	Sum	bor+dig/bor+dig+cpy
massive sulfide/talus	J2-212-4-R1	FW.	0.56	0.00	0.04	0.00	0.00	0.00	0.00	0.00	0.00	0.60	0.01
	J2-212-5-R1	FW.	0.26	0.51	0.00	0.00	0.00	0.00	0.00	0.00	0.00	0.78	0.00
	J2-212-7-R1	FW.	0.45	0.14	0.00	0.00	0.00	0.45	0.03	0.00	0.00	1.07	0.00
	J2-216-7-R1	FW.	0.13	0.58	0.04	0.00	0.00	0.00	0.00	0.00	0.00	0.76	0.00
	J2-216-8-R1-GC	FW.	0.00	0.04	0.48	0.02	0.00	0.00	0.00	0.01	0.00	0.54	-
	J2-216-9-R1-GC	FW.	0.04	0.73	0.00	0.00	0.00	0.14	0.01	0.00	0.00	0.91	0.00
	49ROV-05	FW.	0.00	0.92	0.01	0.00	0.00	0.01	0.00	0.03	0.00	0.98	1.00
	34GTV-1	FW.	0.00	0.36	0.34	0.04	0.00	0.14	0.00	0.02	0.00	0.90	-
	41ROV-12B	FW.	0.13	0.30	0.11	0.00	0.06	0.22	0.00	0.00	0.07	0.90	0.50
	41ROV-12C	FW.	0.02	0.16	0.53	0.01	0.00	0.17	0.01	0.01	0.00	0.91	0.00
	41ROV08	FW.	0.01	0.04	0.00	0.00	0.00	0.00	0.94	0.00	0.00	0.99	0.49
	31ROV-17	S.M.	0.28	0.00	0.00	0.00	0.07	0.01	0.37	0.00	0.19	0.94	0.48
	33GTV-1A	Solwara 8	0.50	0.04	0.00	0.00	0.08	0.01	0.00	0.01	0.30	0.95	0.43
	33GTV-1B	Solwara 8	0.51	0.19	0.03	0.00	0.00	0.02	0.01	0.00	0.24	1.00	0.32
	33GTV-01C	Solwara 8	0.80	0.03	0.00	0.00	0.00	0.02	0.00	0.00	0.12	0.97	0.13
	33GTV-2A	Solwara 8	0.00	0.12	0.11	0.00	0.45	0.12	0.00	0.08	0.04	0.91	1.00
	33GTV-2B	Solwara 8	0.00	0.03	0.20	0.01	0.31	0.15	0.00	0.09	0.13	0.93	1.00
	33GTV-2C	Solwara 8	0.00	0.27	0.04	0.00	0.23	0.17	0.00	0.03	0.15	0.91	1.00
	33GTV-2E	Solwara 8	0.00	0.09	0.07	0.00	0.42	0.08	0.00	0.09	0.19	0.94	1.00
	33GTV-3A	Solwara 8	0.17	0.14	0.15	0.00	0.17	0.08	0.00	0.05	0.17	0.94	0.66
	33GTV-3B	Solwara 8	0.33	0.04	0.02	0.00	0.11	0.11	0.00	0.05	0.23	0.89	0.51
	33GTV-3C	Solwara 8	0.25	0.19	0.02	0.00	0.21	0.03	0.00	0.01	0.23	0.93	0.64
	33GTV-4A	Solwara 8	0.00	0.13	0.44	0.01	0.08	0.14	0.00	0.09	0.00	0.91	1.00
	33GTV-4B	Solwara 8	0.00	0.17	0.48	0.01	0.00	0.15	0.00	0.03	0.00	0.84	-
	37ROV-05	Solwara 7	0.00	0.54	0.18	0.01	0.08	0.10	0.00	0.02	0.01	0.93	0.99
	53ROV-01	Solwara 6	0.00	0.13	0.24	0.01	0.06	0.38	0.00	0.03	0.00	0.86	1.00
	53ROV-02	Solwara 6	0.00	0.18	0.07	0.00	0.17	0.22	0.00	0.16	0.09	0.89	1.00
open conduit chimney	J2-213-2-R1	RMR.	0.54	0.00	0.04	0.00	0.00	0.01	0.14	0.00	0.15	0.88	0.22
	J2-222-4-R1	RMR.	0.49	0.00	0.00	0.00	0.00	0.00	0.05	0.00	0.30	0.85	0.38
	J2-209-1-R1	S.M.	0.54	0.00	0.00	0.00	0.00	0.00	0.09	0.00	0.21	0.85	0.28
	J2-209-7-R1	S.M.	0.58	0.00	0.00	0.00	0.00	0.00	0.13	0.00	0.14	0.86	0.20
	J2-214-3-R1	S.M.	0.21	0.00	0.00	0.00	0.00	0.00	0.13	0.00	0.51	0.86	0.71
	J2-212-1-R1	FW.	0.00	0.27	0.03	0.01	0.03	0.01	0.45	0.08	0.00	0.88	1.00
	J2-212-2-R1	FW.	0.00	0.32	0.02	0.00	0.09	0.01	0.44	0.01	0.00	0.89	1.00
	J2-212-6-R1	FW.	0.00	0.28	0.03	0.01	0.04	0.01	0.54	0.09	0.00	1.00	1.00
	J2-216-15-R1	FW.	0.00	0.21	0.03	0.00	0.05	0.00	0.52	0.06	0.00	0.88	1.00
	J2-216-16-R1	FW.	0.00	0.27	0.01	0.00	0.10	0.00	0.48	0.04	0.00	0.90	1.00
	27ROV-08	SC.	0.60	0.13	0.00	0.00	0.00	0.00	0.00	0.00	0.30	1.03	0.33
	25ROV-03	FW.	0.07	0.14	0.00	0.00	0.01	0.00	0.74	0.02	0.01	0.99	0.20
	53ROV-06	RMR.	0.34	0.29	0.01	0.00	0.00	0.01	0.16	0.00	0.14	0.95	0.30
	39ROV-01	RMR.	0.68	0.05	0.00	0.00	0.00	0.02	0.00	0.00	0.22	0.98	0.25

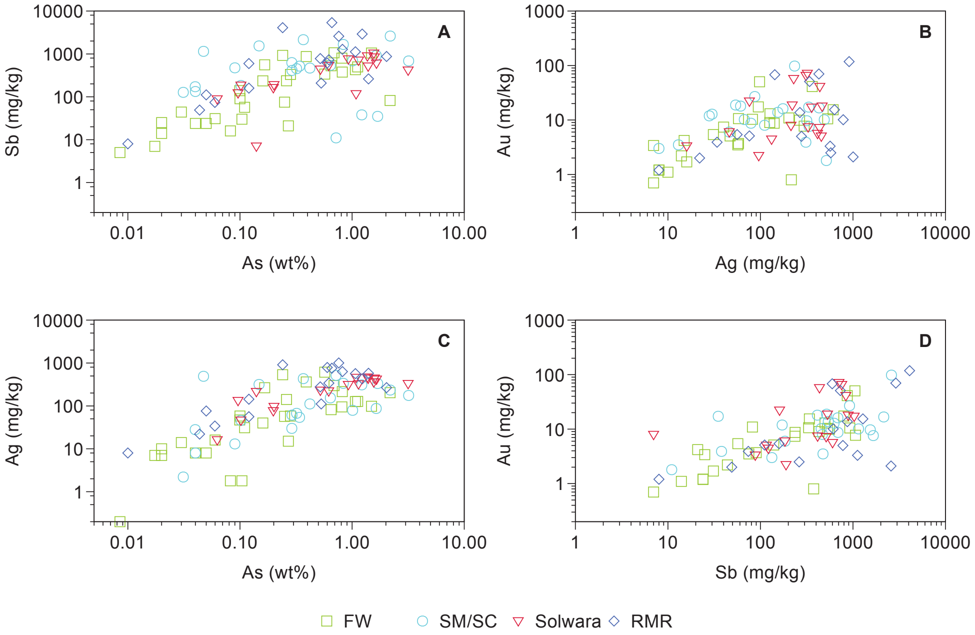

Figure 5.9: Whole rock samples showing relationships between Sb, As, Au, Ag contents of sulfides from Solwara 6-8; FW: Fenway; SM: Satanic Mills and RMR: Roman Ruins (Craddock, 2009).

corresponding the observations from the fluid samples (Figure 5.8).

The strongest correlation is between As-Ag (Figure 5.9c), while Sb-As and Au-Ag have some scatter within the samples from Satanic Mills+Snowcap and Solwara. The strongest correlation between all four elements exists at the Cu-rich Fenway chimneys. The positive correlation between As-Ag and Sb-Au is even more pronounced when looking at the different chimney types (Figure 5.10c and d). The lowest concentrations of all four elements can be found within open conduit chimneys, where no significant concentrations differences can be distinguished. Although the highest scatter between concentrations occur at diffuser chimneys. The same geochemical data was used in comparing the concentration of Sb, As, Ag and Au with calculated mineralogical modes of the sulfide samples, assuming that they are composed of pyrite, anhydrite, barite,

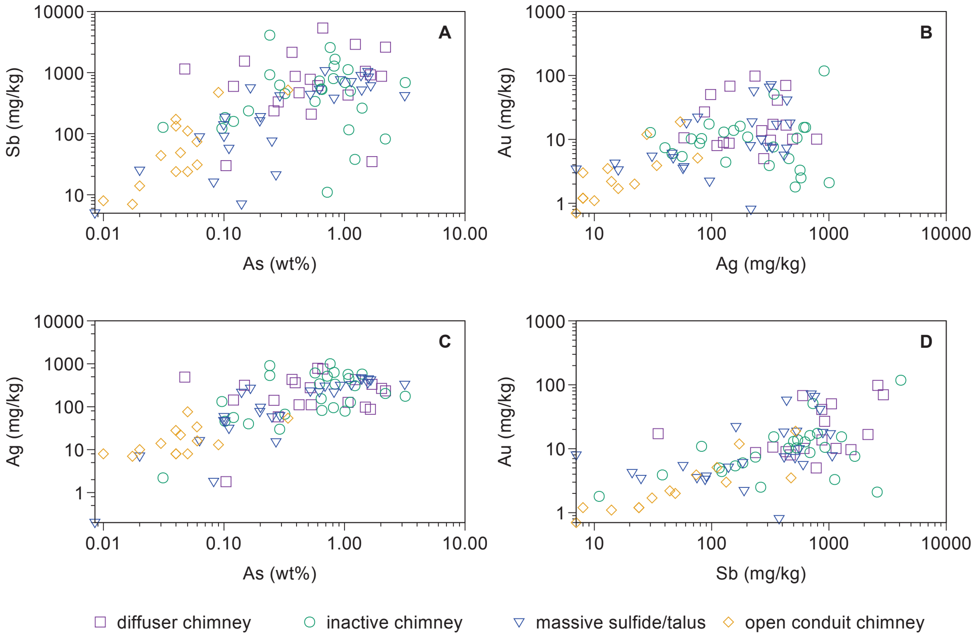

Figure 5.10: Whole rock samples showing relationships between Sb, As, Au, Ag contents from sulfides from Solwara 6-8; FW: Fenway; SM: Satanic Mills and RMR: Roman Ruins categorized into four distinct groups: Open conduit chimney; diffuser chimney; massive sulfide/talus; inactive chimney (Table 5.1) (Craddock, 2009)

amorphous silica, sphalerite, galena, chalcopyrite, bornite, digenite, hematite, tennantite (Table 5.4). These mineralogical modes provide the opportunity to look at the different concentrations within the different chimneys in more depth (Figure 5.11 - 5.14).

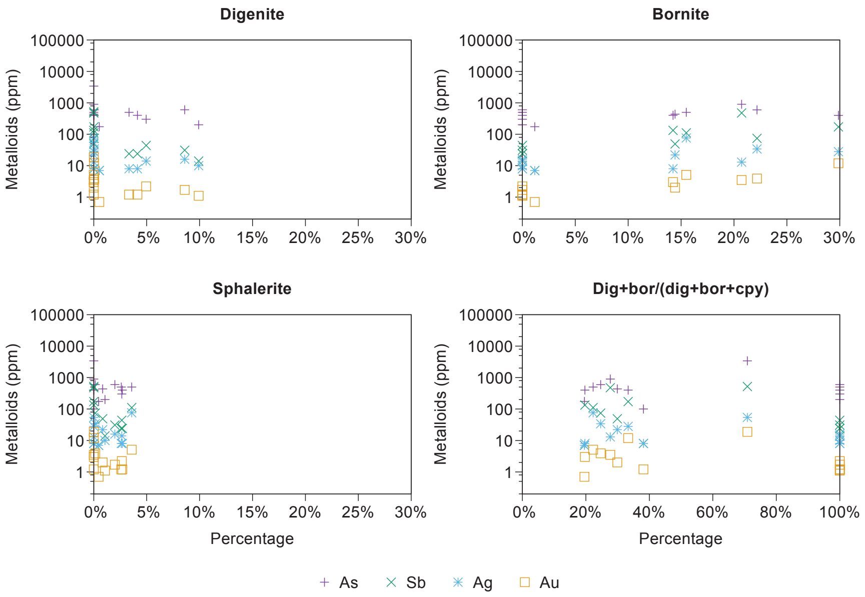

Figure 5.11: Overview mineral mode calculations for the open conduit chimney, with the focus on a) sphalerite, b) bornite, c) digenite and d) Cu-rich minerals (digenite+bornite)/(digenite+bornite+chalcopyrite).

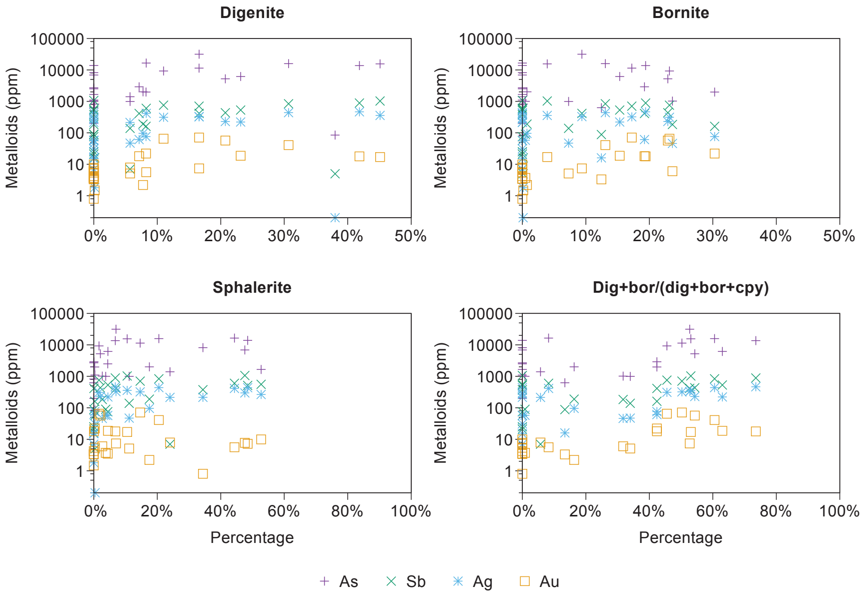

Figure 5.12: Overview mode calculations for the massive sulfide/talus chimney, with the focus on a) sphalerite, b) bornite, c) digenite and d) Cu-rich minerals (digenite+bornite)/(digenite+bornite+chalcopyrite).

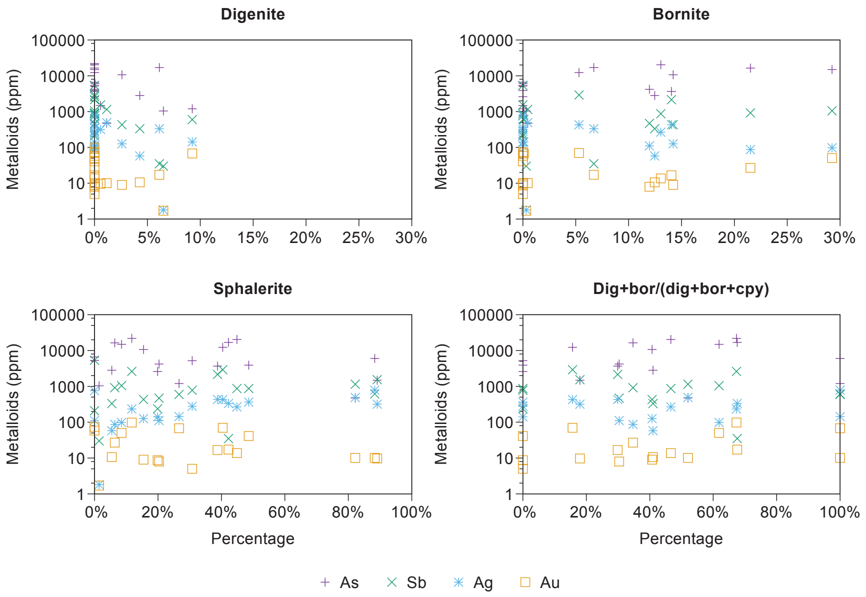

Figure 5.13: Overview mode calculations diffuser chimney, with the focus on a) sphalerite, b) bornite, c) digenite and d) Cu-rich minerals (digenite+bornite)/(digenite+bornite+chalcopyrite).

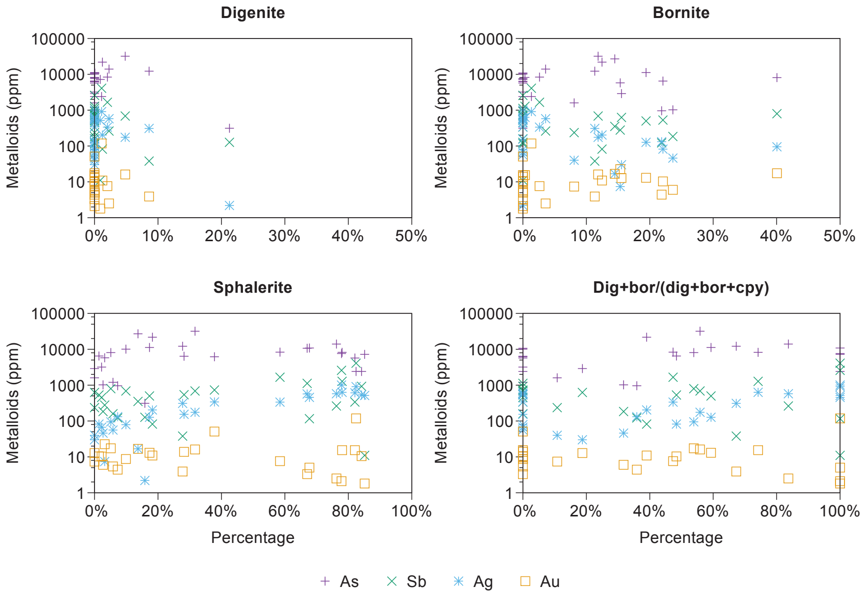

Figure 5.14: Overview mode calculations for the inactive chimney, with the focus on a) sphalerite, b) bornite, c) digenite and d) Cu-rich minerals (digenite+bornite)/(digenite+bornite+chalcopyrite).

Figure 5.11 - 5.14 depict the concentrations of As, Sb, Ag, and Au within the analyzed sulfide samples versus the calculated contents of digenite, bornite, and sphalerite as well as against the ratio of (digenite+bornite)/(digenite+bornite+chalcopyrite). The latter proxy reflects the proportions of secondary Cu-minerals (digenite) and partly secondary Cu-phase (bornite) to the primary Cu-phase chalcopyrite. An unaltered rock will have a ratio close to zero, while the values of strongly altered rocks approach unity. In other words, a low percentage with high concentration of Sb, As, Ag and Au suggests a preference of mineralization of these elements within chalcopyrite, while at high percentages the mineralization is tied to bornite+digenite. Figure 5.11 represents the open conduit style, and corresponds clearly with the outcome of Figure 5.10, indicating that at these sites the concentrations of As, Sb, Ag, and Au are lowest. Overall the plots show scatter and real trends can often not be deduced.

However, there are suggestions of slight correlations between the concentrations of As, Sb, Ag, and Au when plotted against the mode of the sulfide samples in the four different sulfide types (Figures 5.11 - 5.14). The massive sulfide/talus type (Figure 5.12) has the greatest contents of bornite, digenite and sphalerite and represents within this specific mineralization phase proportions the strongest evidence for zone refinement and supergeneous enrichment. The open conduit chimney (Figure 5.11), the other end-member, representing primary sulfide. The inactive chimney samples lie between those of the active chimneys and the mound material in most instances. Both digenite and bornite show an increase for all four elements with increasing dominance of both minerals within the massive sulfide/talus chimneys; concentrations go up two orders of magnitude for between 0 and 10% of digenite and bornite. And these values do no drop, when increasing the amount of bornite and digenite present within a massive sulfide/talus site. In sphalerite these values also increase two orders of magnitude, however Au concentration drops rapidly afterwards, leaving the conjointed Sb, As and Ag behind. The last plot with the (digenite+bornite)/(digenite+bornite+chalcopyrite) proxy shows a increase of Sb, As, Ag and Au in favored digenite and bornite with the same two orders of magnitude, in comparison to a minor increase in chalcopyrite.

Sphalerite is the dominant phase in the diffuser chimneys (Figure 5.13), with low quantities of bornite and digenite and corresponding low concentrations of Sb, As, Ag and Au. Au remains low within sphalerite, however relative high Sb contents, almost reaching the high concentration of As, is prevalent. Au is also low in the (digenite+bornite)/(digenite+bornite+chalcopyrite) plot, while As concentrations are uniformly high. Most notable is a correlation between sphalerite contents and the concentrations of Ag (and to a lesser extent Sb). This reflects a preference of sphalerite for Ag and Sb while sphalerite apparently discriminates against Au. Au within a Zn-dominated diffuser chimney appears to be following As into Cu-mineralization, reflecting a probable preference for tenanntite. As to be expected, digenite is barely present within inactive chimneys (Figure 14). As, Au, Sb and Ag are incorporated here, however, with high scatter and thus no clear relationship.

5.6 Geochemical models

As described in section 5.3, one of the goals of applying geochemical modeling is to look at the solubility differences of Ag, Au, As and Sb and the differences in aqueous speciation as a function of temperature of the hydrothermal fluids without considering hydrothermal alteration or leaching from host rock and/or primary sulfides and mixing or entrainment of seawater. Figure 5.15 shows the different speciations of Sb, As, Ag and Au when cooling a hydrothermal fluid down from 350 °C to 50 °C. Oxidized

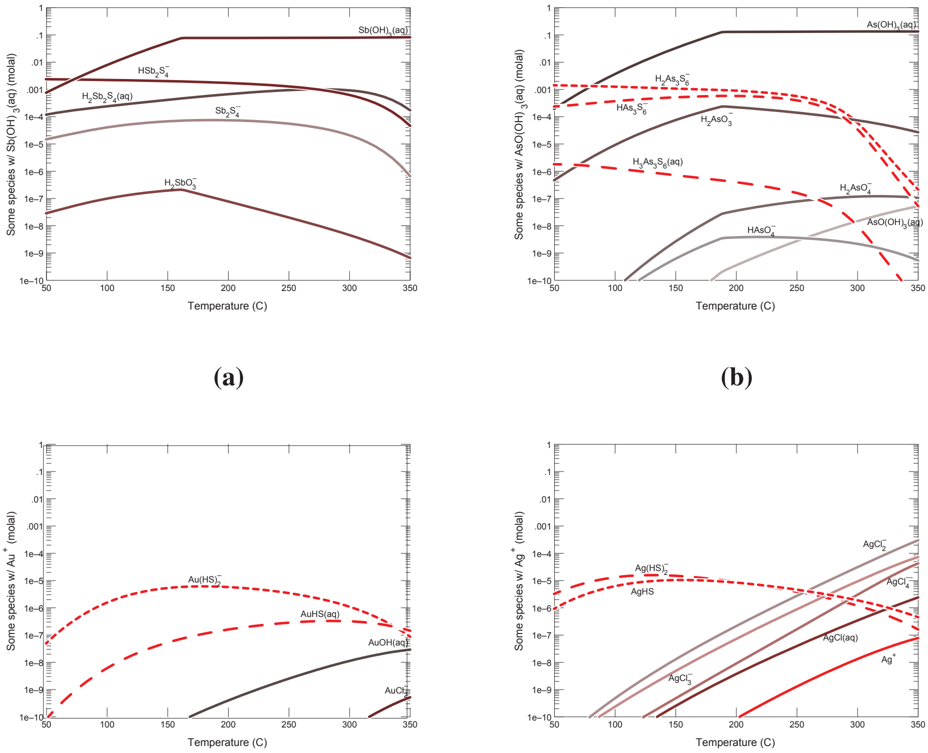

(a)

(b)

(c)

(d)

Figure 5.15: Solubility of Sb, As, Au and Ag in a heated hydrothermal fluid, from 50-350 °C at 250 bar

species, like $Sb(OH)_3$ and $As(OH)_3$, are the dominant Sb- and As-species when cooling down the fluid until T>70 °C. The reduced species, like $H_2Sb_2S_4$ and $HAs_3S_6^-$, show reversed behaviors and are lost from the fluid at high temperatures (>250 °C). This trend is also observed for Au and Ag complexes. Ag follows a more complex behavior as it precipitates upon cooling to 270 °C, and then regains solubility to around 130 °C, from where it starts to precipitate from the fluid again upon further cooling. Overall, Sb, As, and Au are most soluble between 200-270 °C, and Ag between 150-250 °C. These temperature ranges are similar to the temperatures of the fluid samples that showed elevanted concentrations in these elements (Figure 5.4).

Another goal of the modelling was to compute and assemble the T-X sections for the major vent sites at PACManus, mapped out with respect to gangue minerals, Fe-Cu-S, Sb-As-Au-Ag-O-S and Zn-Pb-Mn-Fe-O-S phase assemblages (Figure 5.16-5.18). These plots visualize the mineral assemblages that should prevail within sulfide structures according to varying regimes of seawater entrainment (varying and/or increasing amounts of fraction seawater in mixture) versus conductive cooling (no seawater in mixture). There are a number of coherent messages to be taken home from studying these diagrams:

1. Anhydrite will precipitate above 150°C in mixtures of seawater and hydrothermal fluids; however, in an area in T-X plane where conductive cooling of hydrothermal fluids prevails, anhydrite is missing.
2. Magnetite forms only in specific regions within an area of the T-X plane dominated by conductive heating of entrained seawater.
3. Covellite, hematite (goethite), pyrolusite form at low temperatures over a wide range of mixing ratios between seawater and hydrothermal vent fluid.
4. bornite forms only upon conductive cooling of the hydrothermal fluid; Fe-tennantite is also most stable in that regime, but its stability filed extends to higher proportions of seawater in the mixture.
5. Pyrite and chalcopyrite are stable across large areas of the T-X plane, although at Fenway chalcopyrite may give way to other Cu-phases (bornite and Cu-tennantite) in cases of severe conductive cooling.

Focusing in on the Sb-As-Au-Ag plots, one can recognize that at all three vent sites arsenopyrite, native gold and silver are predicted to precipitate between 150 and 250

°C across a large range of composition. These phases are also predicted to appear at higher temperature in region dominated by conductive cooling. Under these circumstances, this As-AgAu mineralization assemblage is then coeval with the precipitation of bornite. A second group of arsenopyrite will precipitate, when enduring conservative mixing amidst increasing amounts of seawater. At low temperatures (<150 °C) stibnite and berthierite will precipitate, although berthierite is lacking at Satanic Mills, probably due to its low Fe-iron contents (Reeves et al., 2011). Native gold and silver continues to precipitate at 150 °C, independent on the fraction of seawater while enduring conservative mixing.

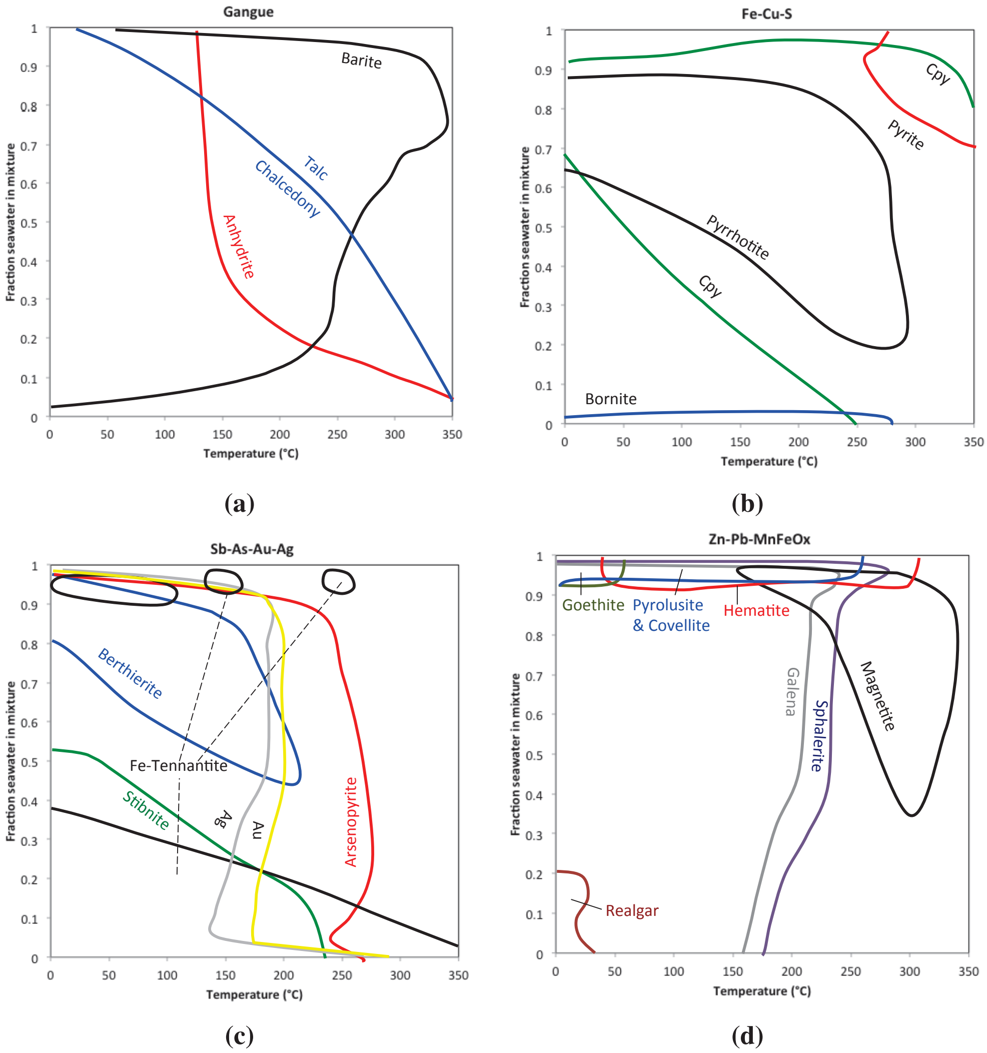

(a)

(b)

(c)

(d)

Figure 5.16: Final T-X sections of Fenway, showing the result of simulating the evolution of seafloor massive sulfide deposits in the critical stages of (i) mound-building, (ii) zone refining within the mound, and (iii) supergeneous enrichment of certain elements in the outmost parts of the mound through reaction path modeling.

A final goal of the modeling was to simulate processes within a hydrothermal sulfide mound using the complex reaction path modeling approach described in Section 5.3. We wish to examine if these processes may be responsible for some of the large compositional variability within the fluid and solid geochemical data and the often-high concentrations of As, Sb, Ag, and Au in some of the moderate temperature fluids venting at PACManus. We focused on the Roman Ruins vent site, but the general patterns discerned should apply to other systems as well.

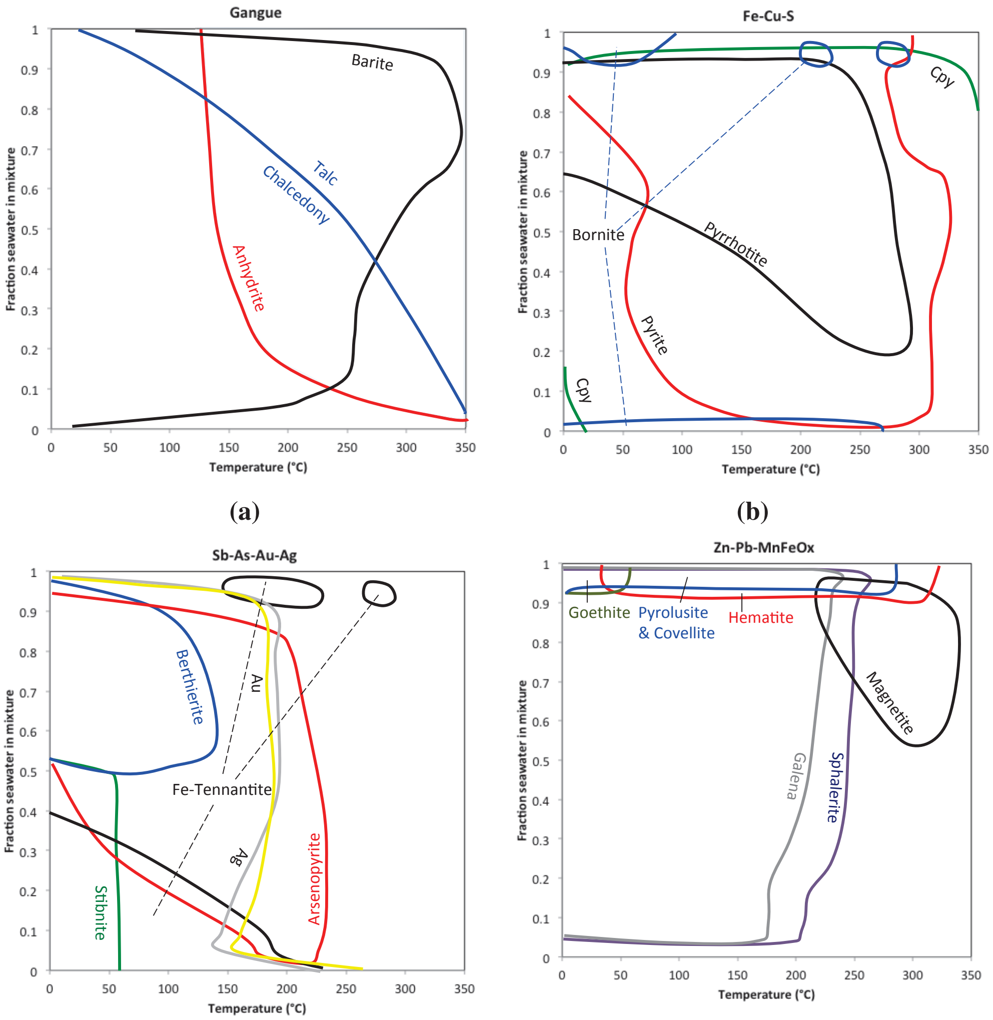

(a)

(b)

(c)

(d)

Figure 5.17: Final T-X sections of Roman Ruins, showing the result of simulating the evolution of seafloor massive sulfide deposits in the critical stages of (i) mound-building, (ii) zone refining within the mound, and (iii) supergeneous enrichment of certain elements in the outmost parts of the mound through reaction path modeling.

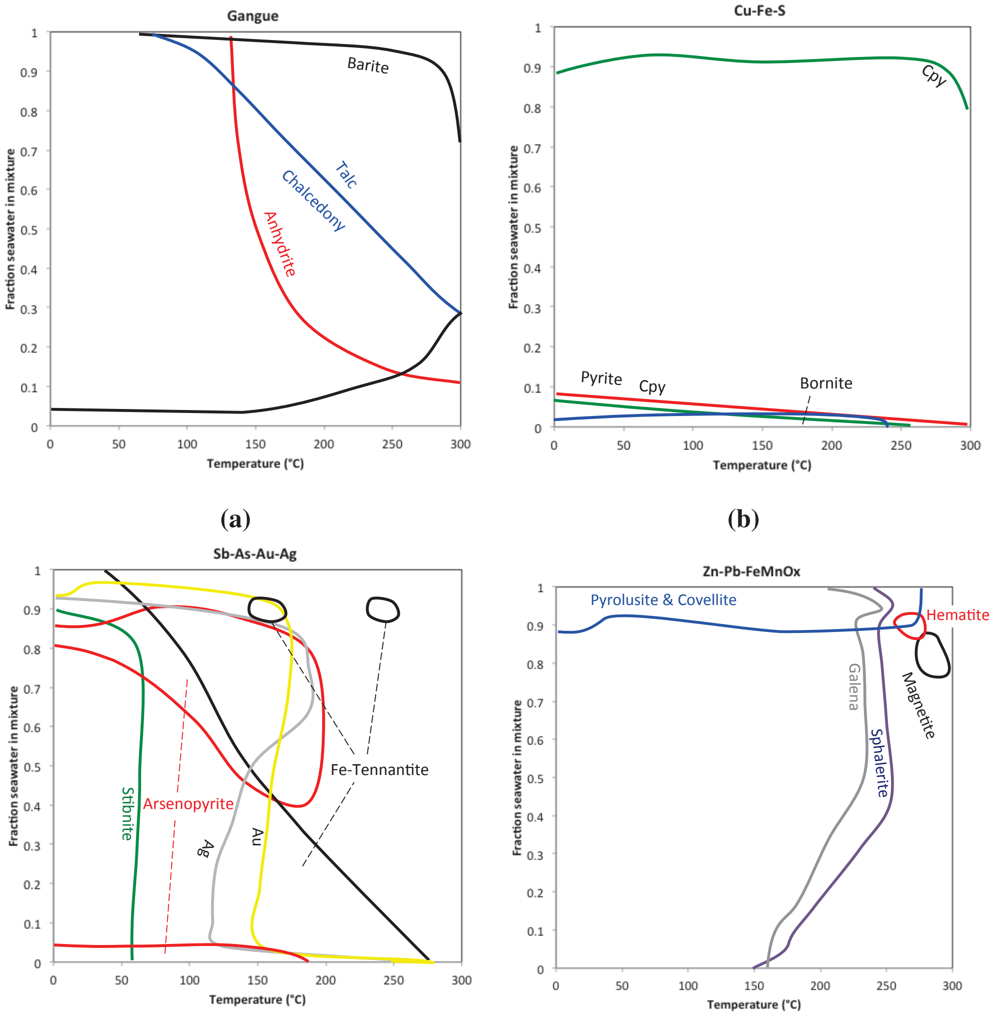

(a) (b)

(c) (d)

Figure 5.18: Final T-X plots of Satanic Mills, showing the result of simulating the evolution of seafloor massive sulfide deposits in the critical stages of (i) mound-building, (ii) zone refining within the mound, and (iii) supergeneous enrichment of certain elements in the outmost parts of the mound through reaction path modeling.

The mineralogical succession of the sulfide formation is depicted in Figure 5.19a. Figure 5.19b and c show the predicted results of interactions between this mixed and cooled fluid with the solids produced in the model run depicted in Figure 5.19a.

They depict the predicted consequences of zone refining, i.e., reactions within the mound upon reaction of the mound material with a mixed fluid (90% endmember vent

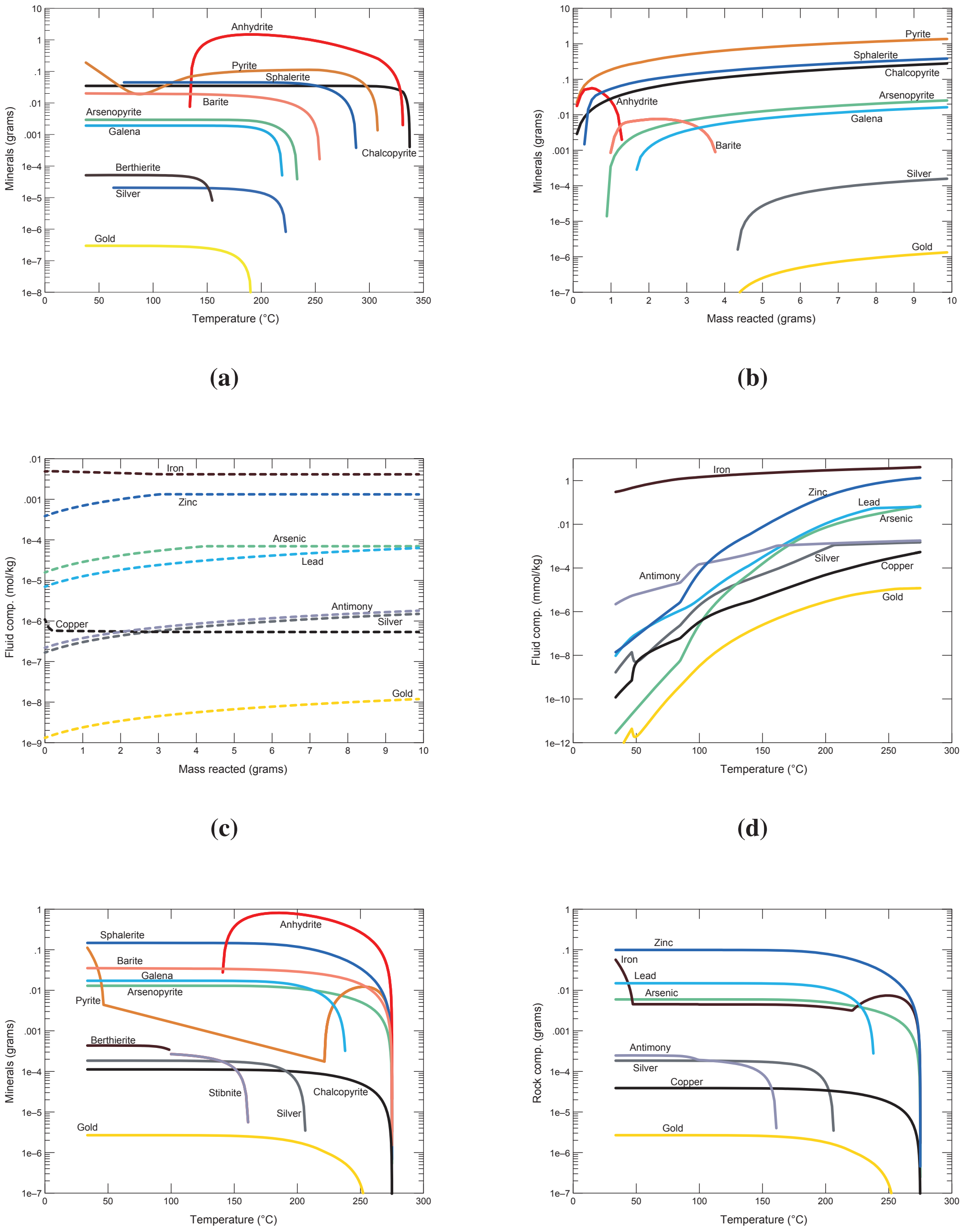

(a) (b)

(c) (d)

(e) (f)

Figure 5.19: Reaction path modeling, with RMR input I

fluid and 10% entrained seawater). Figure 15.19b shows that the minerals expected to form upon this interaction are dominated by pyrite, with lesser amounts of sphalerite, chalcopyrite, galena and arsenopyrite. How these reactions insight the mound would affect fluid composition is shown in Figure 5.15c: Fe and Cu are predicted to decrease in concentration, while the contents of Zn, Pb, As, Sb, Ag, and Au are expected to increase. The predicted consequences of this zone refining process are hence that Fe and Cu become slightly enriched in the mound material, while the other elements shown become depleted in the mound material and enriched in the fluid phase. When this fluid phase percolates up to the surface of the mound, it will mix with cold seawater. Figures 5.19d-e show what is expected to happen in the topmost sections of the mound where this fluid mixing takes place. This reaction path simulates the precipitation of minerals in the supergeneous zone and examines the enrichment of Sb, As, Ag, and Au in these processes The elements picked up by the fluid during zone refining within the mound (As, Sb, Pb, Zn, Ag, Au) are predicted to come out of solution rapidly, whereas Fe concentrations remain high (Figure 5.15d). The minerals expected to form in the outermost part of the mound are sphalerite, Sb and As phases, variable pyrite, and galena. Copper

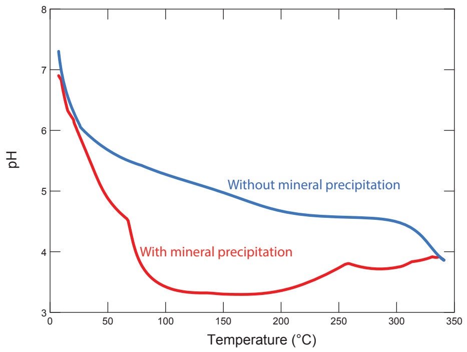

Figure 5.20: Reaction path modeling where addition of CO_2 to the maximum concentrations soluble (several hundred mmol/kg) is responsible for a pH drop.

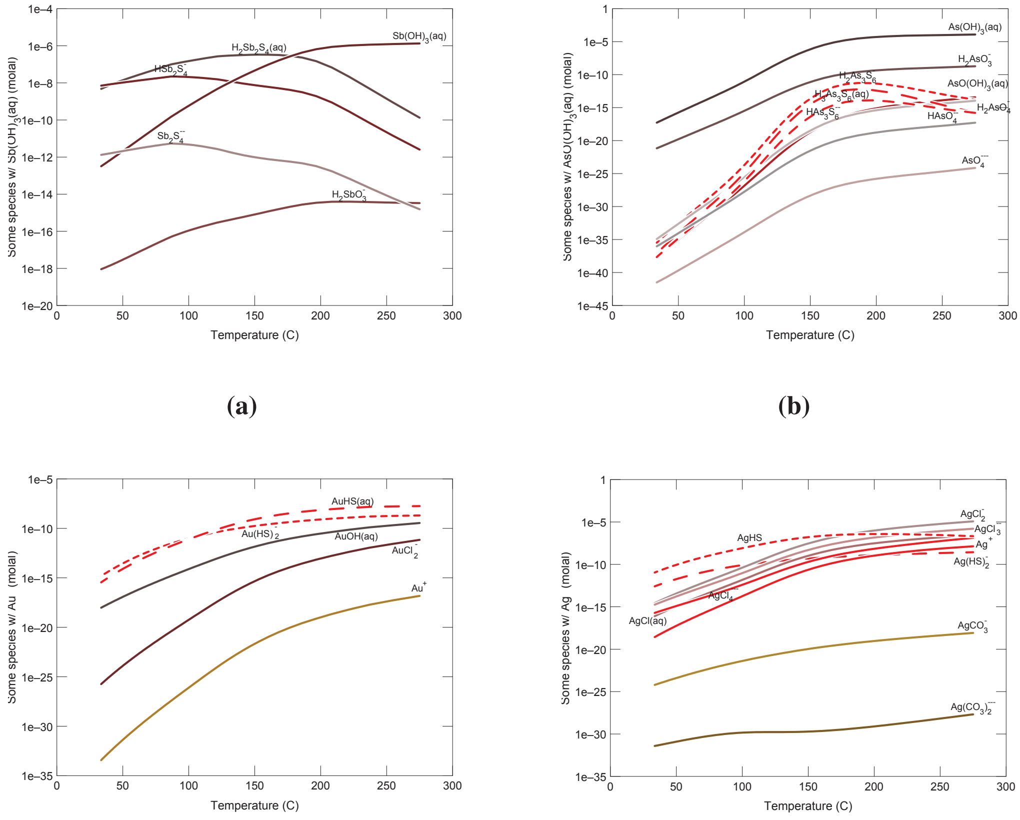

(a)

(b)

(c)

(d)

Figure 5.21: Final solubility plots of Satanic Mills, showing the result of simulating the evolution of seafloor massive sulfide deposits in the critical stages of (i) mound-building, (ii) zone refining within the mound, and (iii) supergeneous enrichment of certain elements in the outmost parts of the mound through reaction path modeling.

phases are subordinate, while Au and Ag are expected to become enriched (Figure 5.19). The elemental composition of the outer mound material is depicted in Figure 5.19f. The material is expected to be essentially Zn-Pb mineralized with high abundances of As, Sb, Ag and Au. This expected loss of Sb, As, Ag and Au from the final hydrothermal fluid at T<270 °C is confirmed in Figure 5.21 and 5.22, where the species are plotted of the fluids from the final stage of Fenway and Satanic Mills.

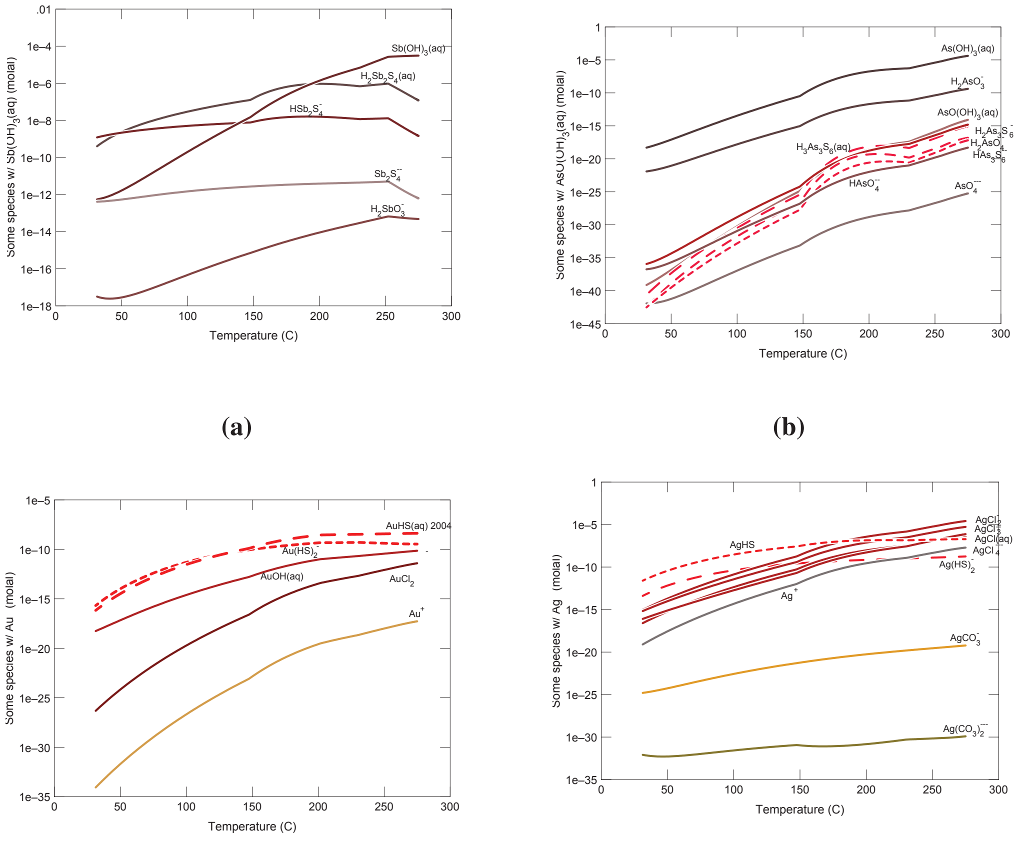

(a)

(b)

(c)

(d)

Figure 5.22: Final solubility plots of Satanic Mills, showing the result of simulating the evolution of seafloor massive sulfide deposits in the critical stages of (i) mound-building, (ii) zone refining within the mound, and (iii) supergeneous enrichment of certain elements in the outmost parts of the mound through reaction path modeling.

5.7 Discussion and conclusion

Due to the tectonic characteristics of the East Manus Basin (EMB) and the bimodal volcanism there, the PACManus hydrothermal field is considered as a rough analogy for land-based auriferous VMS ore deposits (Binns and S. Scott, 1993). Several principal areas of hydrothermal venting have been identified at the PACManus site and used for this study: Roman Ruins, Roger Ruins, Satanic Mills, Fenway, Snowcap, Solwara 6-8 and Tsukushi (Binns, Barriga, et al., 2007; Bach, Rosner, et al., 2011; Reeves et al., 2011). These sites consist of active and inactive black smoker chimneys and spires on sulfide mounds, where the venting fluids are acidic (pH=2.5-3.8) and have temperatures up to 341 °C (Reeves et al., 2011). Like many VMS accumulations, the PACManus site is enriched in As, Sb, Ag, and Au (S. Scott and Binns, 1995; Moss and S. Scott, 2001), but details of a suitable origin, transport and trapping mechanisms for these metals are unknown.

5.7.1 Role of magma degassing

The very gassy and metal-rich fluids observed in the PACManus hydrothermal area are abundant in arc and back-arc hydrothermal systems (Baker et al., 2008; Butterfield et al., 2011; Reeves et al., 2011; Ronde et al., 2001; Seewald, Reeves, et al., 2015).

These fluids show varied compositions from acid-sulfate type (Butterfield et al., 2011) to extremely enriched in carbonic acid (Lupton et al., 2008). Both types of systems are developed sometimes even within individual volcanoes (Ronde et al., 2001; Seewald, Reeves, et al., 2015). It is conceivable that episodes of magmatic degassing or other transients lead to an increased geochemical variability of these vents. How these processes affect metal fluxes to the seafloor and chemosynthesis-based ecosystems remains unknown. We have not attempted comprehensive modeling to examine the consequences of magma degassing on the concentrations of Sb, As, Au and Ag from the Manus back-arc basin. Evidence for magmatic controls on metal and metalloid distribution exist, although we do not know by which mechanism. Evidence from previous work indicating the presence of solid sulfide phases on vesicle walls by scanning electron microscopy and electron microprobe analyses (Kamenetsky et al., 2001; K.H. Yang and S. Scott, 1996). These phases have condensed from trapped magmatic fluids and indicate metal mobility during magma degassing. These condensed phases in the subseafloor can be expected to react with circulating seawater in the root zones of the hydrothermal vents and release some of the magmatically derived metals and metalloids to the hydrothermal fluid. Another enrichment mechanism is direct input of metals and metalloids from degassing magma, but the data presented in Craddock (2009) and Reeves et al. (2011) and Seewald, Reeves, et al. (2015) do not show correlations between established tracers of magma degassing (e.g., the sulfur isotopic composition of H_2S or the concentrations of fluorine) in the fluids from the larger eastern Manus Basin area. This hypothesis is difficult to test by modeling, because phase separation cannot be handled by the codes we were using. Another way magma degassing can affect the solubility of As, Sb, Ag, and Au is by lowering the pH. We have calculated that addition of CO_2 to the maximum concentrations soluble (several hundred mmol/kg) at PACManus) will lower the pH by the reactions $CO_2 + H_2O = HCO_3^- + H^+$ to about 3.5 (Figure 5.20).

This is actually higher than the in situ pH-values calculated of 2.7-3, indicating that another source of acidity is required. CO_2 is also fairly unreactive at temperatures around 300 °C (Bischoff and Rosenbauer, 1996), so we conclude that CO_2 degassing does not affect the transport of the four elements of interest too much. HF is a weak acid that does not dissociate at the low pH-values determined for the PACManus systems. SO_2 gas, however, is very reactive and rapidly disproportionates to sulfuric acid and either native sulfur or H_2S via the reactions:

$$4SO_2 + 4H_2O = 3H_2SO_4 + H_2S \tag{5.1}$$

$$3SO_2 + 2H_2O = 2H_2SO_4 + S \tag{5.2}$$

The sulfuric acid generated by these reactions will immediately dissociate and cause very low pH-values to develop in hydrothermal fluids affected by titration of magmatic SO_2 into the system from underlying degassing magma reservoirs. Seewald, Reeves, et al. (2015) showed that this is exactly what is taking place massively at North Su, 100 km east of PACManus. At PACManus, the evidence magma degassing is more subdued, but still discernable (Bach, Roberts, et al., 2003; Craddock and Bach, 2010; Reeves et al., 2011). Our model calculations have shown that the drop in pH associated with zone refining will increase the solubility of As, Sb, Ag, and Au (along with that of Zn, Pb, but not Cu and Fe). Although we have not conducted any modeling to address the effect of magma degassing on the solubility of As, Sb, Ag, and Au, we anticipate that the effect of lowering the pH by adding sulfuric acid would have very similar results. We expect that magmatic degassing from felsic volcanism (the Pual Ridge hosting the PACManus hydrothermal area is dacitic to rhyodacitic in composition; Beier et al., 2015) is particularly prone to SO_2 degassing, because the speciation of sulfur dissolved in these melts is shifted towards higher oxidations relative to that of basalt (Wallace, 2005).

5.7.2 Transport and deposition

In hydrothermal fluids metals have the ability to form strong aqueous complexes, with various ligands (Williams-Jones and Migdisov, 2014). However, these complexes are not yet understood for Sb, As and Ag. With our modeling, with new created databases, we have made an attempt to model these elements for the first time together and pursued to analyze the geochemical behavior systematically within a hydrothermal system. From Figures 5.15 and 5.22 it is clear that the dominancy of Au and Ag complexes in hydrothermal fluids around 280 °C and at PACManus in specific are from Au(HS)$^{2-}$ and AuHS to AuCl2− and AuOH and for Ag AgCl2− to Ag(HS)2− and AgHS. These results are conform the studies of Stefánsson and Seward (2004) and Williams-Jones, Bowell, et al. (2009), arguing that AuCl2− tends to dominate under acidic and oxidizing conditions, while Au(HS) at acidic to intermediate pH and Au(HS)2− at higher pH, based on the following reactions:

$$AuS + HS^{-} + H^{+} + 1/4O_2 = Au(HS) + 1/2H_2O \tag{5.3}$$

and

$$AuS + 2HS^{-} + H + +1/4O^{2} = Au(HS)^{2-} + 1/2H_2O \tag{5.4}$$

However, around temperatures up to 350 °C, the complexes Au(HS)2− and AuHS are dominant within a hydrothermal system, while at higher T (or at very low pH) stronger bonding between Au and Cl^{-} is expected, based on the hard-soft-acid-base (HSAB) principle (Pearson, 1963; Williams-Jones, Bowell, et al., 2009). The expected strong dependence on the HS^{-} ligand does not apply for Ag, since Ag can form stronger Cl-complexes than Au at lower temperatures (Williams-Jones, Bowell, et al., 2009; Williams-Jones and Migdisov, 2014), verifying the dominant behavior of AgCl2− at PACManus. Sb is dependent on the 'harder' OH- ligand, forming Sb(OH)^{3} T>250 °C

(Figure 5.15 and 5.22) (Zotov et al., 2003). The same behavior is observed for As, where the dominant complex is As(OH)^3. The similarity of this behavior between these two elements, in comparison to Au and Ag, could be explained by the HSAB principle that Sb-As are characterized as stronger acids than Au and Ag, and therefor prefer to make a complex with the stronger OH$^-$ ligand (Pearson, 1963).

A further striking and important observation from the dataset and modeling results, is the notable coherence in the geochemical behavior of Sb, As, Au and Ag. Throughout this dataset a strong relationship has been observed specifically between As-Ag and Sb-Au. These relationships observed, appear to be even stronger than the well acknowledged Sb-As and Au-Ag relationships. Nonetheless, further research is needed to fully comprehend the behavior of Sb, As, Au and Ag.

5.7.3 Zone refining and supergenous enrichment as trapping mechanisms

From the samples taken at PACManus several unique and strong correlations have been deduced: in general the vent fluid temperatures and pH vary between 100 and 350 °C, and 1 and 5 respectively, however As, Sb, Au and Ag are unmistakably enriched in mixed zone-refined fluid and seawater fluids at the sweet spot of T=250-280 °C and pH 2-3, corresponding to fluid samples (Figure 5.4 - 5.7) and reaction path modeling. As suggested by M.K. Tivey (1995), zone refining reactions are driven by a drop in pH caused by the precipitation of pyrite upon seawater-vent fluid mixing within the mound. These processes cause the decreased pH in the 250-280 °C fluids and are responsible for the often increased abundance of As, Sb, Ag, and Au in these fluids. These specific temperatures and acidity conditions apparently represent the ideal setting for metal enrichment through zone refining. Zone refining has been identified as key process in remobilization and redistribution of elements within an mineralization system. Zone refining in the subbasement of marine massive sulfide accumulations is driven by reactions between vent fluids, entrained seawater and minerals, foremost sulfide precipitates, in the basement. These reactions drive radical changes in the compositions of the mixed fluids that make them corrosive and prone to remobilize elements. Figure 5.6 - 5.7 shows how mineral precipitation affects the pH of the mixed fluids, causing the pH to be two log units lower at moderate temperatures than in a scenario in which these reactions with minerals are suppressed. The characteristic drop in pH when vent fluids are mixed with small portions of seawater is a hallmark of subseafloor mineral precipitation that can lead to zone refining processes. This drop in pH is clearly shown by the PACManus vent fluids, in which the in situ pH values drop, as temperatures decrease by 50-70 °C (Figure 5.6a). This drop in pH will increase solubility of an element like Zn by two orders of magnitude ($ZnS + 2\ H^+ = Zn^{2+} + H_2S$), which is clearly visible at Roman Ruins (Figure 5.6d). This behavior indicates that sphalerite is present in the subsurface of Roman Ruins (the biggest sulfide mound within the PACManus hydrothermal area) and that Zn is remobilized upon zone refining reactions. At Fenway and Satanic Mills, zone refining is also taking place, but apparently sphalerite is not present in the subbasement there, so no Zn can get mobilized. Copper shows strong decoupling from Zn (Figure 5.6d), however it is not enriched in the Roman Ruins zone refined fluids, indicating that there is no Cu-accumulations in the subseafloor that release Cu upon zone refining reactions. Fenway shows some increase in Cu and Satanic Miils shows strong enrichment in Cu in one instance. This increased Cu concentration in the Satanic Mills fluid is matched by an equally strong increase in As (Figure 5.7a). This fluid has apparently been affected by dissolution of tennantite. As is somewhat enriched in zone refined fluids from Roman Ruins. These As enrichments could be released from sphalerite that incorporates large amounts of As. Likewise, Ag is enriched in the zone refined fluids from Roman Ruins (Figure 5.7b). Again, Ag is an element that partitions into sphalerite, as indicated by the strong correlations between Zn and Ag contents in the sulfide analyses. Au is mobilized in the gassy Satanic Mills and Snowcap sites (Figure 5.7d), but not in the Roman Ruins site. The coldest of the four fluids from Fenway, on the other hand, does show some Au enrichment. Sb is markedly enriched at Satanic Mills and one from Roman Ruins.

This notion of zone refining processes is not only fully supported by the fluid samples, but also by the geochemical modeling results (Figure 5.17 - 5.18). Remobilization of these elements inside the mound is followed by precipitation of them in the topmost part of the mound, where seawater-derived fluids reside within the void spaces of the rubble pile. There, a Zn-Pb rich mineralization with high abundance of As, Sb, Ag and Au is expected to develop. The modeled concentrations of these four elements are roughly 5wt% As, 3000 ppm Sb, 1800 ppm Ag, and 30 ppm Au. These numbers are similar to the maximum concentrations of As, Sb, Ag, and Au in the PACManus massive sulfide bodies (2.3 wt.% As, 3000 ppm Sb, 400 ppm Ag, and 54 ppm Au; from Table 1 in S. Scott and Binns (1995)). The massive sulfide/talus type (Figure 5.12), which has undergone zone refinement and supergeneous enrichment, has the highest contents of bornite, digenite and sphalerite. The highest Sb and As enrichments are found in altered or secondary Cu-minerals (bornite and digenite) within these massive sulfide/talus sites, independent of the geochemical characteristics of the primary hydrothermal fluid and type mineral assemblage of the primary sulfide mound (Figure 5.16 - 5.18). Sb-minerals are not present, due to lower temperatures required to precipitate stibnite and berthierite. This observation confirms the recognized epithermal character of Sb mineralizing in the form of stibnite and/or berthierite (Figure 5.16 - 5.18) (e.g. Pohl (2011)). At higher temperatures, Sb may partition strongly into tennantite, leading to As-Sb correlations in Cu-rich massive sulfides. PACManus has low Fe values in comparison with other black smoker systems Reeves et al. (2011), which is specifically notable in sphalerite with high As, Sb and Ag, and low Au contents. The low Fe contents in the sphalerite of PACManus has been explained by the high sulfur fugacities in these systems (Keith et al., 2014). An explanation for the high As and low Fe contents could be supercritical phase separation, causing enrichment of As and depletion of Fe in the low salinity phase. Leaching of the primary felsic (dacite-rhyodacite) rocks with high As/Fe ratios and Sb contents could also have played a role (Boyle and Jonasson, 1984; Douville et al., 1999).

In summary, primary Sb, As, Ag and Au enrichments within VMS deposits on the ocean floor are positively affected by these complex reaction following magmatic degassing within a certain range of magma composition, temperature, and acidity. In addition, deep-seated seawater-rock interactions of zone refining and near-seafloor sulfide deposition of supergeneous enrichments, can lead to enrichment in these elements. The data in Figure 5.6, 5.7 and 5.19 show that zone refining is an important mechanism that affects the compositions of vent fluids (and hence distribution of metals and metalloids within the subbasement). Some of these enrichments are straightforward to interpret, e.g., Ag following Zn, others, e.g., the apparently erratic behaviors of Sb and Au cannot be fully understood based on current knowledge of the system.

5.8 Acknowledgements

We thank the captains and crews of expeditions MGLN06 (RV Melville) and SO218 (RV Sonne) and the Jason2 and MARUM Quest4000 ROV teams for excellent support at sea. Chris Heinrich is thanked for helping with thermodynamic data for gold species. Furthermore we would like to thank dr. Thal, for providing the newly produced Figure 5.2. The study is part of the lead author's PhD thesis, which was financed through the MARUM Center for Marine Environmental Research, University of Bremen.

Bibliography

Akinfiev, N.N. and A.V. Zotov (2010). "Thermodynamic description of chloride, hydrosulfide, and hydroxo complexes of Ag(I), Cu(I) and Au(I) at temperatures of 25-500°C and pressures of 1-2000 bar". In: *Geochemistry Int.* 39.10, pp. 990–1006. DOI: 10.1134/S0016702910070074.

Bach, W., S. Roberts, et al. (2003). "Controls of fluid chemistry and complexation on rare-earth element contents of anhydrite from the Pacmanus subseafloor hydrothermal system, Manus Basin, Papua New Guinea". In: *Miner. Depos.* 38.8, pp. 916–935. DOI: 10.1007/s00126-002-0325-0.

Bach, W., M. Rosner, et al. (2011). "Carbonate veins trace seawater circulation during exhumation and uplift of mantle rock: Results from ODP Leg 209". In: *Earth Planet. Sci. Lett.* 311.3-4, pp. 242–252. DOI: 10.1016/j.epsl.2011.09.021.

Baker, E.T. et al. (2008). "Hydrothermal activiy and volcano distribution along the Mariana arc." In: *J. Geophys. Res.* 113, pp. 1689–1699. DOI: 10.1029/2007JB005423. arXiv: arXiv:1011.1669v3.

Beier, Christoph et al. (2015). "Origin of silicic magmas at spreading centres-An example from the South East Rift, Manus Basin". In: *J. Petrol.* 56.2, pp. 255–272. DOI: 10.1093/petrology/egu077.

Bessinger, B. and J.A. Apps (2005). *The Hydrothermal Chemistry of Gold, Arsenic, Antimony, Mercury and Silver*. Tech. rep. Office of Science U.S. Department of Energy, pp. –52.

Binns, R.A. (2004). "Eastern Manus Basin, Papua New Guinea: guides for volcanogenic massive sulphide exploration from a modern seafloor analogue". In: *CSIRO Explor.* Pp. 59–80.

Binns, R.A., F.J.A.S. Barriga, and D.J. Miller (2007). "Leg 193 Synthesis: Anatomy of an active felsic-hosted hydrothermal system, Eastern Manus Basin, Papua New Guinea". In: *Proc. Ocean Drill. Program, Sci. Results* 193.January, pp. 1–71. DOI: 10.2973/odp.proc.sr.193.201.2007.

Binns, R.A. and S.D. Scott (1993). “Actively forming polymetallic sulfide deposits associated with felsic volcanic rocks in the Eastern Manus back-arc basin, Papua New Guinea”. In: *Econ. Geol.* 88, pp. 2226–2236.

Bischoff, J.L. and R.J. Rosenbauer (1996). “The alteration of rhyolite in CO2 charged water at 200 and 350°C: The unreactivity of CO2 at higher temperature”. In: *Geochemica Cosmochim.* 60, pp. 3859–3867.

Boyle, R.W. and I.R. Jonasson (1984). “The geochemistry of antimony and its use as an indicator element in geochemical prospecting”. In: *J. Geochemical Explor.* 20, pp. 223–302.

Butterfield, D.A. et al. (2011). “High SO2 flux, sulfur accumulation, and gas fractionation at an erupting submarine volcano”. In: *Geology* 39, pp. 803–806. arXiv: `arXiv:1011.1669v3`.

Castro, S.H. and L. Baltierra (2005). “Study of the surface properties of enargite as a function of pH”. In: *Int. J. Miner. Process.* 77.2, pp. 104–115. DOI: `10.1016/j.minpro.2005.03.002`.

Craddock, P.R. (2009). “Geochemical traces of processes affecting the formation of seafloor hydrothermal fluids and deposits in the Manus Back-arc basin”. PhD thesis, pp. 1–370.

Craddock, P.R. and W. Bach (2010). “Insights to magmatic–hydrothermal processes in the Manus back-arc basin as recorded by anhydrite”. In: *Geochim. Cosmochim. Acta* 74.19, pp. 5514–5536. DOI: `10.1016/j.gca.2010.07.004`.

Damm, K.L. von et al. (1985). “Chemistry of submarine hydrothermal solutions at 21N East Pacific Rise”. In: *Geochemica Cosmochim.* 49.11, pp. 2197–2220. arXiv: `arXiv:1011.1669v3`.

Dekov, V.M. et al. (2016). “Enargite-luzonite hydrothermal vents in Manus Back-Arc Basin: submarine analogues of high-sulfidation epithermal mineralization”. In: *Chem. Geol.* 438, pp. 36–57. DOI: `10.1016/j.chemgeo.2016.05.021`.

Douville, E. et al. (1999). “Le comportement de I’arsenic (As) et de I’antimoine (Sb) dans les fluides provenant de diffkents systgmes hydrothermaux océaniques”. In: *Earth Planet. Sci.* 328.2, pp. 97–104.

Firdu, F.T. and P. Taskinen (2010). “Thermodynamics and phase equilibria in the (Ni, Cu, Zn)–(As, Sb, Bi)–S systems at elevated temperatures (300–900 C)”. In: *Espoo Aalto Univ. Publ. Mater. . . .* Pp. 1–59.

Gamo, T. et al. (1997). “Acidic and sulfate-rich hydrothermal fluids from the Manus back-arc basin, Papua New Guinea”. In: *Geology* 25.2, pp. 139–142. DOI: `10.1130/0091-7613(1997)025<0139:aasrhf>2.3.co;2`.

Hannington, M.D., C.E.J. De Ronde, and S. Petersen (2005). “Sea-Floor Tectonics and Submarine Hydrothermal Systems”. In: *Econ. Geol.* 100th Anni, pp. 111–141.

Hannington, M.D., I.R. Jonasson, et al. (1995). “Physical and chemical processes of seafloor mineralization at mid-ocean ridges”. In: *Phys. Chem. Biol. Geol. Interact. Seafloor Hydrothermal Syst. Geophys. Monogr. 91*, pp. 115–157. DOI: `10.1029/GM091p0115`.

Hannington, M.D., K.H. Poulsen, et al. (1999). “Volcanic Associated Massive Sulfide Deposits: Processes and Examples in Modern and Ancient Settings”. In: *Rev. Econ. Geol.* Ed. by Barrie M.D. and T.C. Hannington. Volume 8. Society of Economic Geologists. Chap. 14 - Volca, pp. 325–356.

Hedenquist, J.W. and J.B. Lowenstern (1994). “Theole of magmas in the formation of hydrothermal ore deposits.” In: *Nature* 370, pp. 519–527.

Heinrich, C.A., T. Driesner, et al. (2004). “Magmatic vapor contraction and the transport of gold from the porphyry environment to epithermal ore deposits”. In: *Geology* 32, pp. 761–764. arXiv: `arXiv:1011.1669v3`.

Heinrich, C.A., D. Günther, et al. (1999). “Metal fractionation between magmatic brine and vapor, determined by microanalysis of fluid inclusions”. In: *Geology* 27, pp. 755–758. arXiv: `arXiv:1011.1669v3`.

Henley, R.W. and B.R. Berger (2013). “Nature’s refineries - Metals and metalloids in arc volcanoes”. In: *Earth-Science Rev.* 125, pp. 146–170. DOI: `10.1016/j.earscirev.2013.07.007`.

Herzig, P.M. and M.D. Hannington (1995). “Polymetallic massive sulfides at the modem seafloor A review”. In: *Ore Geol. Rev.* 10, pp. 95–115.

Ishibashi, J.-I et al. (2008). “Marine shallow-water hydrothermal activity and mineralization at the Wakamiko crater in Kagoshima bay, south Kyushu, Japan”. In: *J. Volcanol. Geotherm. Res.* 173.1-2, pp. 84–98. DOI: `10.1016/j.jvolgeores.2007.12.041`.

Johnson, J.W., E.H. Oelkers, and H.C. Helgeson (1992). *SUPCRT92: A software package for calculating the standard molal thermodynamic properties of minerals, gases, aqueous species, and reactions from 1 to 5000 bar and 0 to 1000°C.* Vol. 18. 7. Pergmamon Press Ltd, pp. 899–947. DOI: `10.1016/0098-3004(92)90029-Q`.

Kamenetsky, V.S. et al. (2001). “Parental basaltic melts and fluids in eastern Manus backarc Basin: Implications for hydrothermal mineralisation”. In: *Earth Planet. Sci. Lett.* 184, pp. 685–702. DOI: `10.1016/S0012-821X(00)00352-6`.

Kantar, Cetin (2002). “Solution and flotation chemistry of enargite”. In: *Colloids Surfaces A Physicochem. Eng. Asp.* 210.1, pp. 23–31. DOI: `10.1016/S0927-7757(02)00197-8`.

Keith, M. et al. (2014). “Effects of temperature, sulfur, and oxygen fugacity on the composition of sphalerite from submarine hydrothermal vents”. In: *Geology* 42.8, pp. 699–702. DOI: `10.1130/G35655.1`.

Krupp, E (1988). “Solnbility of stibnite in hydrogen sulfide solutions, speciation, and equilibrium constants, from 25 to 350 ° C”. In: *Geochemica Cosmochim.* 52, pp. 3005–3015.

Lupton, J. et al. (2008). “Venting of a separate CO2-rich gas phase from submarine arc volcanoes: Examples from the Mariana and Tonga-Kermadec arcs”. In: *J. Geophys. Res.* 113. DOI: `10.1029/2007JB005467`. arXiv: `arXiv:1011.1669v3`.

Lynch, D C (1982). “Standard Free Energy of Formation of NiAsS”. In: *Metall. Mater. Trans. B* 13.June, pp. 285–288.

Martinez, F. and B. Taylor (1996). “Backarc spreading, rifting, and microplate rotation, between transform faults in the Manus Basin”. In: *Mar. Geophys. Res.* 18.2-4, pp. 203–224. DOI: `10.1007/BF00286078`.

Mercier-Langevin, P. et al. (2011). “The gold content of volcanogenic massive sulfide deposits”. In: *Miner. Depos.* 46.5, pp. 509–539. DOI: `10.1007/s00126-010-0300-0`.

Moss, R. and S.D. Scott (2001). “Geochemistry and mineralogy of gold-rich hydrothermal precipitates from Eastern Manus Basin, Papua New Guinea”. In: *Can. Mineral.* 39.4, pp. 957–978. DOI: `10.2113/gscanmin.39.4.957`.

Padilla, R., C.A. Rivas, and M.C. Ruiz (2008). “Kinetics of Pressure Dissolution of Enargite in Sulfate-Oxygen Media”. In: *Metall. Mater. Trans. B* 39.3, pp. 399–407. DOI: `10.1007/s11663-008-9151-9`.

Patten, C.G.C. et al. (2016). “Mobility of Au and related elements during the hydrothermal alteration of the oceanic crust: implications for the sources of metals in VMS deposits”. In: *Miner. Depos.* 51.2, pp. 179–200. DOI: `10.1007/s00126-015-0598-8`.

Pearson, R.G. (1963). “Hard and soft acids and their bases”. In: *J. Am. Chem. Soc.* 85, pp. 3533–3539.

Pohl, W.L. (2011). *Economic Geology Principles and Practice - Metals, minerals, coal and hydrocarbons - Introduction to formation and sustainable exploitation of mineral deposits*. Vol. 1. July. Wiley-Blackwell, pp. 1–699. DOI: `10.5962/bhl.title.18736`.

Pokrovski, G.S. et al. (2006). "Antimony speciation in saline hydrothermal fluids: A combined X-ray absorption fine structure spectroscopy and solubility study". In: *Geochim. Cosmochim. Acta* 70.16, pp. 4196–4214. DOI: `10.1016/j.gca.2006.06.1549`.

Reeves, E.P. et al. (2011). "Geochemistry of hydrothermal fluids from the PACMANUS, Northeast Pual and Vienna Woods hydrothermal fields, Manus Basin, Papua New Guinea". In: *Geochim. Cosmochim. Acta* 75.4, pp. 1088–1123. DOI: `10.1016/j.gca.2010.11.008`.

Richards, J.P. (2011). "Magmatic to hydrothermal metal fluxes in convergent and collided margins". In: *Ore Geol. Rev.* 40.1, pp. 1–26. DOI: `10.1016/j.oregeorev.2011.05.006`.

Ronde, C.E.J. de (1995). "Fluid chemistry and isotopic characteristics of seafloor hydrothermal system and associated VMS deposits: potential for magmatic contributions". In: *Magmas, fluids ore Depos.* Vol. 23. Mineralogical Association of Canada, pp. 479–509. DOI: `10.1017/CBO9781107415324.004`. arXiv: `arXiv:1011.1669v3`.

Ronde, C.E.J. de et al. (2001). "Intra-oceanic subduction-related hydro- thermal venting, Kermadec volcanic arc, New Zealand". In: *Earth Planet. Sci. Lett.* 193, pp. 359–369.

Schock, E.L. et al. (1997). "Inorganic species in geologic fluids: correlations among standard molal thermodynamic properties of aqueous ions and hydroxide complexes." In: *Geochemica Cosmochim.* 61.5, pp. 907–950. DOI: `10.1017/CBO9781107415324.004`. arXiv: `arXiv:1011.1669v3`.

Scott, S.D. and R.A. Binns (1995). "Hydrothermal processes and contrasting styles of mineralization in the western Woodlark and eastern Manus basins of the western Pacific". In: *Hydrothermal Vent. Process.* Vol. 87, pp. 191–205. DOI: `10.1144/GSL.SP.1995.087.01.16`.

Seal, R.R., E.J. Essene, and W.C. Kelly (1990). "Tetrahedrite and tennantite: Evaluation of thermodynamic data and phase equilibria". In: *Can. Mineral.* 28, pp. 725–738.

Seal, R.R., R.A. Robie, P.B. Barton, et al. (1992). "Superambient heat capacities of synthetic stibnite, berthierite, and chalcostibite; revised thermodynamic properties and implications for phase equilibria". In: *Econ. Geol.* 87.7, pp. 1911–1918. DOI: `10.2113/gsecongeo.87.7.1911`.

Seal, R.R., R.A. Robie, B.S. Hemingway, et al. (1996). "Heat capacity and entropy at the temperatures 5 K to 720 K and thermal expansion from the temperatures 298 K to 573 K of synthetic enargite (Cu3AsS4)". In: *J. Chem. Thermodyn.* 28.4, pp. 405–412. DOI: `10.1006/jcht.1996.0040`.

Seewald, J.S., K.W. Doherty, et al. (2002). “A new gas- tight isobaric sampler for hydrothermal fluids”. In: *Deep Sea Res. Part O Ocean. Res. Pap.* 49.1, pp. 189–196. DOI: `10.1017/CBO9781107415324.004`. arXiv: `arXiv:1011.1669v3`.

Seewald, J.S., E.P. Reeves, et al. (2015). “Submarine Venting of Magmatic Volatiles in the Eastern Manus Basin, Papua New Guinea.” In: *Geochemica Cosmochim.* Pp. 178–199. DOI: `10.1016/j.gca.2015.04.023.`.

Stanton, R.L. (1994). *Ore elements in arc lavas*. Vol. 29. Geophysics, Oxford Monographs on Geology and Geophysics, p. 391.

Stefánsson, A. and T.M. Seward (2003a). “Stability of chloridogold(I) complexes in aqueous solutions from 300 to 600°C and from 500 to 1800 bar”. In: *Geochim. Cosmochim. Acta* 67.23, pp. 4559–4576. DOI: `10.1016/S0016-7037(03)00391-0`.

– (2003b). “The hydrolysis of gold(I) in aqueous solutions to 600°c and 1500 bar”. In: *Geochim. Cosmochim. Acta* 67.9, pp. 1677–1688. DOI: `10.1016/S0016-7037(02)01131-6`.

– (2004). “Gold(I) complexing in aqueous sulphide solutions to 500°C at 500 bar”. In: *Geochim. Cosmochim. Acta* 68.20, pp. 4121–4143. DOI: `10.1016/j.gca.2004.04.006`.

Sverjensky, D.A., E.L. Shock, and H.C. Helgeson (1997). “Prediction of the thermodynamic properties of aqueous metal complexes to 1000 degrees C and 5 kb.” In: *Geochim. Cosmochim. Acta* 61.7, pp. 1359–1412. DOI: `10.1016/S0016-7037(97)00009-4`.

Thal, J. et al. (2014). “Geologic setting of PACManus hydrothermal area — High resolution mapping and in situ observations”. In: *Mar. Geol.* 355, pp. 98–114. DOI: `10.1016/j.margeo.2014.05.011`.

Tivey, M. (2007). “Generation of Seafloor Hydrothermal Vent Fluids and Associated Mineral Deposits”. In: *Oceanography* 20.1, pp. 50–65. DOI: `10.5670/oceanog.2007.80`.

Tivey, M.K. (1995). “Modeling chimney growth and associated fluid flow at seafloor hydrothermal vent sites”. In: *Seafloor hydrothermal Syst.* Ed. by S.E. Humphris et al. Washington, DC: American Geophysical Union, pp. 158–177. DOI: `10.1017/CBO9781107415324.004`. arXiv: `arXiv:1011.1669v3`.

Tivey, M. et al. (2006). *Cruise report R/V Melville MAGELLAN-06*. Tech. rep. Woods Hole Oceanographic Institution, pp. 1–67.

Vink, B.W. (1996). “Stability relations of antimony and arsenic compounds in the light of revised and extended Eh-pH diagrams”. In: *Chem. Geol.* 130.1-2, pp. 21–30. DOI: 10.1016/0009-2541(95)00183-2.

Wagman, D.D. et al. (1982). *The NBS Tables of Chemical Thermodynamic Properties*.

Wallace, Paul J. (2005). “Volatiles in subduction zone magmas: Concentrations and fluxes based on melt inclusion and volcanic gas data”. In: *J. Volcanol. Geotherm. Res.* 140.1-3, pp. 217–240. DOI: 10.1016/j.jvolgeores.2004.07.023.

Welham, N J (2001). “Mechanochemical processing of enargite (Cu3AsS4)”. In: *Hydrometallurgy* 62, pp. 165–173.

Williams-Jones, A.E., R.J. Bowell, and A.A. Migdisov (2009). “Gold in solution”. In: *Elements* 5.5, pp. 281–287. DOI: 10.2113/gselements.5.5.281.

Williams-Jones, A.E. and A.A. Migdisov (2014). “Experimental Constraints on the Transport and Deposition of Metals in Ore-Forming Hydrothermal Systems”. In: *Spec. Publ.* Vol. 18. Society of Economic Geologists. Chap. 5, pp. 77–95.

Williams-Jones, A.E. and C. Norman (1997). “Controls of mineral parageneses in the system Fe-Sb-S-O”. In: *Econ. Geol.* 92.3, pp. 308–324. DOI: 10.2113/gsecongeo.92.3.308.

Yang, K and S D Scott (2006). “Magmatic fluids as a source of metals in arc/back-arc hydrothermal systems: evidence from melt inclusions and vesicles”. In: *Back Arc Spreading Syst. Geol. Biol. Chem. Phys. Interact.* Geophysica.1, pp. 163–184.

Yang, K.H. and S.D. Scott (1996). “Possible contribution of a metal-rich magmatic fluid to a sea-foor hydrothermal system”. English. In: *Nature* 383.6599, pp. 420–423. DOI: 10.1038/383420a0.

Yund, R.A. (1962). “The system NiAsS phase relations and mineralogical significance.pdf”. In: *Am. J. Sci.* 260, pp. 761–782.

Zotov, A.V., N.D. Shikina, and N.N. Akinfiev (2003). “Thermodynamic properties of the Sb (III) hydroxide complex Sb(OH)3 (aq) at hydrothermal conditions”. In: *Geochemica Cosmochim.* 67.10, pp. 1821–1836. DOI: 10.1016/S0016-7037(00)01281-4.

CHAPTER 6

Summary and Outlook

The topic of this PhD project was to deduce new geochemical models of Sb(-As,Au,Ag) mineralization in Archaean and modern hydrothermal settings, through extended datasets from the Murchison Greenstone Belt (MGB) and the Manus back-arc basin. A comparison can be made between these ore deposits, because the prominent Sb-mineralization at the Antimony Line (AL) located at the MGB, South Africa, has been related to seafloor magmatic-hydrothermal processes associated with an Archaean back-arc basin (Schwarz-Schampera et al., 2010). To emphasize the parallels of the AL deposit with modern back-arc massive sulfide mineralization systems, an in depth qualitative and quantitive research of the Sb(-As-Ag-Au) behavior in magmatic-hydrothermal hypogene and supergene deposits has been preformed. This study is built on the notion that a knowledge gap still exists in the field of ore petrology and geochemistry regarding Au-Sb(-As) deposits within (Archaean) suture zones and their possible relationship to recent back-arc settings. Geochemical models of ore deposits, and in specific, Au-As-Sb deposits are classified from low temperature hydrothermal to medium temperature metamorphogone-hydrothermal settings (Obolensky et al., 2007; Pohl, 2011; USGS, 2015) and interpreted to be produced by boiling of CO_2-rich fluids and adiabatic cooling (Hagemann and Lüders, 2003; Pohl, 2011). This is based on the fact that antimony is commonly distributed throughout many different types of mineral deposits and displays no evident affinity to any particular metallogenic period or province (Boyle and Jonasson, 1984). Despite these large diversities in geophysical, mineralogical and geochemical settings, a more detailed geochemical model for Au-Sb(-As-Ag) mineralization is desired.

Studying the MGB provided an insight in the solubility of Sb and As in aqueous solutions from felsic magmatic precursor rocks and the effect of later structural evolution of the greenstone belt and related alteration processes like serpentinization and listvenization. Major and trace elements of gangue material and Sb-As-Fe-Cu mineralization, together with stable isotope $\delta^{18}O$ and $\delta^{13}C$ studies have been employed to comprehend the behavior and relationship of Sb and As mineralization and to investigate the mobilizing and trapping mechanisms of the hydrothermal system combined with their geochemical interaction with the surrounding host rocks. Geochemical reaction path modeling with the use of Geochemical Workbench provided insights into the geochemical characteristics of these geological mechanisms. The MGB has been interpreted as an Archaean orogenic gold deposit, which has been formed under greenschist facies conditions with hydrothermal alteration assemblages developed in ductile to brittle deformation, with temperatures around 200-420°C and CO_2-rich fluids where the primary mineralization is connected to an ore fluid originating from a granitoid magmatic or a metamorphic devolatization model (Hutchinson, 1993; McCuaig and Kerrich, 1998; Ridley and Diamond, 2000), where the phase relations clearly indicate a shift from low $f\ S_2$ and low $f\ O_2$ to high $f\ S_2$ and low $f\ O_2$, caused by carbonation and silicification. The work presented in this thesis has clearly shown tha these alteration processes were induced by serpentinization and listvenization due to mineralization and metasomatic reactions involving the meta-ultramafic rocks and felsic protoliths. Primary mineralization is located at the periphery between these ultramafic and felsic protoliths, and is dominated by As-Sb-Ni-Cu, shifted towards As-Sb-Fe-Cu, as indicated by the loss of ullmanite and enrichment of berthierite followed by the alteration of berthierite into stibnite. From these results we propose that metasomatic reactions involving ultramafic rocks may make for efficient traps of Sb and related elements (As, Ag, Hg, Au). The buffering capacities of the host rocks could play a general role in the formation of many orogenic lode deposits and should be acknowledged as a qualitative parameter for a geochemical model for orogenic gold deposits. The possibility that metasomatic reactions can provide an efficient trapping mechanism for elements like Sb, As, and Au had been neglected before, except by Williams-Jones and Norman (1997). The hypotheses we proposed in chapters 3 and 4 of this thesis provide a solid theoretical and observational foundation upon which these ideas can be further explored. It is likely that the metasomatic processes proposed as trapping mechanisms in the AL in the MGB could also have played a role in other orogenic lode deposits.

Following a similar methodological set up, the auriferous VMS deposit located in the PACManus hydrothermal area in the Manus back-arc basin has been subjected to a similar combination of quantitative observational and theoretical research methods. The geochemical dataset of fluid samples and whole rock samples has been used in geochemical modeling to demonstrate that the elevated concentrations of Sb, As, Au and Ag at PACManus are likely related to magmatic degassing in a terrian dominated by felsic volcanism. The Sb, As, Ag and Au enrichments are positively affected by complex reactions that are in part due to magmatic degassing and are heavily influenced by deep-seated seawater-rock interaction, zone refining in near-seafloor sulfide deposits at temparetures around 250-280°C and pH values between 2-3 followed by supergeneous re-working the topmost sections of the sulfide mounds at lower temperatures.

The dominant Sb complex, responsible for the Sb enrichments at these hydrothermal systems at temperatures between 250°C-400°C has been deduced to be $Sb(OH)_3$, whereas prominent epithermal Sb-mineralization at T<150°C visible as stibnite-berthierite mineralization has been related to reduced bisulfide Sb-complexes. These results are based on our geochemical modeling and imply that Sb is still present within hydrothermal systems at higher temperature and therefore could play an essential role within the (forming) ore deposit. A further striking and important observation is the unmistakable strong correlation between the geochemical behavior between Sb, As, Au and Ag. Throughout the dataset a strong relationship has been observed between As-Ag and Sb-Au. The complexity of the conjoined geochemical behavior is explained by the contradicting behavior or different reduced and oxidized complexes present of Sb, As, Au and Ag, due to the sensitivity to variations in oxygen fugacity, temperature and pH. Lastly, these newly gained comprehension confirms that Sb, As, Au and Ag contents could be used as new tracer elements for felsic magmatic input.

The Sb enrichments in the PACManus systems are moderate (up to 3000 ppm), indicating that these processes can plausibly explain a pre-enrichment of Sb in supra-subduction zone environments. In the Archean analogue, this would be the volcanic-sedimentary Weigel formation that hosts the AL. However, the massive enrichment of Sb in the AL is due to wholesale reworking of the Sb in the region upon orogenic processes that post-date the formation of these primary lithologies by hundreds of millions of years.

The overall result of the thesis wirk underlines the importance of quantitative research, in other words comparing geochemical observations of major and trace elements of both the gangue material and the sulfides of an ore deposit with geochemical reaction path modeling. This approach is well-suited to examine the effects of variations in host lithologies and the influence of (slight) variations in temperature, oxygen fugacity and pH of the ore forming solutions. Both the transferring fluid and buffering capacities of host rock material can cause great diversities in metal and metalloid speciation within hydrothermal fluids, sulfide mounds and suture zones. Finally, the importance of geochemical analyses of non-prominent metal concentrations within the field of ore petrology should be acknowledged. For instance, although further research in this direction is needed, the tight relationships between Sb and Au indicate that Sb could be used as a proxy for Au mineralization in VMS (and some orogenic lode) deposits.

Bibliography

Boyle, R.W. and I.R. Jonasson (1984). “The geochemistry of antimony and its use as an indicator element in geochemical prospecting”. In: *J. Geochemical Explor.* 20, pp. 223–302.

Hagemann, S.G. and V. Lüders (2003). “P-T-X conditions of hydrothermal fluids and precipitation mechanism of stibnite-gold mineralization at the Wiluna lode-gold deposits, Western Australia: conventional and infrared microthermometric constraints”. In: *Miner. Depos.* 38.8, pp. 936–952. DOI: `10.1007/s00126-003-0351-6`.

Hutchinson, R. W. (1993). “A multi-stage, multi-process genetic hypothesis for greenstone-hosted gold lodes”. In: *Ore Geol. Rev.* 8.3-4, pp. 349–382. DOI: `10.1016/0169-1368(93)90022-Q`.

McCuaig, T.C. and R. Kerrich (1998). *P—T—t—deformation—fluid characteristics of lode gold deposits: evidence from alteration systematics*. Vol. 12. 6, pp. 381–453. DOI: `10.1016/S0169-1368(98)80002-4`.

Obolensky, A.A. et al. (2007). “Antimony in hydrothermal processes: solubility, conditions of transfer, and metal-bearing capacity of solutions”. In: *Russ. Geol. Geophys.* 48, pp. 992–1001. DOI: `10.1016/j.rgg.200`.

Pohl, W.L. (2011). *Economic Geology Principles and Practice - Metals, minerals, coal and hydrocarbons - Introduction to formation and sustainable exploitation of mineral deposits*. Vol. 1. July. Wiley-Blackwell, pp. 1–699. DOI: `10.5962/bhl.title.18736`.

Ridley, J.R. and L.W. Diamond (2000). *Fluid chemistry of orogenic lode gold deposits and implications for genetic models*.

Schwarz-Schampera, U., H. Terblanche, and T. Oberthür (2010). "Volcanic-hosted massive sulfide deposits in the Murchison greenstone belt, South Africa". In: *Miner. Depos.* 45, pp. 113–145. DOI: `10.1007/s00126-009-0266-y`.

USGS (2015). *Antimony*. Tech. rep. U.S. Geological Survey, pp. 18–19. DOI: `10.1017/CBO9781107415324.004`. arXiv: `arXiv:1011.1669v3`.

Williams-Jones, A.E. and C. Norman (1997). "Controls of mineral parageneses in the system Fe-Sb-S-O". In: *Econ. Geol.* 92.3, pp. 308–324. DOI: `10.2113/gsecongeo.92.3.308`.